Structural Analysis and Optimum Design of Geodesically Stiffened Composite Panels

by

John L. Phillips

Thesis submitted to the Faculty of the
Virginia Polytechnic Institute and State University
in partial fulfillment of the requirements for the degree of
Master of Science
in
Engineering Mechanics

APPROVED:

Zafer Gürdal, Chairman

O. Hayden Griffin, Jr.

Eric R. Johnson

February, 1990

Blacksburg, Virginia

Structural Analysis and Optimum Design of

Geodesically Stiffened Composite Panels

by

John L. Phillips

Zafer Gürdal, Chairman

Engineering Mechanics

(ABSTRACT)

A simple, computationally efficient analysis approach is developed to predict the buckling of geodesically stiffened composite panels under in-plane loads. This procedure accounts for the discrete flexural contribution of each stiffener through the use of Lagrange multipliers in an energy method solution. An analysis is also implemented for the buckling of simply supported anisotropic rhombic plates. Examples are presented to verify results of the stability analyses and to demonstrate their convergence behavior.

Analysis routines are coupled with a versatile numerical optimizer to create a package for the design of minimum-mass stiffened panels, subject to constraints on buckling of the panel assembly, local buckling of the stiffeners, and material strength failure. The design code is used to conduct a preliminary design study of structurally efficient stiffened aircraft wing rib panels. Design variables include thickness of the skin laminate, stiffener thickness, and stiffener height. Applied loads are uniaxial compression, pure shear, and combined compression-shear. Two different geodesically stiffened wing rib configurations with increasing numbers of stiffeners are considered. Results are presented in the form of structural efficiency curves and are compared with those for minimum-weight longitudinally stiffened panels and unstiffened flat plates. Trends in design parameters, including skin thickness and stiffener height, stiffener thickness, stiffener aspect ratio, stiffener load fraction, and stiffener mass fraction, are also examined for the geodesic panels under compression and shear. The effects of skin laminate geometry and anisotropy on the local buckling behavior of cross-stiffened geodesic panels are examined using the rhombic plate analysis.

Acknowledgements

Funding for this work was provided by the Structural Mechanics Branch of the NASA Langley Research Center, through Grant NAG-1-643. Technical monitor was Dr. James H. Starnes, Jr. The author gratefully acknowledges the financial support.

The author would like to thank his advisor, Professor Zafer Gürdal, for his time, effort, and encouragement over the term of this work. He would also like to thank Professors Hayden Griffin and Eric Johnson for serving on his committee. The help provided by Guy Gendron for the finite element analyses and by Fred Stoll for the stiffener buckling work is appreciated. Finally, thanks are due to Mara Knott, whose perpetually cheerful answers often solved the mysteries of IBM mainframe computing.

Above all, the author would like to thank his family, friends, and Angie for their patience, understanding, and support throughout this ordeal.

Table of Contents

List of Illustrations

List of Tables

1.0 Introduction

Flight performance of aerospace structures is highly weight sensitive. Reduction in vehicle structural weight allows more payload to be carried, improves fuel efficiency, and increases maximum flight range. Weight reduction also has a multiplicative effect, in that decreasing the mass of one component may allow a corresponding reduction in the mass of its neighboring structure, and so on. Since design with metals is relatively mature, significant reduction in vehicle structural weight will require resorting to materials with improved elastic and strength properties. For airframe applications the immediate future appears to lie with fibers such as graphite, boron, aramid, glass, or any combination thereof, in a polymeric matrix. For rocket-type launch vehicles and fighter-type aircraft, these materials have been adopted essentially without regard to cost. For their use to be widespread in commercial aircraft, however, it must be demonstrated that composites are competitive with metals, not just with respect to weight, but also from cost, reliability, durability, repairability, and numerous other standpoints.

Concurrent with the adoption of advanced composite materials, innovative design concepts for aircraft structures must be investigated to realize the full potential of these materials. At first glance, the weight-specific stiffness and strength properties of the new generation fibers appear to be a phenomenal improvement over metals. However, when their properties are "diluted" by the requisite matrix material, off-axis ply orientation for damage tolerance, bulky joints, reinforcement

around fasteners, and so forth, the advantage narrows considerably. Added to this is the high price of raw material, labor-intensive manual layup procedures, and costly autoclaving required for most composite materials systems. For these reasons, the direct replacement of metals with composites in existing designs is marginally successful at best. As far back as the 1940's, attempts have been made to replace metallic aircraft components with fiber-reinforced plastic equivalents[1]. These first attempts ended in failure, with the plastic versions significantly heavier than their metallic counterparts. Although this was due in part to a lack of really good fiber and matrix materials, it was also attributable to the retention of conventional metallic construction methods using many separate parts fastened together[1]. In more recent history, the similar practice of fastening standard quasi-isotropic graphite-epoxy laminates directly in place of metallic sheets has earned them the nickname of "black aluminum."

To put the problem of effective design with composites in perspective, it is worthwhile to briefly discuss metallic structure design practice. Metallic aircraft structures have traditionally used a framework of stiffeners running in two orthogonal, or near orthogonal, directions and covered by a stressed skin. Examples include stringer-rib panels for wings and stringer-frame shells for fuselages. The framework members are extruded, formed, or forged components connected together and to the skin by thousands of fasteners. The unique requirements of rocket-powered vehicles in the 1960's caused a reassessment of this practice. The cylindrical walls for boosters had to be leakproof and, of course, as light as possible. The first requirement led to the adoption of an integrally stiffened shell structure for the case. The second requirement was met by the use of machined stiffeners in a square array, sometimes called a "waffle plate." This orthogonal stiffening pattern can carry certain loads very efficiently. However, it was noted that orthogonal stiffening patterns are "inherently four bar links prevented from collapsing by the integral skin and as a result have little in-plane torsional resistance capability."[2] A NASA-sponsored research project by McDonnell Douglas Astronautics Company concluded that the most promising alternative involved triangulation of the stiffening members to form what was called "isogrid." Isogrid refers to the fact that a grid of stiffeners forming equilateral triangles acts similar to an isotropic material. Isogrid was

subsequently used on two major space programs, the Thor-Delta launch vehicles and Skylab, and was tested for use on the Space Shuttle[2].

Several advantages have been cited for the use of metallic isogrid, including ease of analysis, structural efficiency, damage tolerance, and maintainability[2]. The equilateral triangular grid of stiffeners displays an overall isotropic nature and a Poisson's ratio of 1/3, which is similar to that of many metals. In addition, the grid has many repeating cells so that smeared stiffener theory can be used to mathematically transform the stiffened sheet into an equivalent homogeneous material. This means that many existing analytical solutions for unstiffened isotropic plates can still be used for isogrid design. With regard to structural efficiency, isogrid is claimed to display a high stiffness-to-weight ratio and to be efficient for both in-plane and bending loads. For compression-loaded cylinders, isogrid stiffeners were found to require less depth than a rectangular stiffening system for the same load-carrying capability[2]. As a result, for the same interior size the isogrid-stiffened cylinder had a smaller outside diameter and concomitant lower weight. An isogrid stiffener network forms a complete structure able to support in-plane tension, compression, and shear and out-of-plane bending loads. It can therefore be used either as stiffening for a skin or as an open lattice. It also means that cutouts in an attached skin can be accommodated without excessive weakening of the structure. Thirdly, the isogrid structure is considered highly damage tolerant due to the multiplicity of load paths. Since the stiffener grid does not rely on the skin for support, shear and tensile loads can be carried around a flaw by the redundant lattice system. It is also thought that if a separate lattice and skin are bonded together, this will prevent crack propagation from one to the other. Finally, applications requiring good torsional stiffness may use open isogrid rather than closed torque boxes. This improves inspectability, access to all surfaces, and elimination of moisture entrapment.

Since isogrid appears to be an efficient and practical structural configuration, its applicability to modern composite structures has been studied extensively. McDonnell Douglas conducted a program to test the feasibility of fabricating isogrid panels from short-fiber graphite and polyimide resin. The project involved the development of molding equipment and procedures, material

characterization, and fabrication of prototype panels. Compression testing of these panels, both open lattice and with bonded skin, revealed that local imperfections seem to dominate the buckling behavior[3]. McDonnell Douglas later developed another isogrid panel which was claimed to possess all the benefits of conventional isogrid stiffening as well as the advantages of high performance composites[4]. The new process involved weaving or braiding continuous fibers around a mandrel-like tool to produce what was called "continuous fiber advanced composite isogrid" [CFACI]. In addition to the structural advantages of continuous fiber placement, this process can be completely automated. Automation allows economical fabrication and ensures uniform, high quality parts which can be made in many different shapes. Scatter in experimental buckling loads for the prototype panels revealed that consistent part dimensions are critical. However, the authors felt that this would not pose a problem in a production environment[4]. Correlation of experimental buckling loads and simplified theory gave reasonable agreement but indicated that transverse shear deformation effects are significant[5]. The weaving process renders the stiffeners nearly unidirectional, which is efficient as they carry primarily uniaxial loads. At the same time, the transverse shear stiffness is relatively low as it is largely dependent on matrix properties. An experimental study involving the selective cutting of stiffeners in a compression panel revealed that CFACI is indeed highly damage tolerant[6]. It was further suggested that CFACI be used in applications prone to foreign object damage. A detailed summary of the experimental procedures and data for the CFACI tests can be found in the work by Reddy[7].

The studies on CFACI have demonstrated that filament-wound composite panels represent an efficient integrally stiffened structure, make maximum use of the superior properties and flexibility of an advanced composite materials system, and are amenable to automated manufacturing techniques. The result is a weight efficient, damage tolerant, economical structure. As mentioned earlier, the isogrid concept was originally developed to improve the torsional stiffness of cylinders (or shear stiffness of panels) over conventional orthogonal stiffening. It was also mentioned that isogrid results in a structure which is essentially isotropic in nature, having no preferred stiffness direction. While this may be appropriate for some applications (such as pressure-loaded domes or spheres),

many structures have higher stiffness and strength requirements in specific directions. Indeed, the proponents of isogrid concede that "there will be some applications where weight penalty may be associated with isogrid's uniformity of configuration and isotropic stiffening."[4] As such, it is expected that the efficiency of stiffened composite structures may be improved by going to more general stiffening arrangements, thereby further tailoring their properties to the application. This is the basis of the "geodesic" stiffening concept, where reinforcement is provided by a regular array of intersecting oblique stiffeners. Much as ply angles in a laminate are chosen to maximize certain stiffness or strength characteristics, varying stiffener orientations permits considerable geometric tailoring of component properties to the application. Geodesic stiffening still offers advantages in structural efficiency due to triangulation of stiffening members, in damage tolerance due to multiple load paths, and in production economy through filament winding and preform manufacturing techniques, which have been demonstrated for isogrid.

Research on filament-wound integral geodesic stiffening for aircraft primary structure appears to have focused primarily on fuselage applications. Of course, the large continuous cylindrical shape lends itself to filament winding techniques and the potential for production efficiency improvements through reduction in number of parts and fasteners is enormous. For example, a prototype geodesically stiffened fuselage section with integral bulkheads for the all-composite Beech Starship has been filament wound in only a few hours[8]. The geodesically stiffened fuselage concept is compared to a conventional fuselage in Figure 1. Flat, integrally stiffened panels such as wing spars, ribs, and covers (Figure 2) are also under consideration for use as primary load-bearing structure in future transport aircraft. Advances in automated material placement, such as filament winding techniques for CFACI, have meant that noncylindrical components of many shapes can be manufactured economically. The details of an innovative manufacturing process for the geodesically stiffened wing spar are shown in Figure 3.

Additional work is required to make the best use of geodesically stiffened composite panels, particularly in the areas of structural analysis and design. To this end, the goal of the present research work is to examine methods for the analysis and design of flat, geodesically stiffened panels under

INNOVATIVE FABRICATION CONCEPT

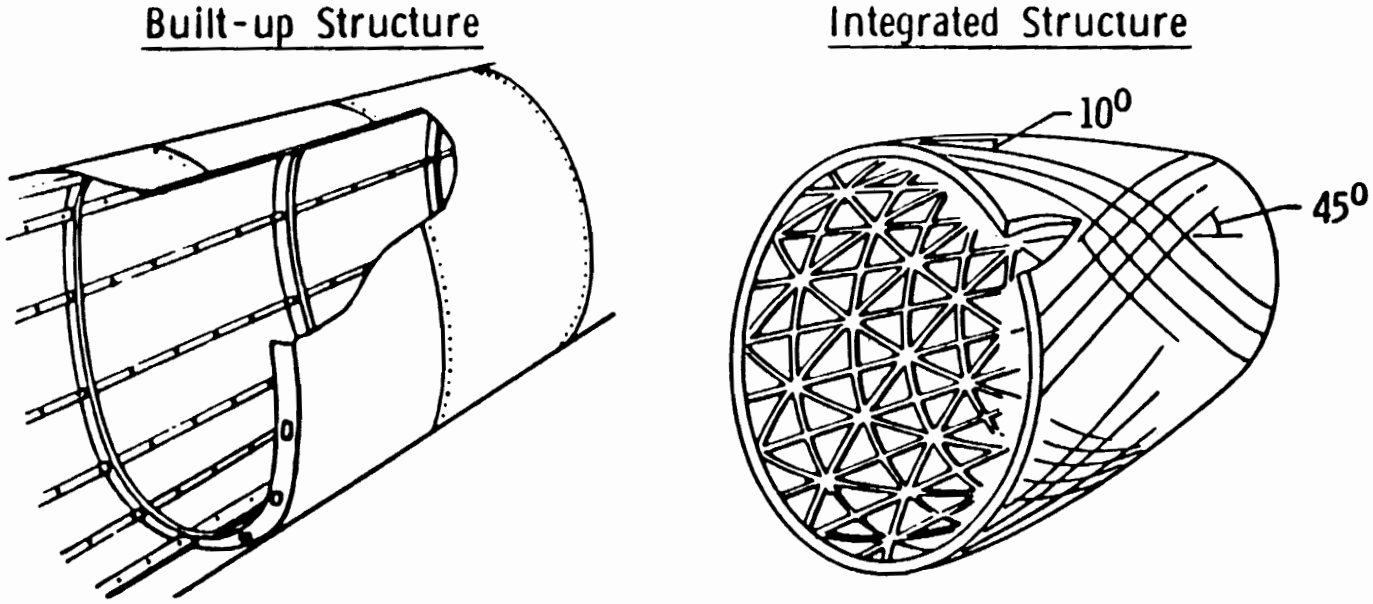

- Highly labor intensive
- Large number of parts
- Large number of fasteners
- High structural assembly costs

- Highly automated fabrication
- Integral stiffened cocured design
- Low cost finished structure

Figure 1. Filament Wound Geodesically Stiffened Fuselage Concept: [After Freeman[9]]

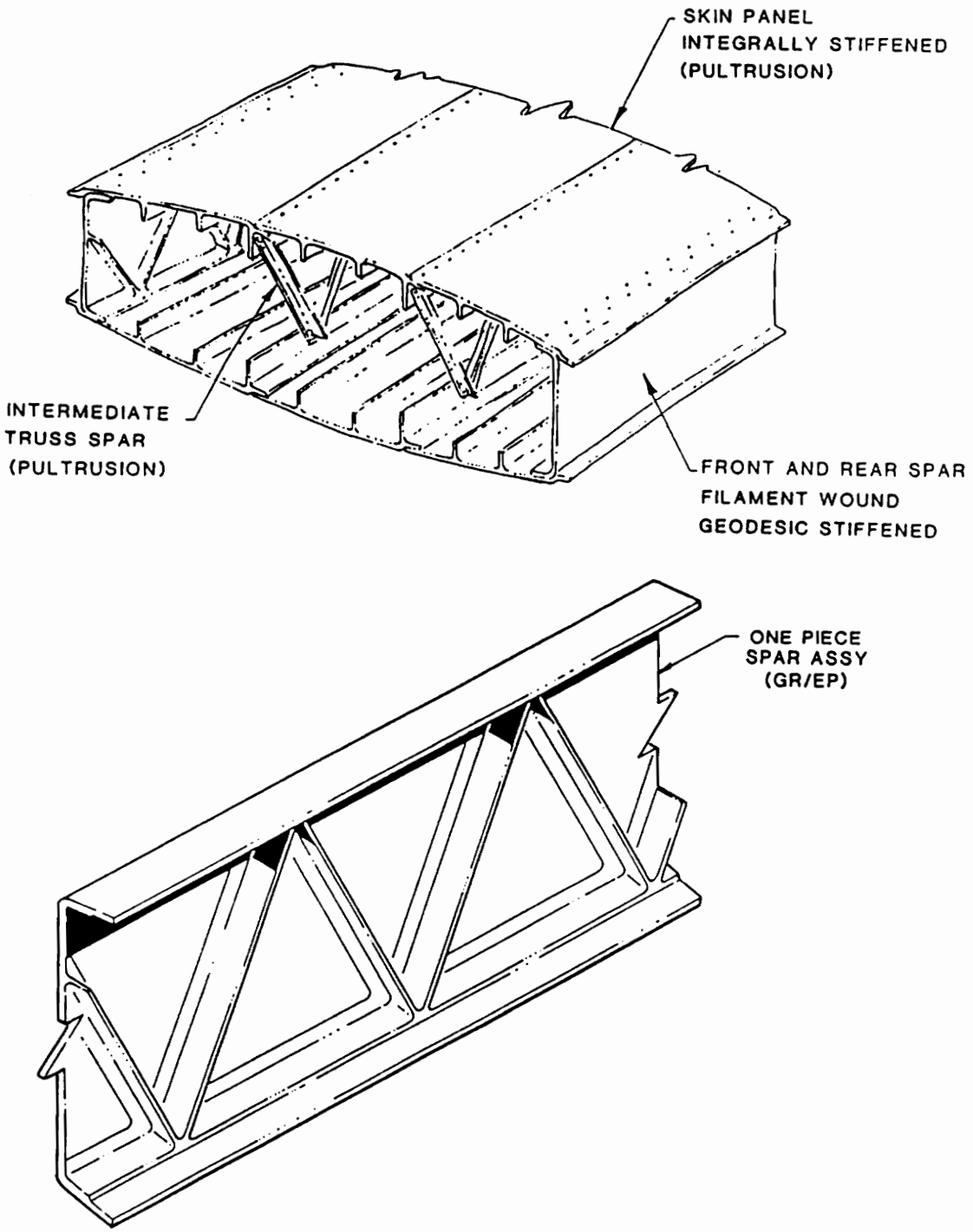

Figure 2. Wing Box Assembly with Geodesically Stiffened Spar: [After Barrie, *et al*[10]]

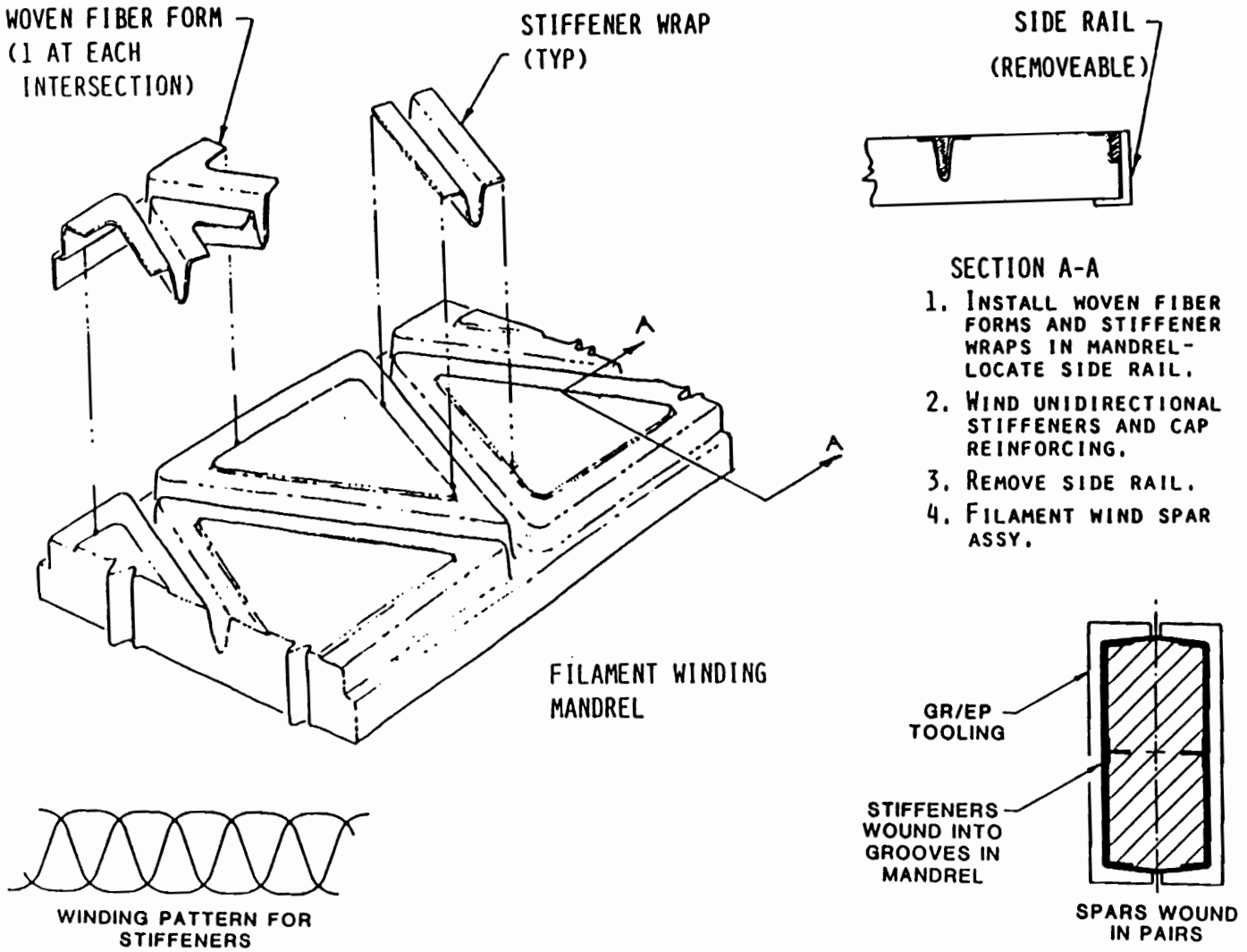

Figure 3. Geodesically Stiffened Spar Fabrication Method: [After Barrie, *et al*[10]]

in-plane loads. The geodesic stiffening concept is then applied to the design of a representative aircraft structural component. To outline following chapters, Section 2.0, Design Study Methods, describes the aircraft component, a wing rib panel, chosen for the study and how it is modelled. Currently available structural analysis and design methods are reviewed for their applicability to this problem. The need for and subsequent development of a new design code developed as part of the research work are then described. Finally, the scope of the design study is outlined. Section 3.0, Analytical Development, describes in detail the theory behind the the analysis methods used in the design work. In Section 4.0, Verification and Examples, the analyses developed in Section 3.0 are compared against established analysis methods and published results, where they exist, for verification. Convergence studies are also conducted to demonstrate how analysis parameters can affect the results. In Section 5.0, Wing Rib Design Study Results, the new design code is used to conduct an optimization study seeking minimum-weight designs for the wing rib panel. Two geodesically stiffened configurations with varying numbers of stiffeners are designed for axial compression, shear, and combined loads and compared with equivalent flat and longitudinally stiffened panels. Results of the research work are summarized in Section 6.0, Concluding Remarks.

2.0 Design Study Methods

As suggested in the introduction, the apparent advantages of applying geodesic stiffening concepts to composite structural components include high stiffness-to-weight ratio, tailorability, damage tolerance, and economy of manufacture. In order to examine the concept further, a representative aircraft component is to be designed with geodesic stiffening. Therefore, computationally efficient means of performing structural analysis and preliminary design optimization of this component, an aircraft wing rib panel, are sought. In Section 2.1, the geometry and load parameters for a typical wing rib are introduced. The manner in which the wing rib is modelled for the present study is also outlined. In Section 2.2, the choices in available design codes and structural analysis methods for use with geodesically stiffened panels are reviewed. The need to develop a new design code and the basis for the analysis approach of that code are subsequently presented. Finally, in Section 2.3, the scope of the present design study is established.

2.1 *Geodesically Stiffened Wing Rib Panels*

A promising application for geodesic stiffening concepts appears to be the wing rib panel for a large transport aircraft (Figure 4). Essentially a wing rib is a short stiffened panel which separates the upper and lower skins of an aircraft wing. The wing rib under consideration is similar to a center wing box rib of a Lockheed C-130 transport aircraft. The rib closes a large torque-box formed by spars fore and aft and wing skins with stringers top and bottom. Aerodynamic loads acting on the wing surfaces and forces due to engines, fuel load, and so forth result in bending and twisting of the wing structure. Bending of the wing causes axial compressive loading of the rib, whereas twisting introduces shear loading. Some wing ribs also act as fuel cell close-out panels where they receive significant pressure loading from the fuel.

For the present study, the wing rib is modelled as a rectangular panel 80 inches wide in the wing chord direction and 28 inches high in the wing thickness direction (Figure 5). The panel incorporates a grid of integral blade stiffeners of constant rectangular cross-section. In view of the current trend towards filament winding manufacturing techniques, the stiffeners are assumed to be composed of unidirectional material oriented along each stiffener axis. Design details, such as stiffener flanges, intersection preforms, or stiffener wraps (as shown in Figure 3) are not considered. To eliminate bending-extension coupling, the skin is symmetrically laminated and stiffening ribs are located on both sides of the skin, symmetrical about the midplane of the skin laminate. This should not be an entirely impractical configuration, as a wing rib is not bound by any aerodynamic requirement to have one smooth surface. Also, the elimination of bending-extension coupling can improve the buckling performance of a component under axial load. To eliminate extension-shear coupling, the skin laminate is balanced (angle plies occur in $\pm\theta$ pairs only) and oblique stiffeners occur in pairs oriented at equal but opposite angles with respect to the panel coordinate axes. Regarding boundary conditions, the actual degree of elastic restraint against edge rotation around the perimeter of the wing rib is unknown and no doubt complex. To assure conservative designs,

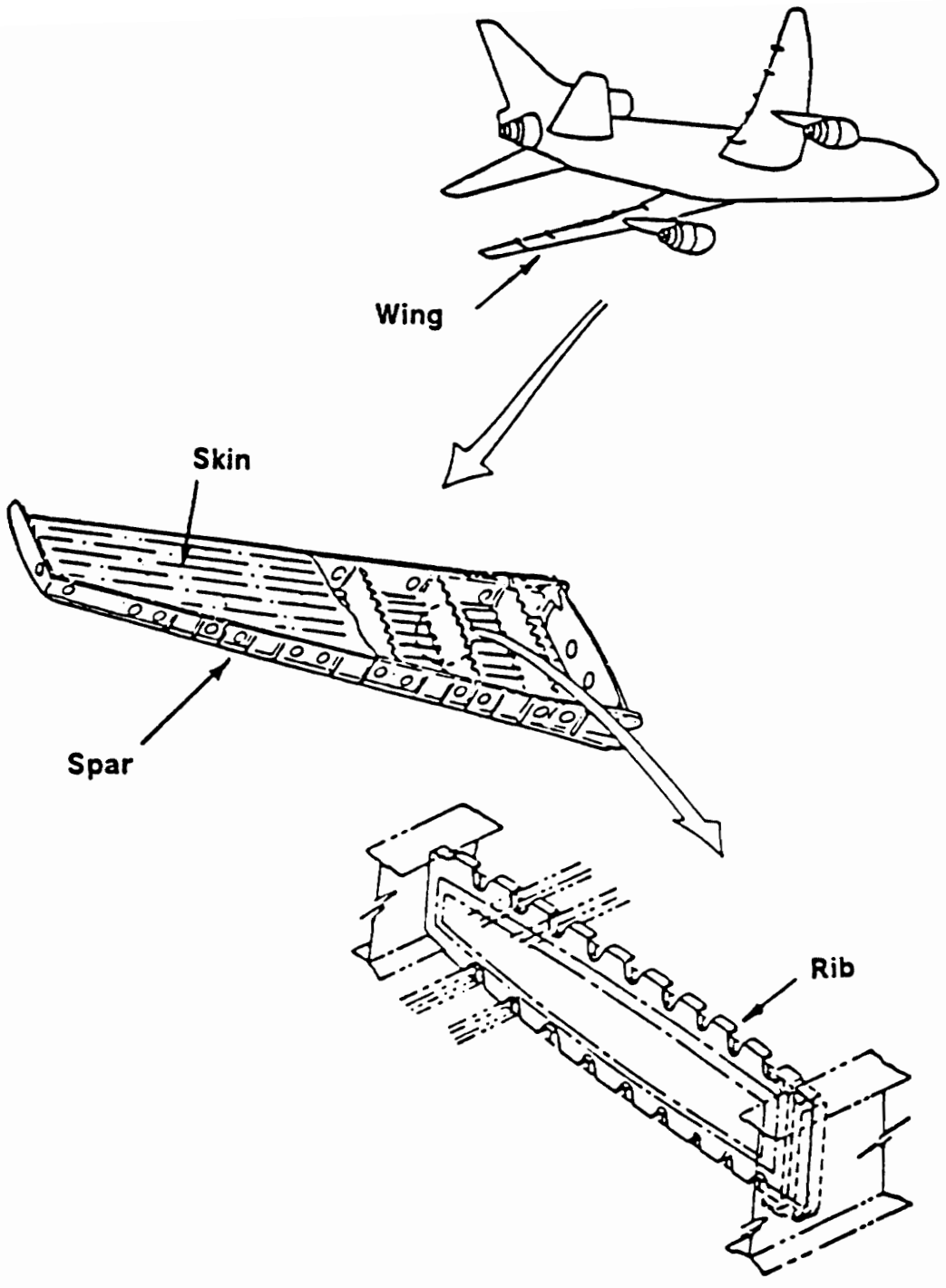

Figure 4. General Wing Structure Diagram: [After Swanson[11]]

the panel edges are treated as simply supported. Also, it is assumed that the structure surrounding the panel is sufficiently rigid that the overall panel extensional deformation in the X direction (due to Poisson effect under axial compression N_y) is zero. This assumption does not affect shear response as there is no coupling between shear and extension for the panels under consideration. Further discussion of assumptions regarding the geometry and boundary conditions, plus their effect on the analysis, may be found in Section 3. Finally, the uniform applied loads considered are uniaxial compression N_y, pure shear N_{xy}, and combined compression-shear. Transverse pressure loading, due possibly to an adjacent fuel cell, is not considered.

Four prospective configurations are considered for the wing rib panel: unstiffened flat plate, longitudinally stiffened panel, diagonally stiffened panel, and cross stiffened panel (Figure 6). The performance of the geodesically stiffened (diagonal and cross) arrangements will be evaluated using the more conventional flat plate and longitudinally stiffened panel for comparison. In Figure 6, the shaded portion of each stiffened panel indicates what is defined as a unit stiffened cell. It should be noted that this definition is arbitrary, but was chosen such that the edge distance between stiffeners is roughly equal between geometries with the same number of cells. Also, the maximum wavelength of inter-stiffener skin buckling modes is approximately equal for all three stiffened configurations. Each panel can have any number of stiffened cells (except for the longitudinally stiffened panel, where the one cell case is undefined).

2.2 *Analysis and Design Tools*

Preliminary design optimization studies are typically conducted using computerized design codes, which consist of two parts. The path taken by the design is controlled by an optimizer which attempts to improve the design, where "improvement" is generally defined as reducing the mass of the component. The optimizer varies specified design variables in accordance with mathematical opti-

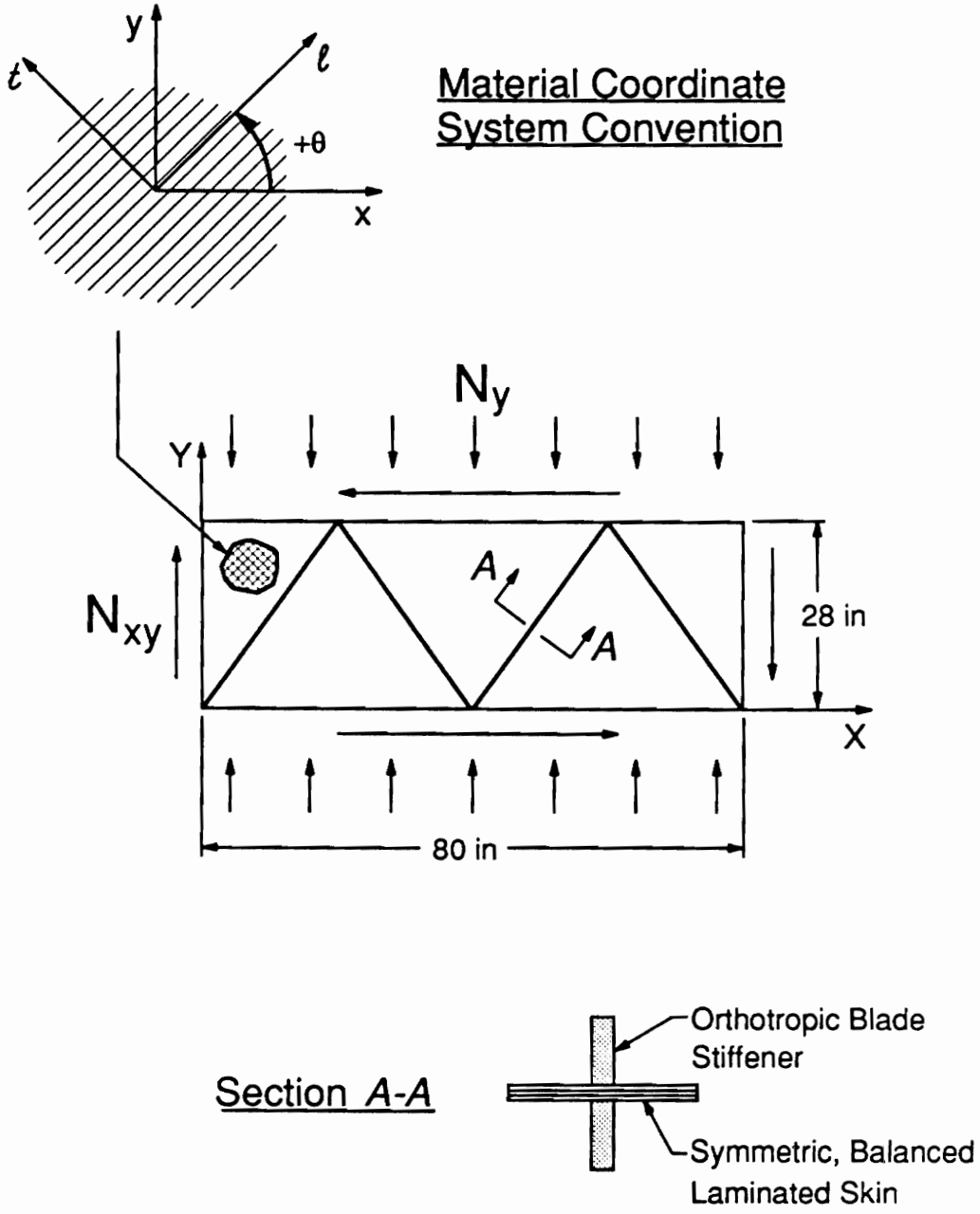

Figure 5. Wing.Rib Panel Model

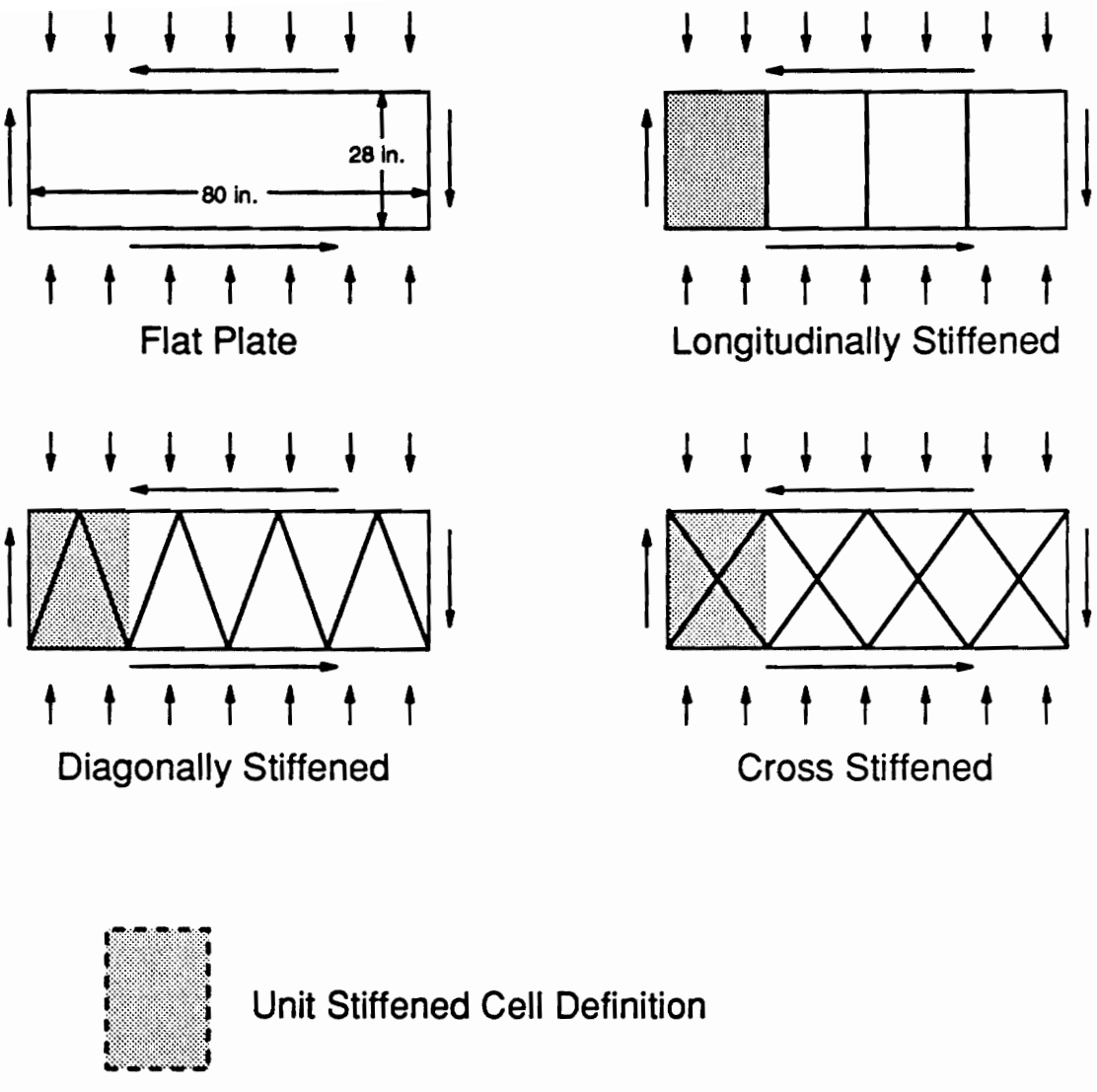

Figure 6. Flat Plate and Stiffened Panel Geometries

mization principles to minimize the mass without violating the imposed constraints. For structural optimization, the constraints are generally limits on buckling, vibration, deflection, or fracture behavior of the component. In conducting the design study a primary consideration is computational efficiency in the analysis package. This is due to the fact that the analysis often must be conducted many times over during the course of a typical design run. On the other hand, realistic and reliable constraints must be imposed on the design to prohibit infeasible configurations which would fail to meet the desired performance criteria.

For complex component geometries, detailed structural analysis generally requires the use of finite element analysis techniques. Unfortunately, for optimization purposes finite element analysis is computationally too expensive and any change in planform geometry requires laborious, often manual, remeshing. As a result, design codes have often incorporated analyses which model the panel as an assemblage of rectangular plates for which closed-form or simple computational buckling solutions exist. One such code is PANDA2[12], which finds minimum-weight designs for flat or curved panels or cylindrical shells with stiffeners in one or two orthogonal directions. Another widely used design code is PASCO [Panel Analysis and Sizing Code][13], which incorporates the optimizer CONMIN [Constrained Minimization] and the analysis code VIPASA [Vibration and Instability of Plate Assemblies including Shear and Anisotropy][14]. PASCO was used in a recent research project by Swanson[11] to conduct an extensive structural efficiency study of longitudinally corrugated, hat-stiffened, and blade-stiffened wing rib panels under compression, shear, and transverse pressure. Swanson also used VICON [Vipasa with Constraints][15] to correct for shear and anisotropy effects which may cause VIPASA to give overly conservative buckling results. The use of these design packages for geodesic configurations is, however, not possible as they are incapable of modelling panels with stiffeners that are rotated with respect to the panel edges. The apparent lack of a suitable design or analysis code leads to the conclusion that it is necessary to develop a procedure with the capability to model panels with non-orthogonal, or oblique, stiffeners.

The first step in developing an analysis procedure is identifying the relevant constraints which must be considered. Based on the results of previous studies for stiffened panels under in-plane loads,

four dominant failure modes have been isolated. The first failure mode is global buckling, where the skin and stiffeners deflect out-of-plane as one (Figure 7). The second mode, local skin buckling, occurs when the stiffeners deflect little, but the inter-stiffener skin sections buckle. The third possible mode addresses local buckling or crippling of the blade stiffeners. The fourth and final failure mode considered is material failure, where the strength of the material in the skin or stiffeners is exceeded.

It is quite possible that at the stiffener intersection points there are highly localized and complex (possibly three-dimensional) stress concentrations that can cause failure of these panels. However, for a preliminary design study of this nature, inclusion of such failure modes may not be possible because of the degree of difficulty of the analysis. Due to the complex geometry of geodesically stiffened panels, the theory used for structural analysis (especially for preliminary design) is often approximate. For example, a geodesically stiffened cylindrical shell was designed by Reddy, *et al*[16] subject to constraints on general instability, skin buckling, and rib crippling only. For general instability, constitutive relations for the stiffened shell were found by smearing out the stiffeners and representing the cylinder as a homogeneous shell. Standard methods for the buckling of cylindrical shells were then used. For local skin buckling, the inter-stiffener skin section was treated as an orthotropic triangular plate with simply-supported edges under in-plane loads, for which an approximate buckling solution can be found. Finally, the crippling load for the ribs was estimated using an approximate formula for the buckling of an orthotropic plate with fixed ends and simply-supported and free edges. A similar approach has also been used by Stroud and Agranoff[17] to model longitudinally corrugated and hat-stiffened panels as assemblies of orthotropic plate elements.

An approach analogous to those described above was explored initially for the analysis of the geodesically stiffened panels in this study. A solution for the crippling of orthotropic stiffeners had recently been derived and implemented[18]. As opposed to the study of Reddy, *et al*, where only equilateral triangular plates were considered, the geodesic panels of the present study, as shown in Figure 6, have subsections which are both rhombic and isosceles triangular in shape. A detailed analysis for the buckling of anisotropic rhombic plates was therefore developed by the author. A

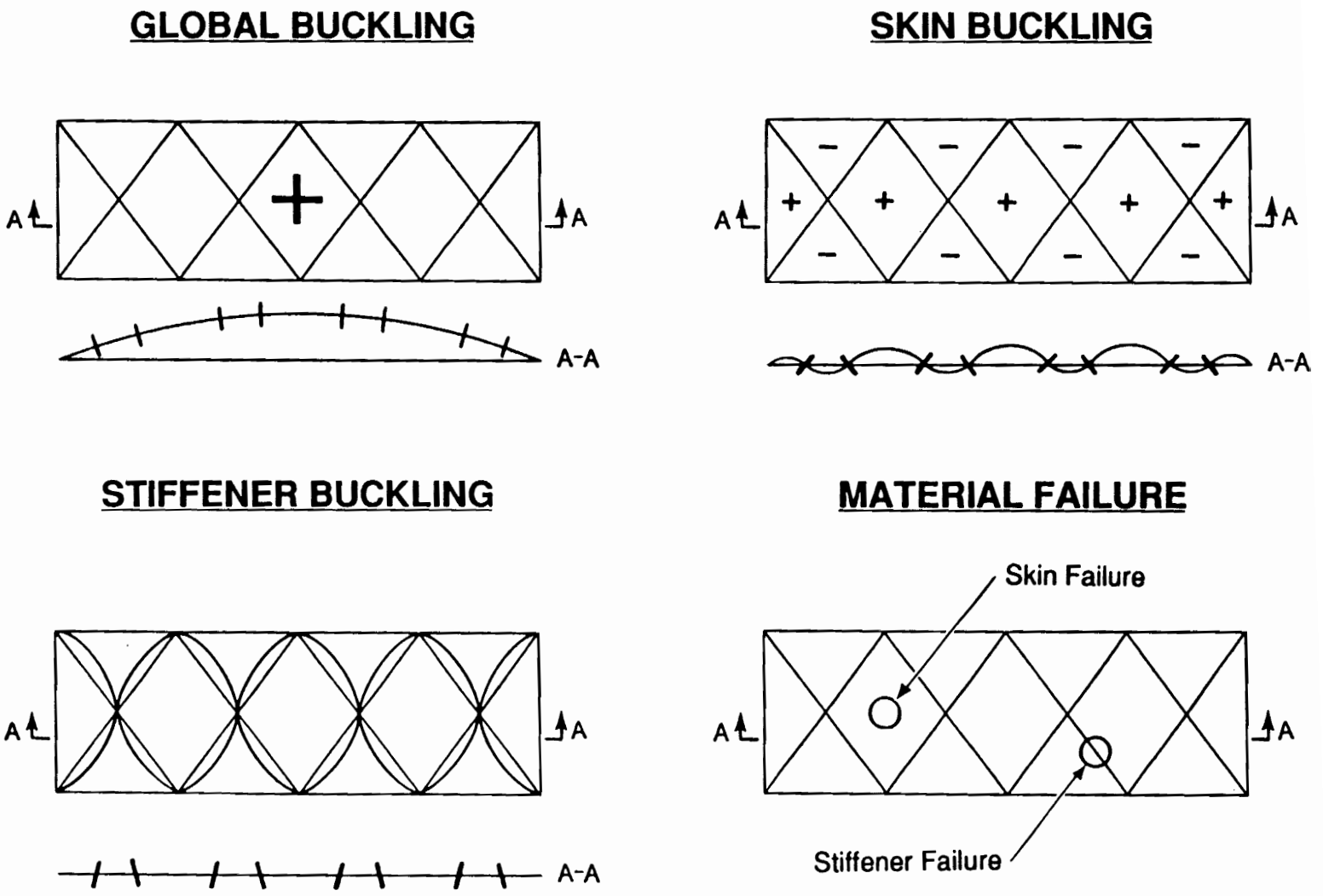

Figure 7. Stiffened Panel Failure Modes

solution for orthotropic isosceles triangular plate buckling exists in the literature, although it does not satisfy boundary conditions completely due to the shape of the plate and the existence of anisotropic coupling terms[19]. The main difficulty of the present study, however, existed in the global buckling analysis. As mentioned earlier, for the analysis of grid-stiffened panel configurations many analysts resort to a smeared stiffener approach which represents the skin-stiffener assembly as an equivalent homogeneous orthotropic plate. This approximation is acceptable if there are many closely spaced stiffeners whose dimensions are small with respect to those of the panel. The geodesic wing rib panel designs under consideration, however, have only a few stiffeners per panel. For a small number of stiffeners the smeared stiffener approach is expected to result in considerable error.

The solution of panel buckling problems where the discrete contribution of each stiffener is accounted for has been explored fairly extensively in the literature for orthogonally stiffened panels. However, the energy approach used by the majority of these studies becomes too unwieldy for stiffeners which are rotated with respect to the panel edges. Therefore, an indirect procedure using Lagrange multipliers has been developed which can accommodate oblique stiffeners at any arbitrary orientation. (The formulation of the Lagrange multiplier method [LMM] analysis is described in detail in Section 3.2.1). Previously it was mentioned that the global instability mode and local skin buckling modes were to be considered via independent analyses. The LMM buckling analysis will account for both of these forms of instability, including intermediate modes where the deflected shape is a combination of both global and inter-stiffener skin buckling. (It will be shown in Section 4.1.2 that the buckled shape depends on the relative bending stiffnesses of the skin and stiffeners).

A requirement of the LMM procedure is that the distribution of in-plane loads must be known before the stability analysis can be performed. Although a prebuckling static analysis using a finite element code would provide this information, it would be advantageous to eliminate it so that limitations related to mesh generation would not be encountered. The smeared analysis approach of Reddy, *et al*[16] has therefore been used to obtain the load-distribution information. It should be emphasized that their approach was to smear both the in-plane and flexural properties of the stiff-

ened panel; here only the in-plane properties are smeared, while the out-of-plane contributions of the stiffeners remain discrete. Comparison of the smeared analysis with a finite element program indicates that the smeared analysis gives good results for the in-plane load distribution. As such, the smeared approach has been adopted for the static analysis portion of the LMM buckling analysis. The load distribution results are also used to estimate stresses and strains in the panel components for use in the material failure analysis.

At the present time, the LMM buckling analysis can model only a specially orthotropic skin laminate, i.e. the effects of bending-twisting coupling terms D_{16} and D_{26} are not accounted for. The effect of these terms can be significant, resulting in reduced buckling loads and, in particular, causing sensitivity to the direction of applied in-plane shear[20 21]. As such, the rhombic plate analysis which has been developed will be retained to estimate the effect of these terms. The rhombic analysis will not be incorporated into the design code, but instead will be used to analyze the final designs.

To summarize, three design constraints are considered in the structural analysis routines. These are buckling of the panel assembly, local buckling of the stiffeners, and material strength. The in-plane load distribution for the panel is estimated by smearing the stiffeners. Using the LMM analysis, the buckling load for a rectangular orthotropic plate with a number of oblique stiffeners is predicted. Buckling of the stiffeners is estimated by modelling the blade as a rectangular orthotropic plate under uniform axial compressive load. Finally, material failure in the skin or stiffeners is estimated using a maximum strain criterion.

The analysis capability described above is coupled with the general purpose optimization package ADS [Automated Design Synthesis][22] to seek minimum-weight designs for geodesically stiffened panels subject to the aforementioned constraints on buckling and material failure. The name given to this new package is PANSYS (**Pan**el **Sy**nthesis **S**ystem). ADS allows several choices for each of the three parts (strategy, optimizer, and one-dimensional search) of the solution to the constrained optimization problem. ADS also permits many of the parameters governing convergence to be changed from the default values. Algorithm choice and any over-riding of default parameters

are easily specified in the input file to PANSYS. An example input file for PANSYS is shown and explained in Appendix A.

2.3 *Scope of Design Study*

The overall objective of the design study is to seek practical, minimum-weight designs for stiffened wing rib panels. Section 2.2 described the actual wing rib, the assumptions and limitations in the modelling, and the four geometries which would be considered. The scope of the study, using the design code PANSYS, is now outlined.

Optimum designs are sought for the two geodesic panels (diagonal and cross, see Figure 6) and the longitudinally stiffened panel. Although a flat plate is also considered, the design problem is trivial as there is only one design variable. The number of stiffened cells is varied incrementally up to a maximum of eight cells per panel; the complete range of panel geometries in the study is shown in Figure 8. The design variables are the skin thickness, stiffener height, and stiffener thickness. Only one skin laminate is considered, with a quasi-isotropic lamination sequence of $[-45/45/90/0]_S$ and all plies of equal thickness. A minimum-gauge constraint of 0.040 inch is imposed on the thickness of the skin and stiffeners. Three levels of external loads are applied in uniaxial compression and pure shear: 100, 1000 and 10000 pounds-force per inch (lbf/in). For eight cell stiffened panels and the flat plate, a combined compression-shear case with loads ranging from 100 to 30000 lbf/in (the latter a worst-case loading scenario) is also considered.

Properties of a typical graphite-epoxy material system (Hercules AS4/3502) are used in all analyses. Material properties for the stiffeners are assumed to be the same as those for the skin laminae. Since the maximum strain theory is used to predict material failure, the material strengths are expressed

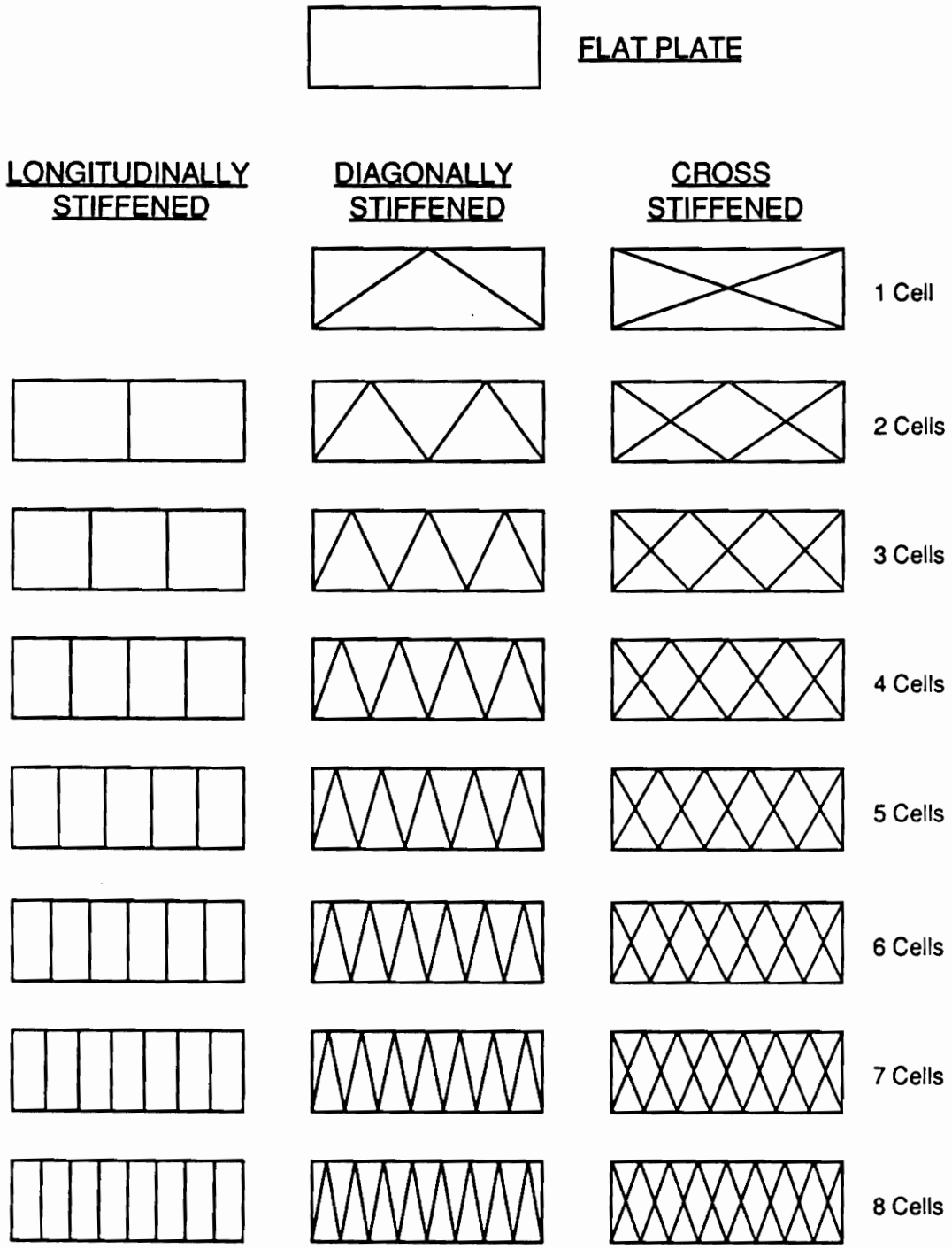

Figure 8. Design Study Panel Configurations

in terms of maximum allowable strain values. The elastic, strength, and physical properties used in the design study are shown in Table 1.

Table 1. AS4/3502 Graphite-Epoxy Material Properties

Elastic Properties:	
Longitudinal Modulus	$E_1 = 18.5 \times 10^6$ lbf/in^2
Transverse Modulus	$E_2 = 1.64 \times 10^6$ lbf/in^2
In-Plane Shear Modulus	$G_{12} = 0.87 \times 10^6$ lbf/in^2
Transverse Shear Modulus	$G_{23} = 0.54 \times 10^6$ lbf/in^2
In-Plane Poisson's Ratio	$\nu_{12} = 0.30$
Strength Properties:	
Longitudinal Tensile Strain Allowable	$\varepsilon_1^t = 0.0090$
Longitudinal Compressive Strain Allowable	$\varepsilon_1^c = 0.0080$
Transverse Tensile Strain Allowable	$\varepsilon_2^t = 0.0055$
Transverse Compressive Strain Allowable	$\varepsilon_2^c = 0.0290$
Shear Strain Allowable	$\gamma_{12} = 0.0250$
Physical Properties:	
Mass Density	$\rho = 0.057$ lbm/in^3

Sources of Data: Swanson[11], Knight[23], Sensmeier, *et al* [24]

3.0 Analytical Development

The purpose of the analysis portion of a design code is to provide meaningful constraints on the design so that it will be feasible, i.e. not suffer structural failure under the applied loads. Three limiting failure modes for flat and stiffened panels are considered in the present analysis procedure. The first failure mode is material strength, where first-ply failure in the skin or stiffeners is assumed to occur when specified strain values are exceeded. This procedure is discussed as part of the static analysis, Section 3.1, which considers in-plane deformation behavior of the panel. The second failure mode is panel buckling, where the skin and stiffeners deflect out-of-plane, transverse to the surface of the panel. The third and final failure mode concerns local buckling or crippling of the stiffeners. Buckling of flat and stiffened panels and stiffener crippling are treated in Section 3.2.

Section 3.3 considers the buckling of an anisotropic rhombic plate. This analysis is not incorporated into the design code, but instead is used post-design to estimate the effect of anisotropic coupling terms which the panel buckling analysis of Section 3.2 does not account for. The rhombic analysis is also used to examine the effects of skewing and laminate geometry on the local buckling behavior of the rhombus-shaped skin sections in the cross-stiffened panels.

3.1 Static Analysis of Stiffened Panels

In order to perform strength or buckling analyses on geodesically stiffened panels with the present approach, it is necessary to determine how externally applied loads are distributed between the skin and each of the stiffeners. In Section 3.1.1, simple smeared stiffener theory is used to derive approximate constitutive relations for the in-plane behavior of the three stiffened panel configurations under consideration. In Section 3.1.2, information from the load-distribution calculations is used to perform the material failure analysis, where first-ply failure in the skin or stiffeners is predicted using a maximum strain criterion.

3.1.1 Load Distribution Analysis

In smeared stiffener theory, the contributions of the stiffeners to the in-plane response of the panel are averaged out so that the stiffener network is represented as a uniform flat sheet with appropriate elastic properties. This allows force-displacement relations (equivalent to the $[A]$ matrix in classical lamination theory) to be derived for the overall in-plane behavior of a stiffened panel. In the derivation, the smeared theory is applied to the in-plane elastic analysis of a single stiffened unit. It is assumed that the behavior of this unit is representative of the overall response of a panel with repetitive geometry. Restrictions on the geometry and basic assumptions behind the static analysis are listed below. A discussion of the reasons for adopting these conditions and their implications follows.

1. The skin is symmetrically laminated. Identical stiffeners are located on both sides of the skin, symmetrical about the midplane of the plate.
2. The skin laminate is balanced. Oblique stiffeners occur in pairs oriented at equal but opposite angles with respect to the panel coordinate axes.

3. Panel deformations do not violate small displacement theory.
4. Panel supports are sufficiently rigid to ensure that the deformed panel shape remains a parallelogram under axial or shear loading. Extensional deformation of the panel in the X direction is assumed to be zero.
5. Stiffeners are treated as isolated structural elements which carry only axial forces. It is assumed that stiffeners have zero flexural stiffness for bending in a plane parallel to the surface of the panel.

The first assumption is a fundamental requirement in applying a linear theory to determine the internal load distribution for the panel at its critical load. It is well known that laminated plates symmetric about the midplane in all respects have no coupling between in-plane extension and out-of-plane bending (i.e. $B_{ij} = 0$). Similarly, placing identical stiffeners on both sides of the skin will preserve this symmetry, and the global response of the panel will not exhibit bending-extension coupling. For plates in which bending-extension coupling is present, in-plane loads will result in large out-of-plane deformations. The buckling problem requires the solution of coupled equations governing both the in-plane and out-of-plane response. However, for symmetric geometries the in-plane and bending problems uncouple and the buckling problem can be solved by considering just the out-of-plane deflection w. Also, a linear deformation theory based on the unbuckled geometry of the panel can be used to determine the internal load distribution of the stiffened panel at the critical point.

The second assumption eliminates a second form of coupling, but is imposed for practical design reasons. Laminates with off-axis plies which do not occur in $\pm\theta$ pairs are unbalanced and will have nonzero A_{16} and A_{26} stiffness terms. These terms imply coupling between in-plane extension and in-plane shear deformations, which is generally not desirable behavior for most structural applications. Analogous to balancing plies in a laminate, placing oblique stiffeners in pairs at equal but opposite angles will cancel their tendency to induce extension-shear coupling. In addition, the balanced stiffener placement minimizes the directional sensitivity of the panel for buckling under shear loads. This results from the stiffener network having an equal number of stiffeners in tension

and compression under positive and negative shear. (Sensitivity to shear direction will still occur in the buckling analysis from bending-twisting coupling if the skin laminate has nonzero D_{16} and D_{26} terms. This topic is discussed in greater detail in Section 5.3).

The third assumption simplifies the geometrical aspects of the problem and permits multiple loads to be considered via superposition. In deriving equations governing the equilibrium of elastic bodies, it is common to make no distinction between the form of the body before loading and the form of the body after loading. This assumes that the usually small deformation displacements do not significantly affect the action of the applied forces. If this assumption is reasonable, calculations can be carried out based on the initial undeformed plate geometry. The small displacement assumption must also be valid in order to justify applying the principle of superposition to determine total displacements under the action of multiple external loads. This principle states that the total displacements of a body are merely a linear combination of the displacements observed when each load is applied independently[25].

The fourth assumption reflects an idealization of the actual restraint conditions at the edges of the panel. The stiffened panels under consideration are intended to be representative of a rib panel for the wing of a large transport aircraft. A typical load scenario for this panel is compression in the Y direction due to bending of the wing. Under this loading, the panel will attempt to expand or contract in the X direction due to the Poisson effect. In geodesically stiffened panels of the type currently under investigation, this effect may be severe due to "scissoring" of the stiffeners. When the panel is installed in an aircraft it would be bounded by a network of spars, stringers, and wing covers. In-plane deformation of the panel is, therefore, restrained to a certain degree by the surrounding structure. However, in the present analysis it is convenient to simplify the degree of restraint by assuming that the panel edges perpendicular to the X axis are either completely fixed in the X direction or free of any restraint in the X direction. Clearly, these assumed boundary conditions represent two extremes which bound the actual degree of elastic restraint. The fixed or zero-transverse-deformation condition has been chosen as it is believed to be closer to the actual degree of restraint, whereas the restraint-free condition will result in excessive stretching of the panel skin

due to stiffener scissoring. It is important to note that the preceding assumption does not affect shear response as there is no coupling between shear and extension for the panels under consideration (see Assumption #2).

The fifth and final assumption simplifies estimating the internal distribution of loads in the stiffened panel. In the actual structure, where the skin and stiffeners form an integral unit, the stress distribution is very complex. By ignoring any interaction between the skin and stiffeners, and between stiffeners where they cross (i.e. components are assumed to be able to slide across one another), the panel can be treated as a truss on top of a flat plate, connected only at the panel perimeter. That is, compatibility of global strains and equilibrium of forces between the stiffener network and the skin are only enforced at the outside edges of the panel.

There are four steps in the load distribution analysis. The first step is to define the constitutive equations for the panel skin, which are given by classical lamination theory. The next step is to calculate equivalent constitutive relations for the stiffener network, which is done through a smeared stiffener analysis. Third, superposition of the skin and stiffener properties yields the stiffnesses for the panel as a whole. Finally, for a given external load, the internal loads on the skin and each stiffener are calculated. This distribution will be dependent on the relative stiffnesses of the skin versus the stiffeners and on the boundary conditions imposed on the panel.

Skin Constitutive Equations

The constitutive equations for a general laminate with multiple orthotropic plies at arbitrary orientations, as defined by classical lamination theory, are [26]

$$\begin{Bmatrix} N \\ M \end{Bmatrix} = \begin{bmatrix} A & B \\ B & D \end{bmatrix} \begin{Bmatrix} \varepsilon^{\circ} \\ \kappa \end{Bmatrix} \tag{1}$$

where $\{N\}$ and $\{M\}$ are vectors of in-plane force and moment resultants, $\{\varepsilon\}$ and $\{\kappa\}$ are strain and curvature vectors, and the zero superscript denotes midplane quantities. For a symmetric laminate

(Assumption #1) all coupling stiffnesses B_{ij} are zero and the in-plane extension and out-of-plane bending relations uncouple. Since the in-plane behavior is to be examined, the required force resultants are

$$\begin{Bmatrix} N_x \\ N_y \\ N_{xy} \end{Bmatrix} = \begin{bmatrix} A_{11} & A_{12} & A_{16} \\ A_{12} & A_{22} & A_{26} \\ A_{16} & A_{26} & A_{66} \end{bmatrix} \begin{Bmatrix} \varepsilon_x \\ \varepsilon_y \\ \gamma_{xy} \end{Bmatrix} \tag{2}$$

where the zero superscript can be dropped as no laminate bending is involved. For a balanced laminate (Assumption #2), where every $+\theta$ ply is matched by an identical $-\theta$ ply, the extension-shear coupling terms A_{16} and A_{26} vanish, leaving

$$\begin{Bmatrix} N_x^P \\ N_y^P \\ N_{xy}^P \end{Bmatrix} = \begin{bmatrix} A_{11}^P & A_{12}^P & 0 \\ A_{12}^P & A_{22}^P & 0 \\ 0 & 0 & A_{66}^P \end{bmatrix} \begin{Bmatrix} \varepsilon_x \\ \varepsilon_y \\ \gamma_{xy} \end{Bmatrix} \tag{3}$$

where the superscript P has been used to indicate that these stiffness coefficients and force resultants are those for a plate, referring to the skin of the stiffened panel. Note that the strains do not carry a superscript, as the strains for the skin are assumed to be identical to those for the panel as a whole.

Stiffener Constitutive Equations

The objective is to develop a set of constitutive equations, similar to those shown in Equation (3) for the skin, which will predict the overall force-displacement behavior of the stiffener network. To achieve this, the behavior of a single representative unit is examined.

<u>Longitudinally Stiffened Panel:</u> The effective width a, over which the influence of one stiffener will be uniformly distributed or "smeared", is the panel width divided by the total number of stiffeners (Figure 9). The total cross-sectional area of the stiffener is denoted by A. The first step

is to relate the axial strain in the stiffener ε_ℓ to the global panel strains ε_x, ε_y, and γ_{xy}. Clearly, since the stiffener is parallel to the Y axis, the axial strain component is simply

$$\varepsilon_\ell = \varepsilon_y \tag{4}$$

Note that ε_ℓ is a function of neither ε_x nor γ_{xy}. The total axial force in the stiffener F is found merely by multiplying the stiffener axial strain by the axial elastic modulus E_ℓ and the cross-sectional area of the stiffener

$$F = AE_\ell(\varepsilon_\ell) = AE_\ell\varepsilon_y \tag{5}$$

The stiffener axial force is now smeared over the effective width a to calculate an average stress resultant

$$N_y = \frac{F}{a} = \frac{AE_\ell\varepsilon_y}{a} \tag{6}$$

The constitutive relations for the longitudinal stiffener can now be expressed in standard matrix form as

$$\begin{Bmatrix} N_x^S \\ N_y^S \\ N_{xy}^S \end{Bmatrix} = \begin{bmatrix} 0 & 0 & 0 \\ 0 & A_{22}^S & 0 \\ 0 & 0 & 0 \end{bmatrix} \begin{Bmatrix} \varepsilon_x \\ \varepsilon_y \\ \gamma_{xy} \end{Bmatrix} \tag{7}$$

where the S superscript denotes values for the stiffener, and the sole non-zero coefficient is

$$A_{22}^S = \frac{AE_\ell}{a} \tag{8}$$

Cross-Stiffened Panel: The unit for a cross-stiffened panel is shown in Figure 10. The effective width a is the panel width divided by the number of cells per panel. The stiffener angled upwards and to the right at angle $+\phi$ is designated as stiffener #1, and the second stiffener, angled down-

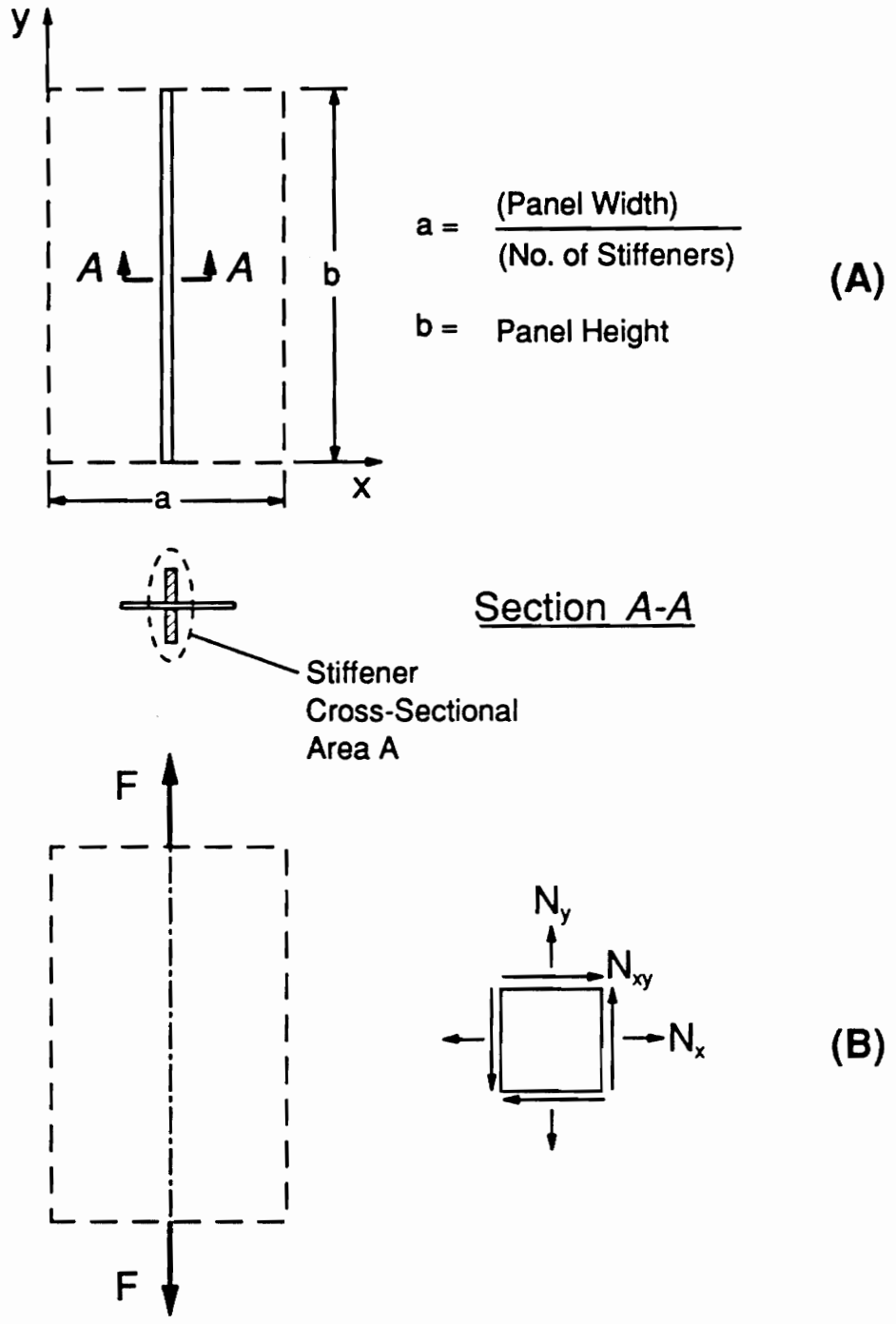

Figure 9. **Longitudinally Stiffened Unit for Load Distribution Analysis:** A) Geometry B) Equilibrium of Stiffener Forces

wards and to the right at angle $-\phi$, is stiffener #2. The total cross-sectional area of each stiffener of the pair is the same and is denoted by A. The approach is the same as that for the longitudinally stiffened example, but it is complicated by the fact that the stiffeners are not parallel to the coordinate system. As before, the strains for the panel, and therefore the representative unit, in the $x-y$ coordinate system are denoted by $\varepsilon_x, \varepsilon_y, \gamma_{xy}$. The strains in a local coordinate system aligned with the stiffener can be determined using the standard strain transformation [26]

$$\begin{Bmatrix} \varepsilon_\ell \\ \varepsilon_t \\ \gamma_{\ell t} \end{Bmatrix} = \begin{bmatrix} \cos^2\theta & \sin^2\theta & \sin\theta\cos\theta \\ \sin^2\theta & \cos^2\theta & -\sin\theta\cos\theta \\ -2\sin\theta\cos\theta & 2\sin\theta\cos\theta & \cos^2\theta - \sin^2\theta \end{bmatrix} \begin{Bmatrix} \varepsilon_x \\ \varepsilon_y \\ \gamma_{xy} \end{Bmatrix} \tag{9}$$

where ε_ℓ denotes the strain component parallel to the stiffener axis or longitudinal direction and ε_t the component perpendicular or transverse to the stiffener. In accordance with Assumption #5, where stiffeners carry axial loads only, the axial component of strain for each stiffener is the only quantity required. To calculate the axial strain component for stiffener #1, the angle $+\phi$ is inserted in the first line of Equation (9), giving

$$\begin{aligned} \varepsilon_1 &= \cos^2\phi\varepsilon_x + \sin^2\phi\varepsilon_y + \sin\phi\cos\phi\gamma_{xy} \\ &= c^2\varepsilon_x + s^2\varepsilon_y + sc\,\gamma_{xy} \end{aligned} \tag{10}$$

where s and c are shorthand notations for $\sin\phi$ and $\cos\phi$, respectively. To calculate the axial strain component for stiffener #2, the angle $-\phi$ is now inserted in the first line of Equation (9) to give

$$\begin{aligned} \varepsilon_2 &= \cos^2(-\phi)\varepsilon_x + \sin^2(-\phi)\varepsilon_y + \sin(-\phi)\cos(-\phi)\gamma_{xy} \\ &= c^2\varepsilon_x + s^2\varepsilon_y - sc\,\gamma_{xy} \end{aligned} \tag{11}$$

Note that Equations (10) and (11) differ only in the sign of the shear strain coefficient. Stiffener axial forces are found by multiplying the axial strain for each stiffener by the axial elastic modulus E_ℓ and cross-sectional area A

$$F_1 = AE_\ell (c^2\varepsilon_x + s^2\varepsilon_y + sc\,\gamma_{xy})$$
$$F_2 = AE_\ell (c^2\varepsilon_x + s^2\varepsilon_y - sc\,\gamma_{xy}) \tag{12}$$

Stiffener axial forces are now resolved into orthogonal components, as indicated in Figure 10-B. Looking at the vertical edge of the unit, the force components in the x direction are $F_1 \cos\phi$ and $F_2 \cos\phi$. Summing these two force components gives the total force in the x direction, F_x. Substituting for F_1 and F_2 from Equation (12) to get the expression in terms of strains gives

$$\begin{aligned} F_x &= F_1 \cos\phi + F_2 \cos\phi \\ &= [AE_\ell (c^2\varepsilon_x + s^2\varepsilon_y + sc\,\gamma_{xy})] \cos\phi \;+\; [AE_\ell (c^2\varepsilon_x + s^2\varepsilon_y - sc\,\gamma_{xy})] \cos\phi \\ &= 2AE_\ell (c^3\varepsilon_x + cs^2\varepsilon_y) \end{aligned} \tag{13}$$

It is important to note that the dependence on the shear strain drops out. An average force resultant for the stiffeners is again constructed by smearing the total force in the x direction along the vertical edge of the unit. The force per unit length along the vertical edge is finally

$$N_x = \frac{F_x}{b} = \frac{2AE_\ell}{b} (c^3\varepsilon_x + cs^2\varepsilon_y) \tag{14}$$

A normal force resultant N_y in the y direction is derived in the same manner as N_x. Summing force components along the horizontal edge of the unit, distributing the result over the distance a, and simplifying gives

$$N_y = \frac{F_y}{a} = \frac{2AE_\ell}{a} (sc^2\varepsilon_x + s^3\varepsilon_y) \tag{15}$$

To determine the shear force resultant, the forces tangential to either the horizontal or vertical faces of the unit can be used with identical results. Considering the vertical edge of the unit, the tangential force components are $F_1 \sin\phi$ in the positive y direction and $F_2 \sin\phi$ in the negative y direction (Figure 10-B). Substituting F_1 and F_2 from Equation (12) gives

$$
\begin{aligned}
F_{xy} &= F_1 \sin\phi - F_2 \sin\phi \\
&= [AE_\ell (c^2\varepsilon_x + s^2\varepsilon_y + sc\,\gamma_{xy})] \sin\phi \;-\; [AE_\ell (c^2\varepsilon_x + s^2\varepsilon_y - sc\,\gamma_{xy})] \sin\phi \\
&= 2AE_\ell (cs^2\gamma_{xy})
\end{aligned} \tag{16}
$$

with the related force resultant following

$$
N_{xy} = \frac{F_{xy}}{b} = \frac{2AE_\ell}{b} (cs^2\gamma_{xy}) \tag{17}
$$

Note that the shear force resultant depends solely on the shear strains. Clearly, Equations (14), (15), and (17) show that there is no coupling between axial and shear response. The constitutive relations for the crossed stiffeners can be expressed in the standard matrix form as

$$
\begin{Bmatrix} N_x^S \\ N_y^S \\ N_{xy}^S \end{Bmatrix} = \begin{bmatrix} A_{11}^S & A_{12}^S & 0 \\ A_{21}^S & A_{22}^S & 0 \\ 0 & 0 & A_{66}^S \end{bmatrix} \begin{Bmatrix} \varepsilon_x \\ \varepsilon_y \\ \gamma_{xy} \end{Bmatrix} \tag{18}
$$

where the S superscript again denotes values for the stiffener network, and the coefficients are defined as

$$
\begin{aligned}
A_{11}^S &= \frac{2AE_\ell}{b} c^3 \qquad & A_{12}^S &= \frac{2AE_\ell}{b} cs^2 \\
A_{21}^S &= \frac{2AE_\ell}{a} sc^2 \qquad & A_{22}^S &= \frac{2AE_\ell}{a} s^3 \\
& & A_{66}^S &= \frac{2AE_\ell}{b} cs^2
\end{aligned} \tag{19}
$$

Note that the relationships for A_{12} and A_{21} appear different. However, the geometric relationship $\frac{s}{b} = \frac{c}{a}$ can be used to show that $A_{21} = A_{12}$ and thus the matrix is indeed symmetric, as expected.

Diagonally Stiffened Panel: Fortunately, results for the cross stiffeners can be adapted, making it unnecessary to repeat the derivation process for diagonal stiffeners. In Figure 11 a diagonally stiffened panel with one cell is compared with a cross-stiffened panel with two cells. Through

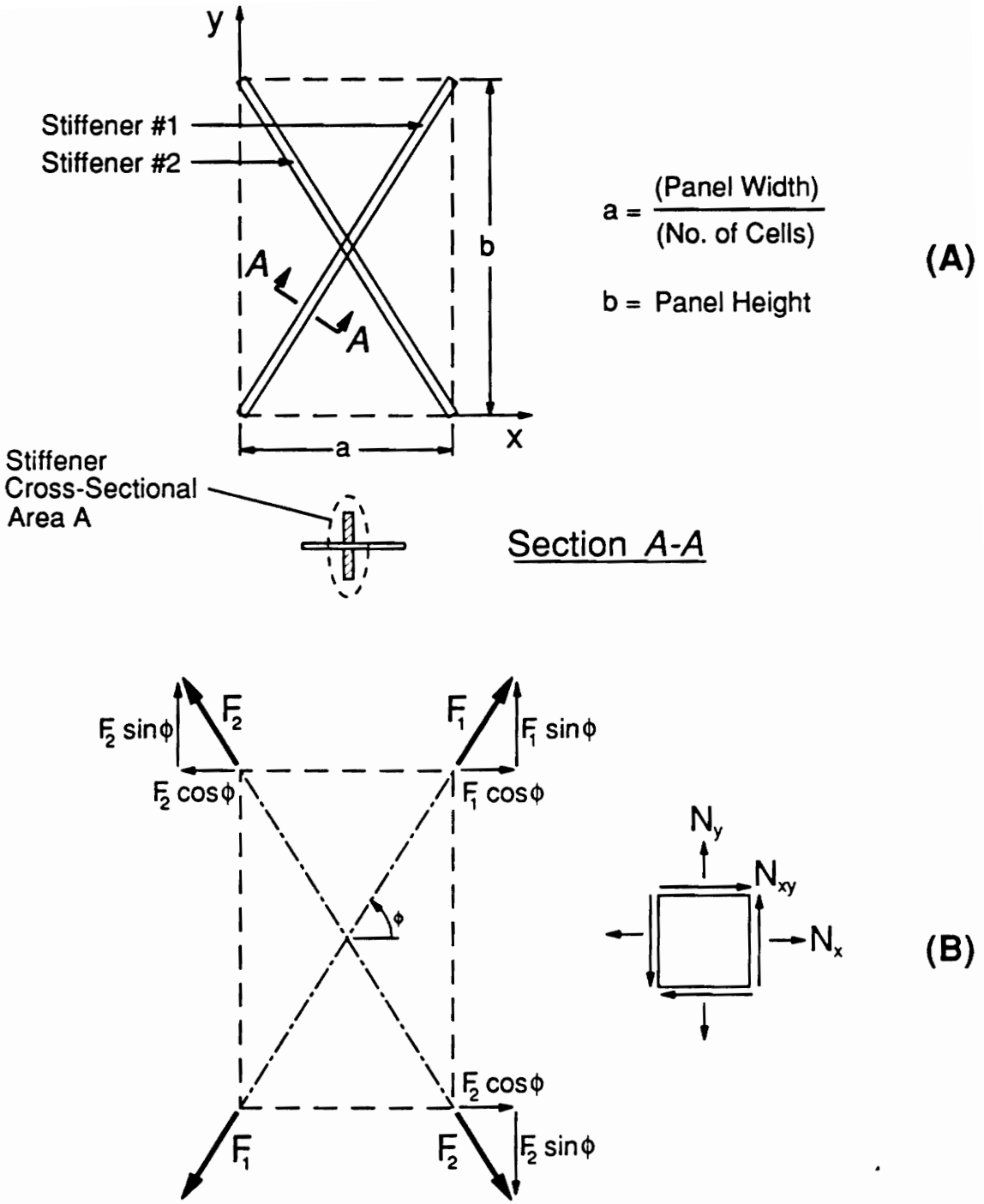

Figure 10. **Cross-Stiffened Unit for Load Distribution Analysis:** A) Geometry B) Equilibrium of Stiffener Forces

superposition, it is demonstrated that the crossed stiffener network in the right-hand column is merely a combination of two mirror-image diagonal stiffener networks in the left-hand column. Taking into account the differences in number of stiffeners and effective widths, equivalent stiffness coefficients are obtained for the diagonal network.

Panel Constitutive Equations

Now that constitutive relations are available for both the skin and the stiffener networks, it is possible to derive equations which predict the response of the panel as a whole. If it is assumed that the stiffener network and skin experience identical strains, equilibrium considerations indicate that the force resultants for the panel will merely be the sum of those for the skin and the stiffeners, i.e.

$$\begin{aligned} N_x &= N_x^P + N_x^S \\ N_y &= N_y^P + N_y^S \\ N_{xy} &= N_{xy}^P + N_{xy}^S \end{aligned} \tag{20}$$

From this it follows that the stiffness coefficients are also sums of those for the skin and stiffeners. Therefore the panel constitutive relations may be summarized as

$$\begin{Bmatrix} N_x \\ N_y \\ N_{xy} \end{Bmatrix} = \begin{bmatrix} A_{11} & A_{12} & 0 \\ A_{12} & A_{22} & 0 \\ 0 & 0 & A_{66} \end{bmatrix} \begin{Bmatrix} \varepsilon_x \\ \varepsilon_y \\ \gamma_{xy} \end{Bmatrix} \tag{21}$$

with

$$\begin{aligned} A_{11} &= A_{11}^P + A_{11}^S \qquad & A_{12} &= A_{12}^P + A_{12}^S \\ A_{22} &= A_{22}^P + A_{22}^S \qquad & A_{66} &= A_{66}^P + A_{66}^S \end{aligned} \tag{22}$$

Explicit expressions for the A_{ij}^S terms are given in Equation (8) for the longitudinally stiffened panel and in Equation (19) for the cross-stiffened panel.

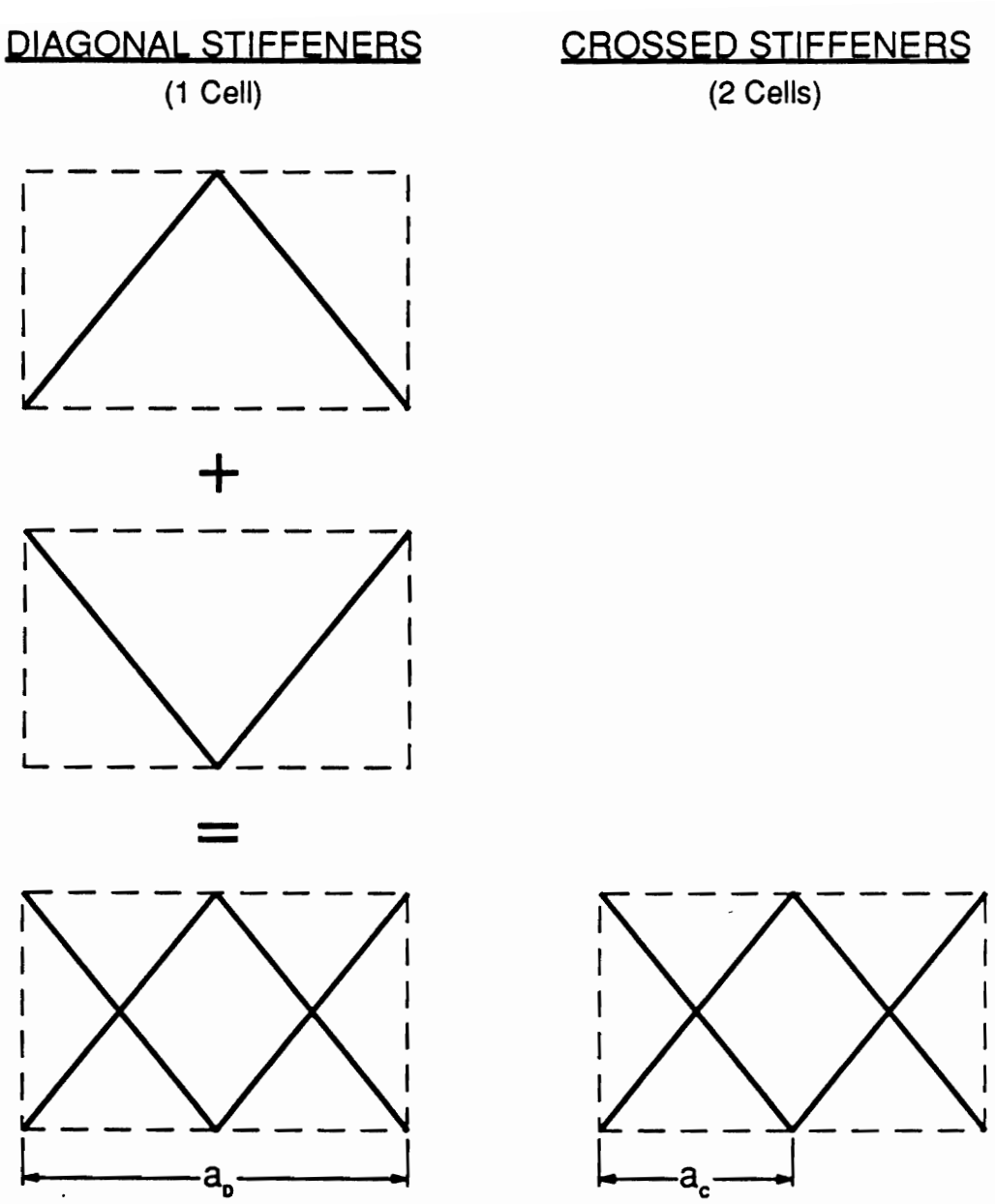

a_D = Effective Width for Diagonal Stiffeners

a_C = Effective Width for Crossed Stiffeners

Figure 11. Comparison of Diagonal and Crossed Stiffener Networks for Load Distribution Analysis

Internal Load Distribution

In following sections, it will be necessary to know what portions of the external loads on the panel are carried by the skin and by each stiffener. The derived stiffnesses for the skin, stiffeners, and panel can be used, in conjunction with the assumed boundary conditions, to estimate this internal load distribution. As was discussed in Assumption #4, a boundary condition of zero extensional deformation in the X direction has been assumed.

The overall panel response to an applied axial load N_y is first determined. To isolate the compressive response, a shear load of $N_{xy} = 0$ is assumed. In accordance with the assumption of zero transverse deformation, ε_x is set to zero. Substituting these conditions in Equation (21) and solving for the resulting strains gives

$$\begin{Bmatrix} \varepsilon_x \\ \varepsilon_y \\ \gamma_{xy} \end{Bmatrix} = \begin{Bmatrix} 0 \\ \left(\frac{N_y}{A_{22}}\right) \\ 0 \end{Bmatrix} \tag{23}$$

It is assumed that the skin experiences uniform strains identical to those of the panel as a whole. Therefore, the global strains in Equation (23) are substituted in the skin constitutive Equations (3) to calculate the force resultants acting upon the skin or plate

$$\begin{aligned} N_x^P &= \left(\frac{A_{12}^P}{A_{22}}\right) N_y \\ N_y^P &= \left(\frac{A_{22}^P}{A_{22}}\right) N_y \\ N_{xy}^P &= 0 \end{aligned} \tag{24}$$

For panel buckling and stiffener buckling analyses in Section 3.2, the axial stiffener forces are required. To find the axial load for the longitudinal stiffener, the strains in Equation (24) are substituted in Equation (5), giving

$$F = \left(\frac{AE_\ell}{A_{22}} \right) N_y \tag{25}$$

Using the definition of A_{22}^S in Equation (8), this can be rewritten as a ratio of the stiffener and skin stiffnesses

$$F = a \left(\frac{A_{22}^S}{A_{22}} \right) N_y \tag{26}$$

For the crossed stiffeners, the global strains in Equation (24) are substituted in Equation (12) to find F_1 and F_2. They are then rewritten in terms of the stiffnesses using the definition of A_{12}^S in Equation (19) with the result

$$F_1 = F_2 = \frac{b}{2c} \left(\frac{A_{12}^S}{A_{22}} \right) N_y \tag{27}$$

Note that $F_1 = F_2$, as expected from symmetry. The axial loads for the diagonal stiffeners follow from those for the crossed stiffeners.

The panel, skin, and stiffener responses to shear are determined in the same manner as the axial response. The global response to the applied shear load N_{xy} and $\varepsilon_x = N_y = 0$ is, from Equation (21)

$$\begin{Bmatrix} \varepsilon_x \\ \varepsilon_y \\ \gamma_{xy} \end{Bmatrix} = \begin{Bmatrix} 0 \\ 0 \\ \left(\frac{N_{xy}}{A_{66}} \right) \end{Bmatrix} \tag{28}$$

Substituting the strains of Equation (28) in Equation (3) gives the shear loads on the skin

$$
\begin{aligned}
N_x^P &= 0 \\
N_y^P &= 0 \\
N_{xy}^P &= \left(\frac{A_{66}^P}{A_{66}} \right) N_{xy}
\end{aligned}
\tag{29}
$$

The stiffener axial forces due to the applied shear load are also found. In Equation (5) the axial force for a longitudinal stiffener is only dependent on ε_y. Since $\varepsilon_y = 0$ in Equation (28) for shear loading of the panel, the longitudinal stiffener axial force is zero and the entire shear load is carried by the skin. For crossed stiffeners, the strains in Equation (28) are substituted in Equation (12) to find the forces F_1 and F_2. Using A_{66}^S in Equation (19), this leads to

$$
F_1 = -F_2 = \frac{b}{2s} \left(\frac{A_{66}^S}{A_{66}} \right) N_{xy} \tag{30}
$$

Again, forces for diagonal stiffeners follow directly from those for the crossed stiffeners.

It is now possible, given applied loads N_y or N_{xy}, to calculate the portion of each load carried by the skin and the stiffeners. The result of combined loads is handled by the principle of superposition; deformations and loads are a linear combination of those quantities when applied independently.

3.1.2 Material Failure Analysis

A possible mode of failure, in addition to buckling-type failures, occurs when the strength of the panel is exceeded. In the field of composite failure mechanics, many criteria have been proposed to predict the onset of this failure mechanism. Some of the more well known of these include the maximum stress criterion, maximum strain criterion, Tsai-Hill criterion, and Tsai-Wu tensor polynomial criterion[26]. The maximum strain failure criterion, where first-ply failure is predicted when any lamina strain component exceeds a prescribed allowable, is adopted for the present design

study. Although this criterion is rather basic and prone to error under certain loading regimes, it is simple to implement and provides direct information as to the failure mode, e.g. failure in transverse tension, longitudinal compression, shear, and so on. In addition, the load distribution analysis in Section 3.1.1 provides only approximate, average values for loads in the panel components. However, the stress and strain distributions in a stiffened panel are very complex due to the abrupt section changes where stiffeners are attached to the skin. In calculating the load distribution with the smeared analysis, any interaction is ignored and it is assumed that the stress distribution in the skin is constant over the planform area. Therefore, these approximations in the load distribution analysis indicate that it would be inappropriate to implement a more sophisticated failure hypothesis.

The maximum strain criterion is used to predict material failure on a lamina level. Therefore, the laminate strains are transformed to strain components in the principal material directions for each lamina under consideration. These strain components are then compared with the strain allowables. Failure is predicted if one or more of the following inequalities is not satisfied

$$\begin{aligned} \varepsilon_1^t &< \varepsilon_{1,\,allowable}^t \\ \varepsilon_1^c &< \varepsilon_{1,\,allowable}^c \\ \varepsilon_2^t &< \varepsilon_{2,\,allowable}^t \\ \varepsilon_2^c &< \varepsilon_{2,\,allowable}^c \\ |\gamma_{12}| &< \gamma_{12,\,allowable} \end{aligned} \tag{31}$$

where

$\varepsilon_{1,\,allowable}^t$ ($\varepsilon_{1,\,allowable}^c$) = maximum allowable tensile (compressive) normal strain in 1 direction
$\varepsilon_{2,\,allowable}^t$ ($\varepsilon_{2,\,allowable}^c$) = maximum allowable tensile (compressive) normal strain in 2 direction
$\gamma_{12,\,allowable}$ = maximum allowable shear strain in the 1-2 plane

Note that a provision is made for the fact that some materials have different strengths under tension and compression. Also, the maximum allowable shear strain criterion is independent of the direction of the applied shear strain in the material coordinate system.

The procedure for implementing the maximum strain criterion in the analysis of composite panels, whether flat or stiffened, is quite straightforward. In Section 3.1.1 the equivalent panel stiffnesses A_{11}, A_{12}, A_{22}, and A_{66} were determined. Of course, for the unstiffened plate, these reduce to A^p_{11}, ... , A^p_{66}. These quantities can be inverted to calculate equivalent panel compliances. Then, given the loads applied to the panel, the resultant panel strains can be calculated directly. For the skin laminate, these global strains are transformed into principal material direction components for each ply and the criteria in Equation (31) applied to test whether failure has occurred. For the stiffeners, the global strains are transformed to calculate the normal strain component coincident with each stiffener axis. Only the first two criteria in Equation (31) need be applied, as the stiffeners are assumed to carry axial loads only. For the present study, the strain allowables for the stiffeners are assumed to be the same as those for the skin laminae and numerical values are shown in Table 1 on page 23.

3.2 Stability Analysis of Stiffened Panels

Two buckling analyses are performed in the panel design code. These are buckling of the panel assembly and local crippling of the stiffeners. In Section 3.2.1, the theory and development are given for the buckling of flat and stiffened simply-supported orthotropic plates under in-plane loads. The stiffener crippling analysis was developed by a previous researcher. However, in Section 3.2.2, the basis for the analysis is briefly reviewed for completeness.

3.2.1 Formulation of Panel Buckling Analyses

One mode of failure for stiffened panels under in-plane loads is panel buckling, where both the skin and stiffeners participate in out-of-plane deflections. Predicting the onset of panel buckling is important as it may lead to catastrophic failure of the panel.

In Section 3.2.1.1, the basic theory of applying energy methods and the Rayleigh-Ritz method to general plate stability problems is reviewed. The use of Lagrange multipliers in the constrained minimization of a general functional is also explained. The two concepts are then combined to provide a method for solving plate buckling problems with unusual constraints, such as complex boundary conditions or attached stiffeners. In Section 3.2.1.2, the Rayleigh-Ritz method is used to solve for the buckling load of a simply-supported rectangular orthotropic plate under compression and shear loads. This solution allows a flat plate capability to be included in the design code and it also represents a step in the development for a stiffened panel. Finally, in Section 3.2.1.3, the method of Lagrange multipliers is used to calculate the buckling load for a simply supported geodesically stiffened rectangular panel.

3.2.1.1 Theory of Energy Methods with Constraints

Methods based on energy principles are very important for the analysis of plate-type structures. In conjunction with variational calculus, energy principles can be used to derive the basic governing equations and natural boundary conditions for anisotropic plates[27]. The practical importance of energy methods is their use in obtaining approximate solutions to complex plate problems. The Rayleigh-Ritz method, which is based on energy methods and is widely used for the bending, buckling, and vibration of plates, will be reviewed. A second topic to be considered is the use of Lagrange multipliers in plate problems. Lagrange multipliers represent a mathematical technique of imposing constraints on any general functional. Energy methods define a single scalar functional,

the total potential energy, which governs the entire plate problem. Therefore, Lagrange multipliers can be used to solve plate problems with unusual constraints such as complex boundary conditions or, in the present study, attached stiffeners.

Energy Methods: Energy methods are useful in those plate problems where a direct solution to the differential equation of equilibrium is not possible. These methods are based on the law of conservation of energy which requires that the work done by external forces on an elastic structure be stored in the form of strain energy. This leads to defining the total potential energy Π as the sum of the strain energy in a plate and the potential energy of the loads on the plate. For a plate under in-plane loads this takes the form

$$\Pi(u^\circ, v^\circ, w) = U + V \tag{32}$$

where u°, v°, w are displacements in the x, y, z directions, U is the strain energy of the plate, and V is the potential energy of the in-plane force resultants. The existence of a stable equilibrium configuration is defined by the "principle of the stationary value of the total potential" and the "principle of the minimum total potential."[30] The first principle states that an elastic system is in equilibrium only if the total potential has a stationary value

$$\Pi(u^\circ, v^\circ, w) = \text{stationary value} \tag{33}$$

The second principle states that only those kinematically admissible deformation fields which make the total potential a minimum correspond to a stable equilibrium. The solution of this extremum problem by an approximate method will now be considered.

Rayleigh-Ritz Method: The Rayleigh-Ritz method (sometimes called simply the Ritz method) is very useful in finding approximate solutions to boundary value problems. The method represents plate displacements in the form of finite series

$$
\begin{aligned}
w &= \sum_{m=1}^{M} \sum_{n=1}^{N} A_{mn} W_{mn}(x,y) \\
u^{\circ} &= \sum_{p=1}^{P} \sum_{q=1}^{Q} B_{pq} U_{pq}(x,y) \\
v^{\circ} &= \sum_{r=1}^{R} \sum_{s=1}^{S} C_{rs} V_{rs}(x,y)
\end{aligned}
\tag{34}
$$

where A_{mn}, B_{pq}, C_{rs} are undetermined coefficients and W_{mn}, U_{pq}, V_{rs} are known functions of the spatial coordinates x and y. These functions are usually chosen in variables separable form $X_i(x)Y_j(y)$ and must satisfy at least the geometric boundary conditions. In general, the Rayleigh-Ritz method gives approximate solutions as the equilibrium equations are not completely satisfied, and critical values will be higher than the true value. Although the choice of shape functions is somewhat arbitrary, a judicious selection may only require a few terms for an adequate solution. If the functions form a complete set and satisfy geometric boundary conditions, then in theory the exact solution will be obtained in the limit. In practice however, this is difficult to achieve (particularly for anisotropic plates) and convergence will be very slow. It has been proven, for example, that the deflection of a simply supported anisotropic plate cannot be represented in variables-separable form[31]. Fortunately, in many cases reasonable results can be obtained for plate deflections, critical loads, and vibration frequencies using energy methods. On the other hand, quantities involving the derivatives of the functions (moments, strains, stresses) may converge slowly, or not at all[27].

Introducing the assumed functions (34) into Equation (33) reduces the stability criterion to that of finding the minimum of Π with respect to the undetermined coefficients

$$
\begin{aligned}
\frac{\partial \Pi}{\partial A_{mn}} &= 0 \qquad m = 1, 2, \ldots, M \\
& \qquad\quad n = 1, 2, \ldots, N \\
\frac{\partial \Pi}{\partial B_{pq}} &= 0 \qquad p = 1, 2, \ldots, P \\
& \qquad\quad q = 1, 2, \ldots, Q \\
\frac{\partial \Pi}{\partial C_{rs}} &= 0 \qquad r = 1, 2, \ldots, R \\
& \qquad\quad s = 1, 2, \ldots, S
\end{aligned}
\tag{35}
$$

These expressions define ($M^*N + P^*Q + R^*S$) simultaneous algebraic equations in the ($M^*N + P^*Q + R^*S$) undetermined coefficients A_{mn}, B_{pq}, C_{rs}. In the case of buckling, they constitute an eigenvalue problem whose nontrivial solutions are found when the determinant of the coefficient matrix vanishes. The use of this procedure will be demonstrated for the buckling of both flat and stiffened plates. For these problems, where only symmetrically laminated plates are considered, the in-plane (u°, v°) and out-of-plane (w) problems uncouple. Therefore, the strain energy contribution of the inplane deformations can be considered an arbitrary constant, and only the first expression of Equations (34) and (35) need be considered[27].

Lagrange Multiplier Method: The procedure for applying the principle of Lagrange multipliers (or undetermined multipliers) as it applies to the minimization of a general functional subject to additional constraints on the function variables is shown below. Application of the Lagrange multiplier method to plate problems will then be discussed. A proof of the validity of the method can be found in Budiansky and Hu[32], as well as many texts on optimization or the calculus of variations.

It is required to minimize a function f of I variables $x_1, x_2, \ldots, x_I$

$$f(x_1, x_2, \ldots, x_I) \tag{36}$$

subject to J independent constraint functions g_j that require

$$\begin{aligned} g_1(x_1, x_2, \ldots, x_I) &= 0 \\ g_2(x_1, x_2, \ldots, x_I) &= 0 \\ &\vdots \\ g_J(x_1, x_2, \ldots, x_I) &= 0 \end{aligned} \tag{37}$$

A composite function L called the Lagrangian is now defined as

$$\begin{aligned} L(x, \gamma) &= f(x) + \gamma_1 g_1(x) + \gamma_2 g_2(x) + \cdots + \gamma_J g_J(x) \\ &= f(x) + \sum_{j=1}^{J} \gamma_J g_j(x) \end{aligned} \tag{38}$$

where x denotes the vector of variables $x_1, x_2, \ldots, x_I$ and γ the vector of undetermined Lagrange multipliers $\gamma_1, \gamma_2, \ldots, \gamma_J$. Note that one Lagrange multiplier γ_j is required for each constraint g_j. The necessary conditions for $f(x)$ to be a minimum while simultaneously satisfying the constraints γ are

$$\begin{aligned} \frac{\partial L(x,\gamma)}{\partial x_i} &= 0 \qquad i = 1, 2, \ldots, I \\ \frac{\partial L(x,\gamma)}{\partial \gamma_j} &= 0 \qquad j = 1, 2, \ldots, J \end{aligned} \tag{39}$$

Substituting Equation (38) in Equation (39) and performing the differentiation results in

$$\begin{aligned} \frac{\partial f(x)}{\partial x_i} + \sum_{j=1}^{J} \gamma_j \frac{\partial g_j(x)}{\partial x_i} &= 0 \qquad i = 1, 2, \ldots, I \\ g_j(x) &= 0 \qquad j = 1, 2, \ldots, J \end{aligned} \tag{40}$$

which represent $(I + J)$ simultaneous equations in the $(I + J)$ unknowns x and γ. These equations are then solved for the original variables x and, if desired, the Lagrange multipliers γ.

The method of Lagrange multipliers represents a powerful analysis tool, particularly for applications where variational methods can be used to express the problem in the form of a functional similar to $f(x)$. Clearly this is the case for energy method solutions to plate problems where the functional is the total potential energy Π. The Lagrange multiplier method can be applied to plate stability problems in several ways. For example, they can be used where it is difficult to find a deflection function which can satisfy the boundary conditions directly[32] [33] [34] [35]. Al-Shareedah and Seireg[36] have even considered problems with mixed boundary conditions along each edge. A second application of Lagrange multipliers is to impose additional constraints on problems where the deflection function already satisfies the boundary conditions. For example, Al-Shareedah and Seireg[37] imposed zero-displacement conditions in the interior of a pressure-loaded plate to represent supporting columns under a floor slab. This method has been used by the author to model the local buckling of various shaped skin sections of heavily stiffened panels by setting $w = 0$ along lines where the

stiffeners would be located. In a third paper, Al-Shareedah and Seireg[38] accurately predicted the transverse deflection of a pressure-loaded rectangular isotropic plate with an oblique stiffener. They used Lagrange multipliers to enforce transverse displacement continuity between the plate and stiffener at a finite number of points. In the present work, their technique is adapted and extended to the stability of orthotropic plates with multiple orthotropic oblique stiffeners under the action of in-plane loads.

3.2.1.2 Buckling of Flat Orthotropic Plate

The methodology for applying the Rayleigh-Ritz method to stability problems was reviewed in the previous section. The method will now be used to predict buckling of an orthotropic simply-supported rectangular plate under in-plane compressive loads N_x, N_y, and shear N_{xy}. The governing differential equation for a homogeneous anisotropic plate, or a symmetrically laminated composite plate, is given by [27]

$$\begin{aligned} D_{11}w_{,xxxx} + 4D_{16}w_{,xxxy} + 2(D_{12} + 2D_{66})w_{,xxyy} + 4D_{26}w_{,xyyy} + D_{22}w_{,yyyy} \\ + N_x w_{,xx} + 2N_{xy}w_{,xy} + N_y w_{,yy} = 0 \end{aligned} \tag{41}$$

where the comma notation denotes partial differentiation with respect to the subscripted variables and the in-plane force resultants N_x and N_y are positive when compressive. The direction of positive shear is also reversed from the standard convention. In the present analysis, it is assumed that the plate is specially orthotropic and the bending-twisting coupling terms D_{16} and D_{26} vanish. For most laminates (other than cross-ply) the D_{16} and D_{26} terms are in fact nonzero. However, using lamination sequences which do eliminate bending-twisting coupling simplifies analysis, maximizes stability loads, and minimizes distortion during manufacture[39]. Data sheets published by ESDU[39] provide a definitive list of layups, containing up to 21 layers, with special orthotropy. These results can be extended to laminates with more plies by combining groups of sublaminates. Even in general laminates, the coupling terms can be decreased by interspersing the angle plies through the thick-

ness. In any event, assuming that D_{16} and D_{26} are zero reduces the governing differential equation to that for a specially orthotropic laminate

$$D_{11}w_{,xxxx} + 2(D_{12} + 2D_{66})w_{,xxyy} + D_{22}w_{,yyyy} + N_x w_{,xx} + 2N_{xy}w_{,xy} + N_y w_{,yy} = 0 \qquad (42)$$

For a rectangular plate of width a in the x direction and height b in the y direction, the conditions for simply-supported boundaries are [27]

$$\left.\begin{aligned} w &= 0 \\ M_x &= -(D_{11}w_{,xx} + D_{12}w_{,yy}) = 0 \end{aligned}\right\} \text{ at } x = 0, a$$
$$\left.\begin{aligned} w &= 0 \\ M_y &= -(D_{12}w_{,xx} + D_{22}w_{,yy}) = 0 \end{aligned}\right\} \text{ at } y = 0, b \qquad (43)$$

If an assumed displacement function of the form

$$w(x,y) = \sum_{m=1}^{M}\sum_{n=1}^{N} A_{mn} \sin\frac{m\pi x}{a} \sin\frac{n\pi y}{b} \qquad \begin{matrix} 0 \le x \le a \\ 0 \le y \le b \end{matrix} \qquad (44)$$

is chosen, all boundary conditions in Equation (43) are exactly satisfied. It should be noted that if the plate were under the action of pure compression (i.e. $N_{xy} = 0$), the differential equation (42) would contain only even derivatives in x and y. The function in Equation (44) would then exactly satisfy both Equations (42) and (43) and the solution could be found directly via substitution in the differential equation. Applying shear, however, introduces odd derivatives in the differential equation so that an approximate solution method must be resorted to. In this example the Rayleigh-Ritz method is used, but the Galerkin method would give an identical result.

Whitney[27] expresses strain energy in bending of a specially orthotropic plate as

$$U = \frac{1}{2}\int_0^a \int_0^b \left[D_{11}(w_{,xx})^2 + 2D_{12}(w_{,xx})(w_{,yy}) + D_{22}(w_{,yy})^2 + 4D_{66}(w_{,xy})^2\right] dx\, dy \qquad (45)$$

and the potential energy of external in-plane loads as

$$V = -\frac{1}{2}\int_0^a \int_0^b \left[N_x(w_{,xx})^2 + 2N_{xy}(w_{,x})(w_{,y}) + N_y(w_{,yy})^2\right] dx\, dy \tag{46}$$

Having chosen a displacement function, explicit expressions for the energies can be written. The required second order derivatives of w in Equation (44) are substituted into the strain energy expression (45) and the products of the series expanded. The order of summation and integration operations are reversed and the trigonometric products evaluated using the identities

$$\begin{aligned}
\int_0^\ell \sin\frac{i\pi x}{\ell}\sin\frac{j\pi x}{\ell}\, dx &= \begin{cases} \frac{\ell}{2} & i = j \\ 0 & i \neq j \end{cases} \\
\int_0^\ell \cos\frac{i\pi x}{\ell}\cos\frac{j\pi x}{\ell}\, dx &= \begin{cases} \frac{\ell}{2} & i = j \\ 0 & i \neq j \end{cases}
\end{aligned} \tag{47}$$

Due to the orthogonal nature of the trigonometric series, only terms in which both the x and y portions have pairs of identical indices, giving $\sin^2$ or $\cos^2$ expressions, remain nonzero. After integration, the strain energy expression simplifies to

$$U = \frac{\pi^4 ab}{8}\sum_{m=1}^{M}\sum_{n=1}^{N} A_{mn}^2\left[D_{11}\left(\frac{m}{a}\right)^4 + 2(D_{12} + 2D_{66})\left(\frac{mn}{ab}\right)^2 + D_{22}\left(\frac{n}{b}\right)^2\right] \tag{48}$$

The corresponding expression for the potential energy V is found by substituting both first and second order derivatives of w into Equation (46) and using the identities in Equation (47) plus

$$\int_0^\ell \sin\frac{i\pi x}{\ell}\cos\frac{j\pi x}{\ell}\, dx = \begin{cases} \dfrac{2i\ell}{\pi(i^2 - j^2)}, & (i+j)\ \text{odd} \\ 0, & (i+j)\ \text{even} \end{cases} \tag{49}$$

to arrive at

$$V = -\frac{\pi^2 ab}{8}\sum_{m=1}^{M}\sum_{n=1}^{N}A_{mn}^2\left[N_x\left(\frac{m}{a}\right)^2 + N_y\left(\frac{n}{b}\right)^2\right]$$
$$-4N_{xy}\sum_{m=1}^{M}\sum_{n=1}^{N}\sum_{p=1}^{M}\sum_{q=1}^{N}A_{mn}A_{pq}\frac{mnpq}{(p^2-m^2)(n^2-q^2)} \tag{50}$$

with the coefficient of N_{xy} nonzero only when $(m+p)$ and $(n+q)$ are both odd. The energy expressions are now abbreviated as

$$U = \sum_{m=1}^{M}\sum_{n=1}^{N}A_{mn}^2 P^{mn}$$
$$V = -\lambda\left\{\sum_{m=1}^{M}\sum_{n=1}^{N}A_{mn}^2 R^{mn} + \sum_{m=1}^{M}\sum_{n=1}^{N}\sum_{p=1}^{M}\sum_{q=1}^{N}A_{mn}A_{pq}S^{mnpq}\right\} \tag{51}$$

where the functions of the indices are

$$P^{mn} = \frac{\pi^4 ab}{8}\left[D_{11}\left(\frac{m}{a}\right)^4 + 2(D_{12}+2D_{66})\left(\frac{mn}{ab}\right)^2 + D_{22}\left(\frac{n}{b}\right)^4\right]$$
$$R^{mn} = \frac{\pi^2 ab}{8}\left[\overline{N}_x\left(\frac{m}{a}\right)^2 + \overline{N}_y\left(\frac{n}{b}\right)^2\right] \tag{52}$$
$$S^{mnpq} = \begin{cases}\overline{N}_{xy}\dfrac{4mnpq}{(p^2-m^2)(n^2-q^2)}, & (m+p) \text{ and } (n+q) \text{ odd} \\ 0, & \text{otherwise}\end{cases}$$

and a common multiplicative factor λ has been extracted from the applied loads

$$N_x = \lambda\overline{N}_x$$
$$N_y = \lambda\overline{N}_y \tag{53}$$
$$N_{xy} = \lambda\overline{N}_{xy}$$

Adding U and V from Equations (51) gives the total potential energy Π as a function of the undetermined coefficients A_{mn}. The solution is determined by satisfying the conditions

$$\frac{\partial \Pi}{\partial A_{ij}} = 0 \qquad \begin{matrix} i = 1, 2, \ldots, M \\ j = 1, 2, \ldots, N \end{matrix} \tag{54}$$

Carrying out the partial derivatives of Equation (54) on the total potential energy results in

$$2A_{ij}P^{ij} - \lambda \left\{ 2A_{ij}R^{ij} + \sum_{p=1}^{M}\sum_{q=1}^{N} A_{pq}S^{ijpq} + \sum_{m=1}^{M}\sum_{n=1}^{N} A_{mn}S^{mnij} \right\} = 0 \qquad \begin{matrix} i = 1, 2, \ldots, M \\ j = 1, 2, \ldots, N \end{matrix} \tag{55}$$

Examining Equation (52) reveals that $S^{mnpq} = S^{pqmn}$, so the two summations in Equation (55) can be combined. Eliminating the common factor of 2 and returning to the original indices m and n produces the final expression

$$A_{mn}P^{mn} - \lambda \left\{ A_{mn}R^{mn} + \sum_{p=1}^{M}\sum_{q=1}^{N} A_{pq}S^{mnpq} \right\} = 0 \qquad \begin{matrix} m = 1, 2, \ldots, M \\ n = 1, 2, \ldots, N \end{matrix} \tag{56}$$

where P^{mn}, R^{mn}, and S^{mnpq} are as given by Equation (52). Equation (56) defines a set of $(M*N)$ algebraic equations in the $(M*N)$ unknowns A_{mn}. This constitutes a classical eigenvalue problem, which may be expressed in matrix form as

$$[\,[K] - \lambda[M]\,]\{A\} = 0 \tag{57}$$

For a nontrivial solution (i.e. $A_{mn} \neq 0$), it is required that the determinant of the coefficient matrix of $\{A\}$ be zero. This will result in $(M*N)$ eigenvalues λ_i with $(M*N)$ associated eigenvectors $\{A\}_i$. The smallest positive eigenvalue λ_{CR}, when substituted in Equation (53), determines the critical loads for the plate. The eigenvector associated with the critical eigenvalue specifies the deformed shape of the buckled plate, although the actual displacements are indeterminate.

3.2.1.3 Buckling of Orthotropic Plate with Oblique Stiffeners

As discussed in earlier sections, buckling analyses for stiffened panels (and particularly so for oblique stiffening) may resort to smearing the stiffeners. For panels with only a few stiffeners, however, this approach does not represent a good approximation. Energy methods which treat the stiffeners as discrete elements were developed for isotropic panels with longitudinal or transverse stiffeners at least forty years ago; e.g. Timoshenko and Gere[25], Budiansky and Seide[40], Seide and Stein[41]. The approach is to minimize the total energy of the stiffened panel, which includes strain energy of the flat plate, potential energy of the loads on the plate, the strain energy of each individual stiffener, and the potential energy of the loads on each stiffener. Since longitudinal and transverse stiffeners are parallel to the plate coordinate system, it is easy to obtain expressions for the stiffener deflections in terms of a single parameter, the skin deflection w. When the stiffeners are oriented at some angle to the coordinate axes, however, the required expression for the skin deflection along an arbitrary oblique line is rather complicated. The problem is exacerbated when products of the derivatives of that expression are required in the energy relations. Hofmeister and Felton[42 43] solved the buckling problem in this manner for a square isotropic plate with a single pair of oblique stiffeners. Although viable for one specific geometry, they stated that this approach was too involved for general stiffener orientations.

An alternate approach based on undetermined, or Lagrange, multipliers has been used by Al-Shareedah and Seireg[38] for the transverse deflection of a pressure-loaded rectangular isotropic plate with an oblique stiffener. Rather than expressing stiffener deflections in terms of complicated functions of w, the deflection of a stiffener is expanded in a function defined in a local coordinate system independent of that for the skin deflection. The strain energy of the stiffener and potential energy of the stiffener loads are then easily found in terms of this simple function. Continuity of out-of-plane deflection between the skin and the stiffener is imposed at a finite number of points along the stiffener axis using Lagrange multipliers. The total energy of the system is then minimized to determine the solution for the stiffened panel assembly while simultaneously satisfying all dis-

placement constraints. In the present work, this technique has been adapted to the stability of orthotropic plates with multiple orthotropic oblique stiffeners under the action of in-plane loads. There are a number of assumptions and limitations inherent to the Lagrange multiplier method approach:

1. Continuity of stiffener-skin displacements is imposed at a finite number of infinitesimal points; the width or shape of the stiffener has no effect other than that on the second moment of inertia of the stiffener cross-section.
2. It is assumed that each stiffener has zero in-plane flexural stiffness (i.e. for bending in a plane parallel to the surface of the skin) and zero torsional stiffness.
3. Small deflection theory for bending of the plate and simple beam theory for bending of the stiffeners are used.
4. The load distribution between the skin and stiffeners must be known in advance.

Expressions for the strain energy and potential energy of external loads for a rectangular orthotropic plate have already been derived and summarized in Equations (51) and (52). Therefore, only energy expressions for the deformation of the specially orthotropic stiffeners are required. In computing the energy expressions for the stiffeners, it is assumed that each stiffener behaves as an orthotropic beam allowed to deform only in out-of-plane bending. Specially orthotropic beams, where all orthotropic plies are oriented parallel to the axis of the beam (cross-ply beams are also specially orthotropic, but are not considered in the present study), can be analyzed by classical isotropic beam theory if the isotropic modulus of elasticity E is replaced by E_ℓ, which is the longitudinal modulus of the plies in a direction parallel to the fibers[27]. The strain energy in bending of an orthotropic beam is then given by [25]

$$u_s = \frac{E_\ell I_s}{2} \int_0^L (\xi_{,\eta\eta})^2 \, d\eta \tag{58}$$

where the S subscript indicates this component of the energy is for a stiffener, ξ is the transverse deflection of the stiffener, and η is the coordinate axis oriented along the stiffener of length L. The total moment of inertia I_s for the two stiffener sections (one above and one below the skin) with respect to an axis coincident with the midplane of the skin is calculated via the parallel axis theorem. The potential energy of external forces on a beam is not dependent on material properties, so the expression will be same as that for an isotropic beam [25]

$$v_s = -\frac{F}{2}\int_0^L (\xi_{,\eta})^2 \, d\eta \tag{59}$$

where F is the total axial load on the stiffener.

In Section 3.2.1.2, simply-supported boundary conditions were assumed for the rectangular plate. Consistent with this assumption, the boundary conditions for a beam with simply-supported ends are

$$\left.\begin{aligned} \xi &= 0 \\ M &= E_\ell I_s \xi_{,\eta\eta} = 0 \end{aligned}\right\} \text{ at } \eta = 0, L \tag{60}$$

Expanding the stiffener deflection in a single sine series

$$\xi(\eta) = \sum_{k=1}^{K} B_k \frac{\sin k\pi\eta}{L} \qquad 0 \le \eta \le L \tag{61}$$

satisfies the zero deflection and moment conditions at both ends. To calculate the strain energy for each beam, the second derivative of Equation (61) is taken with respect to η and the result substituted in Equation (58). As was the case for the plate energy expressions, squaring the series and integrating using Equation (47) eliminates all terms except those with $\sin^2$. The strain energy in bending of the beam is then

$$u_s = \frac{\pi^4 E_\ell I_s}{4L^3} \sum_{k=1}^{K} k^4 B_k^2 \tag{62}$$

The expression for the potential energy of the axial load F on the beam is found by taking the first derivative of Equation (61) with respect to η, substituting in Equation (59) and integrating over the length of the beam

$$v_s = -\frac{\pi^2 F}{4L} \sum_{k=1}^{K} k^2 B_k^2 \tag{63}$$

The energy expressions can be abbreviated for convenience. For completeness, the relations for a flat plate (the skin of the panel), now denoted by a subscript P, are repeated from Equations (51) and (52)

$$\begin{aligned}
U_P &= \sum_{m=1}^{M} \sum_{n=1}^{N} A_{mn}^2 P^{mn} \\
U_S &= \sum_{i=1}^{I} (u_s)_i = \sum_{i=1}^{I} \sum_{k=1}^{K} B_{ik}^2 Q^k \\
V_P &= -\lambda \left\{ \sum_{m=1}^{M} \sum_{n=1}^{N} A_{mn}^2 R^{mn} + \sum_{m=1}^{M} \sum_{n=1}^{N} \sum_{p=1}^{M} \sum_{q=1}^{N} A_{mn} A_{pq} S^{mnpq} \right\} \\
V_S &= \sum_{i=1}^{I} (v_s)_i = -\lambda \sum_{i=1}^{I} \sum_{k=1}^{K} B_{ik}^2 T^{ik}
\end{aligned} \tag{64}$$

where the functions of the indices are defined as

$$P^{mn} = \frac{\pi^4 ab}{8}\left[D_{11}\left(\frac{m}{a}\right)^4 + 2(D_{12} + 2D_{66})\left(\frac{mn}{ab}\right)^2 + D_{22}\left(\frac{n}{b}\right)^4\right]$$

$$Q^k = \frac{\pi^4 E_e I_s}{4L^3} k^4$$

$$R^{mn} = \frac{\pi^2 ab}{8}\left[\overline{N}_x^P\left(\frac{m}{a}\right)^2 + \overline{N}_y^P\left(\frac{n}{b}\right)^2\right]$$

$$S^{mnpq} = \begin{cases} \overline{N}_{xy}^P \dfrac{4mnpq}{(p^2 - m^2)(n^2 - q^2)}, & (m+p) \text{ and } (n+q) \text{ odd} \\ 0, & \text{otherwise} \end{cases}$$

$$T^{lk} = \frac{\pi^2 k^2}{4L} \overline{F}_l$$

and a common multiplicative factor λ has been extracted from the loads

$$N_x^P = \lambda \overline{N}_x^P \quad N_y^P = \lambda \overline{N}_y^P \quad N_{xy}^P = \lambda \overline{N}_{xy}^P \quad F_l = \lambda \overline{F}_l \tag{65}$$

Note that the energy expressions for the stiffeners in Equation (64) are the sum of contributions from I number of stiffeners. It has been assumed that all stiffeners have the same E_e, I_s, and L.

The total energy of the stiffened panel is given by

$$\Pi = U_P + U_S + V_P + V_S \tag{66}$$

where the transverse displacement of the skin and each stiffener were expanded in independent trigonometric series. However, the skin and stiffeners are, of course, physically bonded together. The compatibility of displacements is imposed at a finite number of points along each stiffener (Figure 12). In terms of the displacements this condition is expressed as

$$g_{ij} = \sum_{m=1}^{M}\sum_{n=1}^{N} A_{mn} \sin\frac{m\pi}{a} x_{ij} \sin\frac{n\pi}{b} y_{ij} - \sum_{k=1}^{K} B_{ik} \sin\frac{k\pi}{L} \eta_{ij} = 0 \qquad \begin{matrix} i = 1, 2, \ldots, I \\ j = 1, 2, \ldots, J \end{matrix} \tag{67}$$

where the index i denotes a particular stiffener and the index j a constraint point on that stiffener. It has been assumed that each stiffener has the same number J of constraint points. In order to find

the critical load of the stiffened panel, the total energy is minimized subject to the constraints on displacement compatibility. This is accomplished by the use of Lagrange multipliers, where one multiplier is required for each constraint, in this case each location on the skin (x_{ij}, y_{ij}) and the coinciding point η_{ij} on the stiffener where the displacements are to match. The *(I*J)* constraints are imposed on the total energy of the panel with the multipliers μ_{ij} creating the functional

$$\Phi = \Pi + \sum_{i=1}^{I} \sum_{j=1}^{J} \mu_{ij} g_{ij} \tag{68}$$

Substituting Equations (64) and (67) into Equation (68) gives the complete expression for Φ in terms of the unknown constants A_{mn}, B_{ik}, and μ_{ij}. The conditions for a minimum of Φ are

$$\begin{aligned} &\frac{\partial \Phi}{\partial A_{mn}} = 0 && m = 1, 2, \ldots, M \\ &&& n = 1, 2, \ldots, N \\ &\frac{\partial \Phi}{\partial B_{ik}} = 0 && i = 1, 2, \ldots, I \\ &&& k = 1, 2, \ldots, K \\ &\frac{\partial \Phi}{\partial \mu_{ij}} = 0 && i = 1, 2, \ldots, I \\ &&& j = 1, 2, \ldots, J \end{aligned} \tag{69}$$

which result in the following set of equations

$$\begin{aligned} &2A_{mn}P^{mn} + \sum_{i=1}^{I} \sum_{j=1}^{J} \mu_{ij} \left[\sin \frac{m\pi}{a} x_{ij} \sin \frac{n\pi}{b} y_{ij} \right] && m = 1, 2, \ldots, M \\ &\quad - \lambda \left\{ 2A_{mn}R^{mn} + 2 \sum_{p=1}^{M} \sum_{q=1}^{N} A_{pq} S^{mnpq} \right\} = 0 && n = 1, 2, \ldots, N \\ &2B_{ik}Q^{k} + \sum_{i}^{I} \mu_{ij} \left[- \sin \frac{k\pi}{L} \eta_{ij} \right] - \lambda \{ 2B_{ik}T^{ik} \} = 0 && i = 1, 2, \ldots, I \\ &&& k = 1, 2, \ldots, K \\ &\sum_{m=1}^{M} \sum_{n=1}^{N} A_{mn} \sin \frac{m\pi}{a} x_{ij} \sin \frac{n\pi}{b} y_{ij} - \sum_{k=1}^{K} B_{ik} \sin \frac{k\pi}{L} \eta_{ij} = 0 && i = 1, 2, \ldots, I \\ &&& j = 1, 2, \ldots, J \end{aligned} \tag{70}$$

Equations (70) represent $(M^*N + I^*K + I^*J)$ equations in the $(M^*N + I^*K + I^*J)$ unknowns A_{mn}, B_{ik}, and μ_{ij} . They constitute a classical eigenvalue problem where the lowest positive eigenvalue λ_{CR} determines the critical load of the skin and stiffener assembly.

The set of unknowns, including A_{mn}, B_{jk}, and μ_{ij} , tends to grow rather rapidly as the number of stiffeners, number of constraint points, or the number of terms in the skin or stiffener deflection functions is increased. This is of concern as the eigenvalue solver uses an iterative solution process which becomes computationally expensive as the order of the coefficient matrices increases. As such, it is advantageous to reduce the size of the problem, or condense the coefficient matrices, by eliminating some of the unknowns prior to calling the eigenvalue solver.

The set of equations (70) can be written in matrix form

$$\begin{bmatrix} [K_{11}] & [0] & [K_{13}] \\ [0] & [K_{22}] & [K_{23}] \\ [K_{31}] & [K_{32}] & [0] \end{bmatrix} \begin{bmatrix} \{A\} \\ \{B\} \\ \{\mu\} \end{bmatrix} = \lambda \begin{bmatrix} [M_{11}] & [0] & [0] \\ [0] & [M_{22}] & [0] \\ [0] & [0] & [0] \end{bmatrix} \begin{bmatrix} \{A\} \\ \{B\} \\ \{\mu\} \end{bmatrix} \tag{71}$$

It is observed that the coefficient matrices are, in fact, rather sparse. The first step in the condensation process will be to eliminate $\{\mu\}$. Note that $\{\mu\}$ is absent from the third row, so attention need only be paid to the first two. To isolate $\{\mu\}$ from one of these equations, it is necessary to invert either $[K_{13}]$ or $[K_{23}]$. Of course, in order to invert a matrix it must be square in dimension. However, $[K_{13}]$ has dimensions (M^*N) by (J^*K) while $[K_{23}]$ is (J^*K) by (J^*I). Requiring that (M^*N) equal (J^*K) is not practical as, for example, a panel with only a few stiffeners (small J) would have to have an excessive number of terms in the stiffener function (large K) or only a few terms in the skin function. Alternatively, having $(J^*K) = (J^*I)$, meaning $K = I$, is not too restrictive. That is, as the number of constraint points per stiffener is increased, the number of terms in the stiffener deflection function must increase correspondingly, but the the number of terms in the skin deflection function remains independent. Therefore, it is more practical to set $K = I$ and invert $[K_{23}]$. Multiplying out the second row of Equation (71) and rearranging to isolate $\{\mu\}$

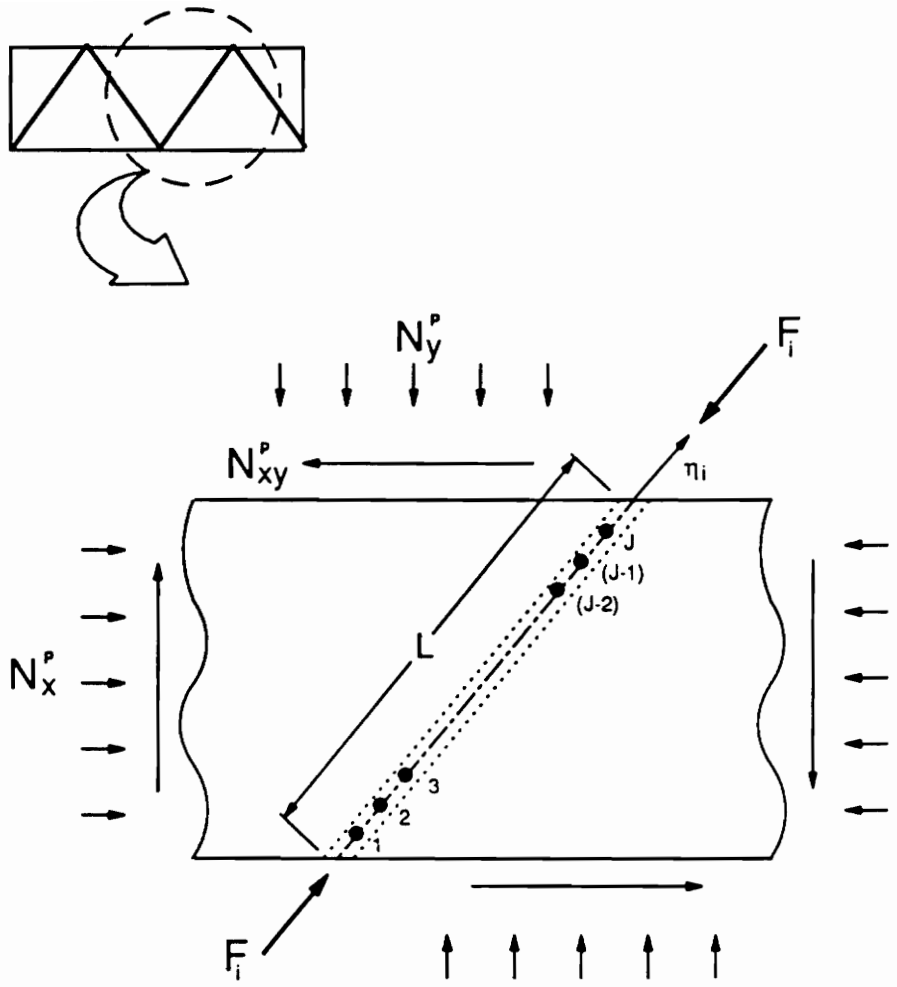

Figure 12. Lagrange Multiplier Model of Plate and Oblique Stiffener

$$\{\mu\} = [K_{23}]^{-1}[\lambda[M_{22}]\{B\} - [K_{22}]\{B\}] \tag{72}$$

This expression can simply be substituted into the first row of Equation (71) to eliminate $\{\mu\}$. Proceeding with this, and then rearranging to isolate nonload terms on the left hand side and the load terms (those with a λ coefficient) on the right gives

$$[K_{11}]\{A\} - [K_{13}][K_{23}]^{-1}[K_{22}]\{B\} = \lambda[M_{11}]\{A\} - \lambda[K_{13}][K_{23}]^{-1}[M_{22}]\{B\} \tag{73}$$

The above equation can be rewritten by labelling the matrix products as new submatrices. Along with the third row of Equation (71), the condensed set of equations becomes

$$\begin{bmatrix} [K_{11}] & [K_{12}] \\ [K_{31}] & [K_{32}] \end{bmatrix} \begin{bmatrix} \{A\} \\ \{B\} \end{bmatrix} = \lambda \begin{bmatrix} [M_{11}] & [M_{12}] \\ [0] & [0] \end{bmatrix} \begin{bmatrix} \{A\} \\ \{B\} \end{bmatrix} \tag{74}$$

with

$$\begin{aligned} [K_{12}] &= -[K_{13}][K_{23}]^{-1}[K_{22}] \\ [M_{12}] &= -[K_{13}][K_{23}]^{-1}[M_{22}] \end{aligned} \tag{75}$$

The second step of the condensation process eliminates either $\{A\}$ or $\{B\}$, leaving the solution only in terms of the other. In order to eliminate $\{A\}$ it is necessary to invert $[K_{31}]$, which is undesirable for previously mentioned reasons. On the other hand, removing $\{B\}$ involves the inversion of $[K_{32}]$. This matrix is already square due to assumptions made in the first condensation step, so no further restrictions are necessary for this route. Choosing the latter by eliminating $\{B\}$, the second row of Equation (74) is multiplied out and rearranged to isolate $\{B\}$

$$\{B\} = -[K_{32}]^{-1}[K_{31}]\{A\} \tag{76}$$

The above is substituted for $\{B\}$ in the first row of Equation (74) to yield

$$[[K_{11}] - [K_{12}][K_{32}]^{-1}[K_{31}]]\{A\} = \lambda[[M_{11}] - [M_{12}][K_{32}]^{-1}[K_{31}]]\{A\} \tag{77}$$

Substituting for $[K_{12}]$ and $[M_{12}]$ from Equation (75), the final condensed solution can be written in terms of the original submatrix components as

$$[K^*]\{A\} = \lambda\,[M^*]\{A\} \tag{78}$$

with

$$\begin{aligned}[K^*] &= [K_{11}] + [K_{13}]\,[K_{23}]^{-1}[K_{22}]\,[K_{32}]^{-1}[K_{31}] \\ [M^*] &= [M_{11}] + [K_{13}]\,[K_{23}]^{-1}[M_{22}]\,[K_{32}]^{-1}[K_{31}]\end{aligned} \tag{79}$$

The order of the matrices to be solved has been reduced from $(M*N + I*K + I*J)$ to just $(M*N)$, which considerably reduces the computational time required by the eigenvalue solver. This has been accomplished through a small number of matrix operations whose computational time is, in general, more than offset by the saving in solver time. For example, a typical test problem was run for a cross-stiffened panel with 5 cells. The skin deflection function had 15 terms in the X direction and 9 in the Y direction. Each of the 10 stiffeners had 7 constraint points and consequently 7 terms in its deflection series. Therefore, the parameters governing the problem were $M = 15, N = 9, I = 10, J = 7$, and $K = 7$. Performing the first stage of condensation, removing $\{\mu\}$ to obtain Equation (74), reduces the coefficient matrix order from 275 to 205. Despite using computer time for condensation matrix operations, the total solution time is cut to 50% of that required to solve the full matrix in Equation (71). Performing the second condensation step, removing $\{B\}$ to yield Equation (78), reduces the matrix order to 135 and the computer time to just 21% of the original.

3.2.2 Summary of Stiffener Buckling Analysis

In Section 3.2.1.3, the overall or generalized buckling of a geodesically stiffened panel was treated. A second possible mode of instability for stiffened panels is local buckling or crippling of the stiffeners. In this mode, the free edge of the blade stiffener is assumed to deflect parallel to the plane

of the panel between the boundaries (see Figure 7 on page 18). The restraint conditions on the three supported edges represent some unknown degree of elastic restraint, but for simplicity classical boundary conditions are assumed. The skin is generally quite thin, so it primarily provides restraint against translation of the adjacent stiffener edge, but little resistance to edge rotation. Also, it is anticipated that for a fully constrained optimum panel design, stiffener and skin buckling will often occur simultaneously, allowing the edge of each component to rotate with little mutual resistance. The loaded ends of the stiffener typically form a junction with other stiffeners or the supporting structure at the edges of the panel. Experimental tests on isogrid stiffened aluminum shells indicated that the degree of restraint at the ends of the stiffeners was close to the clamped condition[44]. On the other hand, many studies in the literature have assumed simply supported ends. Since the simple support assumption results in a conservative design, this condition is adopted for the present work. Therefore, each blade stiffener is modelled as a rectangular plate with simply supported and free unloaded edges and simply supported loaded ends under uniform axial compression (Figure 13). It is assumed that the stiffener buckles in a single half-wave between the loaded ends. The end load is calculated using the results of the in-plane static analysis described in Section 3.1.1.

Geodesically stiffened composite panels are often constructed using a filament-winding technique, as discussed in Section 1.0. The primary advantage of this method is reduced fabrication cost through automation. Coincidentally, it also produces excellent stiffness and strength properties in the primary loading direction of each stiffener by orienting the fibers along the stiffener axis. However, the transverse shear stiffness of this arrangement is governed primarily by the rigidity of the matrix material, which is low for typical high performance composites. In addition, stiffeners are often quite thick with respect to their height and length. It is well known that for plates with low ratios of interlaminar shear to in-plane extensional moduli and low ratios of planform to thickness dimensions (less than about 10), significant error can be incurred by using classical thin plate theory[27]. Experimental tests by Rehfield, *et al*[4,5] on filament-wound isogrid panels have confirmed that transverse shear effects are significant. Therefore, a first order shear deformation theory [FSDT] of plates, in which shear deformation is assumed to vary linearly through the

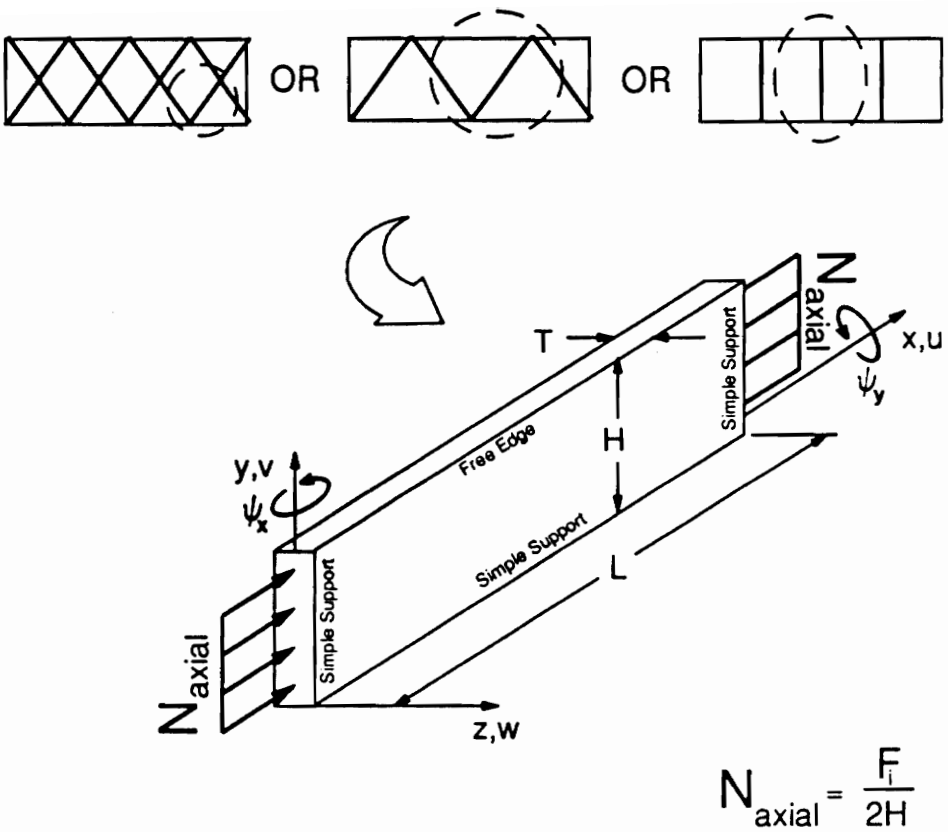

Figure 13. Stiffener Crippling Model

thickness of the plate, is used to formulate the equations governing the stiffener stability problem. Although this formulation is more involved than that for thin plate theory, unidirectional fiber orientation results in specially orthotropic material properties, simplifying the equations considerably. In the following discussion, FSDT is introduced and the Rayleigh-Ritz solution for the buckling of a stiffener with simply supported ends is summarized. The complete derivation for both simply supported and clamped ends is given by Stoll[18].

In FSDT, or Mindlin-type plate theory, the deformation due to transverse shear is assumed to be linear through the thickness of the plate. The general displacement field takes the form

$$\begin{aligned} u(x,y,z) &= u^{\circ}(x,y) + z\psi_x(x,y) \\ v(x,y,z) &= v^{\circ}(x,y) + z\psi_y(x,y) \\ w(x,y,z) &= w(x,y) \end{aligned} \tag{80}$$

where u, v, and w are displacements in the x, y, and z directions, respectively. Midplane displacements in the x and y directions are u° and v°, while the customary assumption of negligible transverse normal strain ε_z implies that w is independent of z. The quantities ψ_x and ψ_y represent rotations about the y and x axes, respectively, of a line initially perpendicular to the midplane surface. In FSDT, the plate deformation is expressed as a function of five independent variables u°, v°, w, ψ_x, ψ_y. In contrast to classical plate theory (which has only three independent variables u°, v°, w), FSDT allows the rotations of the midplane normal line to vary independently of the midplane surface deformation. The two extra degrees of freedom mean that plate response predicted by FSDT will always be "softer", and buckling loads lower, than that predicted by classical theory.

Using strain-displacement and stress-strain relations in conjunction with the usual definition of force and moment resultants leads to the constitutive relations (in abbreviated form)

$$\begin{Bmatrix} N \\ M \end{Bmatrix} = \begin{bmatrix} A & B \\ B & D \end{bmatrix} \begin{Bmatrix} \varepsilon^{\circ} \\ \kappa \end{Bmatrix} \tag{81}$$

where $\{N\}$ and $\{M\}$ are force and moment resultants and the midplane strains and curvatures are defined as

$$\begin{Bmatrix} \varepsilon_x^\circ \\ \varepsilon_y^\circ \\ \gamma_{xy}^\circ \end{Bmatrix} = \begin{Bmatrix} \dfrac{\partial u^\circ}{\partial x} \\ \dfrac{\partial v^\circ}{\partial y} \\ \dfrac{\partial u^\circ}{\partial y} + \dfrac{\partial v^\circ}{\partial x} \end{Bmatrix} \qquad \begin{Bmatrix} \kappa_x^\circ \\ \kappa_y^\circ \\ \kappa_{xy}^\circ \end{Bmatrix} = \begin{Bmatrix} \dfrac{\partial \psi_x}{\partial x} \\ \dfrac{\partial \psi_y}{\partial y} \\ \dfrac{\partial \psi_x}{\partial y} + \dfrac{\partial \psi_y}{\partial x} \end{Bmatrix} \tag{82}$$

Note that the relations in Equations (81) and (82) are identical to those for classical lamination theory, except that the curvatures κ are defined in terms of ψ_x and ψ_y instead of w. In fact, if the rotations were assumed to take the form

$$\psi_x = -\frac{\partial w}{\partial x} \qquad \psi_y = -\frac{\partial w}{\partial y} \tag{83}$$

the governing equations would reduce to those of classical plate theory with only three independent variables. Constitutive relations governing the transverse shear behavior are also required and take the form

$$\begin{Bmatrix} Q_y \\ Q_x \end{Bmatrix} = k^2 \begin{bmatrix} A_{44} & A_{45} \\ A_{45} & A_{55} \end{bmatrix} \begin{Bmatrix} \gamma_{yz} \\ \gamma_{xz} \end{Bmatrix} \tag{84}$$

where

$$\begin{Bmatrix} \gamma_{yz} \\ \gamma_{xz} \end{Bmatrix} = \begin{Bmatrix} \psi_y + \dfrac{\partial w}{\partial y} \\ \psi_x + \dfrac{\partial w}{\partial x} \end{Bmatrix} \tag{85}$$

and

$$A_{ij} = \int_{\left(-\frac{T}{2}\right)}^{\left(\frac{T}{2}\right)} C_{ij}\, dz \qquad i, j = 4, 5 \tag{86}$$

in which k^2 is known as the shear correction factor and T is the total thickness of the plate. Note that if Equation (83) were substituted in Equation (85), the transverse shear strains go to zero, as expected. For homogeneous, specially orthotropic material Equation (86) reduces to

$$A_{44} = G_{23}T, \quad A_{55} = G_{13}T, \quad A_{45} = 0 \tag{87}$$

FSDT specifies a shear strain which is constant through the plate thickness, but to account for the fact that the transverse shear strains are not constant in each ply of a laminate, a shear correction factor is used[45]. Several approaches have been used in the literature to determine the shear correction factor. The value of $k^2 = 5/6$, derived by considering the transverse shear stress distributions in a homogeneous orthotropic plate under static bending loads, is used in this study[27] [46]. This value has been shown to give acceptable accuracy for initial buckling of moderately thick multilayered plates[45].

The governing equations and natural boundary conditions for the stability of the shear deformable plate are derived using the calculus of variations in conjunction with the principle of minimum total potential energy. Only the basic steps of the solution are outlined here; for the complete procedure see Stoll[18]. Restricting the problem to specially orthotropic material eliminates the bending-extensional coupling terms ($B_{ij} = 0$), allowing the out-of-plane problem to be solved independently of the in-plane problem. The Rayleigh-Ritz procedure, described in Section 3.2.1.1, is introduced by assuming approximate solutions for the variables w, ψ_x, and ψ_y in the form

$$w = \sum_{i=1}^{N_w} A_i \phi_i(x,y) \qquad \psi_x = \sum_{i=1}^{N_{\psi_x}} B_i \theta_i^x(x,y) \qquad \psi_y = \sum_{i=1}^{N_{\psi_y}} C_i \theta_i^y(x,y) \tag{88}$$

where $\phi_i(x,y)$, $\theta_i^x(x,y)$, and $\theta_i^y(x,y)$ are shape functions which satisfy the geometric boundary conditions and are part of a complete set while A_i, B_i, and C_i are unknown constant coefficients. The variational procedure results in the system of algebraic equations

$$\sum_{j=1}^{N_w} K_{11}^{ij} A_j + \sum_{j=1}^{N_{\psi_x}} K_{12}^{ij} B_j + \sum_{j=1}^{N_{\psi_y}} K_{13}^{ij} C_j = \lambda \sum_{j=1}^{N_w} M_{11}^{ij} A_j \qquad i = 1,2,...,N_w$$

$$\sum_{j=1}^{N_w} K_{21}^{ij} A_j + \sum_{j=1}^{N_{\psi_x}} K_{22}^{ij} B_j + \sum_{j=1}^{N_{\psi_y}} K_{23}^{ij} C_j = 0 \qquad i = 1,2,..., N_{\psi_x} \tag{89}$$

$$\sum_{j=1}^{N_w} K_{31}^{ij} A_j + \sum_{j=1}^{N_{\psi_x}} K_{32}^{ij} B_j + \sum_{j=1}^{N_{\psi_y}} K_{33}^{ij} C_j = 0 \qquad i = 1,2,..., N_{\psi_y}$$

where the $K_{\alpha\beta}$ ($\alpha, \beta = 1,2,3$) and M_{11} are functions involving the area integral over the plate domain of various combinations of w, ψ_x, ψ_y, and their first derivatives with respect to x and y. The set of Equations (89) can be written in symbolic form

$$\begin{bmatrix} [K_{11}] & [K_{12}] & [K_{13}] \\ [K_{12}] & [K_{22}] & [K_{23}] \\ [K_{13}] & [K_{23}] & [K_{33}] \end{bmatrix} \begin{bmatrix} \{A\} \\ \{B\} \\ \{C\} \end{bmatrix} = \lambda \begin{bmatrix} [M_{11}] & [0] & [0] \\ [0] & [0] & [0] \\ [0] & [0] & [0] \end{bmatrix} \begin{bmatrix} \{A\} \\ \{B\} \\ \{C\} \end{bmatrix} \tag{90}$$

where it should be noted that the coefficient matrices are symmetric (e.g. $[K_{21}] = [K_{12}]$, etc). To reduce the size of the eigenvalue problem, it is possible to condense the system of equations. Due to the zeros on the right hand side of the second and third rows of Equation (90), it is possible to solve for both $\{B\}$ and $\{C\}$ in terms of $\{A\}$. When substituted in the first row of Equation (90), the system of equations is a function of $\{A\}$ only

$$[K]\{A\} = \lambda [M_{11}]\{A\} \tag{91}$$

where $[K]$ is a function of the submatrices $[K_{\alpha\beta}]$ ($\alpha, \beta = 1,2,3$) and $[M_{11}]$ is as before. The order of the coefficient matrices has now been reduced from $(N_w + N_{\psi_x} + N_{\psi_y})$ to just (N_w).

The eigenvalue problem represented by Equations (90) or (91) is valid as posed for a rectangular plate under uniaxial load with any combination of simply supported, clamped, or free edges. The desired configuration is imposed by the choice of appropriate shape functions to represent the plate

deformations. The functions $\phi_i(x,y)$, $\theta_l^x(x,y)$, and $\theta_l^y(x,y)$ are chosen in x and y variables separable form. Rewriting Equation (88) in this fashion gives

$$
\begin{aligned}
w &= \sum_{m=1}^{N_w^x} \sum_{n=1}^{N_w^y} A_{mn}\phi_{mn} \qquad \phi_{mn}(x,y) = f_m^1(x)g_n^1(y) \\
\psi_x &= \sum_{p=1}^{N_{\psi_x}^x} \sum_{q=1}^{N_{\psi_x}^y} B_{pq}\theta_{pq}^x \qquad \theta_{pq}^x(x,y) = f_p^2(x)g_q^2(y) \\
\psi_y &= \sum_{r=1}^{N_{\psi_y}^x} \sum_{s=1}^{N_{\psi_y}^y} C_{rs}\theta_{rs}^y \qquad \theta_{rs}^y(x,y) = f_r^3(x)g_s^3(y)
\end{aligned}
\tag{92}
$$

For a plate with three simply supported edges and one free edge at $y = H$ (see Figure 13), the geometric boundary conditions (for the supported edges) are

$$
\begin{aligned}
&w(0,y) = w(L,y) = w(x,0) = 0 \\
&\psi_x(x,0) = 0 \\
&\psi_y(0,y) = \psi_y(L,y) = 0
\end{aligned}
\tag{93}
$$

which must be satisfied by the shape functions of Equation (92). The natural boundary conditions for the plate are

$$
\begin{aligned}
&M_x(0,y) = M_x(L,y) = 0 \\
&M_y(x,0) = M_y(x,H) = 0 \\
&M_{xy}(x,H) = 0 \\
&Q_y(x,H) = 0
\end{aligned}
\tag{94}
$$

Assuming a single half-wave buckling mode shape in the x direction, the one dimensional shape functions used for this case are

$$
\begin{aligned}
\phi_{mn}(x,y): &\quad f_m^1(x) = \sin(2m-1)\frac{\pi x}{L}, \quad g_n^1(y) = y^n \\
\theta_{pq}^x(x,y): &\quad f_p^2(x) = \cos(2p-1)\frac{\pi x}{L}, \quad g_q^2(y) = y^q \\
\theta_{rs}^y(x,y): &\quad f_r^3(x) = \sin(2r-1)\frac{\pi x}{L}, \quad g_s^3(y) = y^{(s-1)}
\end{aligned}
\tag{95}
$$

All boundary conditions, both geometric and natural, on the supported edges are satisfied by Equations (95). However, none of the boundary conditions on the free edge, which are all natural, is exactly satisfied. In order to solve the stability problem numerically, the functions for ϕ_{mn}, θ^{x}_{pq}, and θ^{y}_{rs} in Equation (95) are substituted in the integral equations for $[K_{\alpha\beta}]$ ($\alpha, \beta = 1,2,3$) and $[M_{11}]$ (not shown here). After evaluating double integrals the system of Equations (90) or (91) is in a form which can be solved on the computer for the approximate critical load of the stiffener. The accuracy of the solution, of course, improves as more terms are taken in the shape function series.

3.3 Formulation of Anisotropic Rhombic Plate Buckling

This section considers the stability of anisotropic rhombic plates under in-plane loads. As discussed in Section 2.2, Analysis and Design Tools, the original intent in developing this solution was to use it as a local buckling criterion for the skin of a geodesically stiffened panel. This approach models the portion of the skin between the stiffeners as a discrete polygonal plate under in-plane loads. For design purposes the simple support boundary condition is usually chosen so that buckling load estimates will be conservative. The foregoing idealizations ignore continuity of the buckling mode shape between adjacent elements of the panel and do not account for rotational restraint between the stiffeners and the skin. The matter of inter-element continuity was resolved when the Lagrange multiplier method [LMM] analysis (see Section 3.2.1.3) was implemented for predicting buckling of stiffened panels, as it models the skin of the stiffened panel as a continuous sheet. Since the LMM analysis is capable of modelling inter-stiffener skin buckling, the local buckling analysis using rhombic plates appears to be somewhat redundant. However, in its present form the LMM analysis can only handle specially orthotropic skin laminates, thereby ignoring the effects of bending-twisting coupling terms D_{16} and D_{26}. It is well known that the presence of these terms can account for a considerable drop in buckling load and sensitivity to the direction of applied shear loads[20] [21]. Therefore, the rhombic plate stability analysis has been retained to provide an estimate of the effect

of neglecting bending-twisting coupling in the geodesic panel designs. The following discussion reviews the range of solution methods for rhombic plate buckling available in the literature. The process of transforming the problem to an oblique coordinate system and formulating the stability criterion is then covered in detail.

Analysis techniques for the buckling of rectangular plates are well documented in the literature, but less well so for skew or rhombic plates. In the past, some attention has been paid to parallelogram, or skew, plates as this shape arises for the skin panels of rib and stringer stiffened swept wings. However, the majority of these references consider only isotropic plates with clamped edges. For simply supported skew plates, the nonrectangular geometry makes it very difficult to satisfy the natural boundary conditions, even for isotropic materials. Only three relevant references have been found which consider simply supported orthotropic skew plates; that by Durvasula[47], who uses the Rayleigh-Ritz method, and two by Kennedy and Prabhakara[48] [49], who employ the Galerkin method.

Upon examining coordinate transformation and solution techniques for solving skew plate problems, it becomes apparent that solution methods for rectangular plates can also be applied to skew plate problems. The differential equation of equilibrium and boundary conditions, expressed in terms of the transverse displacement and elastic properties of a plate, fully define the buckling problem for symmetric laminates in classical thin plate theory. For skew plates, these equations are generally transformed from Cartesian coordinates to an oblique coordinate system. It will be shown that the differential equation and boundary conditions for a rectangular, simply supported, anisotropic plate have the same functional form in Cartesian coordinates as the corresponding equations for a skew plate in skew coordinates. As a result, any methods which have been developed for rectangular anisotropic plates can be adapted for use with skew plates. Unfortunately, the same problems which make the skew plate problem difficult to solve also occur for rectangular anisotropic plates. Most solutions for rectangular anisotropic plates still employ approximate energy methods in conjunction with beam mode functions or trigonometric series. However, one alternate technique, used by Whitney[50] [51] [52] [53] [54] for the buckling and vibration of both simply

supported and clamped rectangular anisotropic plates, has been identified. In summary, three solution methods are discussed for use on the skew plate problem: the standard Rayleigh-Ritz solution such as that used by Durvasula, a Fourier series solution by Whitney, and a Galerkin solution due to Kennedy and Prabhakara.

The difficulty in solving simply supported skew plate and anisotropic rectangular plate problems is in finding a displacement function which will satisfy both the geometric (zero displacement) and natural (zero bending moment) boundary conditions. As such, approximate energy methods such as the Rayleigh-Ritz or Galerkin methods, in which the natural boundary conditions are not satisfied, are often used. This is the approach (Rayleigh-Ritz method) used by Durvasula[47]. However, it is well known from anisotropic rectangular plate studies that these methods always yield non-conservative (over-estimated) critical loads and are slow to converge when the natural boundary conditions are not satisfied[27 55]. It is the bending-twisting coupling terms D_{16} and D_{26} which cause the natural boundary conditions to remain unsatisfied for rectangular anisotropic plates. For skew plates, it will be demonstrated that similar coupling between bending and twisting curvatures exists which is a function of both the plate skewness and the plate material anisotropy. For example, increasing the anisotropy of a rectangular plate has been found to slow convergence of the solution[55]. Similarly, Troitsky[56] has noted that increasing the skewness of a plate hinders the convergence of the skew solution. In view of this, it is unclear to what degree material anisotropy and plate geometry might affect the results predicted by a standard energy method. As a result, the objective has been to develop an analysis approach which yields conservative results, in order to assess the effects of laminate anisotropy and plate skewness on the critical load of a simply supported anisotropic rhombic plate.

An alternative approach used by Whitney[50 51 52 53 54] appears to give quickly convergent, conservative results. Whitney assumes a general trigonometric series deflection function which satisfies neither geometric nor natural boundary conditions. Each higher-order derivative is formally expanded in a new Fourier series. The Fourier coefficients for this series are evaluated using their definition of a double integral over the domain of the problem. A partial integration reduces the area integral

to boundary integrals along the edges of the plate. The value of these boundary integrals accounts for the degree of satisfaction of the boundary conditions of the plate. This technique was originally suggested by Green[57] [58]. These derivatives are then substituted into the governing differential equation and coefficients of like form equated. Constraints are then imposed on the unknown coefficients such that all boundary conditions are satisfied. Truncating the Fourier series results in a finite set of algebraic equations which can be solved for the critical load. This should represent a near exact solution in the sense that both the equilibrium equation and boundary conditions are satisfied, and the only approximation is the truncation of the series. Whitney observed that the method was rapidly convergent and appeared to be conservative (converged from below the true solution). Although this method could be applied to the skew plate problem, the formulation is extremely complex and involves a large number of algebraic equations and unknown constants.

A modification of Whitney's approach has been used by Kennedy and Prabhakara[48] [49] for orthotropic skew plates. In their method a simpler deflection function, satisfying the geometric boundary conditions, is chosen. This allows the Galerkin method to be used for the final solution rather than direct solution by algebraic manipulation of the equilibrium equation. Higher-order derivatives of the deflection function are found using Green's method. Although the use of an approximate solution method produces a problem which is slower to converge, the solution procedure is considerably simplified and the predicted critical loads still appear to be conservative. As a result, Kennedy's method was selected and adapted to anisotropic rhombic plates for the present work. A detailed explanation of the skew coordinate transformation employed, the use of Green's method in formulating derivatives, and Kennedy's method for the solution of the problem follow.

Coordinate Transformation

For the analysis of a skew plate it is advantageous to transform the governing differential equation and boundary conditions into coordinates more suited to the plate geometry. The usual procedure for transforming from rectangular (x,y) to skew (u,v) coordinates, which are parallel to the edges of the skew plate, is accomplished by rotating the v axis an angle ψ from the y axis (Figure 14-A).

The loads can also be expressed in terms of oblique components, but are usually left as an orthogonal system as they retain their true physical significance in this form[47]. The conventional skew transformation poses a problem for the present application because the direction of compressive load application is always parallel with the the major axis or bisector of each rhombus in the panel. In view of this, an alternate coordinate transformation is introduced where the skewing of the plate is specified by a pair of equal half angles ϕ (Figure 14-B). Under this transformation the bisector of the rhombus always remains aligned with the material and external load reference axes. Henceforth, all references to skew coordinates will refer to this new system.

In order to transform the governing differential equation and boundary conditions for the plate from Cartesian (x,y) to skew (u,v) coordinates, it is first necessary to derive the equivalent differential operators. Basic trigonometry gives the following transformation equations

$$\begin{aligned} x &= (u+v)\cos\phi \\ y &= (v-u)\sin\phi \end{aligned} \tag{96}$$

or, conversely

$$\begin{aligned} u &= \frac{1}{2}(x\sec\phi - y\csc\phi) \\ v &= \frac{1}{2}(x\sec\phi + y\csc\phi) \end{aligned} \tag{97}$$

It is apparent that $x = x(u,v)$ and $y = y(u,v)$ are functions of both u and v, so that differentiation with respect to these variables is governed by the chain rule

$$\begin{aligned} \frac{\partial}{\partial x} &= \frac{\partial}{\partial u}\frac{\partial u}{\partial x} + \frac{\partial}{\partial v}\frac{\partial v}{\partial x} \\ \frac{\partial}{\partial y} &= \frac{\partial}{\partial u}\frac{\partial u}{\partial y} + \frac{\partial}{\partial v}\frac{\partial v}{\partial y} \end{aligned} \tag{98}$$

The partial derivatives of u and v with respect to x and y are performed on Equation (97), giving

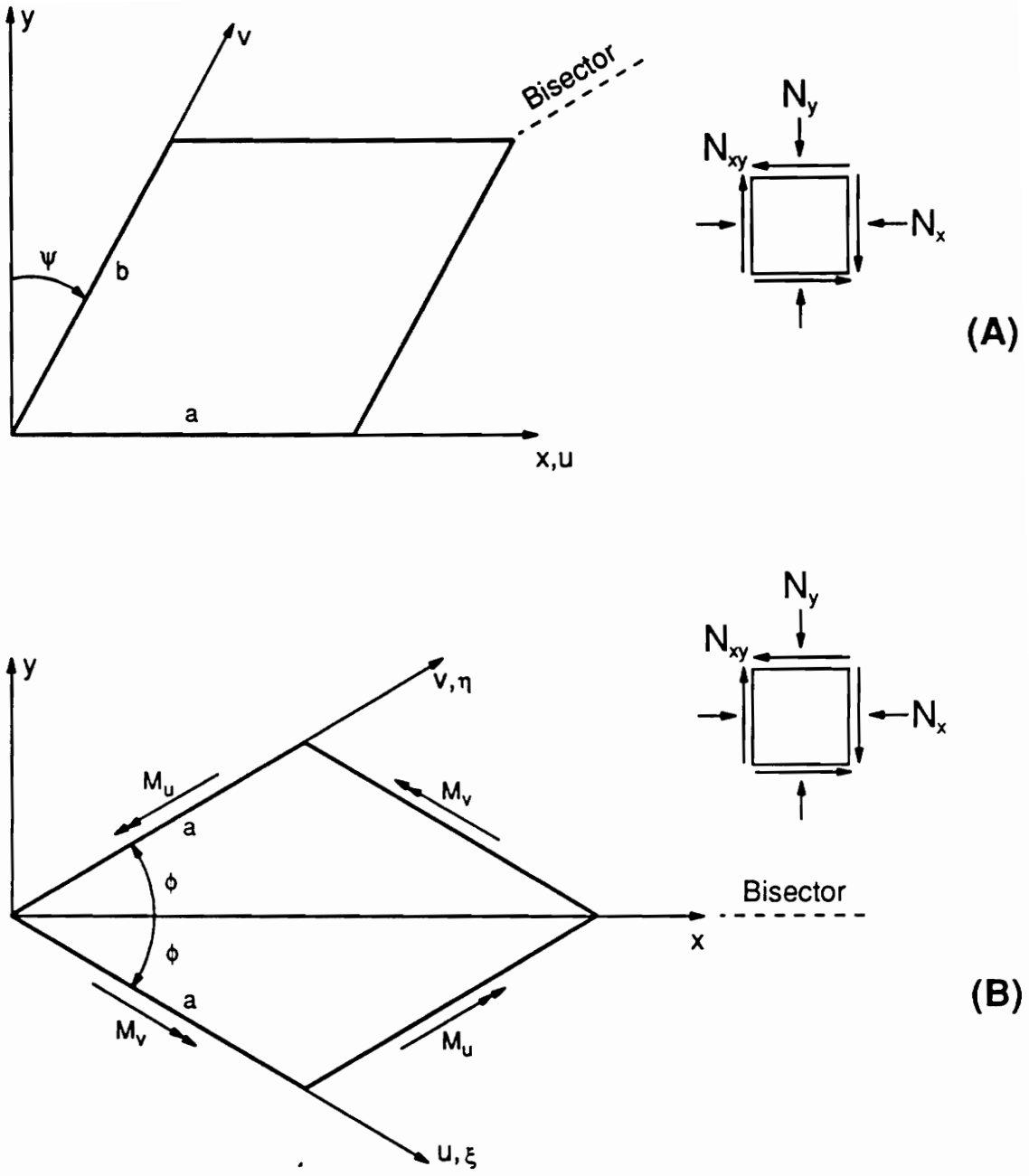

Figure 14. Coordinate Transformations and Loading Geometry for Skew and Rhombic Plates: A) Skew Coordinate System B) Rhombic Coordinate System

$$\begin{aligned} \frac{\partial u}{\partial x} &= \frac{1}{2}\sec\phi & \frac{\partial u}{\partial y} &= -\frac{1}{2}\csc\phi \\ \frac{\partial v}{\partial x} &= \frac{1}{2}\sec\phi & \frac{\partial v}{\partial y} &= \frac{1}{2}\csc\phi \end{aligned} \tag{99}$$

Substituting Equation (99) in Equation (98) gives the relationship between differential operators in the two coordinate systems

$$\begin{aligned} \frac{\partial}{\partial x} &= \frac{1}{2}\sec\phi\left(\frac{\partial}{\partial u} + \frac{\partial}{\partial v}\right) \\ \frac{\partial}{\partial y} &= \frac{1}{2}\csc\phi\left(\frac{\partial}{\partial v} - \frac{\partial}{\partial u}\right) \end{aligned} \tag{100}$$

Higher order derivatives are obtained by repeated applications of Equation (100). These relations can now be used to transform the differential equation and boundary conditions for a rhombic plate into the skew coordinate system. The governing differential equation for a homogeneous anisotropic plate, or a symmetrically laminated composite plate, expressed in orthogonal coordinates, was introduced in Section 3.2.1.2 as

$$\begin{aligned} D_{11}w_{,xxxx} + 4D_{16}w_{,xxxy} + 2(D_{12} + 2D_{66})w_{,xxyy} + 4D_{26}w_{,xyyy} + D_{22}w_{,yyyy} \\ + N_x w_{,xx} + 2N_{xy}w_{,xy} + N_y w_{,yy} = 0 \end{aligned} \tag{101}$$

where the comma notation again denotes partial differentiation with respect to the subscripted variables and the in-plane force resultants N_x and N_y are positive when compressive. The direction of positive shear is also reversed from the standard convention. Abbreviating $\sec\phi$ and $\csc\phi$ as s and c, respectively, Equation (100) gives the derivatives of w in terms of the skew coordinates (u,v) as

$$
\begin{aligned}
w_{,xxxx} &= \frac{s^4}{16}(w_{,uuuu} + 4w_{,uuuv} + 6w_{,uuvv} + 4w_{,uvvv} + w_{,vvvv}) \\
w_{,xxxy} &= -\frac{s^3c}{16}(w_{,uuuu} + 2w_{,uuuv} - 2w_{,uvvv} - w_{,vvvv}) \\
w_{,xxyy} &= \frac{s^2c^2}{16}(w_{,uuuu} - 2w_{,uuvv} + w_{,vvvv}) \\
w_{,xyyy} &= -\frac{sc^3}{16}(w_{,uuuu} - 2w_{,uuuv} + 2w_{,uvvv} - w_{,vvvv}) \\
w_{,yyyy} &= \frac{c^4}{16}(w_{,uuuu} - 4w_{,uuuv} + 6w_{,uuvv} - 4w_{,uvvv} + w_{,vvvv}) \\
w_{,xx} &= \frac{s^2}{4}(w_{,uu} + 2w_{,uv} + w_{,vv}) \\
w_{,xy} &= \frac{sc}{4}(w_{,vv} - w_{,uu}) \\
w_{,yy} &= \frac{c^2}{4}(w_{,uu} - 2w_{,uv} + w_{,vv})
\end{aligned}
\tag{102}
$$

Substituting Equations (102) in Equation (101), dividing through by D_{22}, and designating the coefficients of $w_{,uuuu}$ through $w_{,vvvv}$ as $k_1, \ldots, k_5$ results in

$$
\begin{aligned}
&k_1 w_{,uuuu} + 4k_2 w_{,uuuv} + 2k_3 w_{,uuvv} + 4k_4 w_{,uvvv} + k_5 w_{,vvvv} \\
&+ \frac{1}{D_{22}}\left[(s^2N_x - 2scN_{xy} + c^2N_y)w_{,uu} + 2(s^2N_x - c^2N_y)w_{,uv}\right. \\
&\left. + (s^2N_x + 2scN_{xy} + c^2N_y)w_{,vv}\right] = 0
\end{aligned}
\tag{103}
$$

with

$$
\begin{aligned}
k_1 &= \frac{1}{4D_{22}}\left[s^4D_{11} - 4s^3cD_{16} + 2s^2c^2(D_{12} + 2D_{66}) - 4sc^3D_{26} + c^4D_{22}\right] \\
k_2 &= \frac{1}{4D_{22}}\left[s^4D_{11} - 2s^3cD_{16} + 2sc^3D_{26} - c^4D_{22}\right] \\
k_3 &= \frac{1}{4D_{22}}\left[3s^4D_{11} - 2s^2c^2(D_{12} + 2D_{66}) + 3c^4D_{22}\right] \\
k_4 &= \frac{1}{4D_{22}}\left[s^4D_{11} + 2s^3cD_{16} - 2sc^3D_{26} - c^4D_{22}\right] \\
k_5 &= \frac{1}{4D_{22}}\left[s^4D_{11} + 4s^3cD_{16} + 2s^2c^2(D_{12} + 2D_{66}) + 4sc^3D_{26} + c^4D_{22}\right]
\end{aligned}
\tag{104}
$$

As a large number of integrations are required in the solution process, it is expedient to introduce nondimensional coordinates

$$\xi = \frac{u}{a}$$
$$\eta = \frac{v}{a} \tag{105}$$

where the boundaries of the rhombus are now given by $\xi = 0,1$ and $\eta = 0,1$. This leads to

$$\frac{\partial}{\partial u} = \frac{1}{a}\frac{\partial}{\partial \xi}$$
$$\frac{\partial}{\partial v} = \frac{1}{a}\frac{\partial}{\partial \eta} \tag{106}$$

Introducing Equation (106) into Equation (103) gives the differential equation in terms of nondimensional coordinates ξ and η

$$\begin{aligned}\frac{1}{a^4}\left[k_1 w_{,\xi\xi\xi\xi} + 4k_2 w_{,\xi\xi\xi\eta} + 2k_3 w_{,\xi\xi\eta\eta} + 4k_4 w_{,\xi\eta\eta\eta} + k_5 w_{,\eta\eta\eta\eta}\right] \\ + \frac{1}{a^2 D_{22}}\left[(s^2 N_x - 2scN_{xy} + c^2 N_y) w_{,\xi\xi} + 2(s^2 N_x - c^2 N_y) w_{,\xi\eta}\right. \\ \left. + (s^2 N_x + 2scN_{xy} + c^2 N_y) w_{,\eta\eta}\right] = 0\end{aligned} \tag{107}$$

Multiplying through by a^4 and letting

$$\lambda \overline{N}_x = \frac{a^2 N_x}{D_{22}}$$
$$\lambda \overline{N}_{xy} = \frac{a^2 N_{xy}}{D_{22}} \tag{108}$$
$$\lambda \overline{N}_y = \frac{a^2 N_y}{D_{22}}$$

allows a common scaling factor λ to be extracted from all applied loads. Note that normalizing with respect to a^2 means that the critical load parameter $\lambda \overline{N}$ will be independent of the size of the plate. Similarly, normalizing with respect to D_{22} removes any dependence on plate thickness. Substituting the load parameters (108) in Equation (107) gives

$$
\begin{aligned}
&k_1 w_{,\xi\xi\xi\xi} + 4k_2 w_{,\xi\xi\xi\eta} + 2k_3 w_{,\xi\xi\eta\eta} + 4k_4 w_{,\xi\eta\eta\eta} + k_5 w_{,\eta\eta\eta\eta} \\
&+ \lambda\{(s^2\overline{N}_x - 2sc\overline{N}_{xy} + c^2\overline{N}_y) w_{,\xi\xi} + 2(s^2\overline{N}_x - c^2\overline{N}_y) w_{,\xi\eta} \\
&+ (s^2\overline{N}_x + 2sc\overline{N}_{xy} + c^2\overline{N}_y) w_{,\eta\eta}\} = 0
\end{aligned}
\tag{109}
$$

For brevity, the coefficients of the skew curvatures are grouped into single variables. The final form of the nondimensional governing differential equation is

$$
\begin{aligned}
&k_1 w_{,\xi\xi\xi\xi} + 4k_2 w_{,\xi\xi\xi\eta} + 2k_3 w_{,\xi\xi\eta\eta} + 4k_4 w_{,\xi\eta\eta\eta} + k_5 w_{,\eta\eta\eta\eta} \\
&+ \lambda\{\overline{N}_\xi w_{,\xi\xi} + 2\overline{N}_{\xi\eta} w_{,\xi\eta} + \overline{N}_\eta w_{,\eta\eta}\} = 0
\end{aligned}
\tag{110}
$$

where

$$
\begin{aligned}
\overline{N}_\xi &= s^2\overline{N}_x + c^2\overline{N}_y - 2sc\overline{N}_{xy} \\
\overline{N}_{\xi\eta} &= s^2\overline{N}_x - c^2\overline{N}_y \\
\overline{N}_\eta &= s^2\overline{N}_x + c^2\overline{N}_y + 2sc\overline{N}_{xy}
\end{aligned}
\tag{111}
$$

It is clear that Equation (110), governing the out-of-plane behavior of a rhombic plate in the skew coordinate system, has the same functional form as the differential equation (101) for a fully anisotropic plate expressed in Cartesian coordinates. It is significant to note that even for isotropic materials, i.e.

$$
\begin{aligned}
D_{11} &= D_{22} = 2(D_{12} + 2D_{66}) = D \\
D_{16} &= D_{26} = 0
\end{aligned}
$$

k_1 through k_5 are in general nonzero, so that there is no reduction in the number of terms in the differential equation. For rectangular plates in Cartesian coordinates, considerable simplification of the differential equation occurs for orthotropic and, to a greater degree, isotropic materials.

Relations for the boundary conditions of a simply supported rhombic plate, expressed in skew coordinates, must also be determined. The simple support condition requires that the transverse displacement and normal bending moment be zero on each edge

$$\left.\begin{matrix} w = 0 \\ M_u = 0 \end{matrix}\right\} \text{ at } u = 0, a \qquad \left.\begin{matrix} w = 0 \\ M_v = 0 \end{matrix}\right\} \text{ at } v = 0, a \tag{112}$$

The convention adopted for the bending moments is shown in Figure 14-B. Note that the labels M_u and M_v do not, as is the case in an orthogonal coordinate system, mean that they are integral resultants of normal stresses σ_u and σ_v. Instead, the subscripts merely imply that the moments act on edges parallel to $u = 0$ and $v = 0$, respectively.

The moment acting normal to the edge $u = 0$ oriented at an angle ϕ above the x axis can be expressed as [59]

$$\begin{aligned} M_u &= \sin^2\phi\, M_x + \cos^2\phi\, M_y - 2 \sin\phi \cos\phi\, M_{xy} \\ &= \frac{1}{c^2} M_x + \frac{1}{s^2} M_y - \frac{2}{sc} M_{xy} \end{aligned} \tag{113}$$

where M_x, M_y, and M_{xy} are the usual moment resultants in the Cartesian coordinate system. These moments can be expressed as functions of curvatures as follows [27]

$$\begin{aligned} M_x &= -(D_{11}w_{,xx} + D_{12}w_{,yy} + 2D_{16}w_{,xy}) \\ M_y &= -(D_{12}w_{,xx} + D_{22}w_{,yy} + 2D_{26}w_{,xy}) \\ M_{xy} &= -(D_{16}w_{,xx} + D_{26}w_{,yy} + 2D_{66}w_{,xy}) \end{aligned} \tag{114}$$

Substituting Equation (114) in Equation (113) and collecting coefficients of the curvatures gives

$$\begin{aligned} M_u = -\left[\frac{D_{11}}{c^2} + \frac{D_{12}}{s^2} - \frac{2D_{16}}{sc} \right] w_{,xx} - \left[\frac{D_{12}}{c^2} + \frac{D_{22}}{s^2} - \frac{2D_{26}}{sc} \right] w_{,yy} \\ - 2\left[\frac{D_{16}}{c^2} + \frac{D_{26}}{s^2} - \frac{2D_{66}}{sc} \right] w_{,xy} \end{aligned} \tag{115}$$

Substituting for $w_{,xx}$, $w_{,xy}$, and $w_{,yy}$ from Equation (102) and gathering coefficients of $w_{,uu}$, $w_{,uv}$, and $w_{,vv}$ gives M_u completely in terms of skew coordinates

$$M_u = -\frac{1}{4}\left[\frac{s^2}{c^2}D_{11} - \frac{4s}{c}D_{16} + 2(D_{12}+2D_{66}) - \frac{4c}{s}D_{26} + \frac{c^2}{s^2}D_{22}\right]w_{,uu}$$
$$-\frac{1}{4}\left[\frac{s^2}{c^2}D_{11} + 2D_{12} + -4D_{66} + \frac{c^2}{s^2}D_{22}\right]w_{,vv} \qquad (116)$$
$$-\frac{1}{2}\left[\frac{s^2}{c^2}D_{11} - \frac{2s}{c}D_{16} - + \frac{2c}{s}D_{26} - \frac{c^2}{s^2}D_{22}\right]w_{,uv}$$

The geometric boundary conditions for the pair of simply-supported edges under consideration ($u = 0$ and $u = a$) require that $w(0,v) = 0$ and $w(a,v) = 0$. The displacement function chosen for $w(u,v)$ must satisfy these boundary conditions in order to be an admissible function in the Ritz or Galerkin solution methods. Assuming that w is equal to zero along these edges, then $w_{,vv}$ must vanish along the edges as well. The second requirement for a simply-supported edge is that the moment normal to that edge, M_u, be zero. Setting $w_{,vv} = 0$ and $M_u = 0$ in Equation (116) and multiplying through by $\frac{s^2c^2}{D_{22}}$ yields

$$\frac{1}{4D_{22}}\left[s^4D_{11} - 4s^3cD_{16} + 2s^2c^2(D_{12}+2D_{66}) - 4sc^3D_{26} + c^4D_{22}\right]w_{,uu}$$
$$+\frac{1}{2D_{22}}\left[s^4D_{11} - 2s^3cD_{16} + 2sc^3D_{26} - c^4D_{22}\right]w_{,uv} = 0 \qquad (117)$$

It will be recognized from Equation (104) that the coefficient of $w_{,uu}$ is identical to k_1 and the coefficient of $w_{,uv}$ is equal to $2k_2$. Thus the requirement for moment-free edges can be summarized as

$$w_{,uu} = -\frac{2k_2}{k_1}w_{,uv} \quad \text{at } u = 0,a \qquad (118)$$

An analogous procedure for the other pair of edges yields

$$w_{,vv} = -\frac{2k_4}{k_5}w_{,uv} \quad \text{at } v = 0,a \qquad (119)$$

As was done with the differential equation, the boundary conditions are also converted to nondimensional form, but the expressions remain essentially unchanged. The nondimensional simple support boundary conditions are

$$\begin{aligned} w = 0, \quad & w_{,\xi\xi} = -\frac{2k_2}{k_1} w_{,\xi\eta} \qquad \text{at } \xi = 0,1 \\ w = 0, \quad & w_{,\eta\eta} = -\frac{2k_4}{k_5} w_{,\xi\eta} \qquad \text{at } \eta = 0,1 \end{aligned} \tag{120}$$

Derivatives of Displacement Function

Certain methods for the solution of plate stability problems, including direct substitution and the Galerkin method, use the governing differential equation in a form similar to that in Equations (101) or (110). For these methods it is necessary to differentiate the chosen displacement function up to the fourth order in both spatial variables. When the displacement function is expressed as a Fourier series, this process is generally accomplished via term-by-term differentiation. However, Green[57] [58], and later Whitney[50] [51] [52] [53] [54], Sun[60], and Kennedy and Prabhakara[48] [49] have argued that justification for differentiating a function in this manner implicitly assumes that the function satisfies the boundary conditions. In an alternate method, first proposed by Green[57], each derivative of the function is expanded in a new Fourier series with unknown coefficients that are defined in the usual way. When the Fourier coefficients for a series defining one of the derivatives are evaluated, these coefficients can be related to those of the original series through partial integration. When this method is applied to problems where the function satisfies all boundary conditions, the resulting expression is identical to that found by term-by-term differentiation. However, in problems where the boundary conditions are not automatically satisfied, extra terms will appear in the new Fourier expansion. These account for the unsatisfied boundary conditions and would not appear for differentiation on a term-by-term basis.

As an example, let $f(x,y)$ be a function which can be expanded in a double sine series over the region $0 < x < a, 0 < y < b$ [50]

$$f(x,y) = \sum_{m=1}^{\infty} \sum_{n=1}^{\infty} A_{mn} \sin \frac{m\pi x}{a} \sin \frac{n\pi y}{b} \qquad (0 < x < a, 0 < y < b) \tag{121}$$

If the the partial derivative $f_{,x}$ can be expanded in a cosine-sine series

$$f_{,x}(x,y) = \sum_{m=0}^{\infty} \sum_{n=1}^{\infty} B_{mn} \cos \frac{m\pi x}{a} \sin \frac{n\pi y}{b} \qquad (0 \le x \le a, 0 < y < b) \tag{122}$$

then from Green's method the coefficients are

$$\begin{aligned} B_{0n} &= \frac{a_n}{2} \\ B_{mn} &= \frac{m\pi}{a} A_{mn} + a_n \qquad (m \text{ even}, m \neq 0) \\ &= \frac{m\pi}{a} A_{mn} + b_n \qquad (m \text{ odd}) \end{aligned} \tag{123}$$

with

$$\begin{aligned} a_n &= \frac{4}{ab} \int_0^b [f(a,y) - f(0,y)] \sin \frac{n\pi y}{b} \, dy \\ b_n &= -\frac{4}{ab} \int_0^b [f(a,y) + f(0,y)] \sin \frac{n\pi y}{b} \, dy \end{aligned} \tag{124}$$

Term-by-term differentiability depends on the boundary conditions satisfied by $f(x,y)$. If f vanishes on the boundaries $x = 0$ and $x = a$, then a_n and b_n in Equation (124) vanish, the coefficients in Equation (123) are identical to those found by term-by-term differentiation, and the series in Equation (121) is term-by-term differentiable.

In the present problem the deflection function is chosen in the form of a double sine series

$$w(\xi, \eta) = \sum_{m=1}^{\infty} \sum_{n=1}^{\infty} A_{mn} \sin m\pi\xi \sin n\pi\eta \qquad (0 \le \xi \le 1, 0 \le \eta \le 1) \tag{125}$$

with Fourier coefficients defined by [61]

$$A_{mn} = 4\int_0^1\int_0^1 w(\xi, \eta) \sin m\pi\xi \ \sin n\pi\eta \, d\xi \, d\eta \tag{126}$$

The deflection function (125) satisfies the geometric (zero displacement) boundary conditions, so it can be differentiated term-by-term up to the second order in ξ and η. However, Equation (125) does not satisfy the conditions for zero edge moments in Equations (120). Therefore further term-by-term differentiation of Equation (125) is not valid. First consider the second derivative of Equation (125) with respect to ξ

$$w_{,\xi\xi}(\xi, \eta) = -\pi^2 \sum_{m=1}^{\infty}\sum_{n=1}^{\infty} A_{mn} m^2 \sin m\pi\xi \ \sin n\pi\eta \qquad (0 < \xi < 1, 0 \le \eta \le 1) \tag{127}$$

Expanding $w_{,\xi\xi\xi}$ in a new Fourier cos-sin series

$$w_{,\xi\xi\xi}(\xi, \eta) = \sum_{p=0}^{\infty}\sum_{q=1}^{\infty} B_{pq} \cos p\pi\xi \ \sin q\pi\eta$$

or

$$w_{,\xi\xi\xi}(\xi, \eta) = \sum_{q=1}^{\infty} B_{0q} \sin q\pi\eta + \sum_{p=1}^{\infty}\sum_{q=1}^{\infty} B_{pq} \cos p\pi\xi \ \sin q\pi\eta \tag{128}$$

with the Fourier coefficients defined as

$$\begin{aligned} B_{0q} &= 2\int_0^1\int_0^1 w_{,\xi\xi\xi} \sin q\pi\eta \, d\xi \, d\eta \\ B_{pq} &= 4\int_0^1\int_0^1 w_{,\xi\xi\xi} \cos p\pi\xi \ \sin q\pi\eta \, d\xi \, d\eta \end{aligned} \tag{129}$$

Evaluate B_{0q}, rearranging as

$$B_{0q} = 2\int_0^1 \sin q\pi\eta \left[\int_0^1 w_{,\xi\xi\xi}\, d\xi\right] d\eta \tag{130}$$

The partial integration with respect to ξ gives

$$\begin{aligned}\int_0^1 w_{,\xi\xi\xi}\, d\xi &= [w_{,\xi\xi}]_{\xi=0}^{\xi=1} \\ &= [w_{,\xi\xi}(1,\eta) - w_{,\xi\xi}(0,\eta)]\end{aligned} \tag{131}$$

The moment-free boundary condition relations developed earlier are now used to find expressions for $w_{,\xi\xi}(0,\eta)$ and $w_{,\xi\xi}(1,\eta)$. An expression for $w_{,\xi\eta}$ obtained through term-by-term differentiation of $w(\xi,\eta)$ is still valid at $\xi = 0$ and $\xi = 1$. Differentiating Equation (125) with respect to ξ and η and substituting this expression for $w_{,\xi\eta}$ in the first of Equations (120) gives

$$w_{,\xi\xi}(\xi,\eta) = -\frac{2\pi^2 k_2}{k_1} \sum_{m=1}^{\infty}\sum_{n=1}^{\infty} A_{mn} mn \cos m\pi\xi \cos n\pi\eta \quad \text{at } \xi = 0,1 \tag{132}$$

Evaluating Equation (132) at the boundaries of the domain

$$\begin{aligned}&\text{at } \xi = 0 \qquad w_{,\xi\xi}(0,\eta) = -\frac{2\pi^2 k_2}{k_1} \sum_{m=1}^{\infty}\sum_{n=1}^{\infty} A_{mn} mn \cos n\pi\eta \\ &\text{at } \xi = 1 \qquad w_{,\xi\xi}(1,\eta) = -\frac{2\pi^2 k_2}{k_1} \sum_{m=1}^{\infty}\sum_{n=1}^{\infty} A_{mn} mn(-1)^m \cos n\pi\eta\end{aligned} \tag{133}$$

and substituting the above in Equation (131) yields

$$\int_0^1 w_{,\xi\xi\xi}\, d\xi = -\frac{2\pi^2 k_2}{k_1} \sum_{m=1}^{\infty}\sum_{n=1}^{\infty} A_{mn} mn \cos n\pi\eta[(-1)^m - 1]$$
$$= \frac{4\pi^2 k_2}{k_1} \sum_{m=1}^{\infty}\sum_{n=1}^{\infty} A_{mn} mn \cos n\pi\eta\, F_0^m \tag{134}$$

with the function F_0^m defined as

$$F_0^i \equiv \begin{cases} 1, & i \text{ odd} \\ 0, & i \text{ even} \end{cases} \tag{135}$$

The expression in Equation (134) is substituted for the term in the square brackets in Equation (130) to have for B_{0q}

$$B_{0q} = 2\int_0^1 \sin q\pi\eta \left[\frac{4\pi^2 k_2}{k_1} \sum_{m=1}^{\infty}\sum_{n=1}^{\infty} A_{mn} mn \cos n\pi\eta\, F_0^m \right] d\eta \tag{136}$$

Rearranging to remove terms which are not functions of η from under the integral sign

$$B_{0q} = \frac{8\pi^2 k_2}{k_1} \sum_{m=1}^{\infty}\sum_{n=1}^{\infty} A_{mn} mn\, F_0^m \int_0^1 \sin q\pi\eta\ \cos n\pi\eta\, d\eta \tag{137}$$

and evaluating the integral over η gives the final expression for B_{0q}

$$B_{0q} = \frac{8\pi^2 k_2}{k_1} \sum_{m=1}^{\infty}\sum_{n=1}^{\infty} A_{mn} mn\, F_0^m F_1^{nq} \tag{138}$$

where

$$F_1^{ij} \equiv \begin{cases} \dfrac{2j}{\pi(j^2 - i^2)}, & (i+j) \text{ odd} \\ 0, & (i+j) \text{ even} \end{cases} \tag{139}$$

Returning to Equation (129), the expression for B_{pq} must also be evaluated. First rearrange the second of Equations (129) to isolate functions of ξ under the integral

$$B_{pq} = 4\int_0^1 \sin q\pi\eta \left[\int_0^1 w_{,\xi\xi\xi} \cos p\pi\xi \, d\xi\right] d\eta \tag{140}$$

The integral of the term inside the brackets is evaluated using integration by parts, and leads to

$$I = [w_{,\xi\xi} \cos p\pi\xi]_{\xi=0}^{\xi=1} - \int_0^1 w_{,\xi\xi}[-p\pi \sin p\pi\xi]d\xi \tag{141}$$

where I has been used to designate the integral over ξ in Equation (140). Substituting the limits into the first term (I_1) in I gives

$$I_1 = w_{,\xi\xi}(1, \eta) \cos p\pi - w_{,\xi\xi}(0, \eta) \tag{142}$$

The expressions for $w_{,\xi\xi}(1, \eta)$ and $w_{,\xi\xi}(0, \eta)$ are obtained from Equation (133) while $\cos p\pi = (-1)^p$. These give the final expression for I_1

$$\begin{aligned} I_1 &= -\frac{2\pi^2 k_2}{k_1} \sum_{m=1}^{\infty}\sum_{n=1}^{\infty} A_{mn} mn \cos n\pi\eta[(-1)^m(-1)^p - 1] \\ &= \frac{4\pi^2 k_2}{k_1} \sum_{m=1}^{\infty}\sum_{n=1}^{\infty} A_{mn} mn \cos n\pi\eta \, F_2^{mp} \end{aligned} \tag{143}$$

with

$$F_2^{ij} \equiv \begin{cases} 1, & (i+j) \text{ odd} \\ 0, & (i+j) \text{ even} \end{cases} \tag{144}$$

Replacing the first term in Equation (141) with I_1 from Equation (143) completes the expression for I. Substituting Equation (141) for the bracketed term in Equation (140) and evaluating the integral over η leads to

$$B_{pq} = 4\int_0^1 \sin q\pi\eta \left[\frac{4\pi^2 k_2}{k_1} \sum_{m=1}^{\infty}\sum_{n=1}^{\infty} A_{mn} mn \cos n\pi\eta F_2^{mp} + \pi p \int_0^1 w_{,\xi\xi} \sin p\pi\xi d\xi \right] d\eta$$

$$= \frac{16\pi^2 k_2}{k_1} \sum_{m=1}^{\infty}\sum_{n=1}^{\infty} A_{mn} mn F_2^{mp} \int_0^1 \sin q\pi\eta \cos n\pi\eta d\eta \qquad (145)$$

$$+ 4\pi p \int_0^1 \int_0^1 w_{,\xi\xi} \sin p\pi\xi \sin q\pi\eta \, d\xi \, d\eta$$

From earlier calculations the single integral equals F_1^{nq}. The double integral is merely the definition of the Fourier coefficients for the sine-sine expansion of $w_{,\xi\xi\xi}(\xi,\eta)$. This expansion has already been found through term-by-term differentiation and is shown in Equation (127). Therefore, the double integral is equal to $-\pi^2 p^2 A_{pq}$, leading to

$$B_{pq} = \frac{16\pi^2 k_2}{k_1} \sum_{m=1}^{\infty}\sum_{n=1}^{\infty} A_{mn} mn \, F_1^{nq} F_2^{mp} - \pi^3 p^3 A_{pq} \qquad (146)$$

Replacement of B_{0q} and B_{pq} in Equation (128) by Equations (138) and (146) gives an expression for $w_{,\xi\xi\xi}$ entirely in terms of the original Fourier coefficients A_{mn}

$$w_{,\xi\xi\xi}(\xi,\eta) = -\pi^3 \sum_{p=1}^{\infty}\sum_{q=1}^{\infty} A_{pq} p^3 \cos p\pi\xi \sin q\pi\eta$$

$$+ \frac{8\pi^2 k_2}{k_1} \sum_{q=1}^{\infty} \sin q\pi\eta \sum_{m=1}^{\infty}\sum_{n=1}^{\infty} A_{mn} mn F_0^m F_1^{nq} \qquad (147)$$

$$+ \frac{16\pi^2 k_2}{k_1} \sum_{p=1}^{\infty}\sum_{q=1}^{\infty} \cos p\pi\xi \sin q\pi\eta \sum_{m=1}^{\infty}\sum_{n=1}^{\infty} A_{mn} mn F_1^{nq} F_2^{mp}$$

A procedure completely analogous to that just discussed for $w_{,\xi\xi\xi}$ yields a similar expression for $w_{,\eta\eta\eta}$

$$
\begin{aligned}
w_{,\eta\eta\eta} = & -\pi^3 \sum_{p=1}^{\infty} \sum_{q=1}^{\infty} A_{pq} q^3 \sin p\pi\xi \ \sin q\pi\eta \\
& + \frac{8\pi^2 k_4}{k_5} \sum_{p=1}^{\infty} \sin p\pi\xi \sum_{m=1}^{\infty} \sum_{n=1}^{\infty} A_{mn} mn F_0^n F_1^{mp} \\
& + \frac{16\pi^2 k_4}{k_5} \sum_{p=1}^{\infty} \sum_{q=1}^{\infty} \sin p\pi\xi \ \cos q\pi\eta \sum_{m=1}^{\infty} \sum_{n=1}^{\infty} A_{mn} mn F_1^{mp} F_2^{nq}
\end{aligned} \tag{148}
$$

Fourth order derivatives of w can be obtained by performing term-by-term differentiation of $w_{,\xi\xi\xi\xi}$ and $w_{,\eta\eta\eta\eta}$. The exception is $w_{,\xi\xi\eta\eta}$, where term-by-term differentiation of the original function w in Equation (125) is allowed as the derivatives in ξ and η are each of only second order.

All derivatives required to solve the plate stability problem by the Galerkin method are summarized in Equation (149). Note that the summation indices on the first line of both Equations (147) and (148) have been changed from p,q to m,n to make all summations over A_{mn} consistent. Also, the single summation over q in Equation (147) is changed to one over p to make it the same as that in Equation (148).

$$
\begin{aligned}
w_{,\xi\xi} &= -\pi^2 \sum_{m=1}^{\infty}\sum_{n=1}^{\infty} A_{mn} m^2 \sin m\pi\xi \ \sin n\pi\eta \\
w_{,\eta\eta} &= -\pi^2 \sum_{m=1}^{\infty}\sum_{n=1}^{\infty} A_{mn} n^2 \sin m\pi\xi \ \sin n\pi\eta \\
w_{,\xi\eta} &= \pi^2 \sum_{m=1}^{\infty}\sum_{n=1}^{\infty} A_{mn} mn \cos m\pi\xi \ \cos n\pi\eta \\
w_{,\xi\xi\eta\eta} &= \pi^4 \sum_{m=1}^{\infty}\sum_{n=1}^{\infty} A_{mn} m^2 n^2 \sin m\pi\xi \ \sin n\pi\eta \\
w_{,\xi\xi\xi\xi} &= \pi^4 \sum_{m=1}^{\infty}\sum_{n=1}^{\infty} A_{mn} m^4 \sin m\pi\xi \ \sin n\pi\eta \\
&\quad - \frac{16\pi^3 k_2}{k_1} \sum_{p=1}^{\infty}\sum_{q=1}^{\infty} p \sin p\pi\xi \ \sin q\pi\eta \sum_{m=1}^{\infty}\sum_{n=1}^{\infty} A_{mn} mn F_1^{nq} F_2^{mp} \\
w_{,\eta\eta\eta\eta} &= \pi^4 \sum_{m=1}^{\infty}\sum_{n=1}^{\infty} A_{mn} n^4 \sin m\pi\xi \ \sin n\pi\eta \\
&\quad - \frac{16\pi^3 k_4}{k_5} \sum_{p=1}^{\infty}\sum_{q=1}^{\infty} q \sin p\pi\xi \ \sin q\pi\eta \sum_{m=1}^{\infty}\sum_{n=1}^{\infty} A_{mn} mn F_1^{mp} F_2^{nq} \\
w_{,\xi\xi\xi\eta} &= -\pi^4 \sum_{m=1}^{\infty}\sum_{n=1}^{\infty} A_{mn} m^3 n \cos m\pi\xi \ \cos n\pi\eta \\
&\quad + \frac{8\pi^3 k_2}{k_1} \sum_{p=1}^{\infty} p \cos p\pi\eta \sum_{m=1}^{\infty}\sum_{n=1}^{\infty} A_{mn} mn F_0^m F_1^{np} \\
&\quad + \frac{16\pi^3 k_2}{k_1} \sum_{p=1}^{\infty}\sum_{q=1}^{\infty} q \cos p\pi\xi \ \cos q\pi\eta \sum_{m=1}^{\infty}\sum_{n=1}^{\infty} A_{mn} mn F_1^{nq} F_2^{mp} \\
w_{,\xi\eta\eta\eta} &= -\pi^4 \sum_{m=1}^{\infty}\sum_{n=1}^{\infty} A_{mn} mn^3 \cos m\pi\xi \ \cos n\pi\eta \\
&\quad + \frac{8\pi^3 k_4}{k_5} \sum_{p=1}^{\infty} p \cos p\pi\xi \sum_{m=1}^{\infty}\sum_{n=1}^{\infty} A_{mn} mn F_0^n F_1^{mp} \\
&\quad + \frac{16\pi^3 k_4}{k_5} \sum_{p=1}^{\infty}\sum_{q=1}^{\infty} p \cos p\pi\xi \ \cos q\pi\eta \sum_{m=1}^{\infty}\sum_{n=1}^{\infty} A_{mn} mn F_1^{mp} F_2^{nq}
\end{aligned}
\tag{149}
$$

Solution Procedure

The approximate solution of a boundary value problem can be achieved using a weighted-residual method known as the Galerkin method[62]. In the Galerkin method, a solution is assumed in the form $w = \sum c_i \phi_i$. The unknown parameters c_i are determined using a weighted-integral form of the differential equation, where the weighting function ψ_i is of the same form as the approximation function ϕ_i.

In the present problem, the approximation function has already been chosen with the form $\sin m\pi\xi \sin n\pi\eta$, requiring that the weight function have the corresponding form $\sin i\pi\xi \sin j\pi\eta$. Therefore, the Galerkin equation for this problem is found by multiplying the differential equation (110) by the weighting function and integrating over the domain of the plate [27]

$$\int_0^1 \int_0^1 [k_1 w_{,\xi\xi\xi\xi} + 2k_2 w_{,\xi\xi\xi\eta} + 4k_3 w_{,\xi\xi\eta\eta} + 2k_4 w_{,\xi\eta\eta\eta} + k_5 w_{,\eta\eta\eta\eta} + \lambda\{\overline{N}_\xi w_{,\xi\xi} + \overline{N}_{\xi\eta} w_{,\xi\eta} + \overline{N}_\eta w_{,\eta\eta}\}] \sin i\pi\xi \sin j\pi\eta \, d\xi \, d\eta = 0 \qquad \begin{matrix} i = 1,2,\ldots,\infty \\ j = 1,2,\ldots,\infty \end{matrix} \tag{150}$$

The derivatives of w, as listed in Equation (149), are substituted in this equation and the integrations performed. Since the approximation and weight functions are trigonometric functions, they are orthogonal and the integrations are relatively straightforward. The results of these integrations are abbreviated using the symbols defined in Equations (139) and (144). Common coefficients of summations are collected to present the final solution in the form

$$
\begin{aligned}
&\pi^2\left[k_1 i^4 + k_3 i^2 j^2 + k_5 j^4\right] A_{ij} \\
&-16\pi \sum_{m=1}^{N}\sum_{n=1}^{N} A_{mn} mn\left[k_2 i F_1^{nj} F_2^{mi} + k_4 j F_1^{mi} F_2^{nj} + \pi\left(k_2 m^2 + k_4 n^2\right) F_1^{mi} F_1^{nj}\right] \\
&+256 \sum_{m=1}^{N}\sum_{n=1}^{N} A_{mn} mn \sum_{p=1}^{N} p\left[\frac{k_2^2}{k_1 i} F_0^{i} F_0^{m} F_1^{pj} F_1^{np} + \frac{k_4^2}{k_5 j} F_0^{j} F_0^{n} F_1^{pi} F_1^{mp}\right] \\
&+256\pi \sum_{m=1}^{N}\sum_{n=1}^{N} A_{mn} mn \sum_{p=1}^{N}\sum_{q=1}^{N} F_1^{pi} F_1^{qj}\left[\frac{k_2^2}{k_1} q F_1^{nq} F_2^{mp} + \frac{k_4^2}{k_5} p F_1^{mp} F_2^{nq}\right] \\
&= \lambda\left\{\left[i^2 \overline{N}_\xi + j^2 \overline{N}_\eta\right] A_{ij} + 8\overline{N}_{\xi\eta} \sum_{m=1}^{N}\sum_{n=1}^{N} A_{mn} mn F_1^{mi} F_1^{nj}\right\} \qquad \begin{matrix} i = 1,2,\ldots,N \\ j = 1,2,\ldots,N \end{matrix}
\end{aligned}
\tag{151}
$$

The constants $k_1, \ldots, k_5$ are defined in Equation (104) and expressions for the factors $\overline{N}_\xi$, $\overline{N}_{\xi\eta}$, and $\overline{N}_\eta$ are shown in Equations (108) and (111). To solve the plate stability problem it is, of course, necessary to truncate the infinite summations shown previously. The number of terms is chosen such that the desired degree of solution accuracy has been achieved. Since the plate is of equal dimensions in the ξ and η directions, an equal number N of terms for m and n are usually taken in Equation (125). Therefore Equation (151) represents a set of (N^2) linear equations for the (N^2) unknown coefficients A_{mn} and constitutes a classical eigenvalue problem. If the set of equations is examined, it will be seen that any equation for which $(i+j)$ is odd will contain only coefficients A_{mn} for which $(m+n)$ is also odd. Also, any equation for which $(i+j)$ is even contains only A_{mn} for which $(m+n)$ is even. Thus, these two sets of equations are completely uncoupled and can be split into two separate sets for solving. One set will contain terms in which $(i+j)$ and $(m+n)$ are both even, while the other set will contain terms in which $(i+j)$ and $(m+n)$ are both odd. Physically, the modes for which $(i+j)$ are odd represent antisymmetric modes and those for $(i+j)$ even are symmetric modes. The critical load for the plate is that given by the lower of the two distinct even and odd groups.

It is also interesting to compare this solution to those obtained by use of either the modified Galerkin method with all derivatives computed via term-by-term differentiation or the Rayleigh-Ritz method. If this is done, solutions identical to that in Equation (151) will be obtained, except

that the terms in the third and fourth rows (the terms with a coefficient of 256) would be missing[49]. As a result, comparisons between the standard solutions and Kennedy's solution are easily accomplished by ignoring or including, respectively, those extra terms.

4.0 Verification and Examples

In Section 3, analytical formulations were presented for the prebuckling load distribution and stability of geodesically stiffened panels, the stability of orthotropic stiffeners, and the stability of anisotropic rhombic plates. Since these represent new developments, it is necessary to determine whether they yield results with reasonable accuracy. Where available, results published in the literature are used as benchmarks to verify the present methods. Otherwise, results generated with an established finite element program are used for comparison. The analysis method for buckling of stiffened panels is treated in Section 4.1 and that for buckling of anisotropic rhombic plates in Section 4.2. Verification and examples for the stiffener buckling analysis are covered by Stoll[18], so that topic will not be discussed here.

4.1 Stiffened Panel Buckling

The formulation for the stability of a geodesically stiffened orthotropic panel, using the Lagrange multiplier method [LMM], was presented in Section 3.2.1.3. Since the LMM analysis represents a new approach to the buckling of stiffened panels, the performance of the method is studied in detail.

In Section 4.1.1, LMM analysis results for several different panel configurations are compared with results of other procedures for verification of the method. The first test case is a simple isotropic panel with a single longitudinal blade stiffener under uniaxial compression. An analytical solution to this problem based on energy methods is available in, among others, Timoshenko and Gere[25] and Seide and Stein[41]. The second test case is a square isotropic plate with several longitudinal blade stiffeners under combinations of compression and shear loads. This problem has been analyzed by Stroud, *et al*[63] using a detailed finite element model. For the third example, no references treating the buckling of geodesically stiffened panels have been found in the literature. Therefore, a three cell cross-stiffened panel under compression is analyzed using an established finite element program. In Section 4.1.2, a convergence study is conducted for the LMM analysis to isolate the effect of various parameters on the results. These parameters include the number of constraint points along the stiffeners and the number of terms in the skin deflection function. Illustrative examples are also presented which demonstrate the influence of stiffener flexural rigidity on the critical load and buckled mode shape of a typical geodesically stiffened panel under compression or shear.

4.1.1 Verification of Analysis Method

Three panel configurations are considered for verification of the Lagrange multiplier method [LMM] analysis. The first example is an isotropic plate with a single longitudinal stiffener. This was the first problem attempted during the development of the LMM analysis, as a basic verification of the concept. For this simple geometry, the stability analysis can be accomplished without the use of Lagrange multipliers. An energy formulation for the plate and longitudinal stiffener, similar to that given in Section 3.2.1, is still used. Recall that in the LMM analysis, the deflection of a stiffener (often oblique) is expressed in an independent function and then displacement compatibility with the skin is imposed at a finite number of points. The deflection of a longitudinal stiffener, on the other hand, can easily be expressed in terms of the skin deflection function w directly, resulting in continuous skin-stiffener displacement compatibility. Timoshenko and Gere[25]

have solved the buckling problem for isotropic plates with a single central longitudinal stiffener under uniaxial compression. The chosen test configuration is a plate 12 inches square and 0.1 inch thick with a stiffener 0.527 inch high by 0.228 inch thick. Timoshenko and Gere assume that the stiffener blade is located on one side of the plate only, and calculate an effective moment of inertia for the stiffener with respect to the surface where it meets the plate. Finally, the plate is free to expand in the X direction under Y direction compression. The buckling load predicted by the LMM analysis rises as the number of constraint points increases, and exact agreement with the Timoshenko and Gere solution is achieved with only three constraint points along the stiffener (Table 2).

Table 2. Comparison of Buckling Parameters for Isotropic Plate with One Longitudinal Stiffener

Timoshenko and Gere[25]	Lagrange Multiplier Method		
Buckling Parameter $K_{Timoshenko}$	Constraint Points	Buckling Parameter K_{LMM}	$\frac{K_{LMM}}{K_{Timoshenko}}$
1.170	1	0.457	0.391
1.170	2	0.813	0.694
1.170	3	1.170	1.000
1.170	4	1.170	1.000
1.170	5	1.170	1.000

In a second, more demanding test, results from the LMM analysis are compared with data generated by Stroud, *et al*[63] for square metallic plates with longitudinal blade stiffeners, under compression and shear. Although data for composite blade-stiffened panels is included in the report, an angle-ply stiffener layup was used, while the present analysis can only accommodate unidirectional stiffener material. Internal load distributions and buckling loads were computed by Stroud, *et al* using the linked-plate program PASCO and finite element programs EAL and STAGS. The test panels were 30 inches square with six equally-spaced blade stiffeners on one side of the skin. All four edges of the panel, including both stiffeners and skin, were simply supported. The loads were combinations of uniaxial compression N_y and shear N_{xy}. The panels were modelled with the EAL finite element program using a four-node, quadrilateral, combined membrane and bending element. Two elements were used along the depth of the blade, 4 elements between the

blades, and 36 elements along the stiffener length, for a total of 1296 elements and 1369 nodes. The geometry and finite element mesh for the stiffened panels are shown in Figure 15.

Several modifications to the LMM analysis program were required to accommodate the test panel geometry. The spacing of the longitudinal stiffeners in the paper differs from the convention in the present design study. Also, free expansion in the X direction of the plate under Y direction compression was required. The fact that the stiffeners are only on one side of the plate must also be accounted for. Various approaches have been suggested in the literature to calculate an apparent or effective moment of inertia for stiffeners on one side of a plate. These attempt to account for the fact that bending of the panel causes the skin to undergo significant stretching, thereby increasing the apparent flexural rigidity of the stiffeners. The method proposed by Timoshenko and Gere[25] is to calculate the stiffener moment of inertia with respect to the surface where the stiffener meets the plate. This convention was used in the previous example with the single longitudinal stiffener. For the multiple stiffener panel an effective-width concept described by Donnell[64] was chosen. This approach calculates an effective moment of inertia for each stiffener dependent on its position with respect to the edges of the panel. This results in a different moment of inertia for each of the three (using symmetry) stiffener positions. The LMM analysis program, however, presently assumes that the moment of inertia is the same for every stiffener. Fortunately, the three effective moment of inertia values calculated using the Donnell method varied very little, so they were averaged to arrive at a single value. The changes in stiffener spacing, transverse boundary condition, and stiffener moment of inertia were temporarily implemented in the LMM analysis program for the purposes of this example. The panels were analyzed with 21 and 15 terms in the X and Y direction portions, respectively, of the skin deflection function ($M = 21, N = 15$) and 15 constraint points per stiffener ($K = 15$).

Two different panel skin thicknesses were considered by Stroud, *et al*. The first test panel had a stiffener height of 1.352 inch (measured from the midplane of the skin), a stiffener thickness of 0.058 inch, and a skin thickness of 0.084 inch. The prebuckling internal load distribution was calculated using PASCO, which was then input to EAL for the buckling analysis. In the LMM analysis the

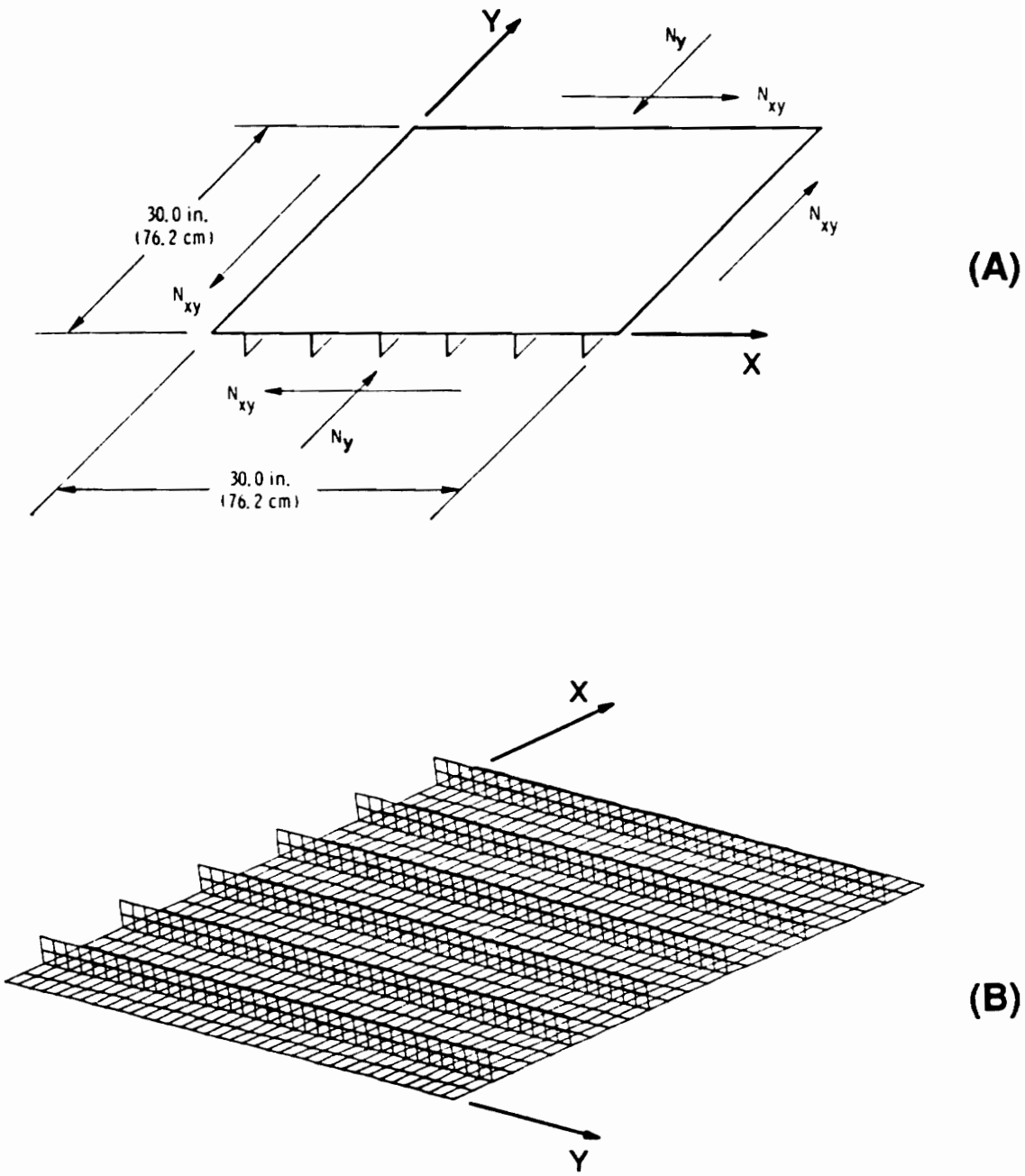

Figure 15. **Longitudinally Stiffened Isotropic Panel for Verification of LMM Analysis:** A) Geometry and Loading B) Finite Element Mesh [After Stroud, *et al* [63]]

static load distribution is predicted by smearing the in-plane properties of the panel, as described in Section 3.1.1. The skin and stiffener loads computed by the smeared analysis are compared with the PASCO results in Table 3. For the combined externally applied load of $N_y = N_{xy} = 1000$ lbf/in the two methods, as expected, are in perfect agreement. Note that the stiffener shear load for the smeared analysis is assumed, not calculated, to be zero.

Table 3. Comparison of Prebuckling Internal Load Distributions for Longitudinally Stiffened Isotropic Panel, Thick Skin

Internal Load Type	Load Applied to Panel: $N_y = N_{xy} = 1000$ lbf/in			
	Skin Load Resultant (lbf/in)		Stiffener Load Resultant (lbf/in)	
	PASCO	Smeared	PASCO	Smeared
Compression	842.67	842.67	581.84	581.84
Shear	1000.00	1000.00	0	≡0

The buckling loads from the EAL finite element method [FEM] analysis and the LMM analysis are compared in Table 4. For all applied load combinations, the LMM analysis critical eigenvalues are higher than those predicted by the FEM analysis, but differ by only 2.8% to 6.2%. Buckled mode shapes for the panel loaded by pure shear are shown in Figure 16. The modes predicted by the two methods are very close in form.

Table 4. Comparison of Buckling Loads for Longitudinally Stiffened Isotropic Panel, Thick Skin

Applied Loads (lbf/in)		Critical Eigenvalues λ_{CR}		$\frac{\lambda_{LMM}}{\lambda_{FEM}}$
Compression N_y	Shear N_{xy}	λ_{FEM}	λ_{LMM}	
0	1000	0.8138	0.8362	1.028
400	1000	0.7195	0.7401	1.029
1000	1000	0.6061	0.6237	1.029
2000	1000	0.4444	0.4588	1.033
5000	1000	0.1929	0.2049	1.062
1000	0	0.9759	1.0358	1.061

The second blade stiffened panel studied by Stroud, *et al* was identical to that in the previous example, except that a thinner skin of 0.050 inch was substituted for the 0.084 inch skin. The prebuckling load distribution as given in the report and as calculated by the present smeared anal-

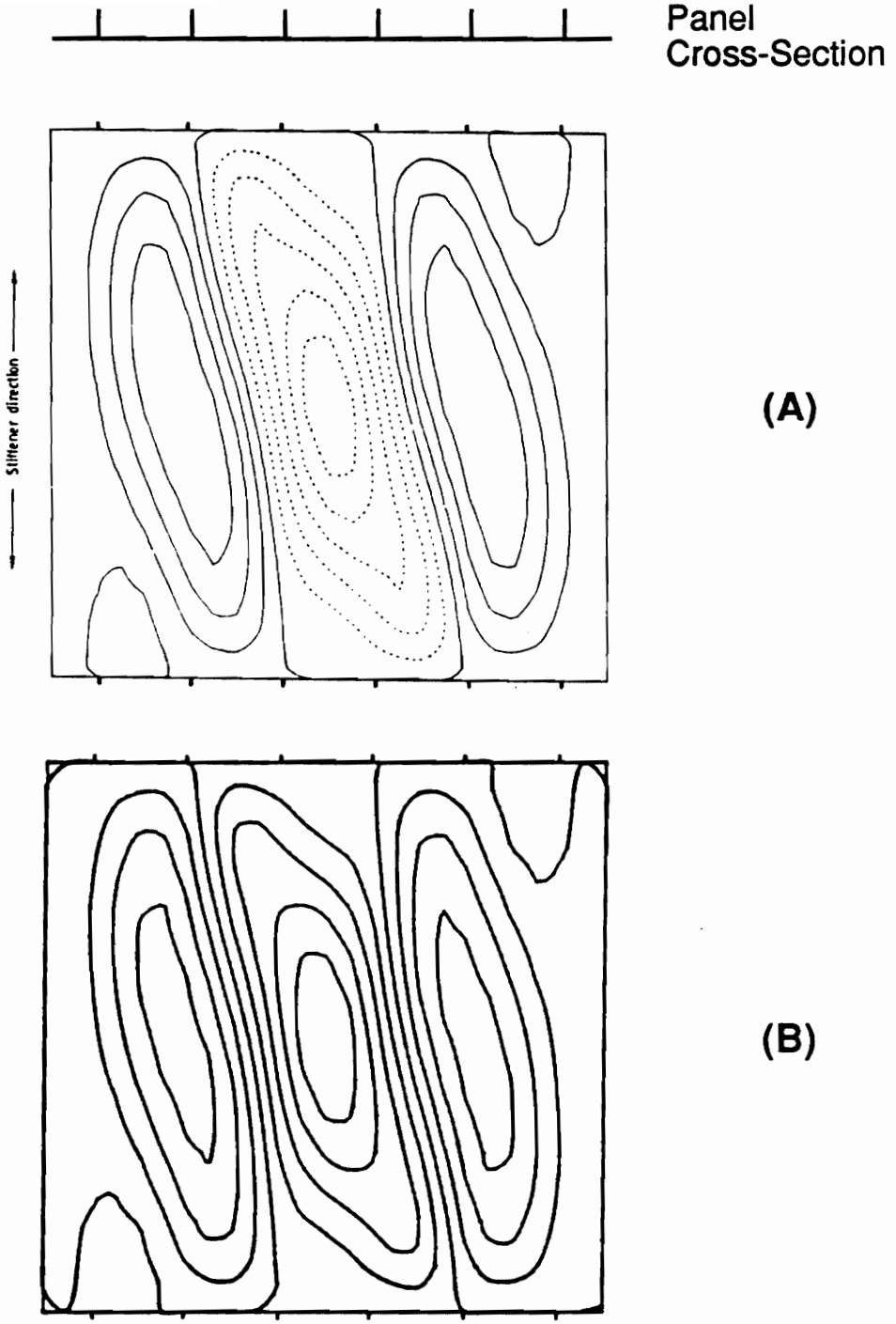

Figure 16. Comparison of Buckled Mode Shapes for Longitudinally Stiffened Isotropic Panel, Thick Skin, Shear: A) FEM Analysis [After Stroud, *et al* [63]] B) LMM Analysis

ysis are again in exact agreement. The buckling analysis results, however, differ from those in the thick skin example as all LMM buckling loads are now more conservative than the FEM predictions (Table 5). The LMM pure shear buckling load is about 5% low while all compression-loaded panel LMM buckling loads are very consistent but around 10% low. The buckled mode shapes predicted by each analysis method are shown in Figure 17 for pure shear and also in Figure 18 for uniaxial compression. For both load conditions the mode shapes appear virtually identical.

Table 5. Comparison of Buckling Loads for Longitudinally Stiffened Isotropic Panel, Thin Skin

Applied Loads (lbf/in)		Critical Eigenvalues λ_{CR}		$\frac{\lambda_{LMM}}{\lambda_{FEM}}$
Compression N_y	Shear N_{xy}	λ_{FEM}	λ_{LMM}	
0	1000	0.2767	0.2633	0.952
400	1000	0.2491	0.2255	0.905
1000	1000	0.1881	0.1693	0.900
2000	1000	0.1253	0.1125	0.898
4000	1000	0.07064	0.06332	0.896
1000	0	0.2965	0.2656	0.896

Some observations may be made regarding the LMM and FEM buckling analysis results. In the first, thick-skin example the panel buckled in three half-waves across the six stiffeners (Figure 16). For this generalized out-of-plane mode with large stiffener deformations, the the LMM results were higher but, in most cases, comparable to the FEM results. The second, thin-skin panel, on the other hand, has buckling modes which are more localized, particularly so for compression. The LMM buckling loads are all conservative with respect to the FEM results, but again to a greater degree when compressive loads are present. It is possible that critical loads for localized buckling modes are underestimated by the present LMM analysis due to the lack of local restraint at the junction of the skin and stiffeners (a result of neglecting stiffener torsional rigidity). Caution should be used in this interpretation, however, as the LMM results for these two panels are somewhat dependent on the method of estimating the effective moment of inertia for the stiffeners.

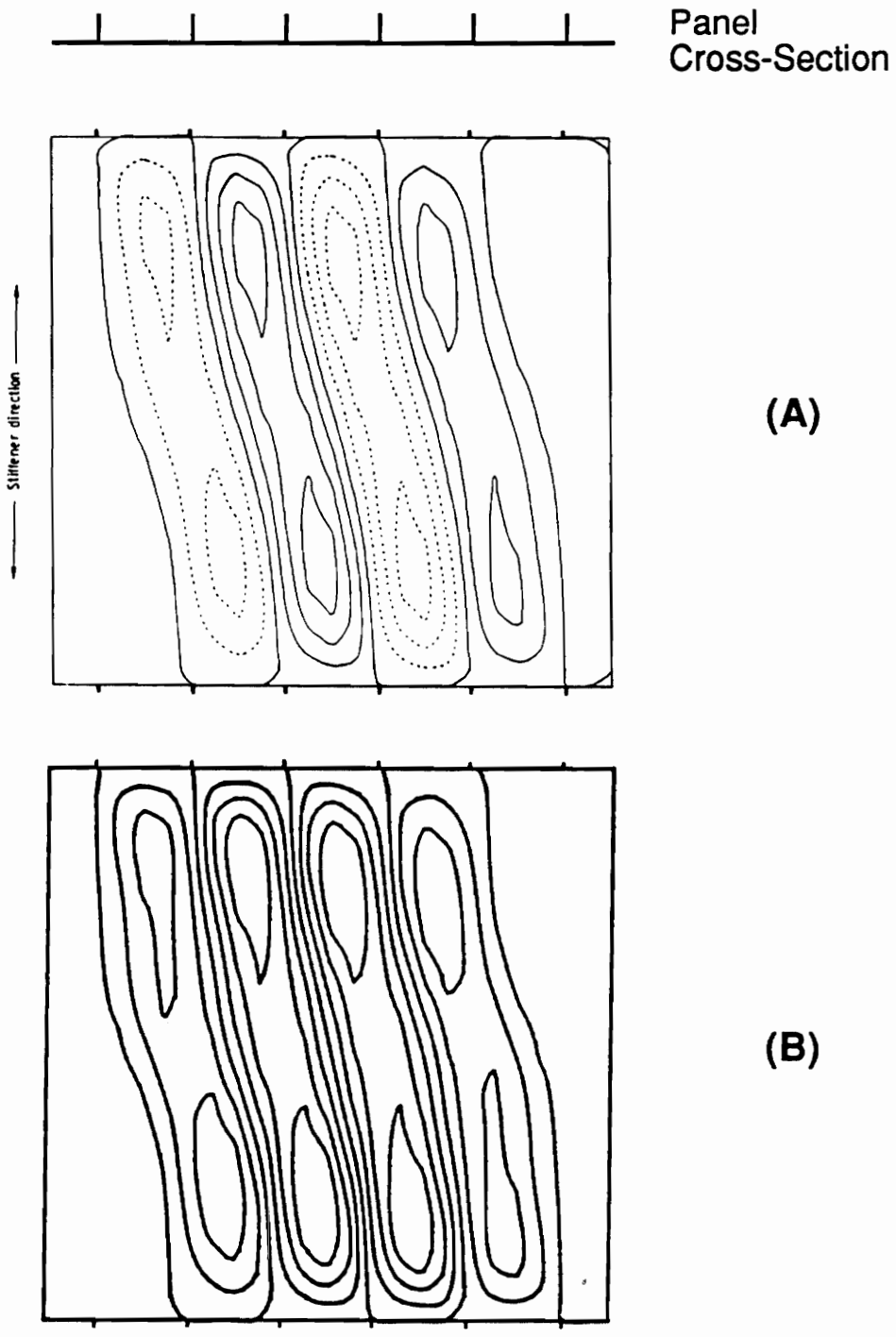

Figure 17. Comparison of Buckled Mode Shapes for Longitudinally Stiffened Isotropic Panel, Thin Skin, Shear: A) FEM Analysis [After Stroud, *et al* [63]] B) LMM Analysis

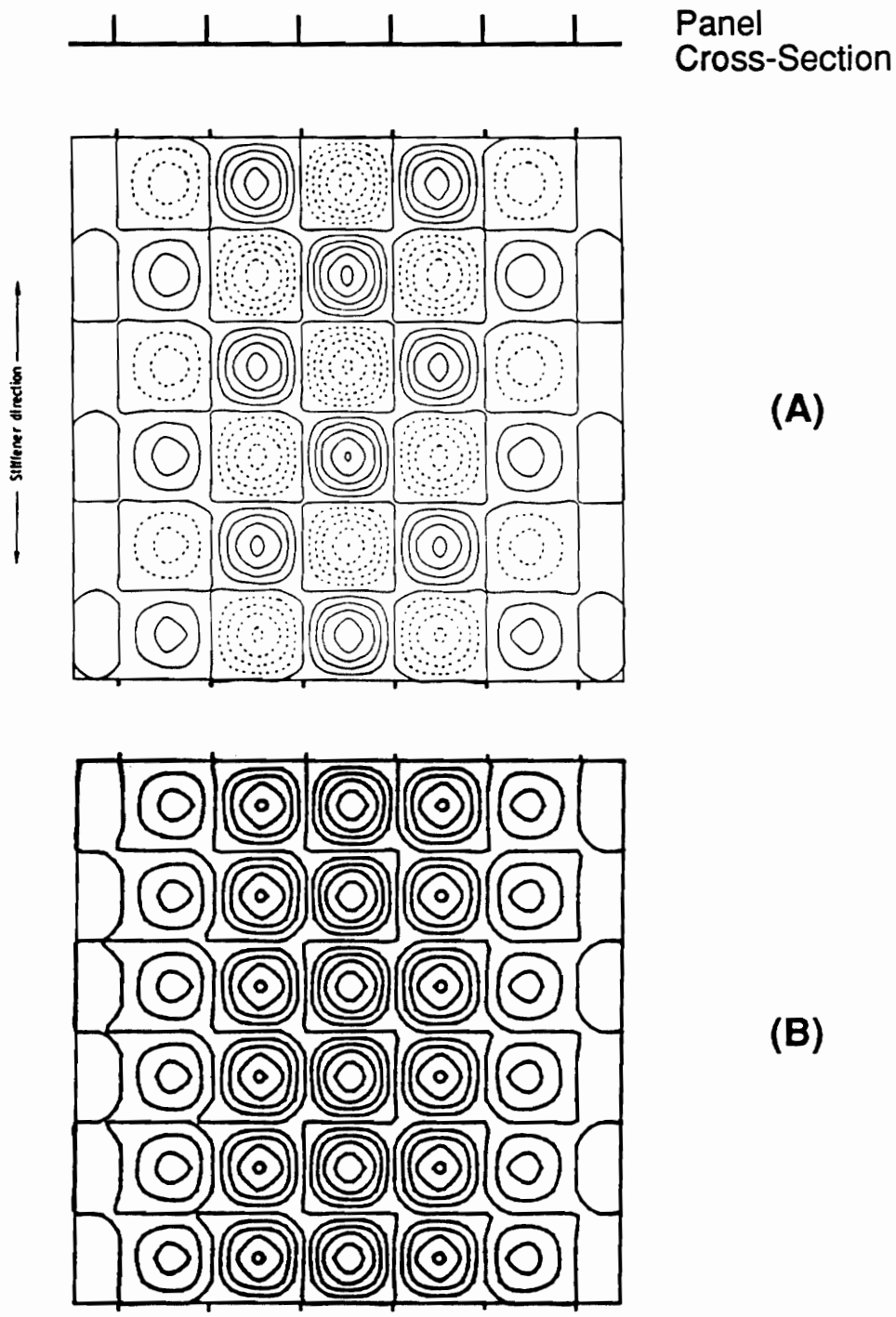

Figure 18. Comparison of Buckled Mode Shapes for Longitudinally Stiffened Isotropic Panel, Thin Skin, Compression: A) FEM Analysis [After Stroud, *et al* [63]] B) LMM Analysis

To complete the verification of the LMM analysis, it was desired to check results for a geodesically stiffened panel. However, no references with buckling data for geodesically stiffened panels were found in the literature. Therefore, the finite element program CSM Testbed[65] was used to analyze a typical geodesic panel under uniaxial compressive load. The test panel, 80 inches long by 28 inches high, had three cross-stiffened cells. The quasi-isotropic $[-45/45/90/0]_S$ skin laminate was 0.2 inch thick, the stiffeners were 0.2 inch thick, and four different stiffener heights of 0.5, 0.75, 1.0, and 1.25 inch were considered. Material properties used are as shown in Table 1 on page 23. For the FEM analysis, the panel was modelled with nine-node combined membrane and bending quadrilateral elements. A mesh 18 elements long by 6 elements wide for the skin along with 6 elements long by 2 elements deep meshes for each stiffener was selected, for a total of 180 elements. The panel geometry and finite element mesh are shown in Figure 19. The LMM analysis used 17 and 9 terms in the X and Y direction, respectively, skin deflection functions and 13 constraint points per stiffener ($M = 17, N = 9, K = 13$).

The first step in the FEM analysis of the panel is a static analysis, where a uniform axial displacement in the Y direction is imposed. Equivalent load resultants are calculated by summing nodal reactions and averaging the total load over the panel width. The distribution of the applied load between the skin and the stiffeners, as predicted by the smeared analysis, agrees closely with the FEM results (Table 6).

Table 6. Comparison of Prebuckling Internal Load Distributions for Geodesically Stiffened Panels

Stiffener Height (in)	Load Applied to Panel: N_y = 1000 lbf/in			
	Skin Load Resultant (lbf/in)		Stiffener Load Resultant (lbf/in)	
	FEM	Smeared	FEM	Smeared
0.5	939.3	939.4	1117	1115
0.75	911.6	911.8	1084	1082
1.0	885.6	885.8	1053	1051
1.25	861.0	861.2	1024	1022

The compressive buckling loads predicted by the FEM and LMM analyses are compared for these same panels (Table 7). The LMM prediction is only 60% of the FEM result for the 0.5 inch

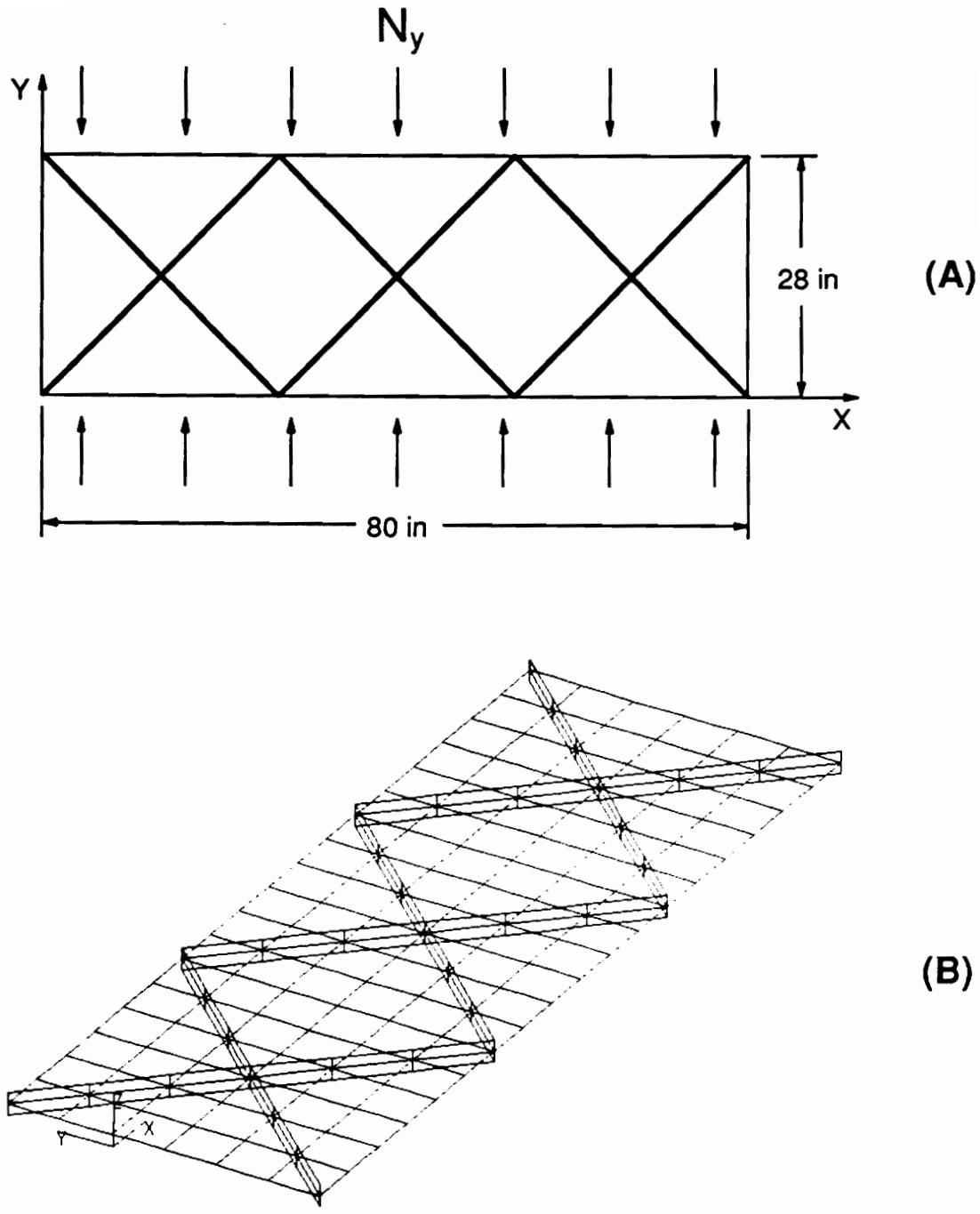

Figure 19. **Geodesically Stiffened Panel for Verification of LMM Analysis:** A) Panel Geometry B) Finite Element Mesh

stiffener, but as the stiffeners become higher the correlation increases to 95% for the 1.25 inch stiffener. In the FEM analysis, the loads on the panel were introduced by imposing a uniform displacement on all skin and stiffener nodes along the top of the panel. Therefore, the end of each stiffener is constrained to remain vertical, thereby simulating a clamped condition at the ends of the stiffeners. However, the condition assumed at the ends of the stiffeners in the LMM analysis is simple support. As such, the stiffeners in the LMM model do not stiffen the skin as effectively as they do in the FEM model, resulting in considerably lower buckling loads. The discrepancy is greater for the short stiffeners as they have a low flexural rigidity and deflect almost as much as the skin. On the other hand, the higher stiffeners possess a large flexural rigidity and hence deflect little, so that the restraint condition at the ends of the stiffeners does not have as much of an effect.

Table 7. Comparison of Buckling Loads for Geodesically Stiffened Panels

	Panel Buckling Load (lbf/in)		
Stiffener Height (in)	N_{FEM}	N_{LMM}	$\frac{N_{LMM}}{N_{FEM}}$
0.5	573	342	0.596
0.75	705	613	0.870
1.0	748	708	0.946
1.25	783	743	0.949

The buckled mode shapes from the FEM analysis are shown in Figure 20 and those from the LMM analysis in Figure 21. The trends seen in the plots seem to correspond with the buckling load data. That is, for the 0.5 inch stiffened panel, the FEM contour plot (Figure 20-A) indicates that the stiffeners have more of an effect on the skin than they do in the LMM plot (Figure 21-A), and therefore the buckling load is higher. As the stiffeners become higher, the contour plots become more similar in form, and the FEM and LMM buckling loads also agree more closely. LMM analysis buckling loads for the more heavily stiffened panels (1.0 and 1.25 in), which buckle in a localized way (Figure 21-C and Figure 21-D), are on the conservative side but agree quite well with the FEM results. In most practical cases, it is expected that optimum geodesic panels will have relatively heavy stiffening. Unless a panel were designed for very light loads, where a minimum-gauge skin thickness bound can force the skin to be thicker than desired, the critical mode will likely

be more localized, as in panels C and D. Therefore, the critical loads predicted with the LMM method should be acceptably accurate, perhaps within 5-10%.

As a final note, the LMM and FEM analyses were run on different computer systems at Virginia Tech. Therefore, no comparison is possible as to the relative computational demands of the two methods. However, it is believed that the LMM analysis runs significantly faster than the corresponding FEM model while, as demonstrated above, retaining a reasonable degree of accuracy for practical panel geometries.

4.1.2 Convergence Study

The influence of several factors, including stiffener flexural rigidity and the analysis parameters M,N, and K, on the buckling behavior of a typical geodesically stiffened panel is examined in this section. First, a qualitative demonstration of panel buckling response under compression or shear is presented by changing the flexural rigidity of the stiffeners. Second, it will be remembered that the Lagrange multiplier method [LMM] analysis, presented in Section 3.2.1.3, is dependent on several analysis parameters. These include the number of constraint points K along each stiffener and the number of terms M,N in the X,Y directions of the skin deflection function. Since these parameters determine the accuracy of the results obtained, their influence on the solution for a typical geodesically stiffened panel is examined. The geodesic configuration chosen for the study is a four cell cross-stiffened panel. In all examples, the thickness of the panel skin and the cross-sectional area of each stiffener remain unchanged, fixing the panel mass.

<u>Stiffener Flexural Rigidity:</u> To examine the influence of stiffener flexural rigidity on the panel buckling mode, the rigidity of the stiffeners is increased by making the aspect ratio (aspect ratio [AR] is defined as stiffener height divided by stiffener thickness) larger while keeping the cross-sectional area constant. Since the present LMM analysis does not account for the torsional rigidity

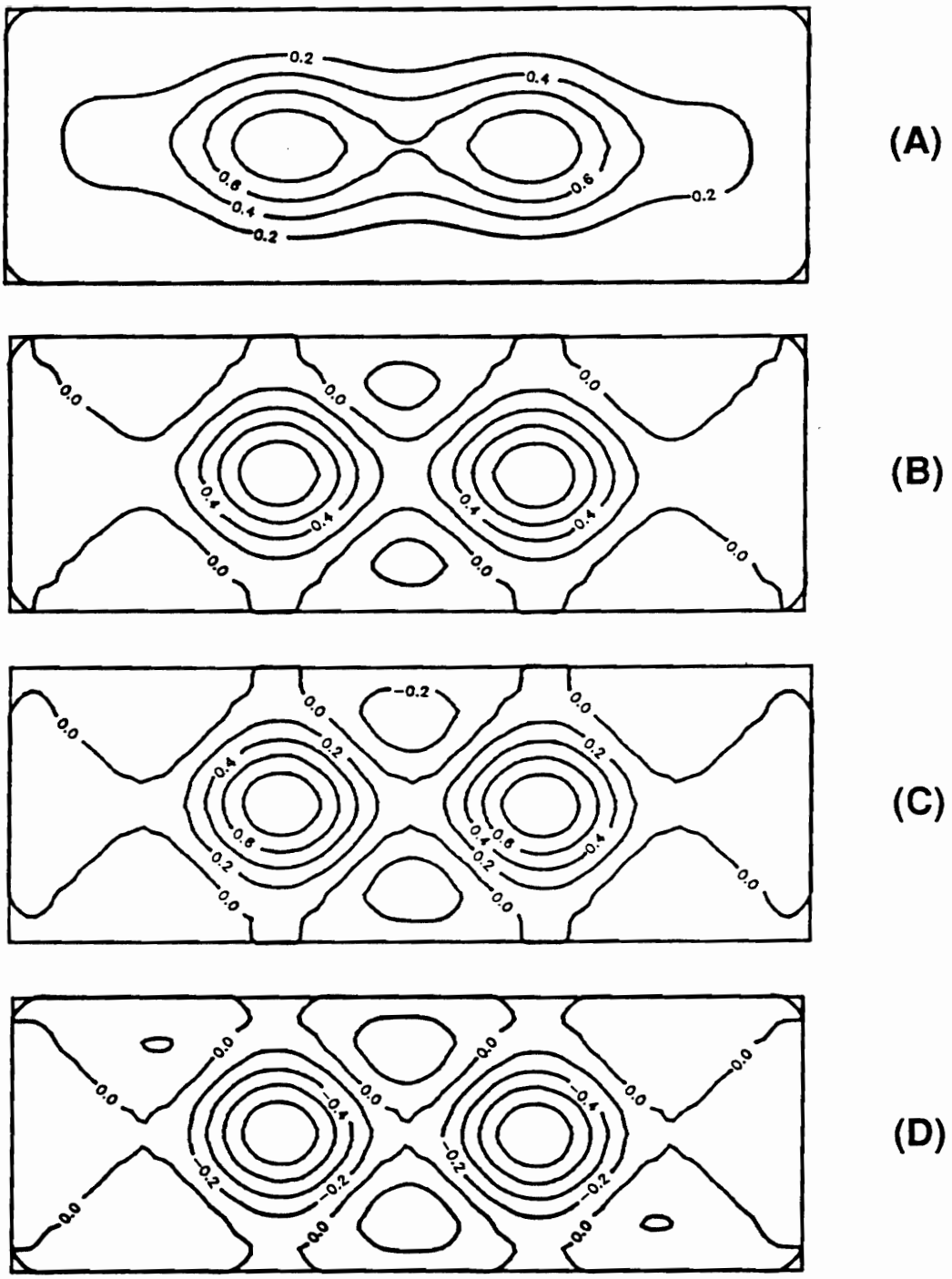

Figure 20. Buckled Mode Shapes for Geodesically Stiffened Panels, FEM Analysis: A) SH = 0.5 B) SH = 0.75 C) SH = 1.0 D) SH = 1.25, SH = Stiffener Height (in)

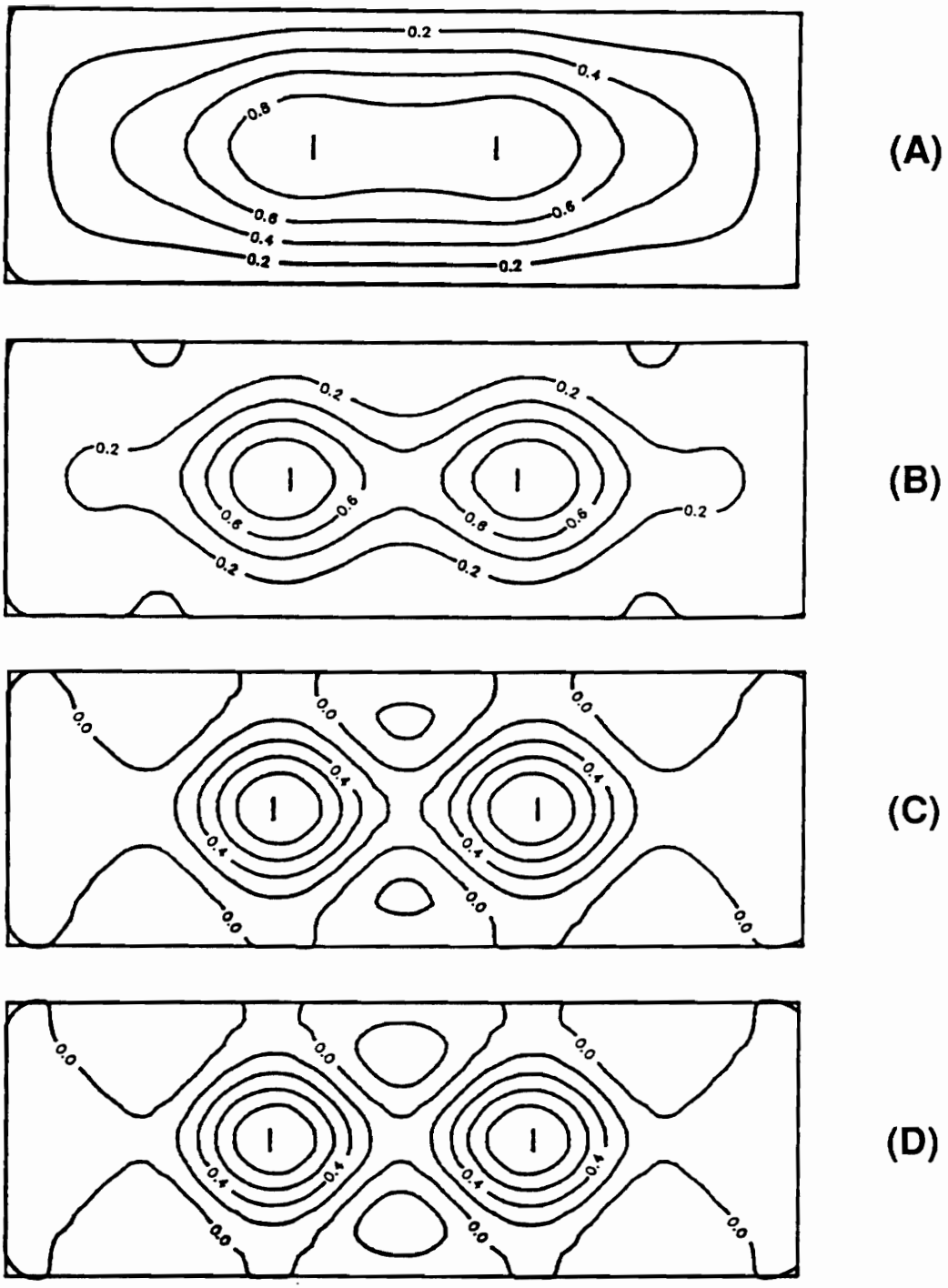

Figure 21. Buckled Mode Shapes for Geodesically Stiffened Panels, LMM Analysis: A) SH = 0.5 B) SH = 0.75 C) SH = 1.0 D) SH = 1.25, SH = Stiffener Height (in)

of the stiffener, the only effect of changing aspect ratio is on the stiffener moment of inertia. For a short, thick, and therefore flexible stiffener (for example, AR = 0.4), the buckling mode of the panel in compression is a single half-wave in each direction with a large out-of-plane excursion by the stiffeners (Figure 22-A). As the aspect ratio is increased, the stiffeners become more rigid, stiffener deflection is reduced, and local inter-stiffener buckling of the skin emerges (AR = 6.1, Figure 22-B; AR = 66, Figure 22-C). In Figure 23 the stiffened panel buckling load, normalized with respect to the maximum value achieved, is shown as a function of the stiffener moment of inertia, which is similarly normalized. For a given skin thickness, the buckling load does not increase indefinitely, instead approaching the maximum value asymptotically. Once skin buckling becomes the limiting mode of instability, subsequent increases in stiffener rigidity produce no increase in the load carrying capacity of the panel. Although high, thin stiffeners are efficient due to their large moment of inertia, their aspect ratio is limited by the stiffener crippling constraint. In Figure 23, the solid circle on the curve indicates the point at which the stiffener cripples (using the analysis of Section 3.2.2), rendering designs to the right of this point infeasible.

The panel buckling response to shear loading is analogous to that for compression. That is, a global mode involving considerable deflection of the flexible stiffeners progressively changes to a localized, short wavelength mode between rigid stiffeners as the stiffener moment of inertia is increased (Figure 24). For panels under pure shear loading, oblique stiffeners with an axial tensile load (angled upwards and to the left) tend to enforce lines of zero deflection even when they have a small moment of inertia. On the other hand, those stiffeners with an axial compressive load (upwards and to the right) are more likely to deflect in multiwave modes. The curve for critical shear load versus stiffener moment of inertia is very similar to that in Figure 23 for compressive loading, so it is not shown. For shear loaded panels, the aspect ratio of stiffeners with compressive axial loads is again limited by the stiffener crippling constraint. The tension-loaded stiffeners are required to have identical dimensions to the compression-loaded ones to prevent panel designs which would be sensitive to the direction of applied shear.

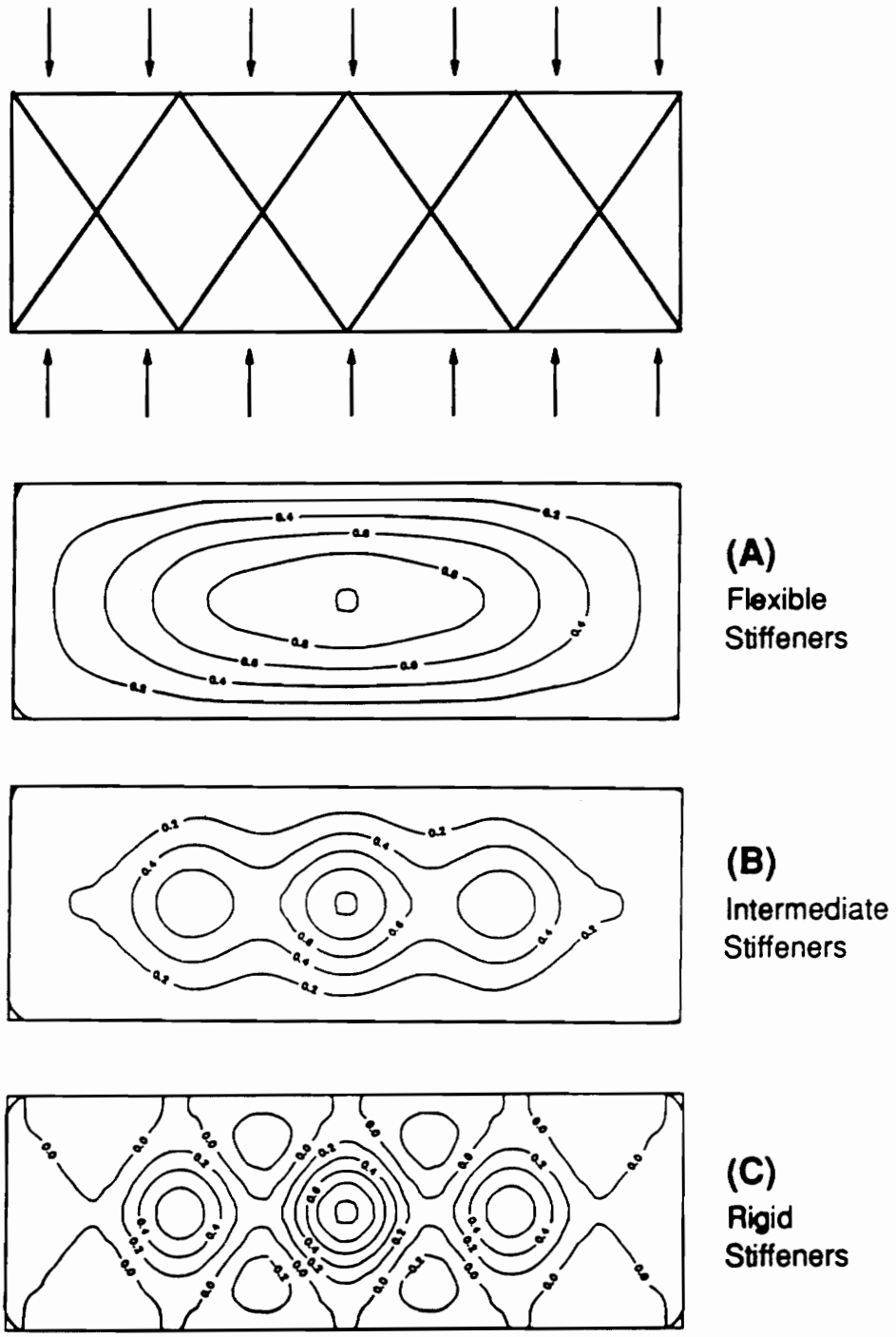

Figure 22. Influence of Stiffener Flexural Rigidity on Buckled Mode Shapes of Cross-Stiffened Panels, Compression: A,B,C correspond to points on Figure 23

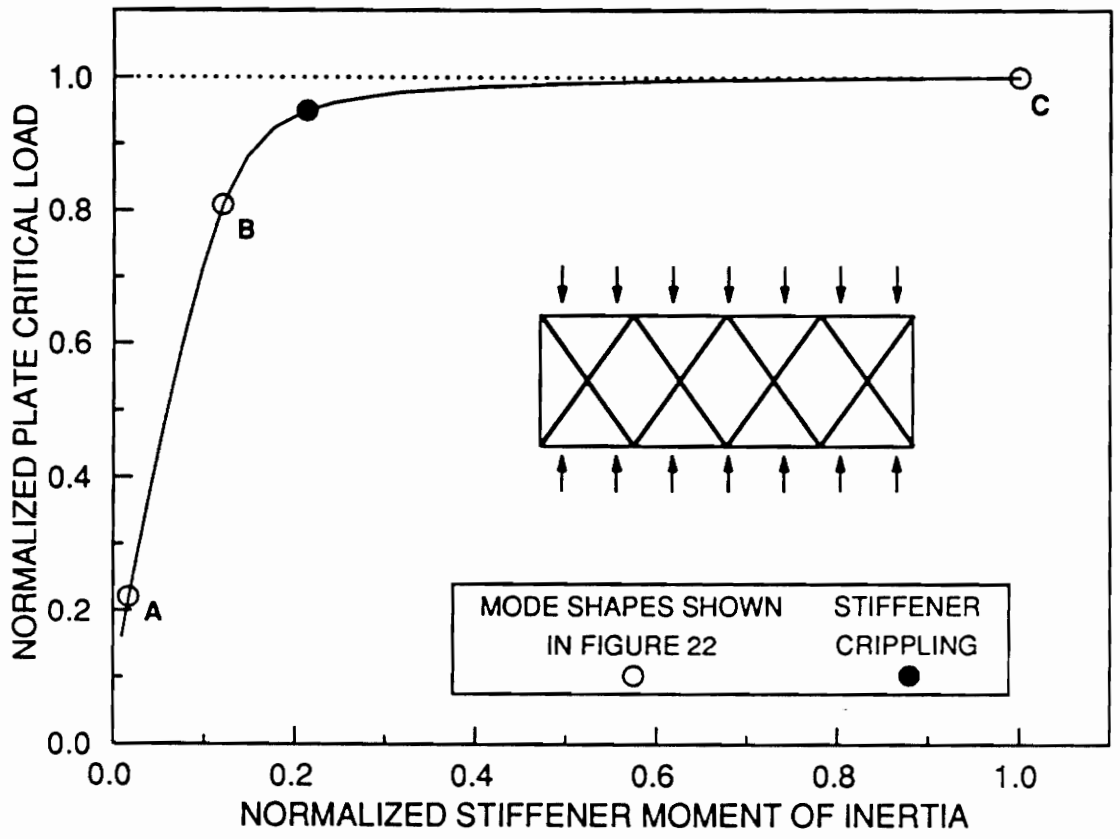

Figure 23. Influence of Stiffener Flexural Rigidity on Buckling Load of Cross-Stiffened Panels, Compression

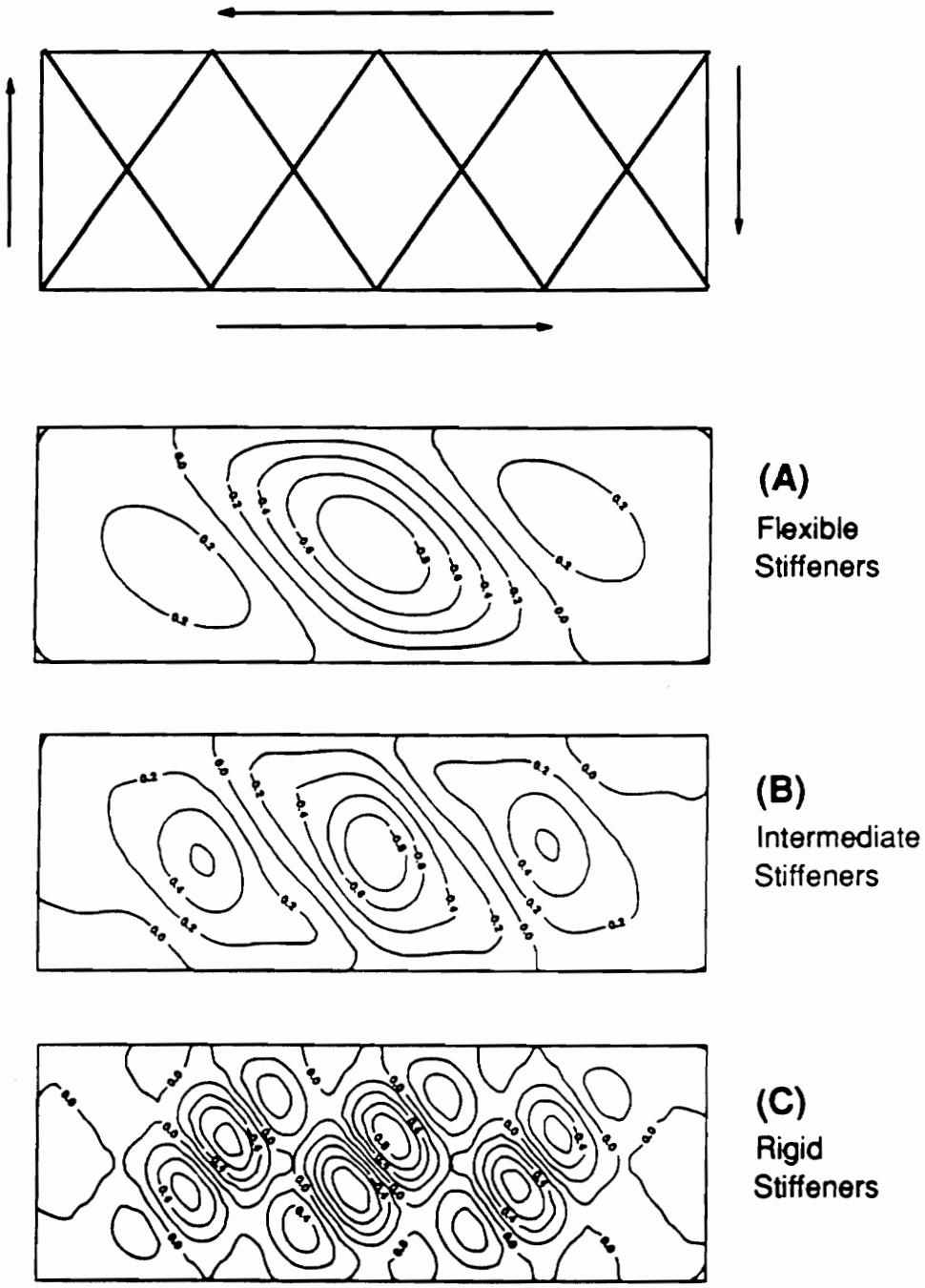

Figure 24. Influence of Stiffener Flexural Rigidity on Buckled Mode Shapes of Cross-Stiffened Panels, Shear

Constraint Points K: To demonstrate how the number of constraint points per stiffener K influences the LMM analysis, examples start with a single point at the center of each stiffener and the number of points evenly distributed along the stiffener length is then increased. For a simple example, return to the compressed isotropic plate with a single central stiffener from Section 4.1.1. The buckling load is very low for a single constraint point at the panel center, as the skin merely pivots about the constraint point, leaving the stiffener undeflected (Figure 25-B1). However, using two (Figure 25-B2) and then three (Figure 25-B3) constraint points forces the skin and stiffener deflections to quickly coincide to a satisfactory degree.

For a more practical demonstration, a moderately stiffened (sufficient to enforce local skin buckling) four cell geodesically stiffened panel is analyzed under both compression and shear loads. In Figure 26 the panel critical load, normalized with respect to the maximum load achieved, is shown as a function of the number of constraint points per stiffener. For the compression-loaded panel, only four constraint points per stiffener are required to reach 99% of the stable critical load reached with a larger number (11) of points (Figure 26, upper curve). Although slower to converge, the shear-loaded case still requires only eight points per stiffener to reach the 99% level (Figure 26, lower curve).

Skin Deflection Function Terms M,N: The number of terms required in the skin deflection function is estimated by increasing the number in each direction until a relatively constant buckling load is reached. A compression-loaded four cell cross-stiffened panel is considered first. In Figure 27 the panel critical load, normalized with respect to the minimum critical load achieved, is shown as a function of the number of terms. The number of constraint points is set to the maximum value, $K = 11$, from the previous example. To isolate the Y direction dependence, the number of terms in the X direction, M, is set to a large number (in this example, 17) while the number of terms in the Y direction, N, is varied. When N is set to unity, the skin is forced to have only a single half-wave in the loading direction Y. Constraining the buckled shape in this manner artificially stiffens the panel. The buckling load for $N = 2$ does not change because this term accounts for a deflection antisymmetric about the panel midheight, which is not the fundamental buckling mode for com-

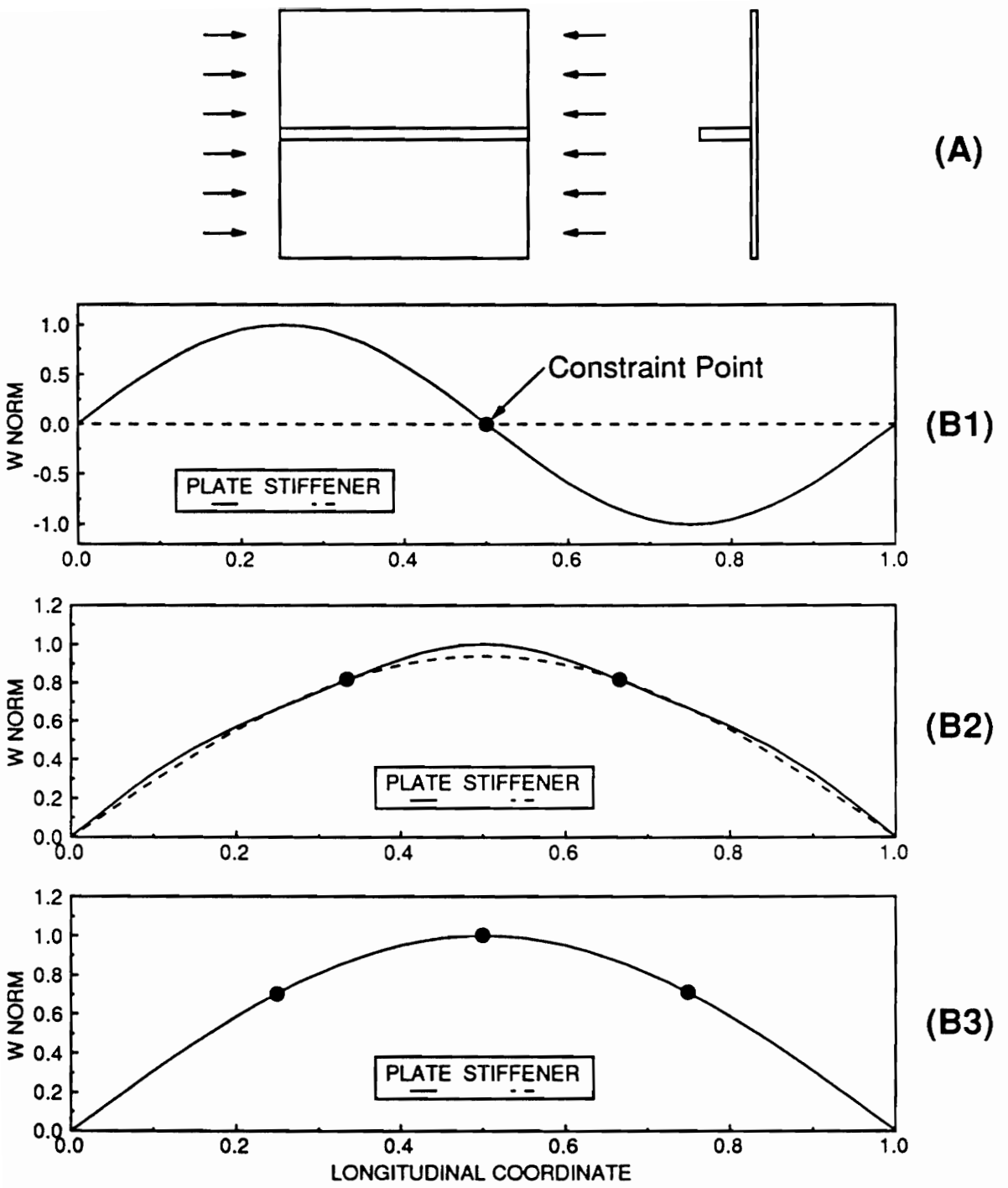

Figure 25. Influence of Number of Constraint Points on Buckled Profile of Isotropic Plate with One Longitudinal Stiffener: A) Plate Geometry B) Skin and Stiffener Buckled Profiles

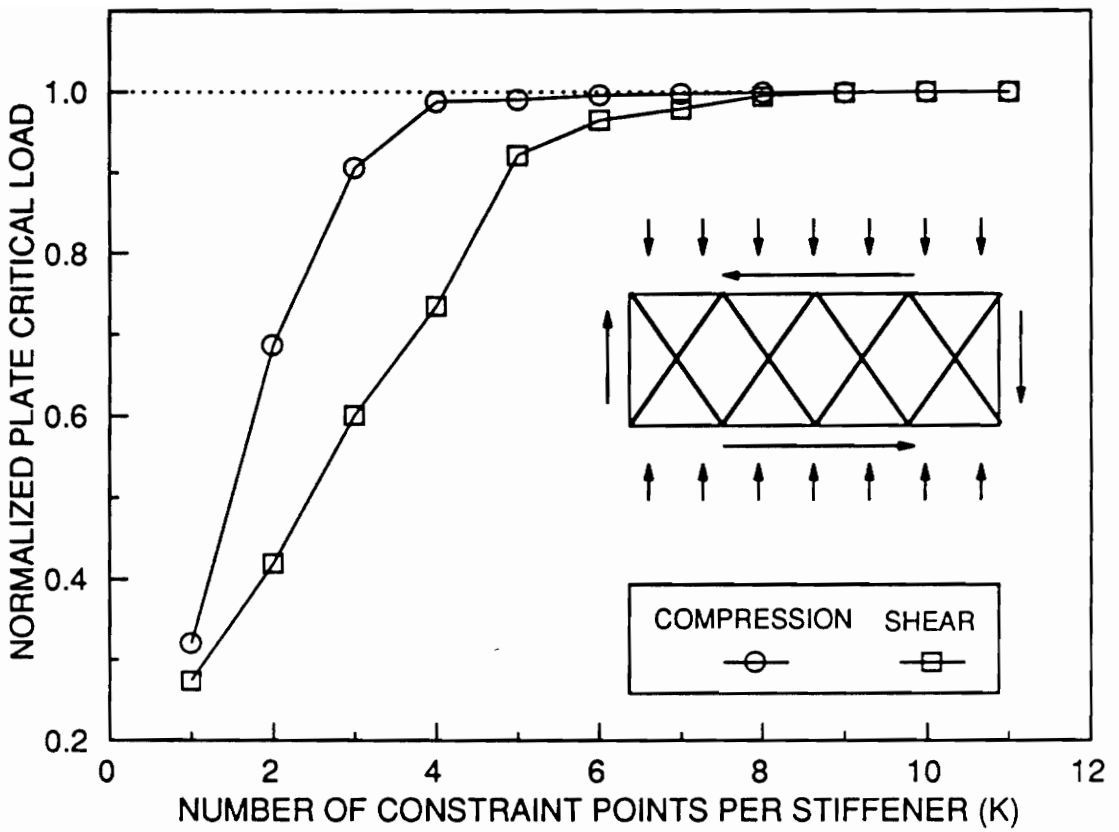

Figure 26. Influence of Number of Constraint Points on Buckling Load of Cross-Stiffened Panel, Compression and Shear

pression. The critical load to drops sharply at $N = 3$, when a sufficient number of terms are included to allow the lowest critical mode to be reached (Figure 27, lower curve). Further increases in N cause the critical load to drop slightly as small improvements in the buckled mode shape are incorporated. Analogous behavior results when N is fixed (at $N = 11$) and M is incremented, except that an intermediate mode occurs for $M = 7$ and $M = 8$ (Figure 27, upper curve). A rough estimate for the minimum number of terms required in each direction of a compressed panel is given by the maximum number of inter-stiffener sections crossed by a line drawn in each direction. In the present example, a line can be drawn in the Y direction passing through three subsections and in the X direction traversing nine (see inset sketch, Figure 27). This rule-of-thumb agrees very well with the results in Figure 27 for this example. For panels with many cells, it is clear that a large number of terms are required in the X direction to model the many inter-stiffener skin waves. Since the number of skin deflection function terms is the primary factor determining the computational cost of the LMM buckling analysis, this sets a practical limit on the number of stiffeners which can be accommodated.

In Section 3.2.1.2, the buckling of a flat orthotropic plate under compression and shear was considered. It was noted that an exact solution can be found for the compression case with a limited number of skin deflection function terms. Under shear loads, however, the skewed deflection pattern cannot be represented exactly by a finite number of terms in the chosen double-sine function, thereby slowing convergence of the solution. For the geodesically stiffened panel, similar behavior is observed. Whereas the solution for the compression-loaded stiffened panels drops off suddenly, the convergence of the shear solution is more gradual and more terms are required (Figure 28) (note critical load normalized with minimum value, as before). However, a well defined minimum is still reached, indicating that the solution has converged to an acceptable degree. Note that a single term in either direction ($N = 1$ or $M = 1$) is incapable of modelling the anti-symmetric mode, resulting in an infinite critical load.

The number of deflection function terms required for a given panel is both geometry and loading-dependent, but a detailed convergence study cannot be performed for every panel configuration in

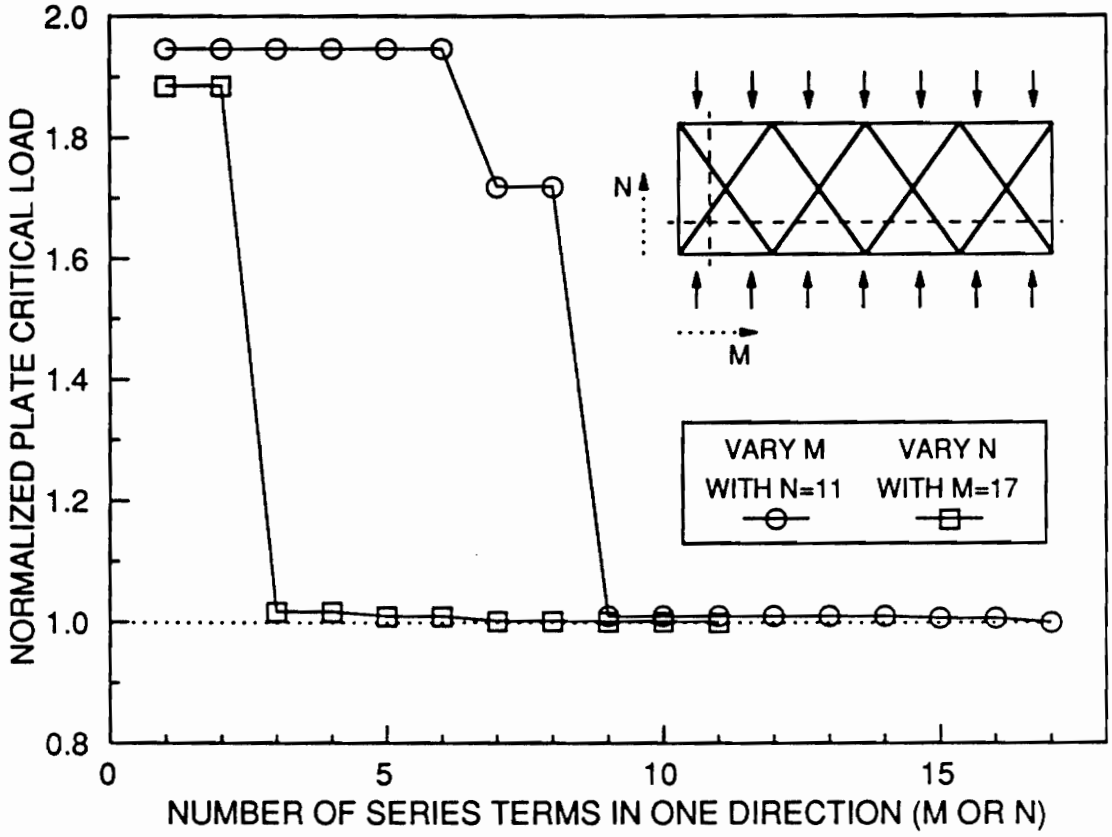

Figure 27. Influence of Number of Skin Deflection Function Terms on Buckling Load of Cross-Stiffened Panel, Compression

a design study. Therefore, the practice has been to first optimize the panel design using an estimated number of terms. The final design is then analyzed with the number of terms in both the X and Y directions perturbed by $+2$. If the change in critical load is small (less than 1% is the criterion used in the design study), it is assumed that a sufficient number of terms has been used. Otherwise, the panel is redesigned using a larger number of terms and the perturbation procedure is repeated.

4.2 *Rhombic Skin Section Buckling*

There are several reasons motivating the study of laminated rhombic plate buckling. One objective is to use the rhombic analysis to estimate the influence of anisotropic coupling terms D_{16} and D_{26}, which has not been included in the LMM panel buckling analysis. A second aim is to isolate the effects of changing skin section shape or size from other variables in the panel design. A final goal is to be able to conduct skin laminate optimization considering just the rhombic plate, rather than analyzing the full stiffened panel. In solving the rhombic plate stability problem, however, it is well known that standard energy methods give nonconservative results and may be slow to converge when anisotropy is present. Skewing the shape away from a rectangular planform exacerbates the convergence problem. For this reason, there is some concern that the effects of changing plate shape or laminate geometry might be over-estimated by standard methods. The alternate method adopted for the present work appears to possess the advantage of providing a lower bound to the critical loads, albeit at the expense of greater computational time. Section 4.2.1 presents a test problem to demonstrate the performance of both standard and new methods. As mentioned above, the ultimate goal of the work with rhombic plates is to apply the rhombic results to the design of geodesically stiffened panels. Therefore, Section 4.2.2 presents a correlation study between the LMM analysis buckling loads for cross-stiffened panels and the buckling solutions for equivalent rhombic plates.

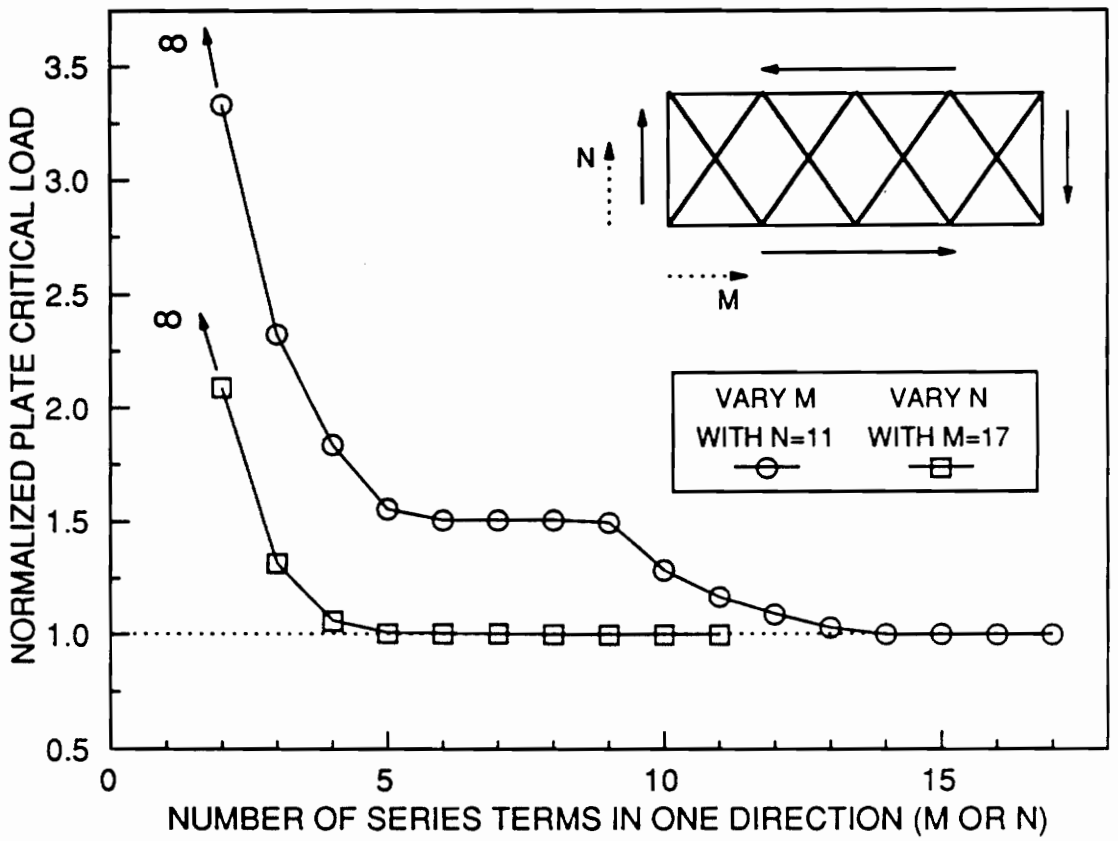

Figure 28. Influence of Number of Skin Deflection Function Terms on Buckling Load of Cross-Stiffened Panel, Shear

4.2.1 Convergence Study and Comparison With Standard Method

As was noted in Section 3.3, a standard Galerkin or Ritz analysis (hereafter referred to as "Standard" method) will always predict buckling loads higher than the exact solution. On the other hand, the solution due to Kennedy and Prabhakara[48] ("Kennedy" method) appears to give conservative results. That is, the solution converges to the exact result from below rather than above. Although the Kennedy solution is more expensive computationally than the Standard solution, it is this element of conservatism which makes the analysis attractive. It is felt that these two methods can be used to establish upper and lower bounds on the solution, to provide a realistic measure of component behavior.

Unfortunately, there does not appear to be an exact solution available for the buckling of a rhombic or skew plate under in-plane loads, even for the isotropic case, with which to confirm the validity of the Kennedy method. However, it is possible to construct a viable test problem using a geometric analogy. Consider an isotropic rhombic plate with an interior angle of 60 degrees under uniform biaxial compression (Figure 29-A). The lowest odd or antisymmetric buckling mode has a nodal line bisecting the rhombus into two equilateral triangles (Figure 29-B). The transverse deflection along the nodal line is, of course, zero and the existence of an inflection point across the nodal line indicates that the curvature normal to the line is also zero. For an isotropic plate, the zero curvature condition is sufficient to guarantee that the bending moment normal to the nodal line is also zero. The supported edges satisfy the geometric boundary conditions, which ensures that the solution should converge to that for simply supported boundaries. Therefore, this antisymmetrically-buckled rhombic plate is analogous to a simply supported equilateral triangular plate under biaxial compression. The exact solution for latter problem has been derived by Timoshenko and Gere[25] and Taylor[66], so it can be used to test the rhombic solutions.

The equilateral triangular plate under consideration has a height of π and unit flexural rigidity ($D = 1$), which results in an exact critical load of $N = 4$. Comparison of the Kennedy solution with

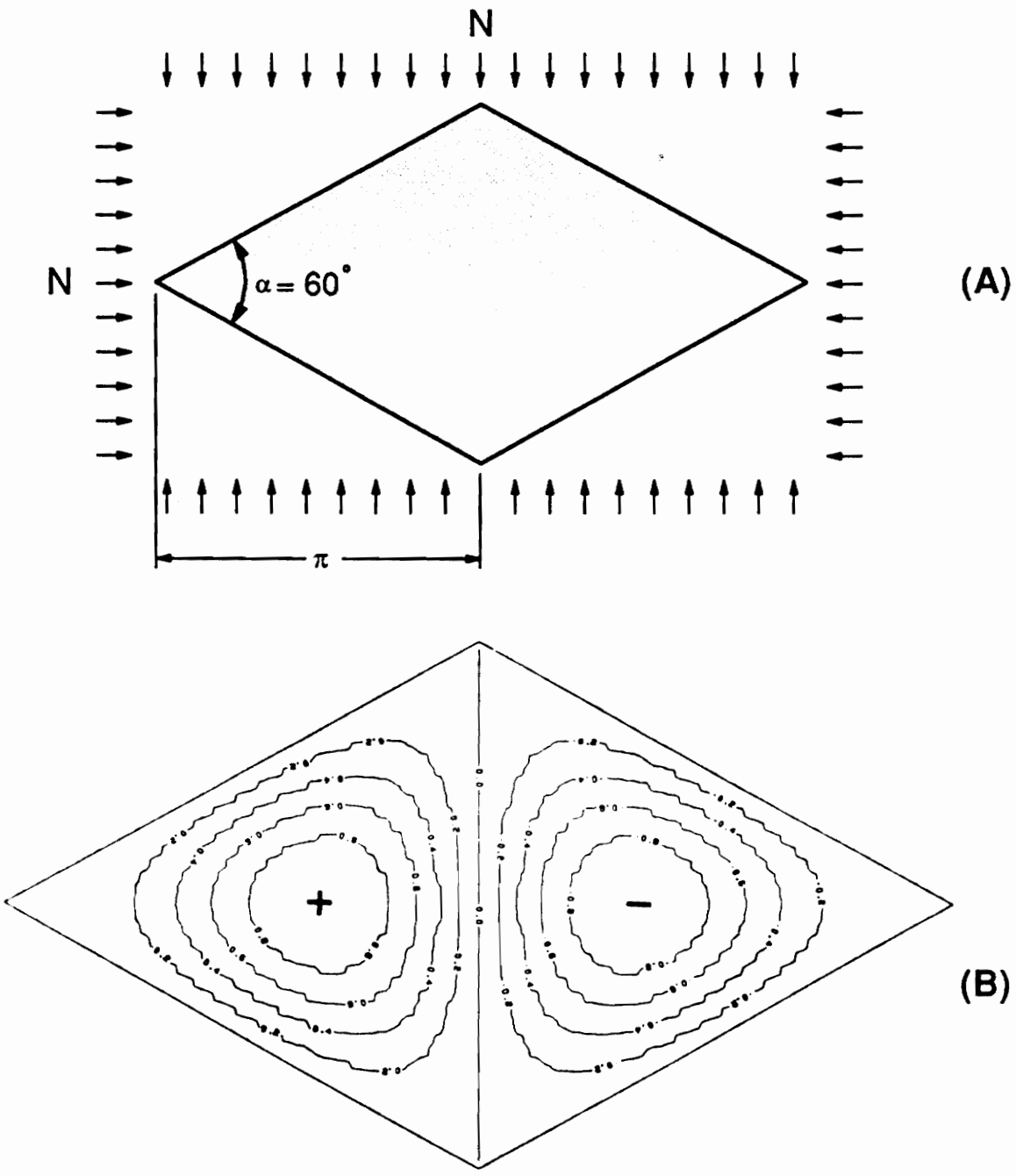

Figure 29. Buckling of Biaxially Compressed 60 Degree Isotropic Rhombic Plate: A) Plate Geometry and Loading B) Lowest Antisymmetric Mode

the Standard solution is shown in Figure 30, along with the exact solution. As the number of terms is increased, the standard solution converges, as expected, from above the exact solution and the Kennedy solution from below (Figure 30-A). Aside from the first few terms, the degree of convergence for a given number of terms appears to be about the same for each method. As the number of terms N increases, the dimension of the coefficient matrices expand as N^2. Since both methods have the same size matrices, the solver time required for each rises at about the same rate. However, extra summations in the Kennedy method formulation (see Equation 151 in Section 3.3) require many more calculations to form the coefficient matrices (on the order of N^6 for Kennedy versus N^4 for Standard). This results in greatly increased overall computational time (Figure 30-B) for the Kennedy method. Although it is significantly more expensive computationally, the added cost may be justified in problems where severe over-estimation of critical loads with Standard methods is suspected.

4.2.2 Correlation With LMM Panel Buckling Analysis

In the past, stiffened panels have been analyzed by viewing the panel as an assemblage of discrete plates under in-plane loads[16] [17]. For the present study this approach will be used to explore several aspects of the design of laminated composite skins for geodesically stiffened panels. These topics include the effects of skin laminate anisotropy, skin section shape, and laminate orientation on the buckling loads of the panel skin. The purpose of this section, then, is to examine the relationship between the buckling of a simply supported discrete rhombic plate and the local buckling behavior of rhombus-shaped skin sections in a cross-stiffened panel. The rhombic plate dimensions which correspond to the skin sections for two to eight cell cross-stiffened panels are shown in Table 8. The rhombus interior angle α referred to here is equal to 2ϕ in the rhombic coordinate transformation (see Part B of Figure 14 on page 75).

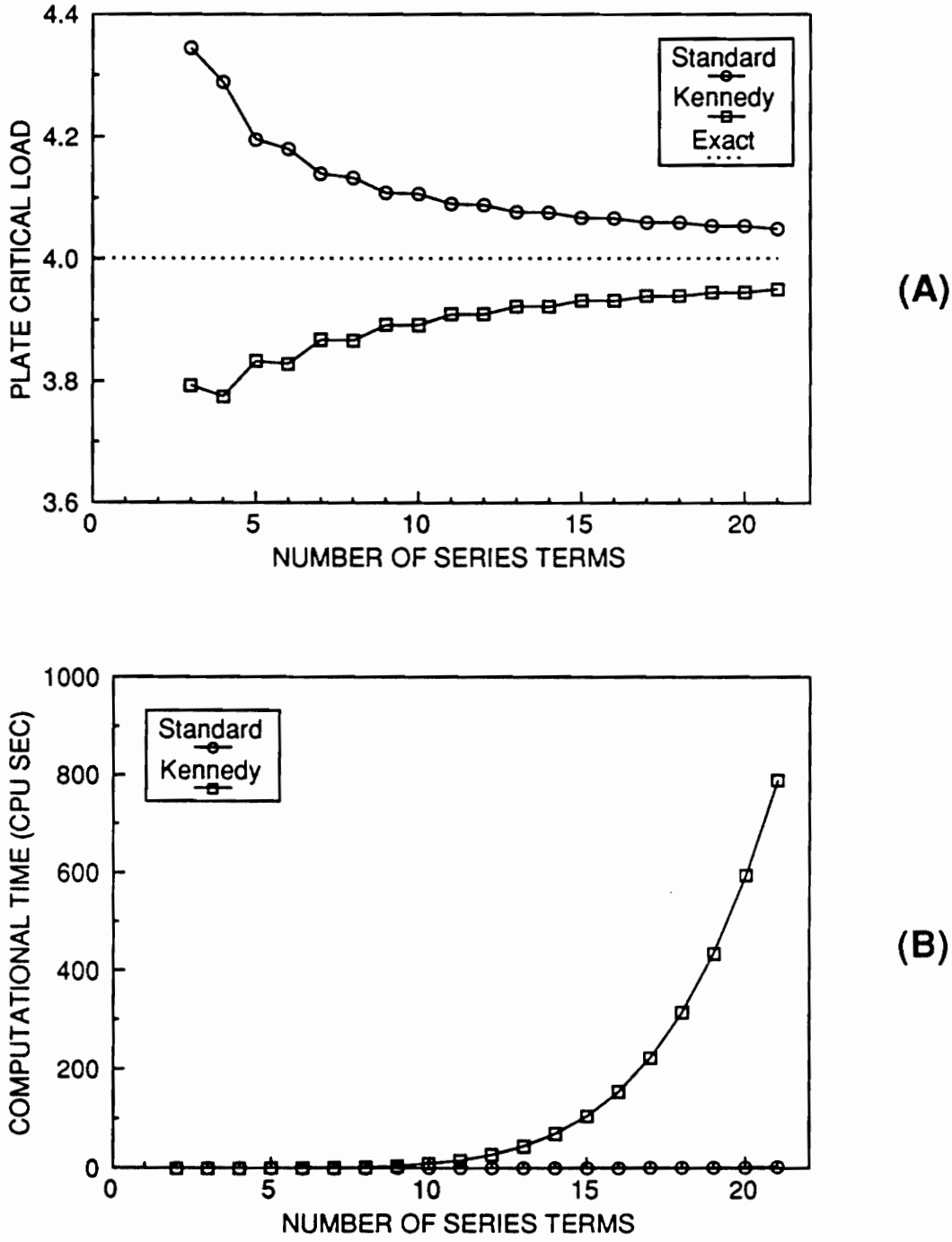

Figure 30. Comparison of Standard and Kennedy Methods for Equilateral Triangular Plate Buckling Analogy: A) Convergence Behavior B) Computational Time Required

Table 8. Equivalent Rhombic Plate Dimensions for Skin Sections of Cross-Stiffened Panels

Number of Cells	Interior Angle α (degrees)	Side Length a (inches)
2	69.98	24.41
3	92.79	19.33
4	108.9	17.20
5	120.5	16.12
6	129.1	15.51
7	135.6	15.12
8	140.7	14.87

The analysis of Section 3.3 assumes classical simple support boundary conditions (zero displacement, zero bending moment) on all four edges of the rhombic plate. This idealization ignores continuity of the buckling mode between adjacent skin elements in a stiffened panel, and does not account for the rotational restraint of the stiffeners on the skin. The present LMM buckling analysis also neglects the effects of stiffener restraint, but since the skin is modelled as a continuous sheet, inter-element continuity is maintained. For purposes of the rhombic/LMM correlation, panels with very rigid stiffeners are used in order to limit stiffener deflection and enforce local skin buckling. This is an effort to make the conditions at the edges of the panel skin sections approximate as closely as possible classical boundary conditions. In fact, it was observed that the correlation results were independent of the thickness of the panel skin, due to the rigidity of the stiffeners. Since it is geometric approximations which are being examined here, the coupling terms D_{16} and D_{26} are set to zero in the rhombic analysis, as they are in the LMM analysis.

The static analysis of Section 3.1.1 calculated what portion of loads applied to a panel would be carried by the skin (with the remainder carried by the stiffeners). Although the stiffened panels in this study are subjected to uniaxial compression, the panel skin is under biaxial compression due to the X direction zero-displacement boundary condition and the Poisson effect. For the $[-45/45/90/0]_S$ laminate used in this study, this results in transverse compression of $\overline{N}_x^P = 0.30282$ lbf/in for each $\overline{N}_y^P = 1.0$ lbf/in longitudinal compression. The skin load resultants for a particular cross-stiffened panel are imposed on an equivalent rhombic plate (same size, shape, and skin thickness as the inter-stiffener rhombic sections in the panel). Using the critical eigenvalue for the

rhombic plate and the internal load distribution information, it is straightforward to calculate an estimate of the buckling load for the whole panel.

As discussed previously, two forms of the rhombic plate buckling solution are available: the Standard method, which provides an over-estimate to the critical load, and the Kennedy method, which is believed to provide an underestimate. The difference in results between the two methods is dependent on the skewness of the plate. For example, rhombic plates under compression have Standard and Kennedy buckling loads which are virtually identical for the three-cell geometry, because the interior angle α is approximately 90° and skewing effects are at a minimum. As the plate is skewed away from the square shape the two solutions diverge, with the Standard solution 27.3% higher than the Kennedy solution for the eight-cell geometry (13 terms taken in series). The solution behavior under shear is similar to that for compression; that is, the solutions are nearly identical when the plate is square but diverge otherwise. For an eight-cell rhombus under shear, the Standard solution is 12.1% higher than the Kennedy solution. In the previous section, it was seen that the Standard and Kennedy solutions converged at roughly the same rate with respect to the exact solution. Therefore, for the remainder of this study, the rhombic buckling load used is the mean of the values provided by these two methods.

The rhombic/LMM buckling load correlation is examined for both compression and shear. For compression, the rhombic buckling predictions are rather conservative with respect to the LMM results, with correlation values ranging from 47% to 61% (Table 9). This conservatism is likely due primarily to the rhombic analysis ignoring continuity of the buckled skin shape between neighboring cells. That is, the adjacent skin sections in the stiffened panels provide significant rotational restraint at the edges of a typical rhombus-shaped skin section. Therefore, the LMM analysis predicts higher panel buckling loads. The shear correlation results are not quite as conservative as those for compression, at 65%-74%.

Table 9. Correlation of Buckling Loads for Rhombic and LMM Models of Cross-Stiffened Panels, Compression and Shear

	Ratio of Critical Eigenvalues $\frac{\lambda_{Rhombic}}{\lambda_{LMM}}$	
Number of Cells	Compression N_y	Shear N_{xy}
2	0.47	0.65
3	0.56	0.73
4	0.61	0.74
5	0.60	0.73
6	0.57	0.66
7	0.53	0.68
8	0.51	0.65

5.0 Wing Rib Design Study Results

Panel buckling and stiffener crippling analyses for stiffened panels were introduced and tested in Sections 3 and 4, respectively. This analysis capability, along with the material failure analysis, has been coupled with a numerical optimization program to create a stiffened panel design package. This design tool is used to conduct a preliminary design study for minimum-weight aircraft wing rib panels, the scope of which was outlined in Section 2.3. In Section 5 the results of the design study are presented and discussed. In Section 5.1, structural efficiencies for geodesic panel designs under three loading conditions (uniaxial compression, pure shear, combined compression-shear) are compared with those for minimum-weight unstiffened and longitudinally stiffened panels. In Section 5.2, the results from the design study are analyzed in more detail. Trends in design variables and other parameters are examined to determine what contributes to a structurally efficient panel design. In Section 5.3, the effects of skin laminate anisotropy and skin section geometry for the cross-stiffened designs are estimated using the rhombic plate buckling analysis.

5.1 Optimum Geodesic Panels

The analysis capability described in Sections 3.1 and 3.2 is coupled with a general purpose optimization package, Automated Design Synthesis[22] (ADS), to create the stiffened panel design code PANSYS (use and capabilities of the code are summarized in Appendix A). PANSYS is used to seek minimum-weight wing rib designs subject to constraints on both buckling resistance and material strength. Constraints considered in the analysis are material strength of the skin and stiffeners (covered in Section 3.1.2), buckling of the flat plate (Section 3.2.1.2) or stiffened panel assembly (Section 3.2.1.3), and local crippling of the stiffeners (Section 3.2.2). To briefly review the scope of the design study, covered in Section 2.3, four panel designs are considered: flat plate, longitudinally stiffened panel, diagonally stiffened panel, and cross stiffened panel (see Figure 6 on page 15). The number of stiffeners in the panel is varied in an incremental fashion, up to a maximum of eight stiffened cells in the X direction (Figure 8 on page 22). The design variables for the study are the thickness of the skin laminate, the height of the stiffeners, and the thickness of the stiffeners. Only one skin laminate is considered, with a quasi-isotropic lamination sequence of $[-45/45/90/0]_S$, and it is assumed that all plies are of equal thickness. A minimum-gauge lower bound of 0.040 inch is imposed on the thickness of the skin and stiffeners. Three levels of external loads are applied in uniaxial compression and pure shear: 100, 1000, and 10000 pounds-force per inch (lbf/in). A compression-shear combined-load case of up to 30000 lbf/in is also considered. Numerical design data for all optimum panel designs is documented in Appendix B. Buckled mode shapes for all panels are shown in Appendix C.

The optimization package ADS allows several choices for each of the three parts (strategy, optimizer, and one-dimensional search) of the solution procedure for the constrained optimization problem. Numerous other parameters also govern the optimization process itself, through specifying internal tolerances, bounds, convergence criteria, and so on for the algorithm. An informal study was conducted to test prospective combinations of these parameters for their performance

on the present problem. The test design was a three cell cross-stiffened panel under compression, for which several different starting designs were used. Each combination of parameters was rated on reliability (consistently converging to near-optimum), accuracy (lowest objective function, no severe constraint violations), and efficiency (least number of iterations). Based on these tests, the options chosen were Sequential Convex Programming strategy, Method of Feasible Directions optimizer, and Bounded Polynomial Interpolation one-dimensional search. It is worth noting that during this study it was discovered that there are a multitude of non-optimal designs where both panel and stiffener buckling constraints are active. In general, these take the form of a thick plate and very thin stiffeners. These heavy designs are comparable in weight to an unstiffened plate and the light stiffeners play only a token role. In the design study this region of the design space was avoided by using starting designs with thin plates and few problems of this nature were encountered.

A number of parameters governing the structural analysis of the panel must be specified. The parameters for the shape functions in the stiffener crippling analysis (N^x_w, N^y_w, $N^x_{\psi_x}$, $N^y_{\psi_x}$, $N^x_{\psi_y}$, and $N^y_{\psi_y}$) were all set to 5. This value appears to give good results and yet the analysis is still very fast. For the Lagrange multiplier method [LMM] stiffened panel buckling analysis, the parameters governing the analysis are number of constraint points K per stiffener and the number of skin deflection function terms M,N in the X,Y directions. The value of K was varied such that the inter-point distance remained approximately constant over the range of panel geometries and numbers of cells. Only odd numbers of points were used as it is most effective to have a point at the center of the stiffener. For cross-stiffened panels, the center points also force displacements of the crossing stiffeners to match. The process of choosing M and N was discussed in Section 4.1.2. An initial guess is made, depending on number of cells and loading, and the adequacy of the guess ascertained after a design has been found by perturbing each parameter. The computational cost of the buckling analysis is almost entirely dependent on the dimension $(M*N)$, so every effort was made to keep the size of this number reasonable. To summarize, several guidelines were followed in making and evaluating the design runs:

1. Number of constraint points chosen for consistent inter-point distance and good matching of skin-stiffener displacements.
2. Sufficient number of skin deflection terms used in the analysis so that panel response would not be artificially stiffened excessively.
3. Ensure that design converged sufficiently well that constraints also well converged (i.e. active, if it appears that they should be active) but not excessively violated.

The results from the design runs are now presented for the three loading configurations, in the form of structural efficiency curves for the various geometries. In this study "structural efficiency" is defined as minimum panel mass for a given load carrying capability.

5.1.1 Compression Loading

Panel structural efficiency versus the number of stiffened cells, for three levels of compressive load, is shown in Figure 31. In this figure, dotted lines represent 100 lbf/in designs, dashed lines 1000 lbf/in, and solid lines 10000 lbf/in. Individual designs are indicated by filled symbols for longitudinal (circle), diagonal (square), or cross (triangle) stiffened panels. Note that a single cell configuration is not defined for longitudinal stiffeners. Also note that comparison of the longitudinal, diagonal, and cross-stiffened panel geometries on a number-of-cells basis is somewhat dependent on how the unit cell is defined for each configuration. The flat plate design (star) is, of course, independent of the number of cells, and is shown by a horizontal line for reference purposes. As the number of cells, and consequently the number of stiffeners, increases there is a clear downward trend to the panel mass for all stiffened geometries, particularly for the heaviest loads. The minimum panel mass is achieved at all load levels, and for all geometries, by using eight stiffened cells. Although a minimum has not yet been reached, the curves are levelling off (at least for lighter loads) so that further mass reduction due to increasing the number of cells may be modest. The diagonal and cross geodesically stiffened panels are lighter than the longitudinally stiffened panel at all load

levels, although their structural efficiency advantage over the latter is reduced as the number of cells increases. At the 100 and 1000 lbf/in loads, there is little difference in mass between the diagonal and cross-stiffened panels. At 10000 lbf/in the diagonal stiffened panel is superior to the cross panel from 3 to 6 cells, but there is little difference between them after that. For eight-cell panels the diagonal geometry is lightest of all, weighing just 31%, 34%, and 38% of a flat plate for the 100, 1000, and 10000 lbf/in loads, respectively.

5.1.2 Shear Loading

A study analogous to that for compressed panels is performed for panels under shear. Because the skin laminate is assumed to be specially orthotropic (D_{16} and D_{26} are set to zero) for this study, the results do not depend on the direction of applied shear. For equal load magnitudes, the shear panel designs shown in Figure 32 are lighter than the compressed panels in Figure 31 (note ordinate axis scales are the same), particularly for a fewer number of cells. Under combined compression-shear loads, then, it would appear that the design would probably be dominated by applied compression. The minimum-weight shear configuration is still achieved, in most cases, by using the maximum number of cells. The lightest designs for the 100 and 1000 lbf/in load cases are eight cell cross-stiffened panels, which weigh 45% and 48%, respectively, of equivalent flat plates. At the lowest load intensity, the cross and diagonal stiffened panels are both lighter than the longitudinally stiffened panel. As the load is increased to 1000 lbf/in the longitudinally stiffened panel becomes lighter than the diagonally stiffened panel for eight cells only, and at 10000 lbf/in it is lighter for 3 or more cells. Longitudinally stiffened panels represent a special case here, however; in the present load analysis, it is assumed that longitudinal stiffeners have no axial load whatsoever when the panel is under pure shear. This allows them to be very thin (always at the minimum-gauge bound) and tall, which provides efficient stiffening. This configuration is not realistic for most applications as a small amount of compression applied to the panel would cause the stiffeners to cripple.

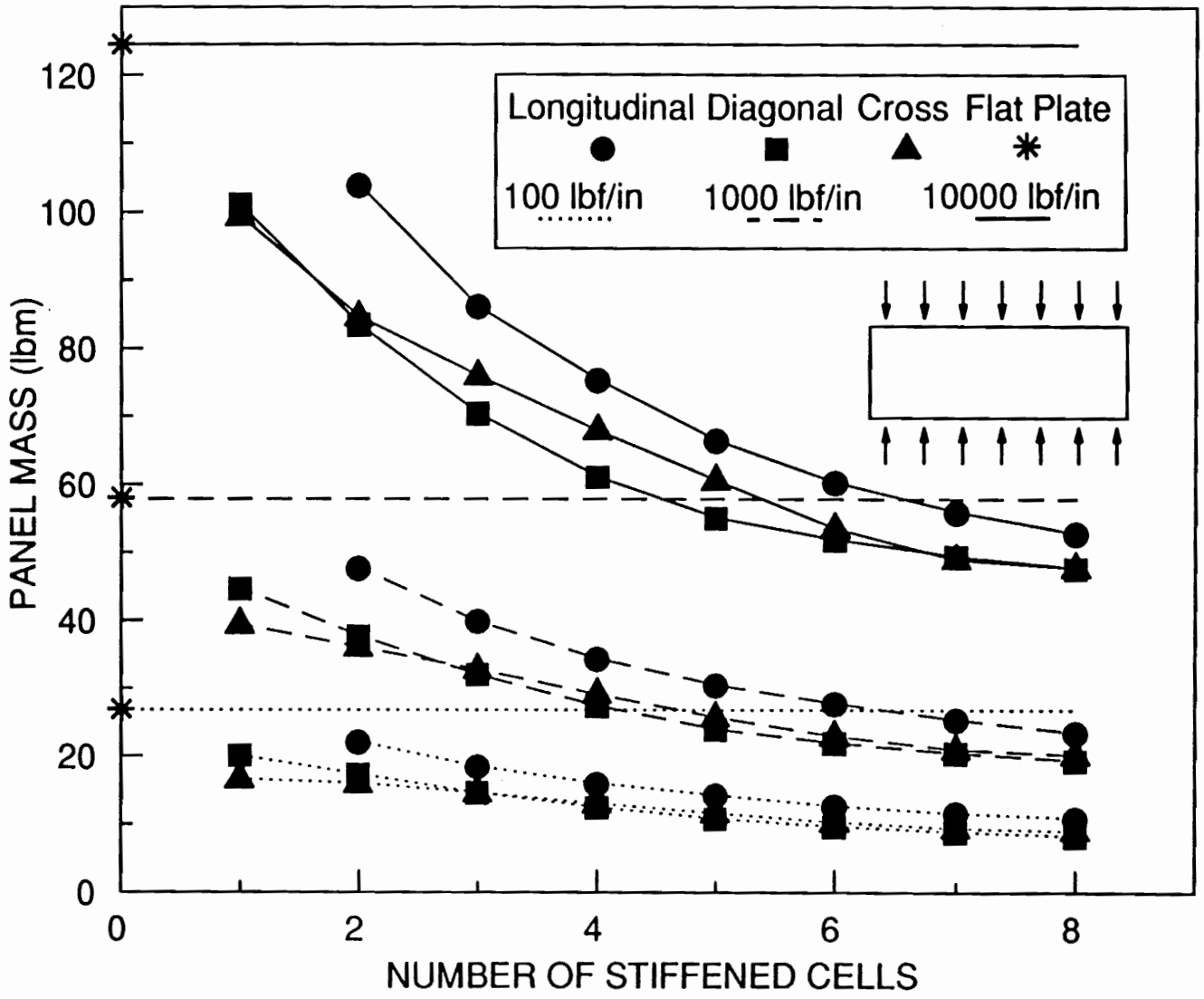

Figure 31. Structural Efficiency of Flat Plate and Stiffened Panels, Compression

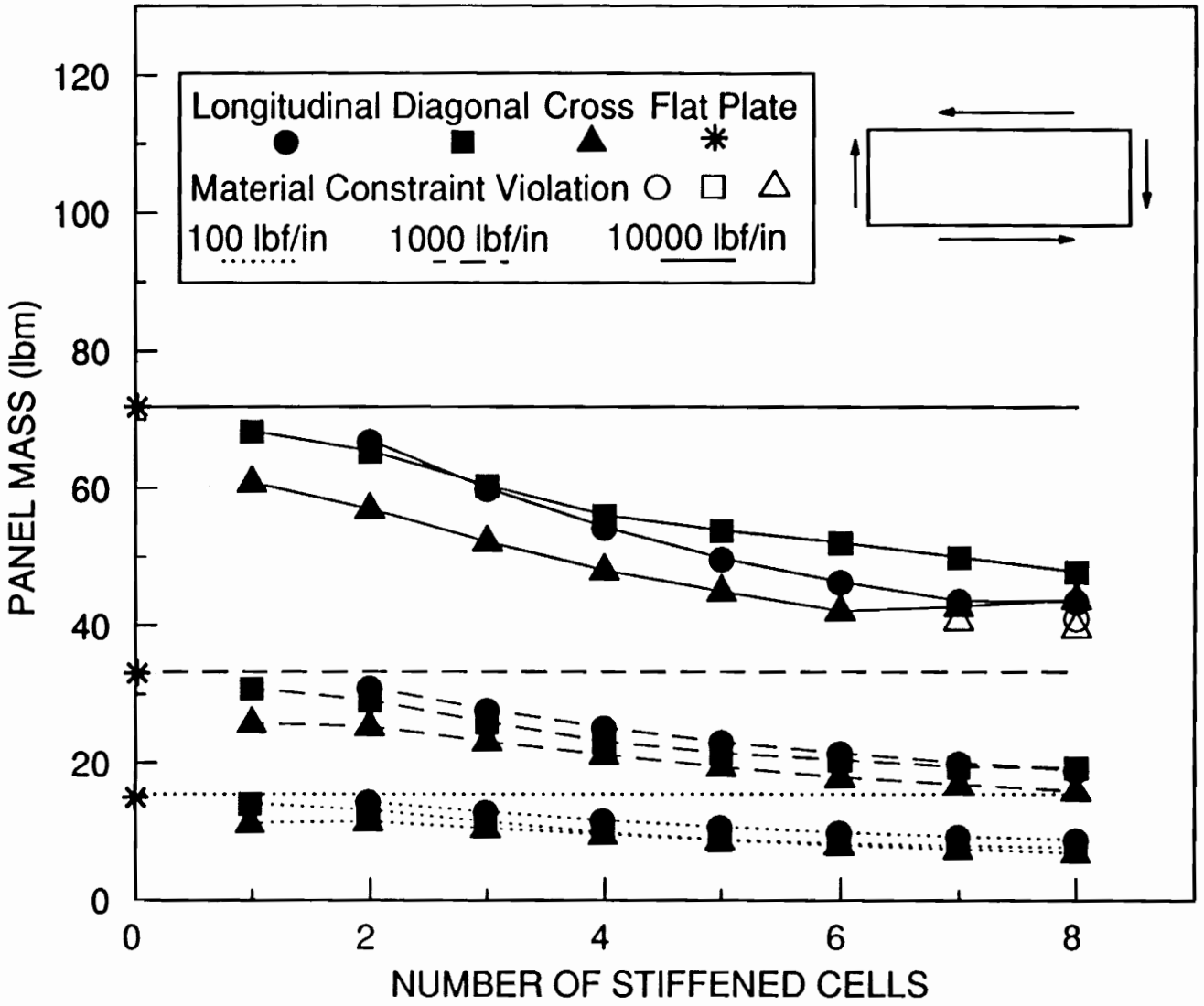

Figure 32. Structural Efficiency of Flat Plate and Stiffened Panels, Shear

The designs considered to this point have not had the material failure constraints active. For 10000 lbf/in shear loading, however, the skin material failure constraint becomes active for the seven and eight-cell longitudinally and cross-stiffened panels. (The material failure constraint is slightly violated for the eight-cell diagonally stiffened panel as well, but does not affect the design significantly). When active, this constraint forces the skin to become thicker, imposing a weight penalty on the design. The cross-stiffened panel appears to be most sensitive to changes in skin thickness, as demonstrated by the immediate reversal in the decreasing-weight trend when the skin material failure constraint becomes active. Therefore, the lightest completely feasible design (feasible designs shown by solid markers in Figure 32) for 10000 lbf/in shear is the six cell cross-stiffened panel, which weighs 59% of the flat plate. When the material failure constraint is active the critical mode is transverse tension failure of the 45° plies in the panel skin. Designs governed by this mode are generally conservative as the transverse tension mode merely indicates the onset of matrix cracking. A laminate will usually carry considerably larger loads before catastrophic failure (defined as fiber breakage) occurs. For this reason, shear panels redesigned with the skin material failure constraint removed are also shown in Figure 32, indicated by hollow markers. Both the longitudinally and cross-stiffened panels regain their former decreasing-weight trend and the cross-stiffened panel remains the lightest configuration for these designs as well.

5.1.3 Combined Compression-Shear Loading

Finally, a compression-shear combined-load case is considered. In both the previous uniaxial compression and pure shear loading cases, the trend towards minimum panel weight generally indicated using the maximum number of stiffened cells. Therefore, only an eight cell panel is studied under combined loads. The panel is subjected to equal magnitudes of shear and uniaxial compression, ranging from 100 lbf/in to 30000 lbf/in. The cross-stiffened panel is lightest throughout this range of loading, weighing just 33% of the flat plate at the lightest load and increasing to 64% of the corresponding plate at the heaviest load (Figure 33). The longitudinally and diagonally

stiffened panels are very similar in weight throughout the loading range, with the diagonally stiffened panel showing a small advantage at light loads but the converse true at heavy loads. As suggested in the previous section, the design of a combined-load panel appears to be most sensitive to the compressive loads. For example, the masses of panels designed for 1000 lbf/in compression (from Section 5.1.1) are compared with those designed for 1000 lbf/in compression-shear. The addition of 1000 lbf/in shear causes the masses of the flat plate, longitudinally stiffened panel, and cross-stiffened panel to rise by only 0.71%, 11.8%, and 9.0%, respectively. The diagonally stiffened panel is the most sensitive to additional shear, with an increase in mass of 28.6%.

For panels under pure shear, in Section 5.1.2, the skin material failure constraint became active at 10000 lbf/in. Under combined loads, however, constraint activation is delayed until the 30000 lbf/in load level. For the longitudinally and diagonally stiffened designs, only the skin material strength constraint becomes active. The cross-stiffened panel, however, has both the skin and stiffener material strength constraints active. As discussed previously, violation of the skin material strength constraint in the transverse tension or compression modes may be tolerable. However, for the combined load case, all three stiffened panels would exceed skin strain allowables in other, more critical modes as well. Of course, violation of the crossed stiffener material strength constraint would also be considered catastrophic. Therefore, no violation of material strength constraints was allowed for the combined-load designs. Making the stiffeners larger in order to satisfy the stiffener failure constraint reduced the weight advantage of the cross-stiffened design between the 10000 and 30000 load levels, but it remained the lightest nonetheless.

5.2 Interpretation of Design Study Results

In Section 5.1, optimum panel designs were presented for a flat plate, as well as longitudinal, diagonal, and cross-stiffened panels. Presenting the design data in terms of panel mass for a given

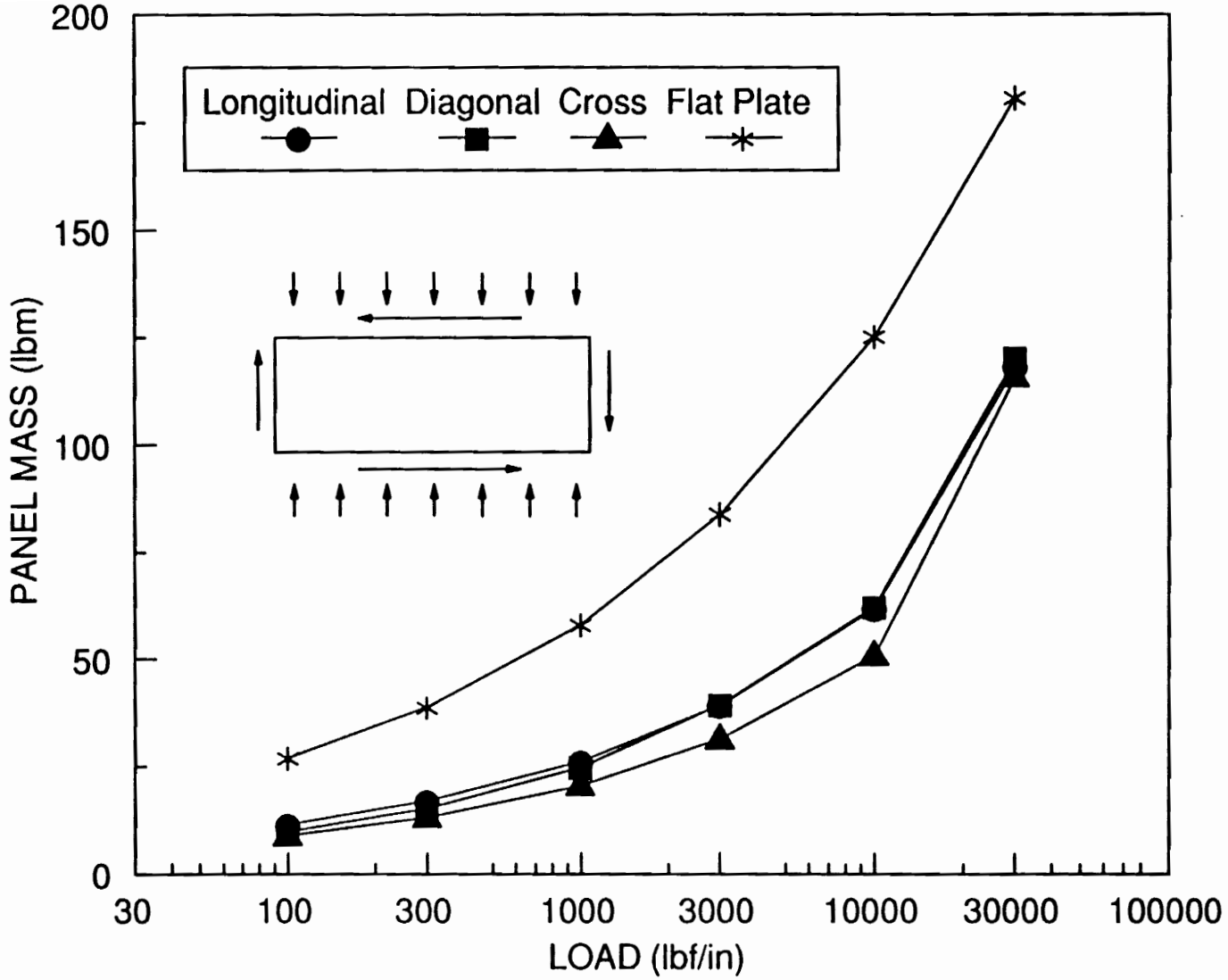

Figure 33. Structural Efficiency of Flat Plate and Eight Cell Stiffened Panels, Combined Compression-Shear

load-carrying capability provides an efficient means of choosing an appropriate panel design for a given loading regime. However, it is instructive to examine other aspects of the designs in greater detail. To this end, trends in geometric design variables and trends in distribution of load and mass between the skin and stiffeners are examined in this section.

The design variables in the present study include stiffener height, stiffener thickness, and skin laminate thickness. The trends in each of these parameters is examined in order to identify trends over the range of optimum designs. Two other factors, the distribution of panel mass and distribution of external load between the skin and stiffeners, are also considered. In this discussion, only the geodesically stiffened configurations (diagonal and cross) are considered. The longitudinally stiffened panel results are excluded for reasons to be explained shortly. For each parameter under consideration, behavior under uniaxial compression is considered first, followed by that under pure shear. The ordinate axis scales for the plots of each parameter are identical for ease in making comparisons.

5.2.1 Convergence Behavior

The results for longitudinally stiffened panels were not considered suitable to include in the parameter study for two reasons. First, for the compression-loaded panels, the stiffeners are often thicker and/or shorter than necessary due to poor convergence of the stiffener crippling constraint. Second, the longitudinal stiffeners for the shear-loaded panels are unrealistically thin as they carry no axial load. The problem for compression-loaded panels will be discussed first. For optimum structural efficiency a stiffener should have the highest aspect ratio (aspect ratio is stiffener height over stiffener thickness) possible, within the limit imposed by stiffener crippling. In optimized designs, the only valid reasons for the stiffener crippling constraint to be inactive are having the stiffener thickness design variable at its lower bound (observed for the lightly loaded panels) or the stiffener material failure constraint active (which only occurred for one design under maximum

combined loads). If the stiffener crippling constraint is not active, this implies that the same moment of inertia could be achieved by a higher, thinner, and lighter stiffener. For the longitudinally stiffened panels under compression, however, it was difficult to get good convergence on the stiffener buckling constraint. Consequently, the stiffener height and thickness design variables are not consistent design to design. This phenomenon can be explained by considering the influence of the stiffener rigidity on the buckling load of the stiffened panel. In Section 4.1.2, an exercise was performed for a cross-stiffened panel where the panel critical load was observed as a function of stiffener aspect ratio (see Figure 23 on page 112). In that example the critical load approached the maximum asymptotically; although the curve levels off appreciably, there still exists a finite slope. The buckling load for the longitudinally stiffened panel, however, reaches a certain level and then remains constant, irrespective of further increases in the stiffener aspect ratio. When the longitudinal stiffeners reach a threshold flexural rigidity, the skin of the longitudinally stiffened panel buckles in a series of inter-stiffener waves in the X direction with the stiffeners located along nodal lines. Since the stiffeners do not deflect and the effect of stiffener torsion is ignored in this analysis, as long as the stiffener flexural rigidity is above the threshold level required to enforce a nodal line, changes in stiffener rigidity do not influence the panel buckling load. Timoshenko and Gere[25] confirm this phenomenon for buckling of isotropic plates with longitudinal stiffeners, noting that the dimensions of the stiffeners should in fact be chosen such that they will "just remain straight during buckling of the plate." For the present approach, however, having the panel buckling load independent of the stiffener dimensions in certain areas of the design space appears to cause problems for the optimizer. Even though the panel buckling load is independent of the stiffener dimensions in this region, the optimizer should still attempt to reduce stiffener size to decrease the mass. However, the stiffeners make up at most 15.5% (and often less than 10%) of the total longitudinally-stiffened panel mass. Therefore, the incentive for the optimizer to reduce the stiffener mass is not that great. The two problems of "threshold" buckling and low stiffener mass appear to account for the poor convergence of the stiffener design variables for the compressed, longitudinally stiffened panels.

The behavior of the longitudinally stiffened panels under shear, as mentioned in Section 5.1.2, presents a problem different from that for those under compression. Assumptions made in the load distribution analysis cause the stiffeners to have no axial load when the panel is under pure shear. The stiffener crippling constraint then becomes meaningless and the stiffeners will always have the minimum allowable thickness. This leads to designs which may be impractical, and points to one of the dangers of optimized structures, that of off-design performance. This topic has led Stroud[67] to state that "structures tailored for a specific load condition can perform poorly in an off-design condition. Since composite materials provide additional design variables for more refined tailoring, optimized composite structures can be especially susceptible to this problem." As an example of this, consider an eight cell longitudinally stiffened panel which was designed under a pure shear load. Although this panel will carry 1000 lbf/in in shear, the thin stiffeners cripple when an external compressive load of only 30 lbf/in is applied to the panel! Therefore, since the shear-loaded longitudinally stiffened panels may have unrealistically large stiffener aspect ratios, the parameter trends for these panels are not considered.

The optimization process for the geodesically stiffened panels was better behaved than that for the longitudinally stiffened cases, but convergence problems were still experienced. The stiffener buckling constraint would often not converge to the same degree as the panel buckling constraint. The cause of this would appear to be the stiffeners making up less than 30% of the total panel mass. Although errors in the stiffener dimensions will not have a large effect on the structural efficiency, design variable trends in the figures may not always be smooth. For some geometries and loadings, problems were also experienced in achieving good convergence for the panel buckling constraint. For some designs it is believed that the critical loads for different buckling modes may be very close to each other. For example, the mode shapes for the optimally designed eight cell cross-stiffened compression designs are shown in Figure 34. The mode for 100 lbf/in has eight cell-width half-waves, which switches to an inter-stiffener mode for the 1000 lbf/in design, and back to the first mode for the heaviest load design. If mode switching behavior were to occur as design variables were perturbed in the design run, inconsistent gradient information and lack of progress on the

design would result. Imposing an additional constraint often helped convergence of the problem considerably. For example, in cases where the skin material failure constraint was active, the designs often converged to a very tight tolerance and did so within a small number of iterations.

In studying the parameter trends, it should be noted that both the panel and stiffener buckling analyses are highly nonlinear functions of the panel design variables. The analyses are more sensitive to some parameters than others, resulting in inconsistent degrees of convergence in the design variables. The skin thickness is generally the best-converged design variable, as the skin accounts for the majority of the panel mass. The panel buckling load is also highly sensitive to skin thickness, with the flexural rigidity of the skin roughly proportional to the cube of the skin thickness. The stiffener height is the next-best converged parameter, as the stiffener flexural rigidity is a function of the stiffener height cubed. Finally, the stiffener thickness is likely the least-well converged parameter. The stiffener flexural rigidity is only a linear function of the stiffener thickness, so the panel buckling load is not overly sensitive to it. Although the stiffener crippling analysis itself is highly dependent on the thickness, it has been noted that the optimization process in turn is not very sensitive to satisfaction of the crippling constraint. Another point to note is that extra care was taken to achieve the best convergence possible for the axially-loaded cross-stiffened panels. This required multiple runs for many of the designs, with changes being made in the starting designs, optimizer parameters, and analysis parameters to improve convergence. Therefore, the curves for the compressed cross-stiffened panels may tend to be smoother than those for the other cases.

5.2.2 Skin Thickness Trends

Trends in the skin thickness parameter are first examined for cross and diagonally stiffened panels under uniaxial compression. The total (i.e. not ply) thickness for the skin of the cross-stiffened (Figure 35, top plot) and diagonally stiffened (Figure 35, bottom plot) panels is shown as a function of the number of stiffened cells per panel. For both panels, the skin thicknesses decrease

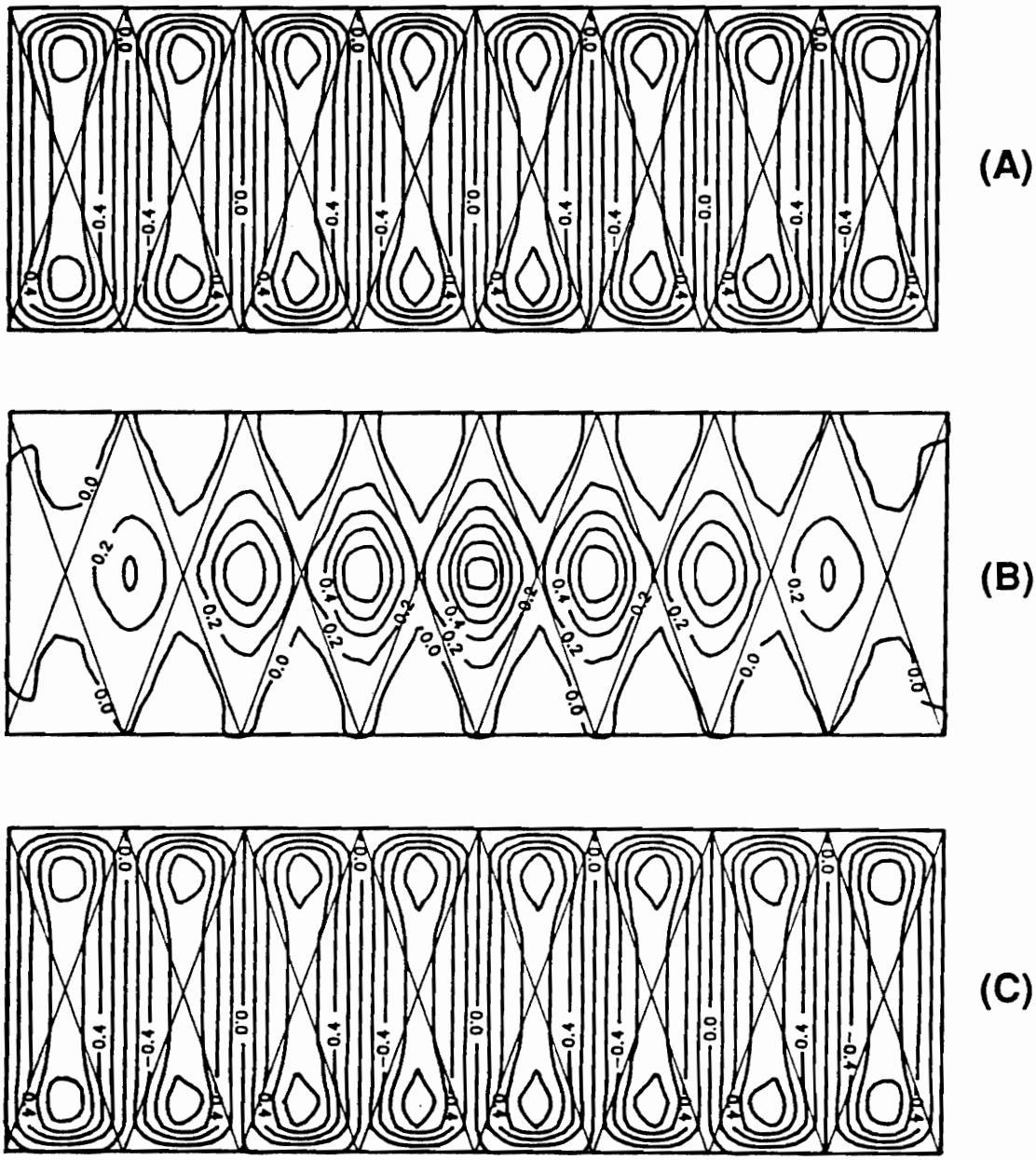

Figure 34. Change in Buckling Modes for Optimum Eight Cell Cross-Stiffened Panels, Compression: A) 100 lbf/in B) 1000 lbf/in C) 10000 lbf/in

smoothly as the number of cells is increased and all are above the minimum thickness bound of 0.040 inch. For a single diagonally stiffened cell the skin is very thick, probably due to the large inter-stiffener skin areas (see Figure 8 on page 22). The skin for the cross-stiffened single cell design, on the other hand, is not appreciably thicker than that for two cells. The triangular shapes of the skin sections in the single cell design may account for this. The percentage reduction in skin thickness as the number of cells increases is larger for more heavily loaded panels. The eight cell cross-stiffened skin thicknesses are 48%, 44%, and 39% of the single cell thicknesses for 100, 1000, and 10000 lbf/in, respectively. Values for the diagonally stiffened counterparts are 34%, 31%, and 30%. For the eight cell designs, the diagonally stiffened skins are slightly thinner than those for the cross-stiffened panels, being 92%, 89%, and 99% of the latter.

In the case of pure shear loading the skin thicknesses, with several exceptions, also display a downward trend as the number of cells is increased, as shown in Figure 36. The first deviation from this trend is a slight increase in skin thickness between one and two light and medium loaded cross-stiffened cells. This may be due to the all-triangular single cell design restraining the skin more effectively than the two cell design with a central rhombus. The second exception is the dramatic increase in skin thickness for the seven and eight cell cross-stiffened panel, when the skin material failure constraint becomes active. The skin material failure constraint also becomes active for the eight cell diagonally stiffened panel, but the increase in skin thickness is so small as to be indiscernible. The final exception is for the diagonally stiffened panel, in the area of five to six cells. This appears to be due to a change in the buckling mode of the panel. Since the change is more pronounced in other parameter trends, a discussion of this phenomenon will be delayed. Overall, the cross-stiffened skin tends to be thinner than the diagonally-stiffened skin for a small number of cells, but the two become closer as the number of cells increases. Except for the atypical trends in the 10000 lbf/in shear-loaded panels, the skins for the shear-loaded panels tend to be thinner than skins for compression-loaded panels. The difference is most apparent for a small number of cells, and decreases to almost nil for many cells.

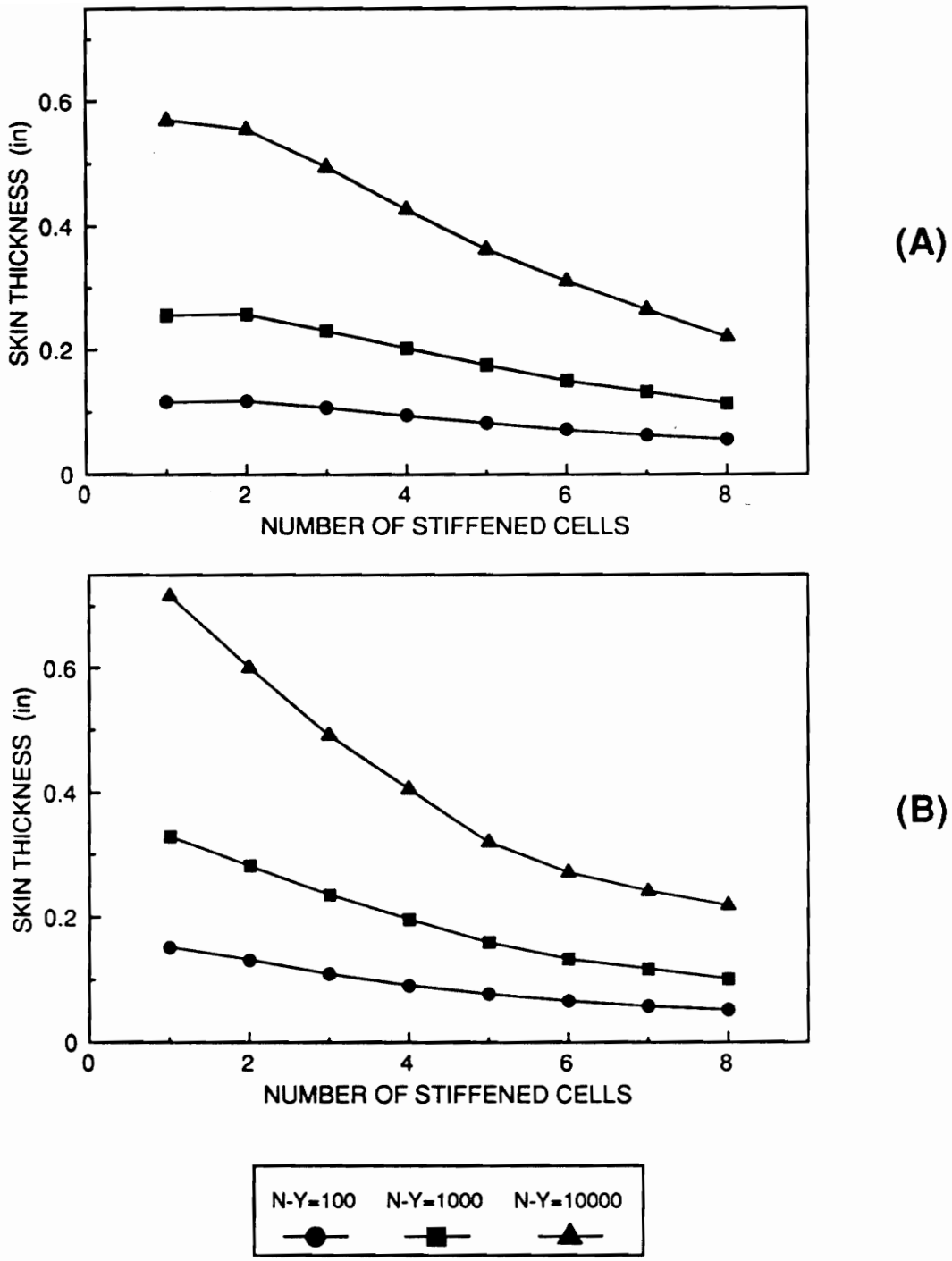

Figure 35. Skin Thickness Trends for Optimum Geodesically Stiffened Panels, Compression: A) Cross Stiffened B) Diagonally Stiffened

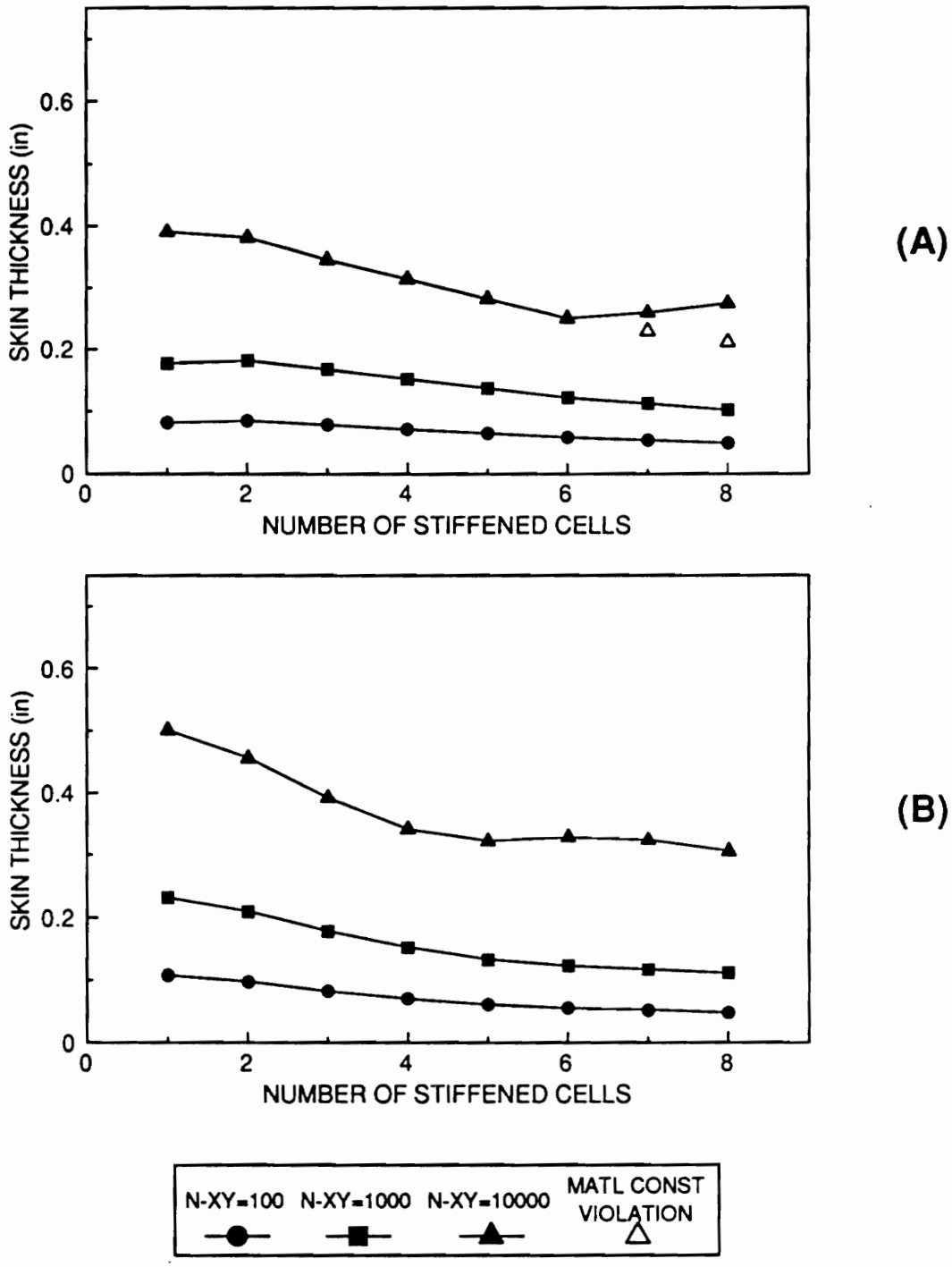

Figure 36. **Skin Thickness Trends for Optimum Geodesically Stiffened Panels, Shear:** A) Cross Stiffened B) Diagonally Stiffened

5.2.3 Stiffener Height Trends

The trends in stiffener height, again as a function of the number of cells, are shown in Figure 37 for axial compression. Stiffener heights decrease as the number of cells are increased, with the reduction more pronounced for the cross-stiffened panels. The large drop in height between one and two cells for both geometries is due to a significant decrease in stiffener length; the cross stiffener length decreases 42%, while the diagonal stiffeners decrease 30%. The decrease in length between two and three cells is only 21% and 10%, respectively, and the change becomes progressively smaller as more cells are added. The relationship between stiffener lengths and number of stiffened cells is shown in Figure 38. Two lengths are shown for cross stiffeners; overall length and effective length. The overall length is important for panel buckling considerations as this is the length of stiffener between fixed supports. The effective cross stiffener length (one-half of the overall length) is the length assumed for the stiffener crippling analysis. The overall and effective lengths are identical for the diagonal stiffeners. Returning to the discussion of Figure 37, adding cells causes the stiffeners to both decrease in length and, of course, increase in number. Therefore, each stiffener does not have to be as rigid to stabilize the skin and can therefore be lower in height. At eight cells, the cross stiffeners are 72%, 79%, and 92% of the diagonal stiffeners' height, for 100, 1000, and 10000 lbf/in. As the loads increase, it appears that the cross and diagonal stiffeners are tending to a similar height.

The plots of stiffener height versus number of cells for shear loading are shown in Figure 39. Again the trend, with some exceptions, is to lower-height stiffeners as the number of cells increases. The 100 and 1000 lbf/in cross-stiffened panels show a slight increase in stiffener height between seven and eight cells. For 1000 lbf/in, this may be due to a change in buckling mode from inter-stiffener buckling at six cells, to trans-stiffener mode for seven cells, and back to an inter-stiffener mode at eight cells (Figure 40). Both panel and stiffener buckling constraints were poorly converged for the seven cell case, which may have prompted (or resulted from) the change in mode shape. This demonstrates that the buckling modes can be very sensitive to panel geometry and design variables.

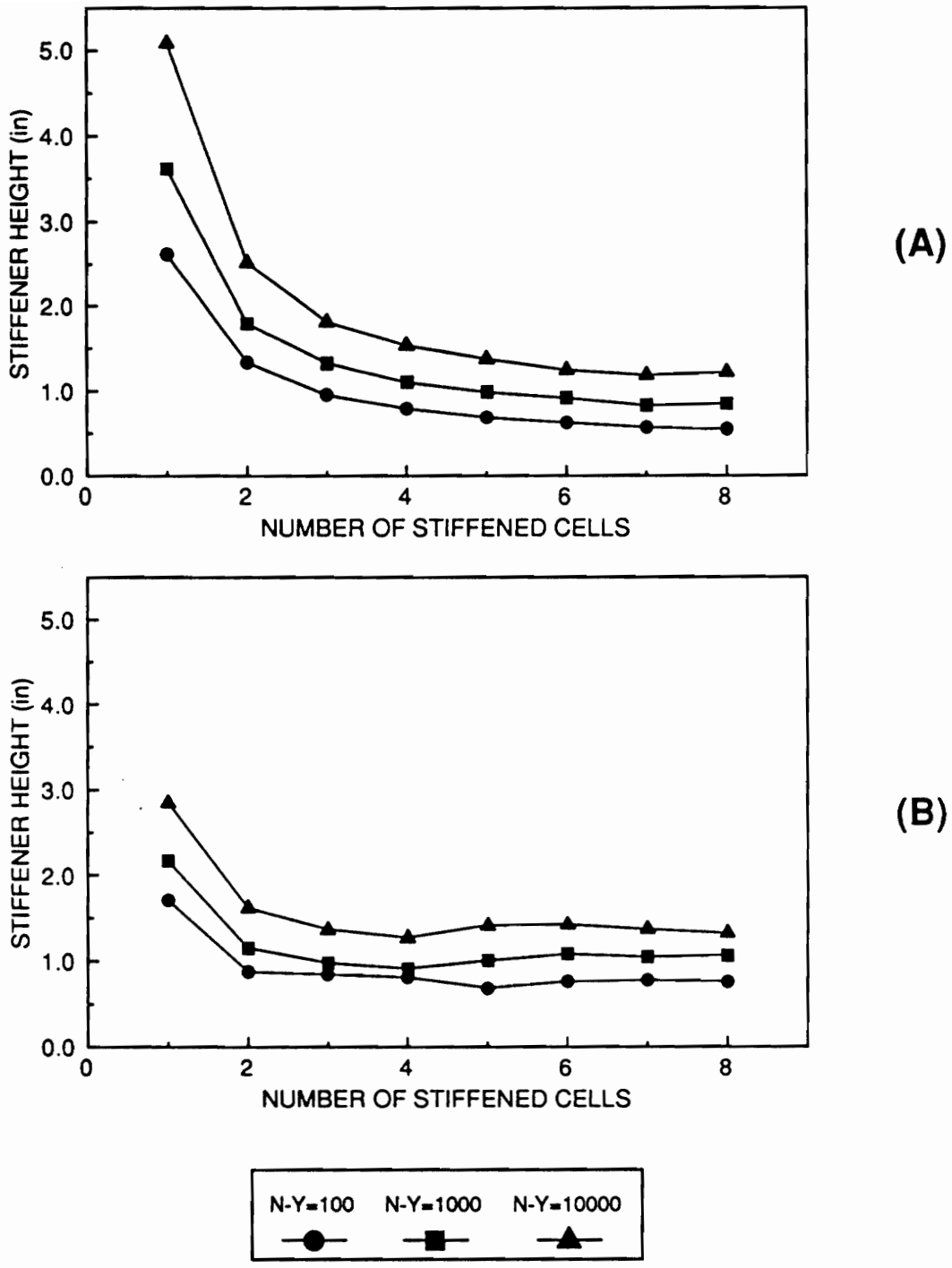

Figure 37. Stiffener Height Trends for Optimum Geodesically Stiffened Panels, Compression: A) Cross Stiffened B) Diagonally Stiffened

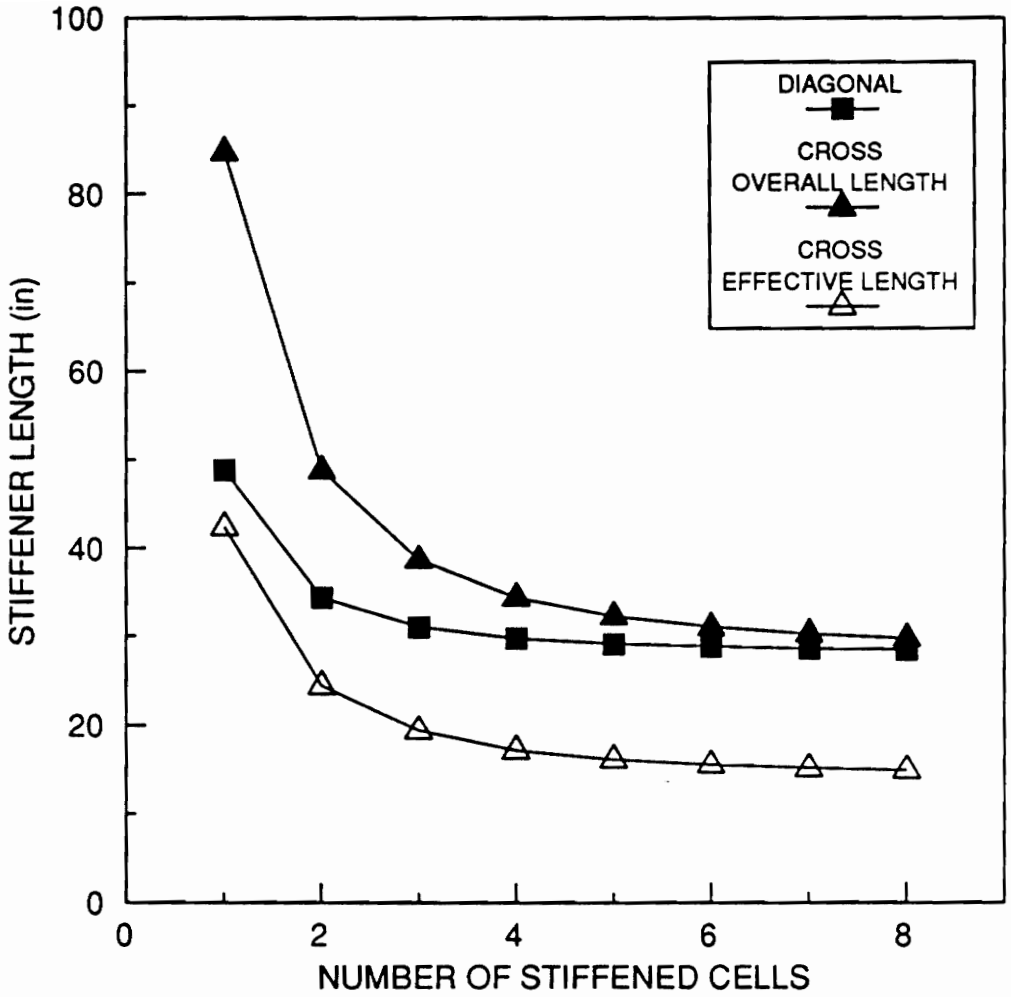

Figure 38. Diagonal and Crossed Stiffener Lengths Versus Number of Stiffened Cells in Panel

Stiffener heights for the 10000 lbf/in panel are fairly constant for more than about four cells, except when the material failure constraint becomes active. When this happens, the skin thickness increases considerably (see Figure 36), allowing the stiffeners to be reduced in size. Stiffener heights for shear-loaded panels are significantly smaller in comparison to those for compression-loaded panels. This is more apparent for a small number of cells and the difference is reduced for a larger number of cells.

The diagonal stiffener height trends for pure shear loading are somewhat more unusual. At all three load levels, the stiffeners increase in height slightly between one and two cells. Above two cells, the stiffener height for the 100 and 1000 lbf/in panels remains nearly constant. The stiffener height for the 10000 lbf/in panels actually increases up to four cells, then dramatically drops off to a height below even that for 1000 lbf/in, for seven and eight cells. It is believed that there is a fundamental change in stiffening modes between the designs for a few cells, and that for more than about four cells. In all designs, the stiffeners with tensile loads (angled upwards and to the left) enforce lines of zero-displacement in the skin. In the designs with a few cells, the compressed stiffeners are fairly rigid to limit out-of-plane displacement along this line and make the buckling mode largely inter-stiffener in nature. (Figure 41). As the number of cells increase, however, it is more efficient to allow the compressed stiffeners to deflect to a considerable degree. The buckling mode then assumes almost a full half-wave shape between the tensile-loaded stiffeners with the load carried essentially by membrane action in the skin.

5.2.4 Stiffener Thickness Trends

Trends in the stiffener thickness for compression are shown in Figure 42. For the lowest load intensity of 100 lbf/in, the stiffener thicknesses for both the cross and diagonally stiffened panels are at the minimum-gauge limit of 0.040 inch for all designs. At higher load levels, cross stiffener thicknesses decrease initially but then change little. The diagonal stiffener thicknesses show the same

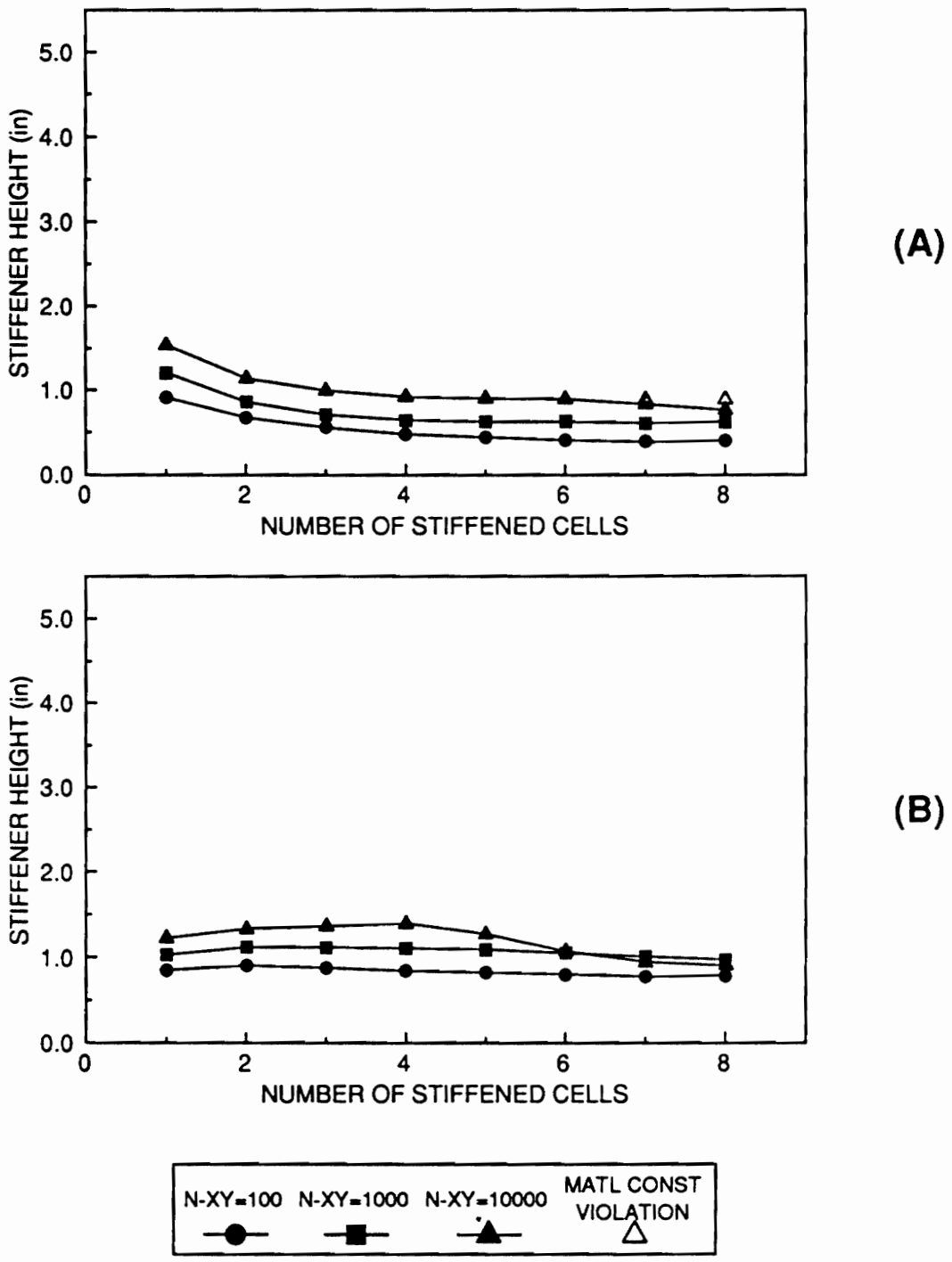

Figure 39. Stiffener Height Trends for Optimum Geodesically Stiffened Panels, Shear: A) Cross Stiffened B) Diagonally Stiffened

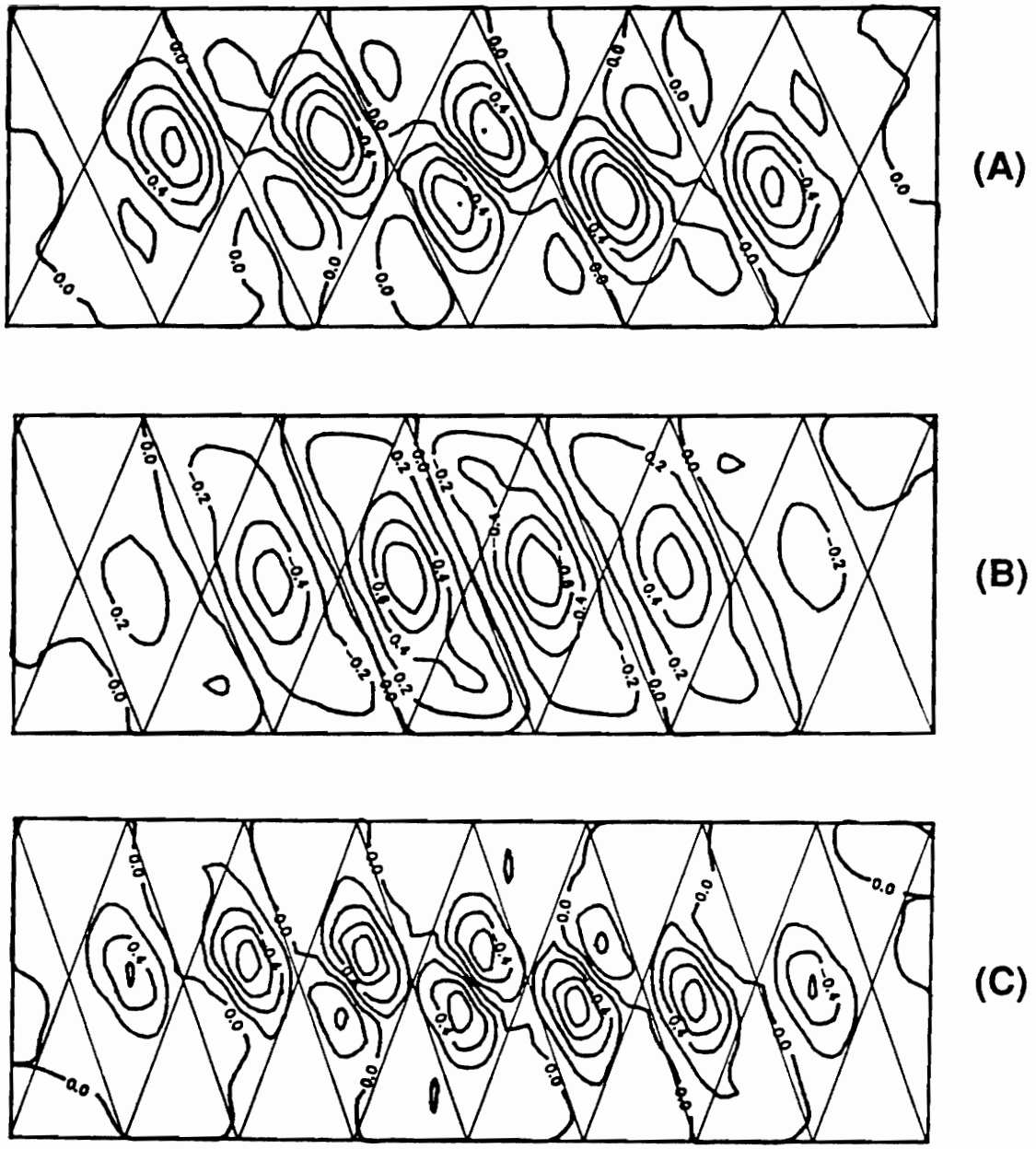

Figure 40. **Change in Buckling Modes for Optimum Cross-Stiffened Panels, 1000 lbf/in Shear:** A) 6 Cells B) 7 Cells C) 8 Cells

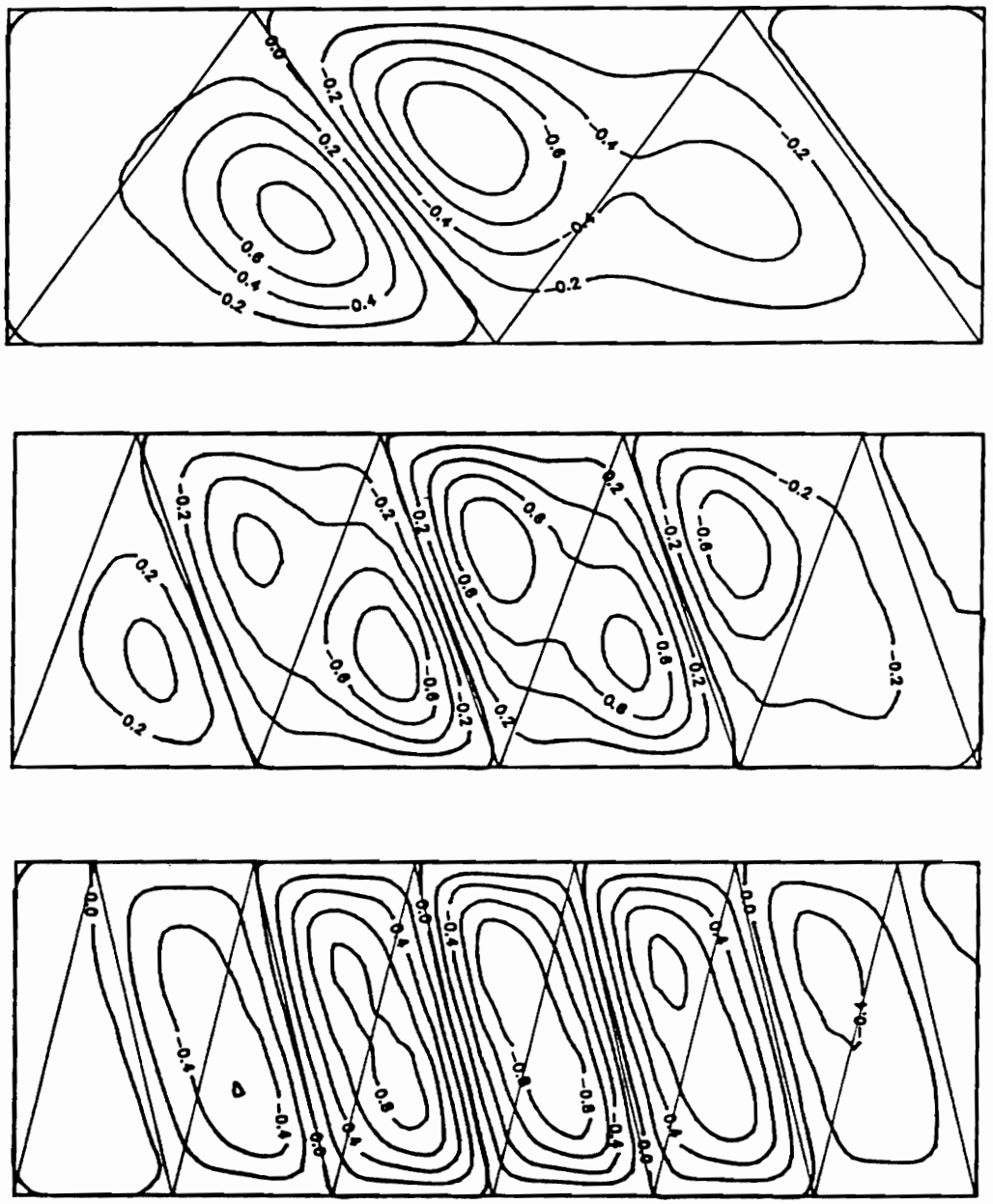

Figure 41. Change in Buckling Modes for Optimum Diagonally Stiffened Panels, 10000 lbf/in Shear: A) 2 Cells B) 4 Cells C) 6 Cells

initial decrease, but then increase again. The initial decrease is explained by the rapid drop in stiffener length as cells are first added. As explained in the previous section, when the panels have only a few cells the stiffeners are long and therefore high to have sufficient rigidity. This requires that the stiffeners also be thick to prevent crippling. After the rapid initial drop in stiffener length, it soon changes very slowly, resulting in relatively constant stiffener thicknesses. The slight increase in cross stiffener thickness for eight cells may be due to a change in buckling mode (inter-stiffener to trans-stiffener) for the 10000 lbf/in panel (see Figure 34) and poor convergence of the stiffener crippling constraint for the 1000 lbf/in panel. The increase in diagonal stiffener thickness around five cells, for the 1000 and 10000 lbf/in cases, appears to be due to a change in buckling mode. For the 1000 lbf/in panel, the mode changes from solely inter-stiffener buckling for five cells to a mode with buckling across the center pair of stiffeners at six cells. For the 10000 lbf/in panel, the mode is inter-stiffener for four cells, five full half-waves for five cells, and trans-stiffener buckling for six or more cells (Figure 43). Overall, the cross stiffeners tend to be thinner, perhaps because their effective length (distance between supports) for the crippling analysis can be as little as one-half of diagonal stiffener length.

The plots of stiffener thicknesses for shear loading are shown in Figure 44. For 100 lbf/in loads, cross stiffeners are at the minimum thickness bound for three or more cells and diagonal stiffeners are at the bound for seven and eight cells. The cross stiffeners display a more-or-less constant trend towards decreasing stiffener thickness. The flattening-off behavior above four cells at 10000 lbf/in appears to be due to a change from an inter-stiffener mode at four cells to a mode with a single elongated wave between the tensile-loaded stiffeners for five and above (including seven and eight cell material-constraint-violation cases). The six cell mode is not a clear inter-stiffener or trans-stiffener mode, but more a mixture of the two. The diagonal stiffeners show, in most cases, a decreasing-thickness trend. The thicknesses for the 10000 lbf/in panels show a dramatic dropout above four cells, similar to what was seen for the stiffener heights in Figure 39. Again, the design appears to make no attempt to limit deflection of the compression-loaded stiffeners and merely makes them heavy enough not to cripple while the tensile-loaded stiffeners enforce a nodal line.

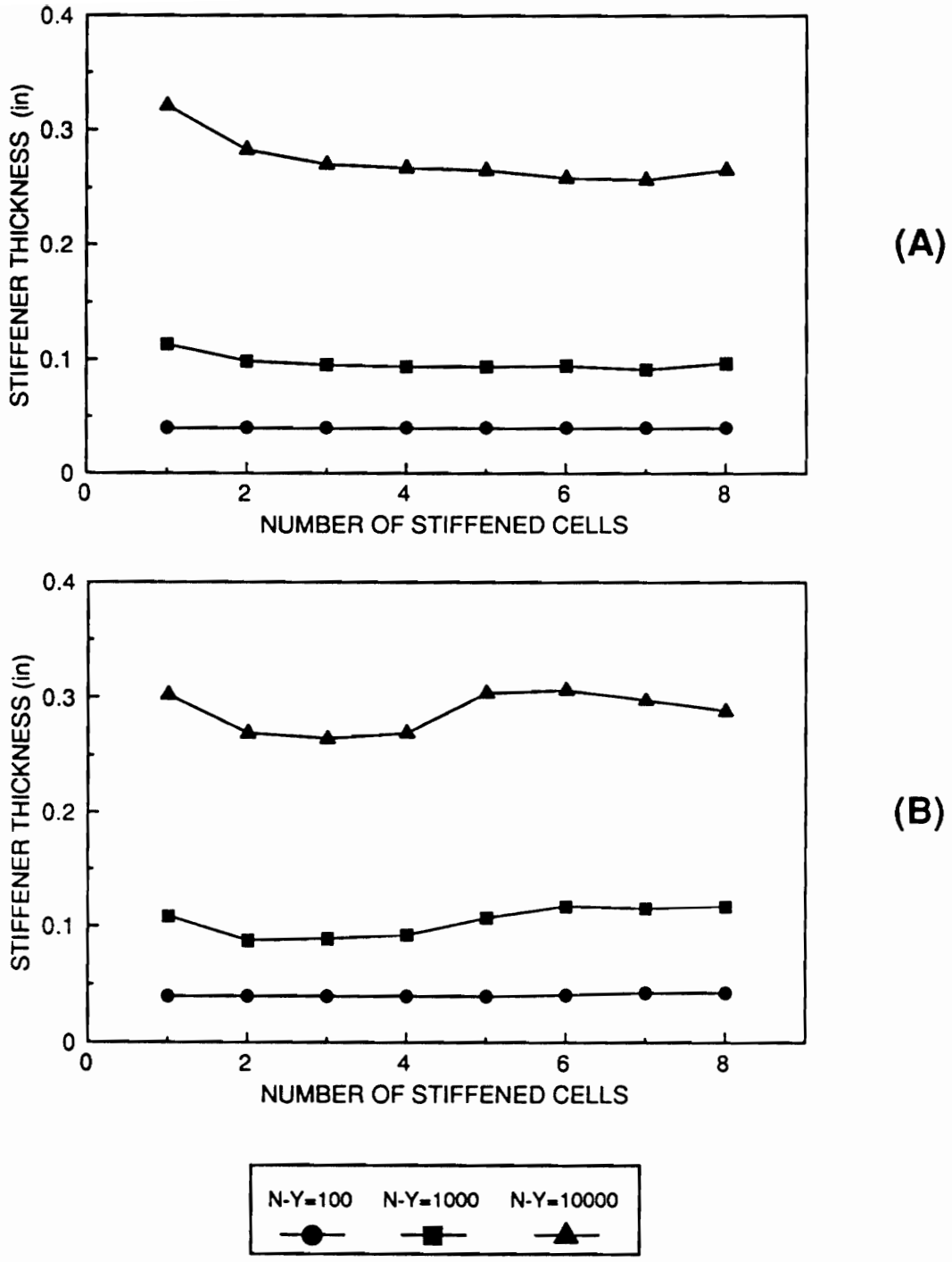

Figure 42. Stiffener Thickness Trends for Optimum Geodesically Stiffened Panels, Compression: A) Cross Stiffened B) Diagonally Stiffened

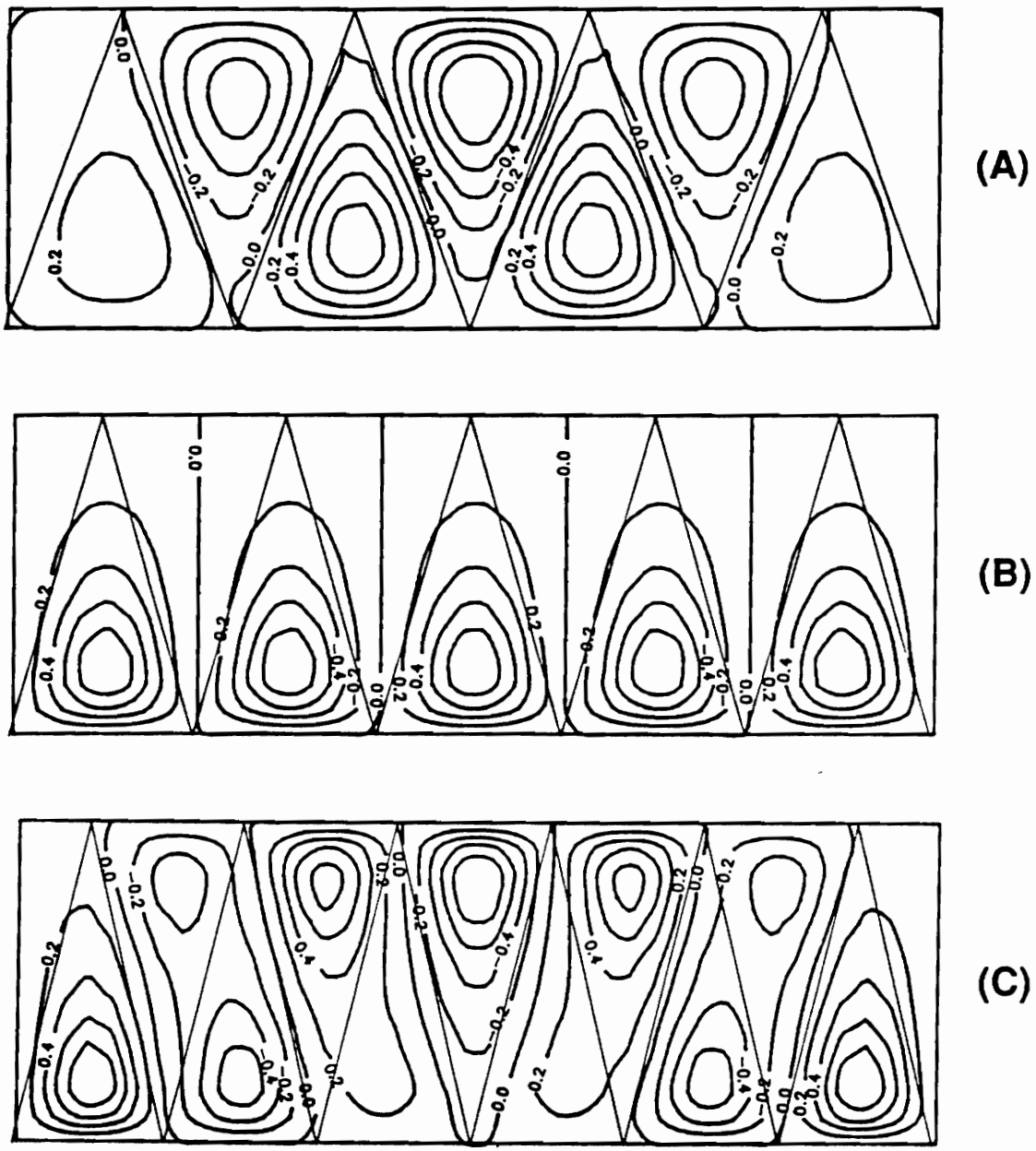

Figure 43. Change in Buckling Modes for Optimum Diagonally Stiffened Panels, 10000 lbf/in Compression: A) 4 Cells B) 5 Cells C) 6 Cells

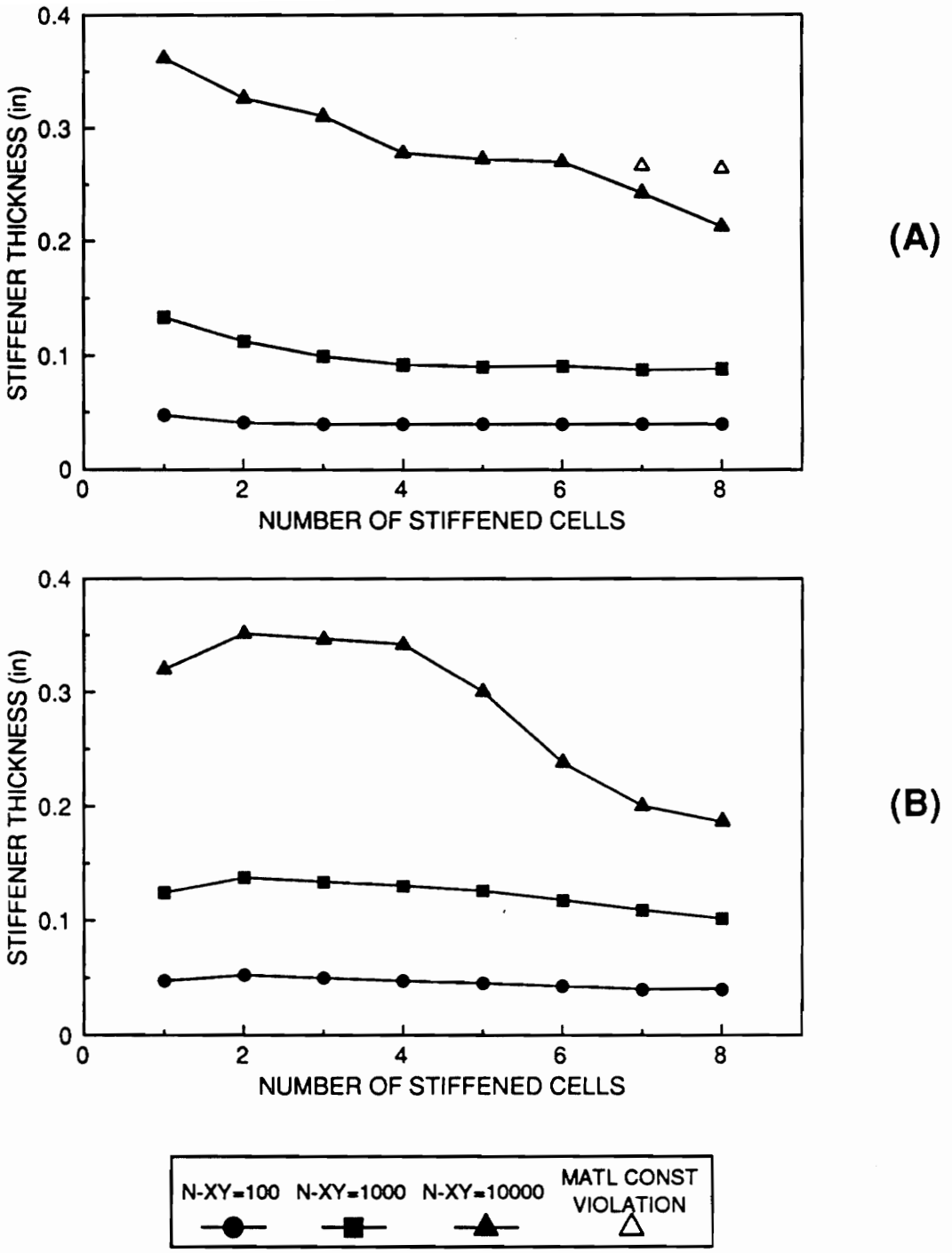

Figure 44. Stiffener Thickness Trends for Optimum Geodesically Stiffened Panels, Shear: A) Cross Stiffened B) Diagonally Stiffened

5.2.5 Stiffener Aspect Ratio Trends

The stiffener aspect ratio (stiffener height/stiffener thickness) trends are shown in Figure 45. The aspect ratio consistently decreases as the number of cells increases, for both cross and diagonally stiffened panels. The highest aspect ratios occur for the lightly-loaded panels, while the stiffeners tend towards a more square cross-section as the loads increase. For the 10000 and even 1000 lbf/in panels, the large number of stiffeners with aspect ratios below 10 indicates the need for using a higher-order theory for the buckling of the stiffeners.

The plots of stiffener aspect ratio versus number of cells for pure shear loading are shown in Figure 46. Note that the aspect ratio is again highest for the lightly loaded panels and lowest for the heavily loaded panels. The aspect ratios for shear panels do not change as markedly as those for compression-loaded panels. The cross stiffeners do show a decreasing trend as the number of cells is increased, especially for heavier loads. The aspect ratios for diagonal stiffeners, however, are nearly constant and in fact increase slightly as the number of cells is increased. Note that the aspect ratios are in general much lower for the shear panel stiffeners than the stiffeners in the compressed panels. All stiffeners for panels loaded with 1000 lbf/in shear have aspect ratios below 10, and those with 10000 lbf/in are all below 5. These aspect ratios do not fall within the ranges normally associated with the use of classical plate theory.

5.2.6 Stiffener Load and Mass Fraction Trends

A parameter termed stiffener load fraction is displayed in Figure 47. The load fraction is defined as the portion of the total applied load carried by the stiffeners; the remainder of the load is carried by the skin. The load fraction carried by the stiffeners consistently increases as the number of cells increases, for both stiffened geometries. Overall, the diagonally stiffened panels have a higher stiffener load fraction than the cross-stiffened panels. For example, for the load level of 100 lbf/in

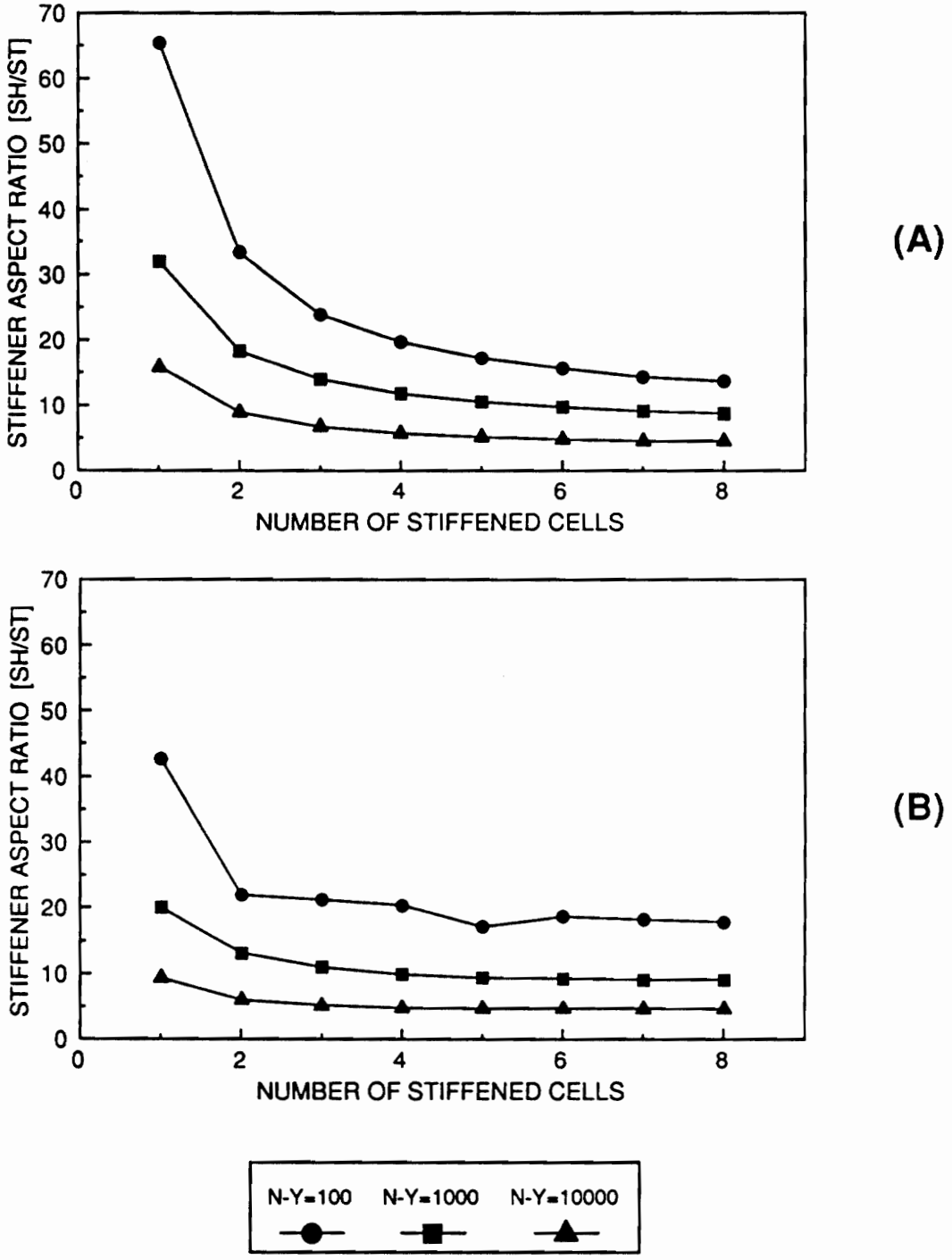

Figure 45. Stiffener Aspect Ratio Trends for Optimum Geodesically Stiffened Panels, Compression: A) Cross Stiffened B) Diagonally Stiffened

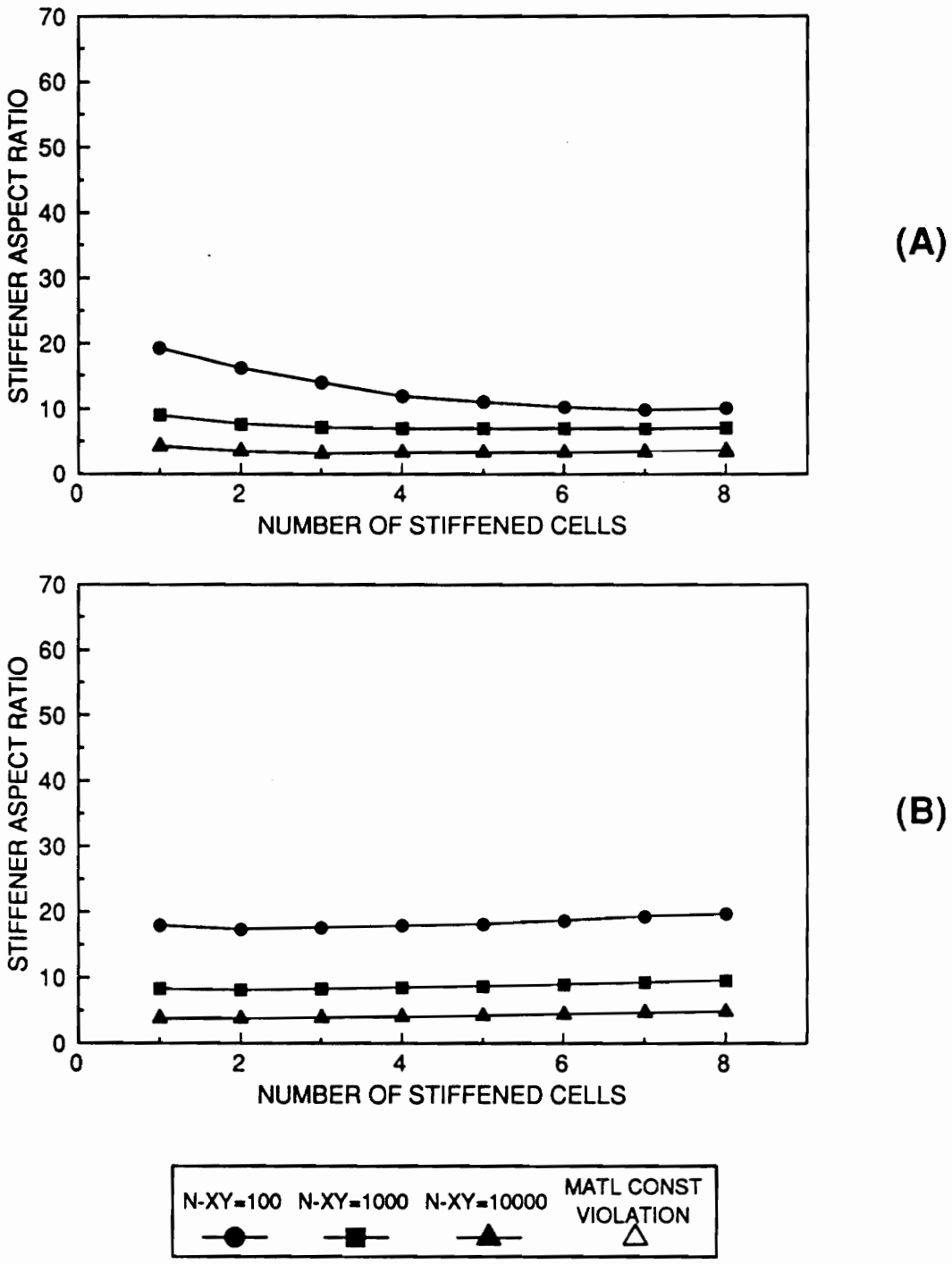

Figure 46. Stiffener Aspect Ratio Trends for Optimum Geodesically Stiffened Panels, Shear: A) Cross Stiffened B) Diagonally Stiffened

eight cell panels have 35% of the applied load carried by diagonal stiffeners, but only 23% carried by cross stiffeners. The highest level reached is that for the diagonally stiffened panel under 10000 lbf/in, with the stiffeners carrying 60% of the applied load.

The plots of stiffener load fraction for shear-loaded geodesic panels are shown in Figure 48. The portion of the load carried by the stiffeners is considerably lower than that for compression-loaded panels. The highest load fraction for the cross-stiffened geometry is 24% for a six cell panel under 10000 lbf/in and that for the diagonally stiffened geometry is 16.2% for a four cell panel under 10000 lbf/in. For 100 and 1000 lbf/in loaded cross and diagonally stiffened panels, the portion of the load carried by the stiffeners stays relatively constant. For 10000 lbf/in cross-stiffened panels, the load fraction rises between one and three cells, and then stays relatively constant (including seven and eight material-constraint-violated cells). When the skin material failure constraint becomes active, the skin is forced to become thicker, and the portion of the load carried by the stiffeners drops. For the 10000 lbf/in diagonally stiffened panels, it was shown earlier that the stiffener height and thickness decreased dramatically above four cells. This is revealed in the drop in stiffener load fraction for more than four cells. At eight cells, the stiffeners are carrying only 4.3% of the applied shear load.

The fraction of the total panel mass made up by the stiffeners, called the stiffener mass fraction, is examined in Figure 49 for compression. Except for an initial drop between one and two cells, the trend is an increase in stiffener mass fraction as the number of cells increases. The stiffeners make up a larger fraction of the panel mass for a single cell because the stiffeners are long and thus must be very robust in order to provide adequate reinforcement. The effect is more pronounced for the cross stiffeners as they are considerably longer (84.8 in) than the diagonal stiffeners (48.8 in) for the single cell. The difference in length between the two narrows considerably, even for just two cells (cross, 48.8 in; diagonal, 34.4 in), which is reflected in the mass fractions for the two geometries becoming progressively closer.

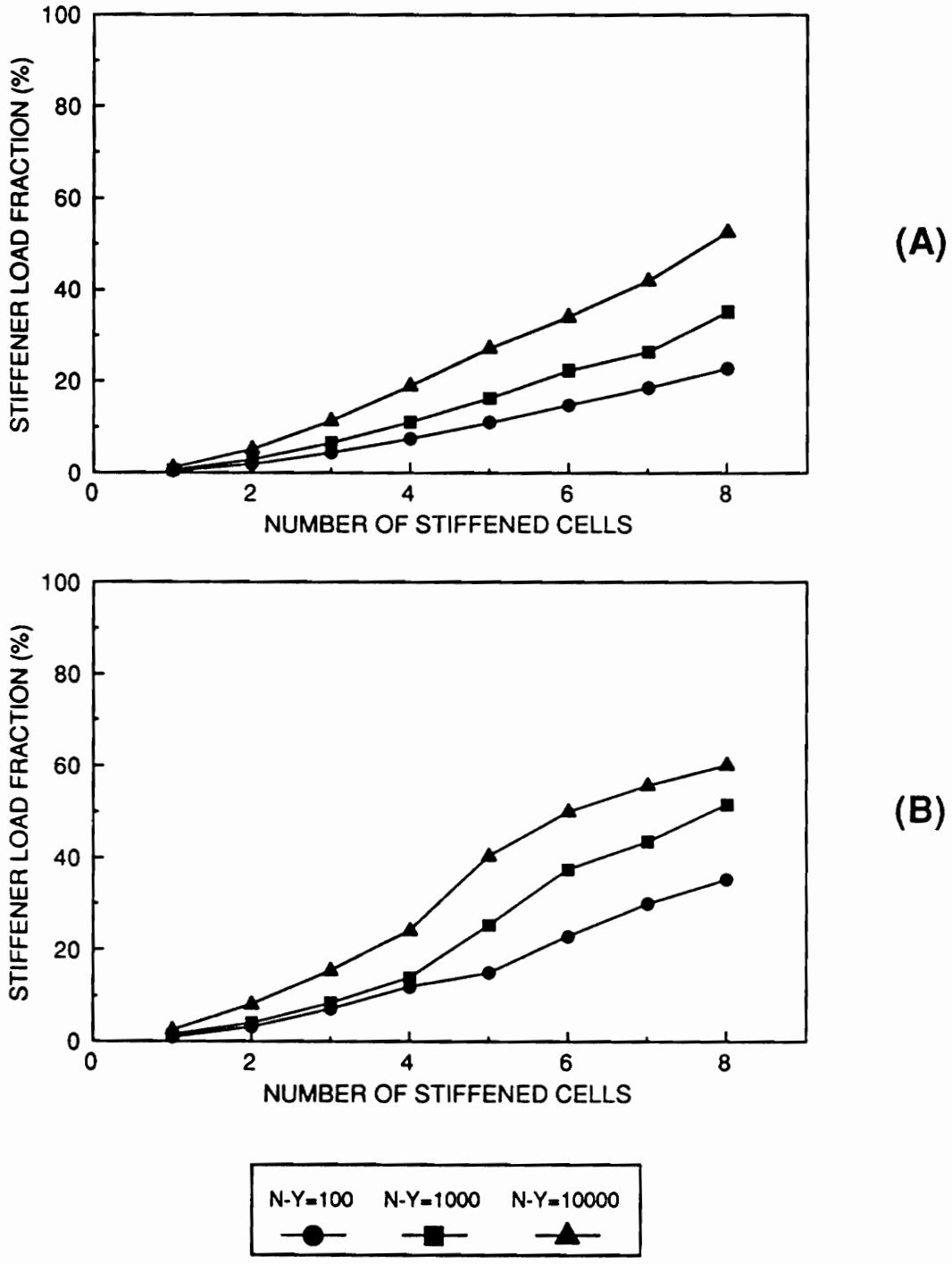

Figure 47. Stiffener Load Fraction Trends for Optimum Geodesically Stiffened Panels, Compression: A) Cross Stiffened B) Diagonally Stiffened

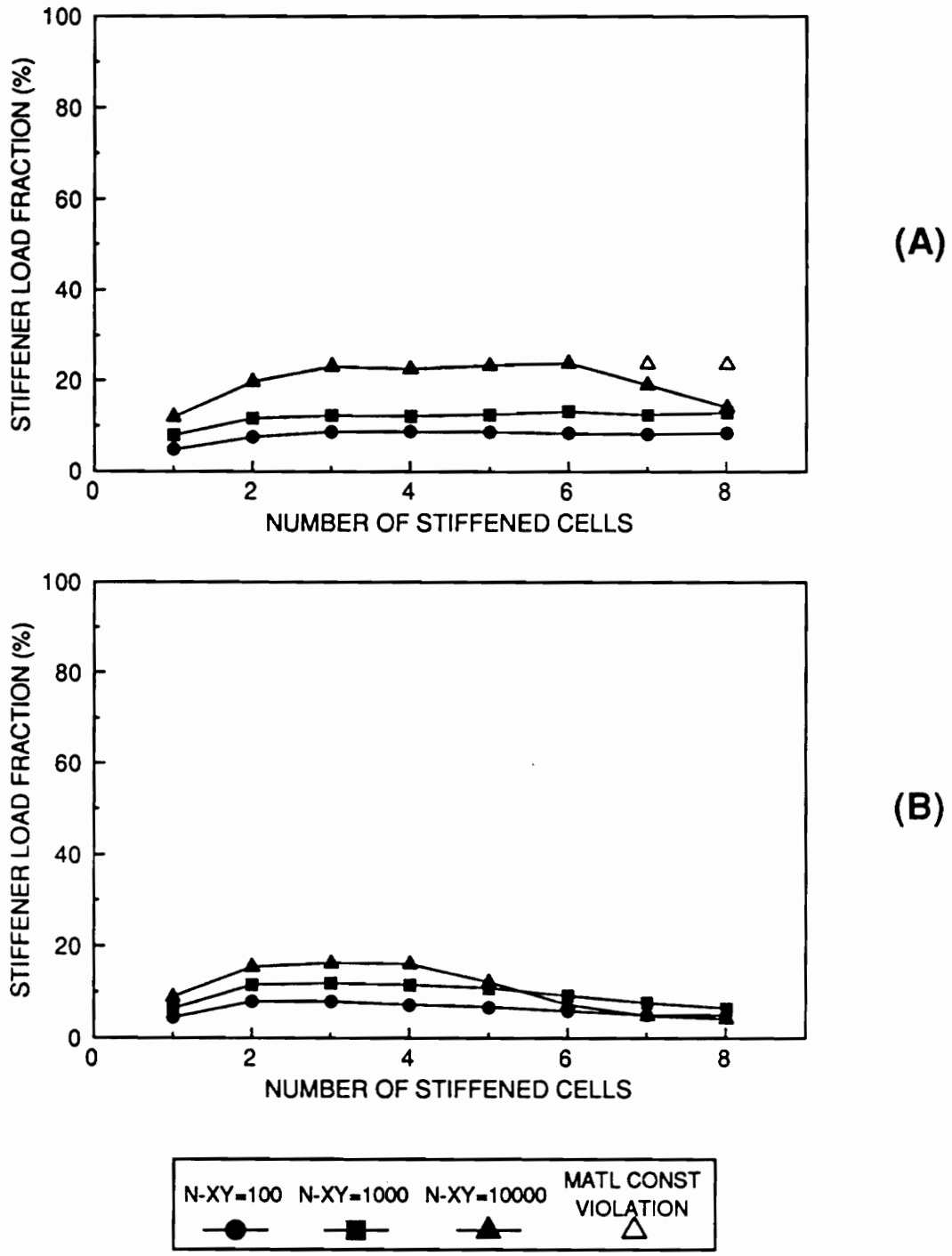

Figure 48. Stiffener Load Fraction Trends for Optimum Geodesically Stiffened Panels, Shear: A) Cross Stiffened B) Diagonally Stiffened

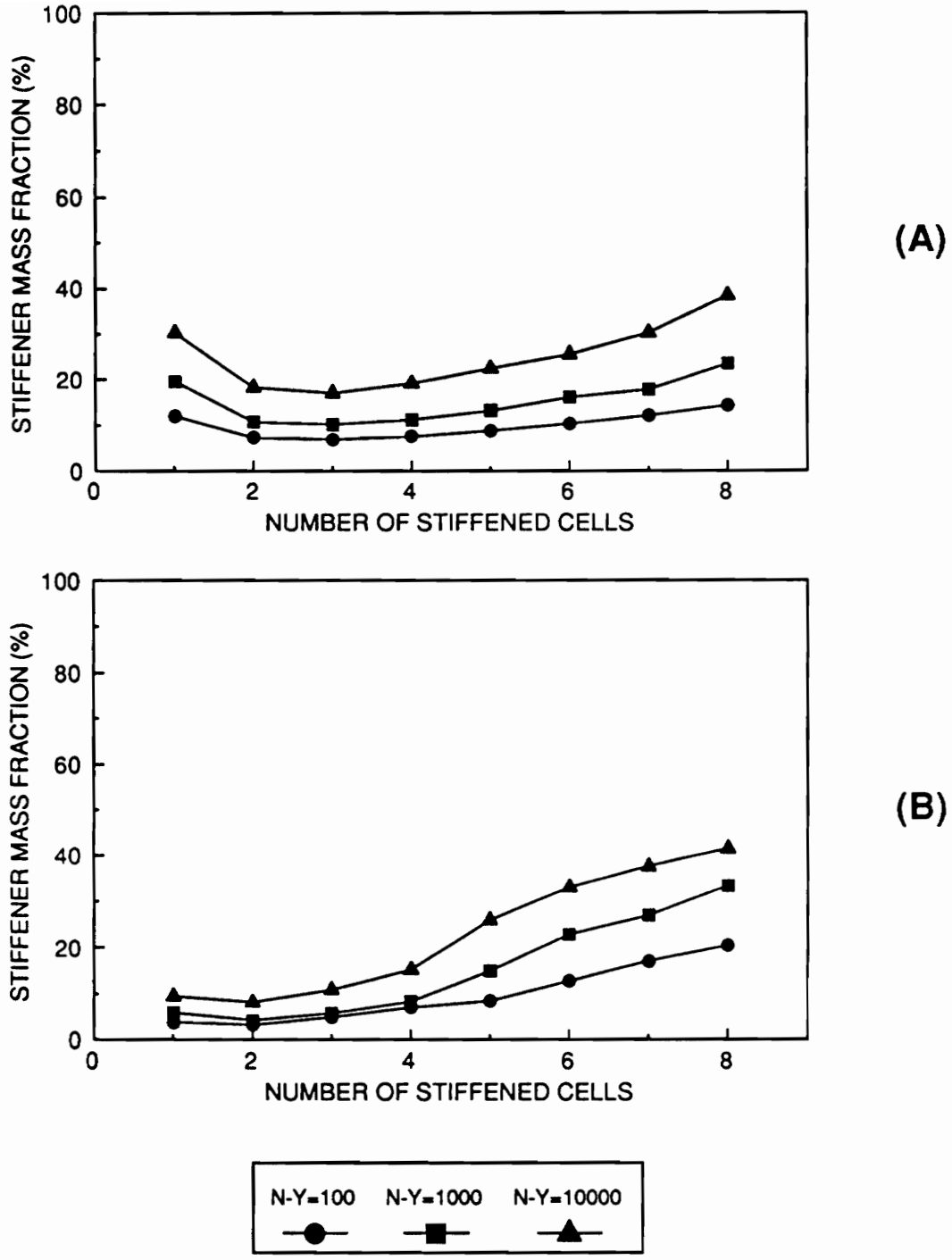

Figure 49. Stiffener Mass Fraction Trends for Optimum Geodesically Stiffened Panels, Compression: A) Cross Stiffened B) Diagonally Stiffened

Stiffener mass fractions for pure shear loading are shown in Figure 50. The cross-stiffened panels show a small initial decrease in stiffener mass fraction, between one and two cells, then a consistent increasing trend (including the material-constraint violation points). Again, as the material failure constraint becomes active, the skin becomes much thicker so the stiffener mass fraction drops off for seven and eight cell fully feasible designs. The cross-stiffened panel under heavy loads has a thinner skin than the diagonally stiffened panel and yet carries considerably more load with the skin (24% versus 7.3% for 6 cells, 10000 lbf/in shear). Therefore, the cross-stiffened panel is affected more than the diagonally stiffened panel by the skin material failure constraint becoming active. The mass fraction curves for the 100 and 1000 lbf/in loaded diagonally stiffened panels show a constant upward trend over the whole range of cells. The 10000 lbf/in curve levels off between four and five cells, drops down considerably to six, then begins to increase again. Even though the stiffener height and stiffener thickness decrease constantly from four cells and higher (see Figure 39 and Figure 44), the mass fraction is mainly dependent on the skin thickness as it comprises approximately 80% of the panel mass. The skin thickness rises slightly between five and six cells (Figure 36) and then falls decreases for seven and eight cells, accounting for the large changes in stiffener mass fraction.

5.3 Effects of Skin Laminate Geometry and Anisotropy

As mentioned in previous sections, a simplified structural analysis approach sometimes taken is to model a stiffened panel as an assemblage of plates under in-plane loads. Although this approach is approximate, it can be useful for preliminary design study purposes. In Section 3.2.1.3, the Lagrange multiplier method [LMM] analysis was introduced to predict buckling of geodesically stiffened panels. In the development, it was noted that the skin is assumed to be specially orthotropic, that is the effect of D_{16} and D_{26} terms is ignored. However, most practical skin laminates will in fact have nonzero bending-twisting coupling terms. For this reason additional insight into

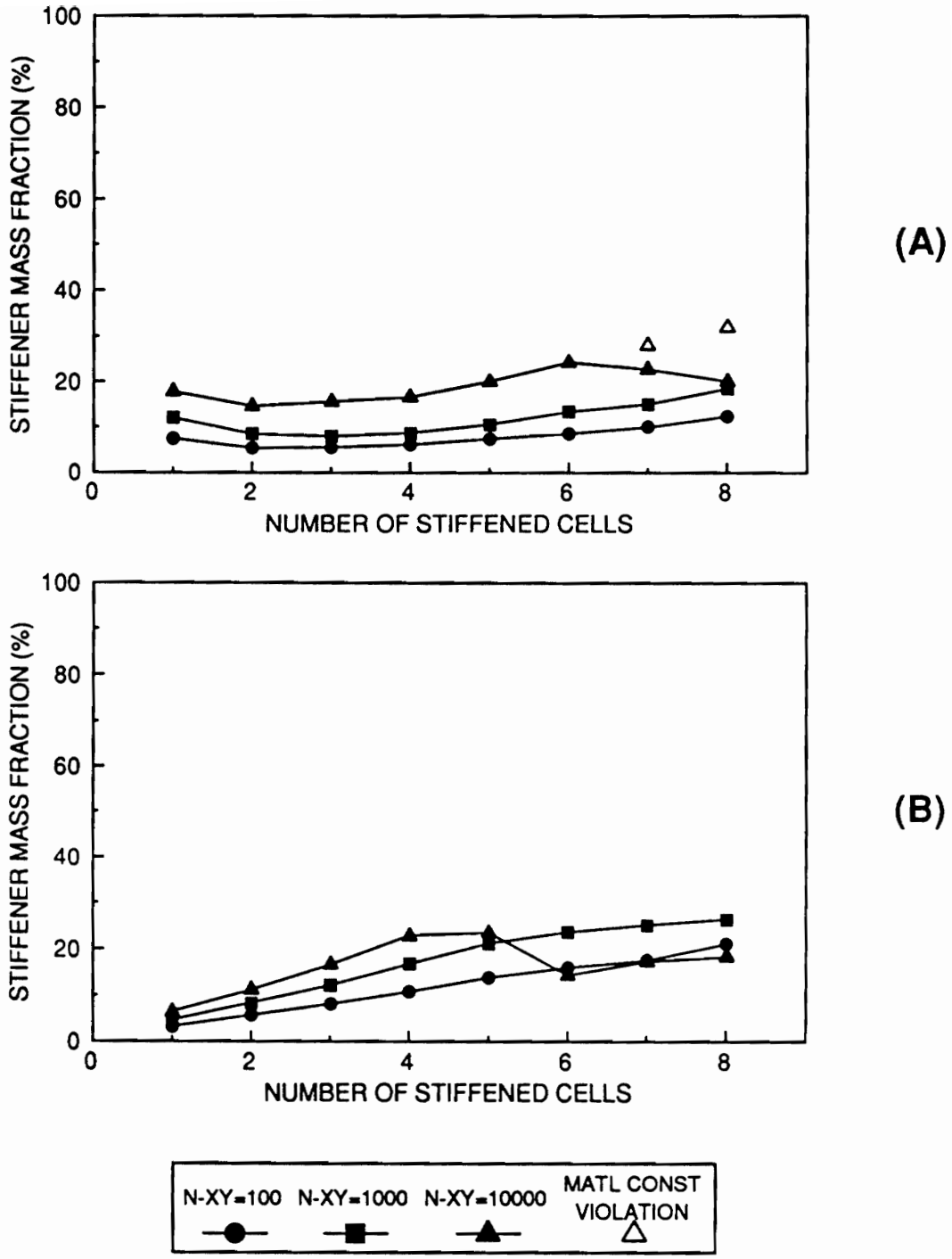

Figure 50. Stiffener Mass Fraction Trends for Optimum Geodesically Stiffened Panels, Shear: A) Cross Stiffened B) Diagonally Stiffened

the effect of these terms is sought. Therefore, one purpose in considering the stability of anisotropic rhombic plates is to gauge the effect of anisotropic effects which have been neglected in the LMM panel buckling analysis. An additional motivation for the study of rhombic plates is to isolate the effect of changing the plate shape. In the optimization of a complete stiffened panel, changes in design performance are a complex interaction of changes in multiple design variables. Therefore, examining the trends for buckling of various-shaped rhombic plates may be indicative of trends for similar skin sections in a stiffened panel. If so, it is possible that the rhombic analysis may be used to determine an optimum laminate configuration without analyzing the entire stiffened panel. However, before the rhombic plate studies are undertaken, the applicability of the rhombic plate analysis to the local buckling of a stiffened panel is examined once more.

In Section 4.2.2, a brief study examined the correlation between the LMM solution for cross-stiffened panels and the rhombic plate solution for equivalent rhombus-shaped skin sections. The panels for that study, however, had very rigid stiffeners such that the buckling deformation was virtually all inter-stiffener skin buckling. The question arises as to whether optimized panel designs have stiffeners sufficiently rigid to enforce localized skin buckling (see, for example, Panel C in Figure 22 on page 111 for compression, or Panel C in Figure 24 on page 114 for shear), or whether they are lightly stiffened and buckle in a more generalized, trans-stiffener manner (as in Panels A of Figure 22 or Figure 24), or perhaps a combination of the two. The use of the rhombic analogy implicitly assumes that the critical mode is one of local, inter-stiffener buckling of the skin. If the critical mode is more global, however, use of the rhombic analogy is not appropriate.

To address the question of rhombic plate applicability to stiffened panels, optimum cross-stiffened panel designs from Section 5.1 are examined. The stiffener aspect ratio for each optimum design is increased by a factor of four, thereby increasing the stiffeners' flexural rigidity by a factor of about 15. Since the stiffener cross-sectional areas remain the same, the load distribution between the skin and stiffeners is also unchanged. Therefore, any increase in panel buckling load is due to the increase in stiffener moment of inertia only. The relationship between compressive buckling loads for panels with optimized and rigid stiffeners, for different numbers of cells, is displayed in Table 10. Panels

designed under light compressive loads are the closest to being "rigidly stiffened" designs, as the buckling loads only differ by 3% to 4%. The panels designed under heavy loads are not as close to being rigidly stiffened, with the lowest correlation being 88%. This indicates that optimum designs are not always close to a local-skin-buckling-only condition. In fact, for most optimum designs the buckling mode is a combination of both global and local buckling. The two designs marked with a star, even though the eigenvalue agreement is close to 100%, buckle in a manner which does not result in rhombus-shaped skin sections. Their mode shapes are shown as Panels A and C in Figure 34 on page 142. Clearly, the rhombic analogy is not appropriate for these panels.

Table 10. Correlation of Buckling Loads for Cross-Stiffened Panels with Optimum and Rigid Stiffeners, Compression

	Ratio of Critical Eigenvalues $\frac{\lambda_{Optimum}}{\lambda_{Rigid}}$		
Number of Cells	$N_y = 100$ (lbf/in)	$N_y = 1000$ (lbf/in)	$N_y = 10000$ (lbf/in)
2	0.96	0.91	0.88
3	0.97	0.94	0.90
4	0.97	0.94	0.92
5	0.97	0.94	0.93
6	0.96	0.95	0.91
7	0.96	0.94	0.93
8	0.96 *	0.97	0.97 *

The relationship between optimum and rigid stiffener designs is also examined for shear loading, in Table 11. The worst correlation value of 48% points out that some panel designs may be very far away from the idealized rigid stiffener configuration. Again, the designs marked with a star buckle in a manner which does not result in rhombic skin sections. These panels have parallelogram-shaped buckled sections between the tension-loaded stiffeners, while the compression-loaded stiffeners deflect with the skin (similar to Panel B in Figure 40 on page 151). These results indicate that caution must be exercised in using discrete plate buckling results to estimate critical loads for stiffened components. However, when panels are reinforced by adequately rigid stiffeners, it may still be reasonable to estimate the effects of parameters such as anisotropy or laminate geometry using the rhombic analogy.

Table 11. Correlation of Buckling Loads for Cross-Stiffened Panels with Optimum and Rigid Stiffeners, Shear

	Ratio of Critical Eigenvalues $\frac{\lambda_{Optimum}}{\lambda_{Rigid}}$		
Number of Cells	$N_{xy} = 100$ (lbf/in)	$N_{xy} = 1000$ (lbf/in)	$N_{xy} = 10000$ (lbf/in)
2	0.96	0.94	0.93
3	0.98	0.95	0.96
4	0.97	0.95	0.95
5	0.95	0.94	0.94 *
6	0.94	0.91	0.91
7	0.94	0.91 *	0.70 *
8	0.94	0.93	0.48 *

The buckling behavior of rhombic plates as a function of plate skewness is now examined for compression, shear, and combined compression-shear loads. Critical loads for the rhombic plates are expressed in the form of the buckling parameter

$$\lambda_{CR} = \frac{N_{\alpha\beta}}{\overline{N}_{\alpha\beta} D_{22}} \qquad \alpha, \beta = x, y$$

where $\overline{N}_{\alpha\beta}$ are the specified load quantities, $N_{\alpha\beta}$ are the true critical loads, and D_{22} is the plate bending stiffness in the Y direction. Including the latter factor renders the results independent of plate thickness. As the rhombic plates represent the rhombus-shaped skin sections of the cross-stiffened panels, appropriate values for the rhombus interior angle and side length (shown in Table 8 on page 125) are specified for a given number of cells. As discussed in Sections 3.2.2 and 4.2, the present formulation allows two forms to the solution: the Standard method, which provides an over-estimate to the critical load, and the Kennedy method, which is believed to provide an underestimate. Unless specified otherwise, the rhombic buckling load used in this section is the mean of the values predicted by these two methods, and 13 terms are taken in the deflection series. Solutions for both fully anisotropic and specially orthotropic plates are easily found by either including D_{16} and D_{26} terms in the analysis or setting them to zero, respectively. The latter condition

of special orthotropy is assumed in the LMM panel buckling analysis, and so represents the baseline for determining anisotropy effects.

The behavior of a rhombic plate is first examined under compression. Although the stiffened panels in this study have uniaxial compressive applied loads, the skin of the panel is under biaxial compression due to the X direction zero-displacement boundary condition and the Poisson effect. The compression results for orthotropic and anisotropic plates under the equivalent biaxial compressive load are shown in Figure 51. Looking first at the orthotropic solution (denoted by solid line), it is clear that skewing the rhombic plate (i.e. equivalent to increasing the number of cells) increases the critical load considerably. The buckling load for the eight-cell equivalent plate is 8.0 times higher than that for the two-cell plate. This could account, in part, for the large reduction in skin thickness displayed by the compressed, cross-stiffened panels when the number of cells was increased (see Chart A of Figure 35 on page 144). Comparing the orthotropic (solid line) and anisotropic (dashed line) solutions in Figure 51, material anisotropy causes an almost negligible drop in load. The anisotropic solution is 0.05% below the orthotropic solution for two cells, increasing to a still-small 0.6% drop at eight cells.

The rhombic buckling results for pure shear loading are shown in Figure 52. Considering the orthotropic solution (solid line), the skewing effect increases the buckling load of the eight-cell plate 5.5 times over the two-cell geometry. Since an eight-fold increase was seen for compression, it appears that skewing does not influence the critical load for shear as much as it does for compression. Indeed, the skin thickness reductions for cross-stiffened designs did not decrease as markedly for shear (Chart A of Figure 36 on page 146) as for compression (Chart A, Figure 35). In Figure 52, it is important to note that the solution for orthotropic plates is independent of the direction of applied shear. Including anisotropy in the shear analysis of the rhombic (and other) plates not only alters the predicted critical load, but also makes the solution sensitive to the direction of shear. For the present ply orientation and load direction conventions (see Figure 5 on page 14), the plates buckle at lower levels of positive shear (lower, dotted curve in Figure 52) than negative shear (upper, dashed curve). Mathematically it is the existence of bending-twisting coupling

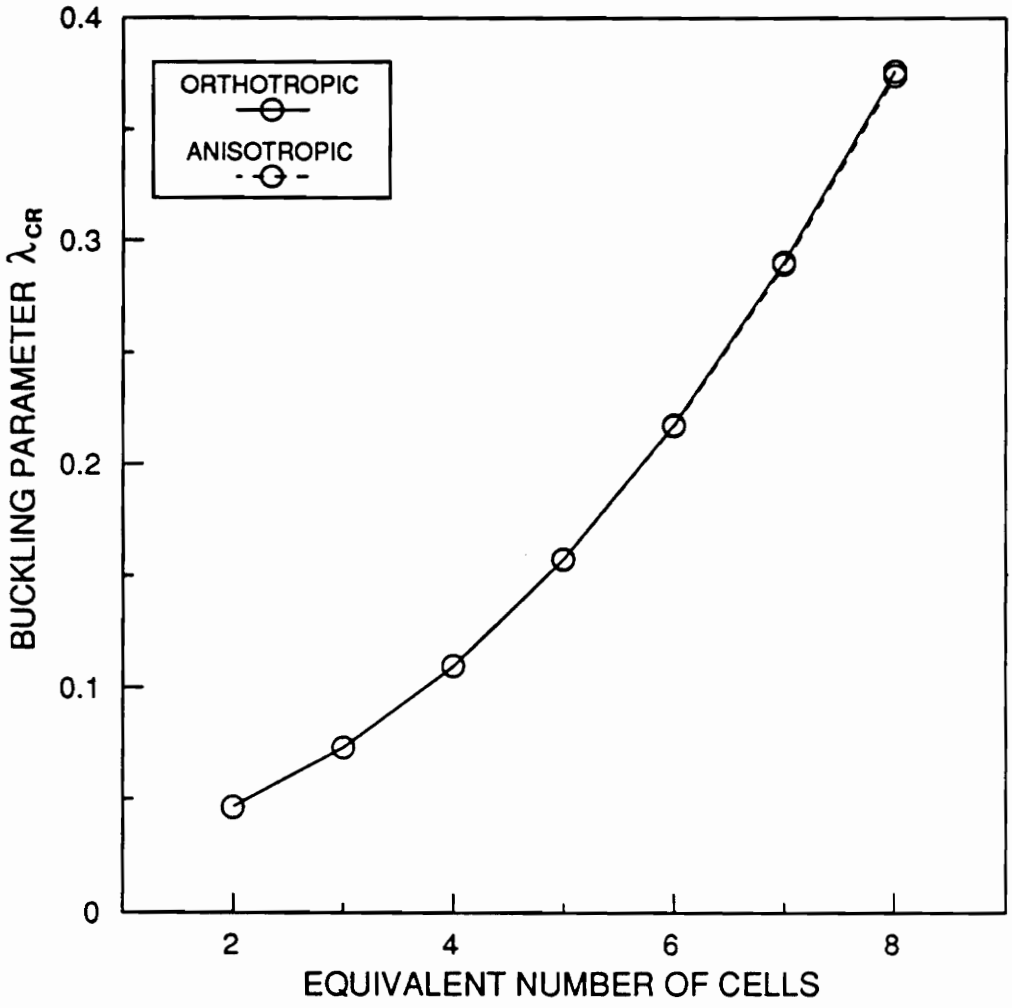

Figure 51. Rhombic Plate Buckling Load Versus Equivalent Number of Stiffened Cells, Compression

terms D_{16} and D_{26} which account for this behavior. Physically the phenomenon can be explained by the relative positions of the $+45°$ and -45° plies within the stacking sequence. The maximum shear buckling load is achieved when the outermost 45° ply is in fiber-direction compression. Obviously this directional dependence is important in the design of the wing rib if it is to see reversed shear loads. The effect is minimized as the number of plies in the laminate increases and if $\pm 45°$ ply pairs are interspersed through the thickness. Unfortunately, many of the optimized designs in this study have thin skin laminates with only a few plies, which may mean that coupling effects cannot be reduced significantly. In general, the anisotropic shear buckling loads deviate about 17-18% from the orthotropic solution. Under positive shear, the anisotropic buckling load for the two-cell plate is 18.0% below the orthotropic buckling load, decreasing slightly to a 17.5% drop for the eight-cell plate. For negative shear, the corresponding differences are 17.9% and 17.0%, but the anisotropic values are above the orthotropic.

Buckling of the rhombic plates under equal combined compression and shear loads is considered in Figure 53. From Figure 51 and Figure 52 it is known that a given rhombic plate will buckle under a compressive load which is only 30-40% of the critical shear load. Since the plates are more sensitive to compressive loads, the plate response should be dominated by the amount of compression applied, which in fact is the case. Comparing Figure 53 with Figure 51 clearly indicates that the addition of shear has virtually no effect on the critical load of the compressed plate. The increase in critical load due to skewing the plate from the two to the eight-cell geometry is 7.9 times, which is very close to the value of 8.0 for pure compression. Furthermore, the appreciable anisotropy effects shown in Figure 52 for pure shear loading are suppressed to a large degree. The maximum deviation from the orthotropic solution is now only -3.1%, for the eight-cell plate under positive shear.

One topic related to laminate optimization is now discussed briefly. As noted earlier, optimized stiffened panels may be restricted to very thin skin laminates. Besides having a limited number of plies to begin with, opportunities for altering the skin layup may be further restricted by strength, stiffness, damage tolerance, or other considerations. Since the present skin laminate is quasi-

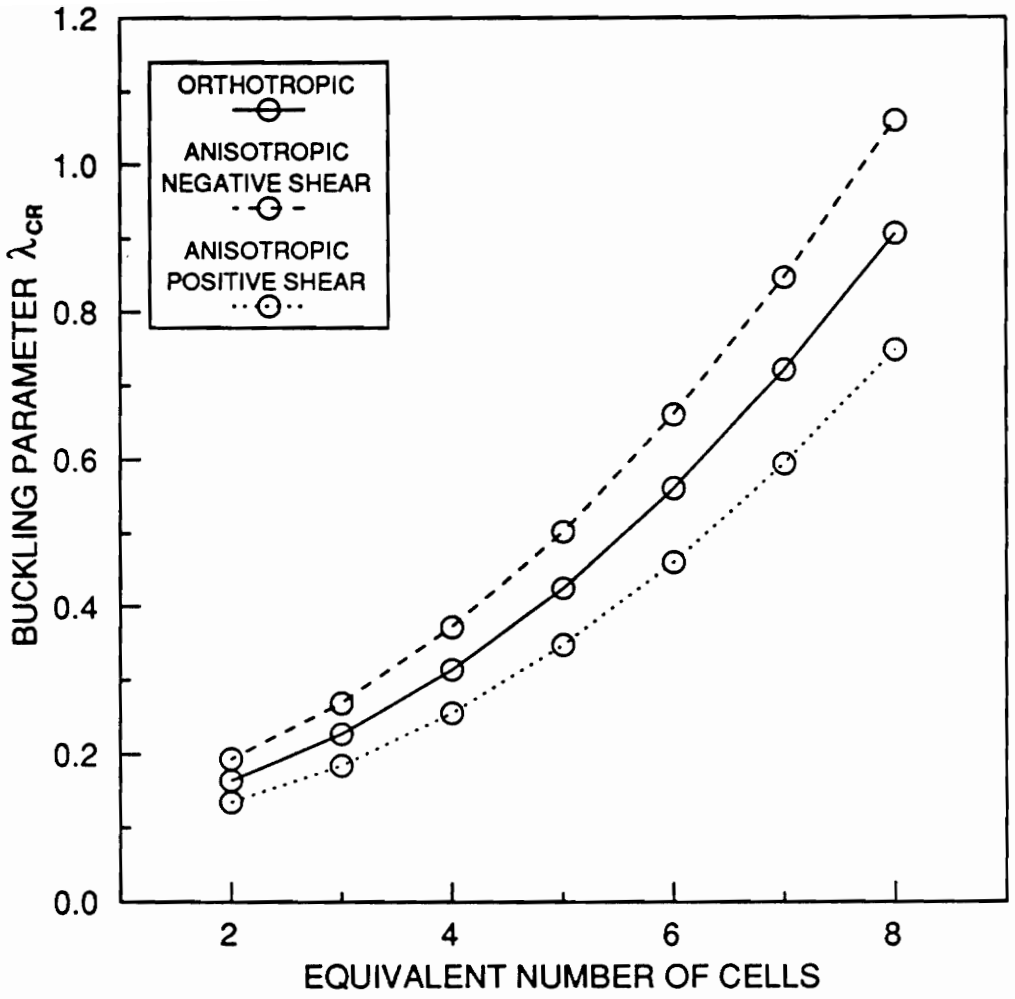

Figure 52. Rhombic Plate Buckling Load Versus Equivalent Number of Stiffened Cells, Shear

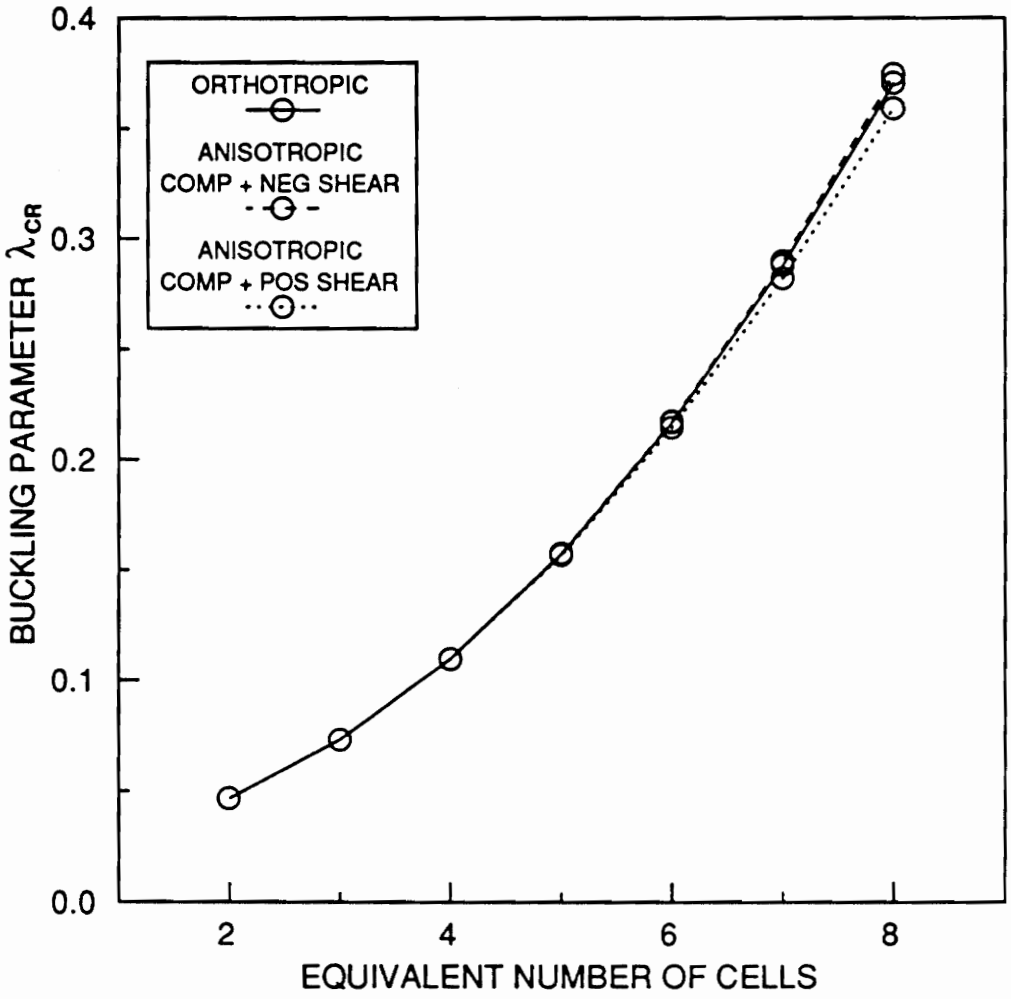

Figure 53. Rhombic Plate Buckling Load Versus Equivalent Number of Stiffened Cells, Combined Compression-Shear

isotropic, it has no preferred in-plane stiffness directions. Therefore, the entire laminate can be rotated without affecting the in-plane elastic response. Rotating the laminate will, however, have considerable impact on the out-of-plane response. It is well known that the shear-buckling response of laminates is dependent on the magnitude of the bending-twisting coupling terms D_{16} and D_{26}, which change with laminate orientation. For rhombic plates it has been demonstrated that the shear-buckling response of rhombic plates is also dependent on the degree of skewness. Laminate orientation is examined within the context of rhombic plate shear-buckling to determine the worst-case error which might be incurred by ignoring anisotropic coupling effects (i.e. assuming that $D_{16} = D_{26} = 0$) for the present laminate. A second objective is to determine if there are any advantages to be gained through laminate rotation.

Three rhombic plate interior angles α of 90°, 120°, and 150° are considered in the study. The $[-45/45/90/0]_S$ laminate is rotated through the range of 0° to 180° by 7.5° increments for each rhombus; the response for the 180°-360° interval is identical. The anisotropic buckling loads under positive and negative shear and the orthotropic buckling loads are computed through the range of laminate orientations. Due to the large number of analyses involved, the Standard analysis with 9 series terms is used for computational economy. The critical loads as a function of laminate orientation are shown in Figure 54 for the three rhombus angles. Note that the ordinate axis scale for each plate is different, with the critical loads increasing significantly between $\alpha = 90°$ and $\alpha = 150°$. In each plot, the solid line represents the orthotropic buckling load, and the dotted and dashed lines represent anisotropic solutions for positive and negative shear loads, respectively. Clearly, a design based on orthotropic results could be appreciably under or over-designed, depending on the loading and laminate geometry. For each rhombus angle, the point of maximum deviation from the orthotropic solution is indicated by the double-headed arrow. The maximum deviation between anisotropic and orthotropic solutions is found to be approximately constant at $\pm 20\%$ for all three rhombus angles. Therefore, the deviation is independent of, or a very weak function of, the rhombus angle (the absolute maximum for each case was not found as the increment in laminate rotation angle was 7.5°). As a point of interest, the maximum deviation for a $[0/60/-60]_S$ quasi-

isotropic laminate was found to be approximately constant at ±40%. The location of the maximum deviation does appear to change slightly with changing rhombus angle. It is significant that the maximum-deviation location is never more than 15° away from the baseline (0° rotation) configuration. A second important point is that there exist two laminate orientations (indicated by the black dots) at which there is no shear directional dependence. This laminate orientation could then be used to design a component with equal shear-buckling resistance under reversed shear. Clearly, these cross-over points (particularly the right-hand one) change location with changing rhombus angle.

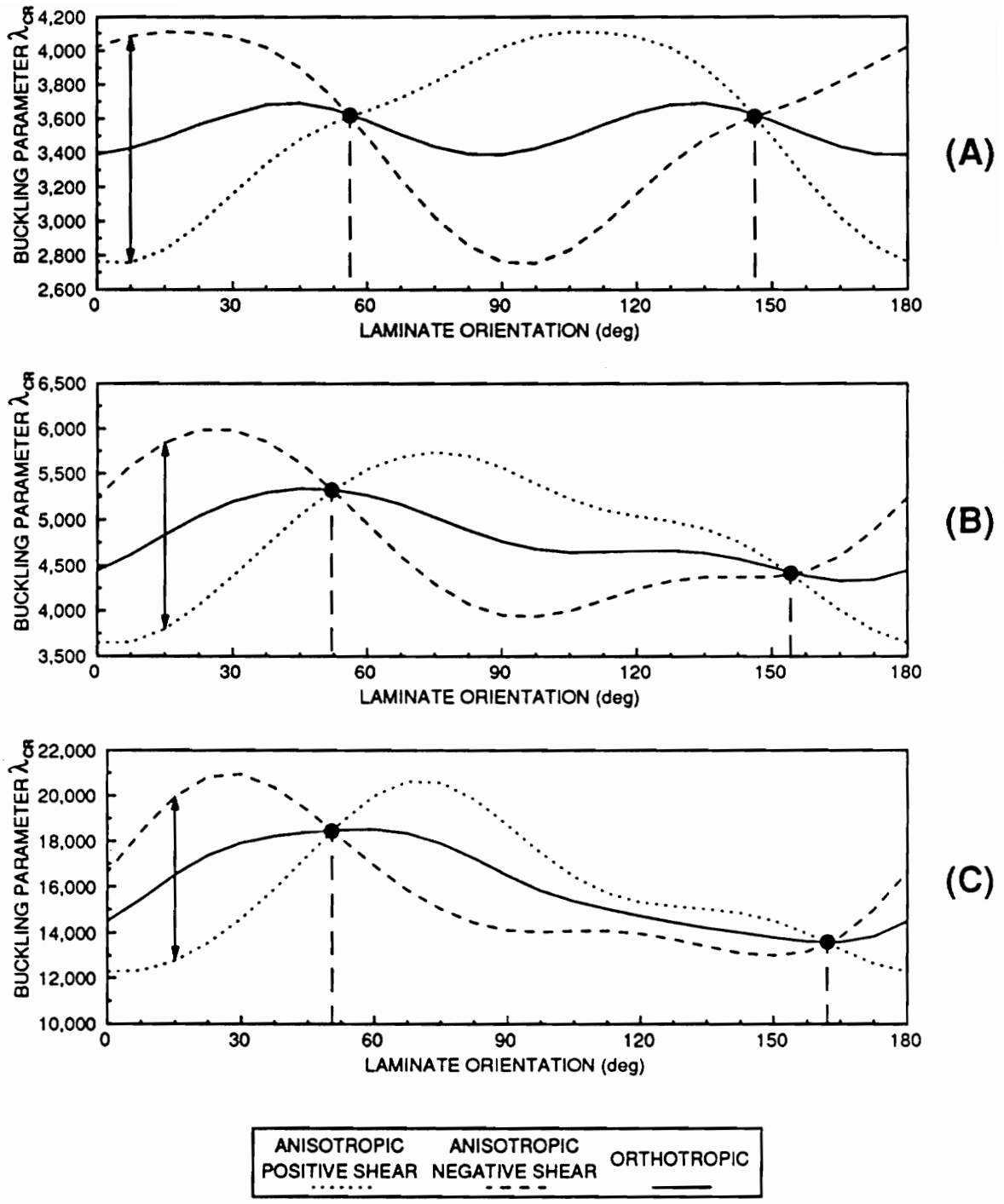

Figure 54. **Shear-Buckling Loads for Rhombic Plates with Rotated Laminate:** A) $\alpha = 90°$ B) $\alpha = 120°$ C) $\alpha = 150°$, $\alpha =$ Rhombus Interior Angle

6.0 Concluding Remarks

6.1 Summary

The aim of the present work was to evaluate the geodesic stiffening concept for possible use in weight-efficient aircraft structures. A wing rib panel similar to that of a large transport aircraft was chosen as the object of the preliminary design study. The lack of a suitable design code led to the development of structural analysis methods as part of the research effort. The resulting design code was used to conduct an optimization study for several wing rib panel geometries under representative loads. The results of the design study, including structural efficiencies and geometric parameter trends, are presented and discussed. Effects of skin laminate geometry and anisotropy on the local skin buckling behavior of a stiffened panel were examined using an analysis for the buckling of a simply supported rhombic plate.

The wing rib was modeled as a rectangular panel 80 inches wide by 28 inches high. The boundary conditions were idealized as simply supported, with the in-plane extensional deformation in the width direction assumed to be zero. Balanced pairs of rectangular cross-section blade stiffeners of unidirectional material were symmetrically located on both sides of a balanced, symmetric skin

laminate. Combinations of uniaxial compression and shear loads representative of rib loads for a commercial transport aircraft were applied. Diagonal and cross geodesically stiffened geometries, as well as longitudinally stiffened and flat plate configurations, were considered.

There did not appear to be an existing design code which met the needs, including computational efficiency and analysis accuracy, of the design study for geodesically stiffened panels. As such, analysis procedures were implemented to consider three design constraints: buckling of the panel assembly, local buckling of the stiffeners, and material strength failure. The in-plane load distribution for the panel was estimated by smearing the stiffeners. The Lagrange multiplier method [LMM] panel buckling analysis was used to predict the critical load for a rectangular orthotropic plate with a number of oblique stiffeners. Local buckling of the stiffeners was estimated by modelling the blade as a rectangular orthotropic plate under uniform axial compressive load. Material failure in the skin or stiffeners was estimated using a maximum strain criterion. These analysis routines were combined with a versatile numerical optimizer to create a stiffened panel design package.

Several examples were introduced to demonstrate the convergence behavior of the LMM buckling analysis. Comparison with finite element models for longitudinally and cross-stiffened panels indicated that the smeared analysis gives a very good estimate for the in-plane load distribution. For the longitudinally stiffened panels, the LMM analysis buckling loads are 3-6% higher for a thick skin and 5-10% lower for a thin skin, compared with the published finite element results. For a three cell cross-stiffened panel, the LMM results range from 40% lower for low-flexural-rigidity stiffeners to only 5% lower for rigid stiffeners. Since optimum panels generally have relatively rigid stiffeners, the LMM analysis should give a reasonable estimate of the true buckling load for this application.

In the design study, optimum or minimum-mass panel designs were sought for the two geodesically stiffened panels and the longitudinally stiffened panel, with up to eight cells. The unstiffened flat plate was also considered. The design variables were thickness of the skin laminate, stiffener height,

and stiffener thickness. A quasi-isotropic $[-45/45/90/0]_s$ skin laminate with equal thickness plies was assumed. A minimum thickness bound of 0.040 inch applied to the skin and stiffeners. Three levels of external loads (100, 1000, 10000 lbf/in) were applied in uniaxial compression and pure shear. Combined compression-shear of 100 to 30000 lbf/in was considered for the flat plate and the eight-cell stiffened panels.

Structural efficiency trends from the design study indicated that there is, in general, a clear downward trend in mass of the panels as the number of cells is increased. This is the case for all three stiffened geometries, and the trend is more pronounced for heavier loads. Under compressive load, the minimum-mass configuration is an eight cell diagonally stiffened panel, although the cross-stiffened eight cell designs are very close in mass. Under shear, the trend is also towards a minimum-mass design at eight cells, with the cross-stiffened designs being lightest. However, for the heaviest shear loading, the material failure constraint becomes active, causing the minimum-mass design to occur at six (cross-stiffened) cells. For both compressive and shear loading, differences in structural efficiency between the three stiffened geometries become less pronounced as the number of cells is increased. For combined loads, the cross-stiffened geometry is lightest at all loading levels.

Trends in several geometric parameters were examined for the optimum diagonal and cross-stiffened panels under compression and shear. In general, the trends are similar for both the diagonal and cross parameters, although to varying degrees. For a given loading regime, either compression or shear, the trends of a given parameter are quite consistent, with two exceptions. The first exception occurs for shear-loaded, cross-stiffened panels with 7 and 8 cells, where significant deviations in parameter trends can occur when the material failure constraint becomes active. The second occurs primarily for the 10000 lbf/in shear-loaded, diagonally stiffened panel. In this case the exception is thought to be the result of a change in buckling mode trends not observed at other load levels.

Panel skin thickness generally decreases as the number of cells is increased, with the decrease more substantial for compression than for shear. There is a large increase in skin thickness when the skin material constraint becomes active.

Stiffener heights are quite large for compressed panels with only a few cells, but there is a significant decrease as the number of cells is increased. For panels under shear, however, the stiffeners are much shorter for a few cells and the height does not change much. There is a small drop in stiffener height when the material failure constraint becomes active.

Stiffener thicknesses are on the minimum-thickness bound for the lowest level of compression and shear load. For most of the heavier loads, the stiffener thicknesses are relatively constant under compression. Under heavy shear load, however, a significant drop in stiffener thickness is observed, primarily due to changing buckling modes.

Since stiffener thicknesses are relatively constant, the stiffener aspect ratio trends are similar to those for stiffener height. That is, aspect ratios for compressively loaded panels are much higher than those for panels under shear. Also, as the number of cells is increased, the aspect ratios for compression panels decreases significantly, whereas for panels under shear they remain quite constant, particularly for light loading. In general, the geodesic stiffeners are rather thick, with most having aspect ratios less than 20 and many less than 10.

The fraction of the load carried by the stiffeners for compression-loaded panels starts near zero for few cells and increases steadily as the number of cells increases, reaching nearly 60% for a cross-stiffened panel. The load fraction tends to increase as the applied load becomes larger. For shear-loaded panels, the load fraction remains below about 20%, and in general varies little. However, it does drop significantly when the material failure constraint becomes active. For both compression and shear, the stiffener mass fraction generally increases as the number of cells increases, and is higher for heavier loads. It too drops when the material failure constraint is active.

At the present time, the LMM panel buckling analysis can model only a specially orthotropic skin laminate. However, a solution for the buckling of anisotropic rhombic plates was developed during the course of the work. This was used to estimate the effects of anisotropy, as well as skin section shape and laminate orientation, on the local skin buckling behavior of a cross-stiffened panel.

A convergence example for the rhombic plate buckling analysis demonstrated that the new Kennedy solution approaches the exact result from below, while the Standard solution convergences from above, as the number of series terms is increased. The two solutions appear to converge at about the same rate for this example. The computational cost of the Kennedy analysis is, however, much higher than that for the Standard solution. The difference between the solutions increases as the skewness of the rhombic plate increases. For a rhombus equivalent to an eight cell panel under compression, the Standard analysis solution is 27% higher than the Kennedy solution (results for orthotropic plate). For the same plate under shear, the Standard analysis critical load is 12% higher than the Kennedy result.

Comparing the rhombic plate solution with LMM solutions for cross-stiffened panels showed that the rhombic plate model for local buckling produces highly conservative estimates of the panel buckling loads. For a panel with artificially rigid stiffeners, the buckling loads predicted by the rhombic analysis are only 47-61% (compression) and 65-74% (shear) of those local buckling loads predicted by the LMM analysis. It appears that the edges of rhombus-shaped panel skin sections may be restrained due to the presence of skin in the adjacent cells. Therefore, boundary conditions may be closer to the clamped condition, as opposed to the simply supported condition assumed for the rhombic plate analysis. Also, since the correlation is not constant over the range of cells, it is not possible to simply apply a correction factor to the rhombic estimates. In addition, the design study results revealed that optimum cross-stiffened panels, particularly under shear, may not always buckle in a manner which produces a rhombus-shaped buckled skin section. Therefore, discrete plate models for local buckling analyses should be used with caution.

The rhombic plate analysis was used to estimate the effects of skin section skewing, laminate anisotropy, and laminate orientation. Results from the rhombic plate study indicated that increasing the skewness of a rhombic plate increases the plate buckling load significantly. The increase is more substantial for compression (8.0 times) than for shear (5.5 times). This result is qualitatively the same as trends seen in the design study for cross-stiffened panels. The maximum difference between the anisotropic and orthotropic buckling loads for compressive loading of the present $[-45/45/90/0]_S$ laminate is 0.6%. Anisotropy causes the panel to be sensitive to the direction of applied shear. The maximum drop from the orthotropic solution is almost 18% for positive shearing of an eight-cell panel. Plate buckling loads are lower for compression than for shear, so under combined compression-shear the buckling response is dominated by the compressive component. That is, under combined compression-shear, anisotropy effects are suppressed but skewing of the plate still has a large effect.

Rotation of the $[-45/45/90/0]_S$ laminate revealed that a maximum error of $\pm 20\%$ in the buckling load could be incurred by ignoring anisotropic effects. The maximum deviation between positive/negative shear anisotropic buckling loads and the orthotropic solution appears to be independent of the rhombic plate geometry. The orientation at which the maximum deviation occurs, however, appears to be a weak function of rhombic skewness. For each rhombus shape, there exist two orientations of the $[-45/45/90/0]_S$ laminate at which the buckling load shows no preference for the direction of applied shear. The laminate orientation at which these points exist is a function of the skew angle of the rhombic plate.

6.2 Conclusions

- The Lagrange multiplier method [LMM] panel buckling analysis produces physically meaningful buckled mode shapes for stiffened panels. Convergence of the critical load can be achieved with

relatively few stiffener-skin constraint points and series terms in the skin deflection function. The method generally appears to be conservative, but usually by less than about 10% when localized buckling is predominant.

- In general, LMM panel buckling results show a significant degree of interaction between local inter-stiffener and global trans-stiffener buckling modes. Therefore, a simplified approach which assumes solely local or global buckling will not always be capable of predicting the panel behavior with certainty.
- The restraining effect of a continuous skin in stiffened panels makes the assumed classical simple-support boundary conditions for a discrete plate element very conservative. In view of the large degree of approximation in the boundary conditions for the rhombic plate, the additional expense of the Kennedy analysis may not be justified for this application.
- Design study trends indicate that minimum-weight wing rib panels will use relatively closely spaced stiffeners. As the number of cells (and stiffeners) increases, and the stiffeners become closely spaced, the structural efficiencies of the three stiffened panel configurations become quite close. However, the cross-stiffened geometry appears to be the most efficient stiffening arrangement for most loading conditions.
- The panel designs for compression appear to be more sensitive to the number of cells used. That is, for a compression-loaded panel both the skin thickness and stiffener height change markedly as the number of cells is increased, but the same quantities remain relatively constant for a shear-loaded panel.
- The stiffeners appear to play a more active role in stabilizing the panels under compressive loads than shear loads. The fraction of the load carried by the stiffeners is significantly higher for compression-loaded panels. Also, the stiffeners for compression-loaded panels appear to support larger bending loads, as the stiffeners are relatively tall and have high aspect ratios. Conversely, the stiffeners for heavily-loaded shear panels may be quite flexible (short heights, low aspect ratios), with the tensile-loaded stiffeners enforcing nodal lines and the compression-loaded members deflecting considerably.

- It would appear that anisotropic effects are not significant (less than 1%) for compressive loading of the present $[-45/45/90/0]_S$ laminate. Anisotropy causes the panel to be sensitive to the direction of applied shear. The maximum error in shear buckling load due to assuming a state of special orthotropy is an over-estimate of about 18%.
- Rotation of the $[-45/45/90/0]_S$ laminate reveals that a maximum error of $\pm 20\%$ in the buckling load is possible by assuming special orthotropy with this laminate. Also, the standard laminate orientation is near the orientation for maximum error. Laminate rotation may be a useful design tool, as there are two orientations for each design at which the laminate shows no preference for the direction of applied shear.

6.3 *Recommendations for Future Work*

<u>Lagrange Multiplier Method Buckling Analysis</u>

- The present Lagrange multiplier method [LMM] analysis code should be revised to incorporate the effects of skin laminate bending-twisting coupling terms D_{16} and D_{26} by including the appropriate strain energy term. Convergence studies should also be performed to assess the effect of anisotropy on the convergence of the problem.
- LMM solution accuracy should be enhanced by incorporating the effect of torsion rigidity of the stiffeners. This requires including the strain energy due to stiffener torsional deformation and enforcing continuity of rotations between the skin and stiffeners. This should improve the accuracy of the analysis for the present blade stiffeners, and also allow considering closed-section stiffeners which have a torsional stiffness which cannot often be ignored.
- A future concept would be to model the blade stiffeners as plate elements rather than beams. This would eliminate the need for considering stiffener crippling independently, eliminate the approximation due to using assumed classical boundary conditions for the stiffener, and allow

interaction of simultaneous skin-stiffener buckling modes. Also, other than specially orthotropic stiffeners could be considered.

PANSYS Design Code

- To allow more freedom in trying design concepts, the design code should allow more general stiffening arrangements to be specified, such as any combination of longitudinal, transverse, or oblique stiffeners.
- At the present time, the stiffened panels have no structure around the perimeter, and in-plane transverse deformation of the panel is assumed to be zero. An elastic frame around the panel edges, with the X direction in-plane boundary condition unrestrained would be more realistic and should be incorporated. This feature would be more meaningful if torsional effects are included in the LMM analysis, as the torsional restraint of the frame would also be included.

Geodesically Stiffened Panel Designs

- Further design studies should examine the effects of optimizing individual ply thicknesses, optimizing ply orientations, using other skin laminate layups, and orientation of the entire skin laminate. These studies may reduce the sensitivity of the cross-stiffened panel design to the material failure constraints.
- It may be worthwhile to consider performance criteria other than load carrying capability. These may include component stiffness (many structures are deflection-constrained), performance under off-design load conditions (e.g. compression-carrying capacity of a shear panel), or sensitivity to non-optimal design parameters (e.g. discrete ply thicknesses).

Rhombic Plates

- If a rhombic plate buckling solution is to be used to estimate local skin buckling behavior of stiffened panels, clamped boundary conditions may give a better correlation.

7.0 References

1. McMullen, P., "Fibre/Resin Composites for Aircraft Primary Structures: A Short History, 1936-1984," *Composites,* Vol. 15, No. 3, July 1984, pp. 222-230.

2. McDonnell Douglas Astronautics Company, "Isogrid Design Handbook," NASA Contractor Report No. CR124075, July 1977.

3. Hyer, M.W., and Douglas, D.O., "Results of Graphite-Polyimide Isogrid Panel Testing," Old Dominion University Research Foundation, Interim Report, June 1977.

4. Rehfield, L.W., Deo, R.B., and Renieri, G.D., "Continuous Filament Advanced Composite Isogrid: A Promising Structural Concept," *Fibrous Composites in Structural Design,* Plenum Publishing Corporation, 1980, pp. 215-239.

5. Rehfield, L.W., Reddy, A.D., Yehezkely, O., and Armanios, E., "Buckling of Continuous Filament Composite Isogrid Panels: Theory and Experiment," *Progress in Science and Engineering of Composites,* ICCM-IV, Tokyo, 1982, pp. 545-553.

6. Rehfield, L.W., and Reddy, A.D., "Damage Tolerance of Continuous Filament Composite Isogrid Structures: A Preliminary Assessment," *Composite Materials,* Proc. Japan-U.S. Conference, Tokyo, 1981, pp. 471-477.

7. Reddy, A.D., "Behavior of Continuous Filament Advanced Composite Isogrid Structure," PhD Thesis, Georgia Institute of Technology, November 1980.

8. Freeman, W.T., and Stein, B.A., "Filament Winding: Waking the Sleeping Giant," *Aerospace America,* Vol. 24, No. 10, October 1985, pp. 44-49.

9. Freeman, W.T., "History and Future of Large Composite Structure Fabrication," Review for Virginia Tech Center for Composite Materials and Structures, February 8, 1989.

10. Barrie, R., Biggers, S., Campion, M., and O'Brien, D., "Design Methods and Considerations for Composite Transport A/C Primary Structure," Lockheed-Georgia Company Presentation, April 1, 1987.

11. Swanson, G.D., "Structural Efficiency Study of Composite Wing Rib Structures," MS Thesis, Virginia Polytechnic Institute and State University, November 1987.

12. Bushnell, D., "PANDA2 - Program for Minimum Weight Design of Stiffened, Composite, Locally Buckled Panels," *Computers & Structures,* Vol. 25, No. 4, 1987, pp. 469-605.

13. Anderson, M.S., and Stroud, W.J., "General Panel Sizing Code and Its Application to Composite Structural Panels," *AIAA Journal,* Vol. 17, No. 8, August 1979, pp. 892-897.

14. Stroud, W.J., Agranoff, N., and Anderson, M.S., "Minimum-Mass Design of Filamentary Composite Panels Under Combined Loads: Design Procedure Based On A Rigorous Buckling Analysis," NASA Technical Note No. D-8417, July 1977.

15. Anderson, M.S., Williams, F.W., and Wright, C.J., "Buckling and Vibration of Any Prismatic Assembly of Shear and Compression Loaded Anisotropic Plates With An Arbitrary Supporting Structure," *Int. J. Mech. Sci.,* Vol. 25, No. 8, 1983, pp. 585-596.

16. Reddy, A.D., Valisetty, R.R., and Rehfield, L.W., "Continuous Filament Wound Composite Concepts for Aircraft Fuselage Structures," *Journal of Aircraft,* Vol. 22, No. 3, March 1985, pp. 249-255.

17. Stroud, W.J., and Agranoff, N., "Minimum-Mass Design of Filamentary Composite Panels Under Combined Loads: Design Procedure Based On Simplified Buckling Equations," NASA Technical Note No. D-8257, October 1976.

18. Stoll, F., "Stiffener Failure Constraints for the Design of Isogrid-Stiffened Panels," ESM Internal Report, Virginia Polytechnic Institute and State University, 1987.

19. Valisetty, R.R., and Reddy, A.D., "Design Data and Buckling of Laminated Composite Triangular Plates," SAE Technical Paper No. 850890, presented at the General Aviation Aircraft Meeting and Exposition, Wichita, Kansas, April 16-19, 1985.

20. Nemeth, M.P., "Importance of Anisotropy on Buckling of Compression-Loaded Symmetric Composite Plates," *AIAA Journal,* Vol. 24, No. 11, November 1986, pp. 1831-1835.

21. Young, R.D., and Gurdal, Z., "Importance of Anisotropy on Design of Compression-Loaded Composite Corrugated Panels," *AIAA Journal,* to be published.

22. Vanderplaats, G.N., "ADS - A FORTRAN Program for Automated Design Synthesis," Version 3.00, Engineering Design Optimization, 1987.

23. Knight, M., "Three-Dimensional Elastic Moduli of Graphite/Epoxy Composites," *Journal of Composite Materials,* Vol. 16, March 1982, pp. 153-159.

24. Sensmeier, M.D., Griffin Jr., O.H., Johnson, E.R., "Static and Dynamic Large Deflection Flexural Response of Graphite-Epoxy Beams," CCMS-87-7, Virginia Polytechnic Institute and State University, May 1987.

25. Timoshenko, S.P., and Gere, J.M., "Theory of Elastic Stability," McGraw-Hill Book Co., 1961.

26. Jones, R.M., "Mechanics of Composite Materials," Hemisphere Publishing Corp., 1975.

27. Whitney, J.M., "Structural Analysis of Laminated Anisotropic Plates," Technomic Publishing, Inc., 1987.

28. Ashton, J.E., and Whitney, J.M., "Theory of Laminated Plates," Technomic Publishing, Inc., 1970.

29. Timoshenko, S.P., and Woinowsky-Krieger, S., "Theory of Plates and Shells," McGraw-Hill Book Co., 1959.

30. Simitses, G.J., "An Introduction to the Elastic Stability of Structures," Krieger Publishing Co., Inc., 1986.

31. Wang, J.T., "On the Solution of Plates of Composite Materials," *Journal of Composite Materials,* Vol. 3, July 1969, pp. 590-592.

32. Budiansky, B., and Hu, P.C., "The Lagrangian Multiplier Method of Finding Upper and Lower Limits to Critical Stresses of Clamped Plates," *Thirty-Second Annual Report of the NACA,* Report No. 848, 1946.

33. Bulson, P.S., "The Stability of Flat Plates," Clarke, Irwin and Co. Ltd., 1970.

34. Budiansky, B., Hu, P.C., and Connor, R.W., "Notes on the Lagrangian Multiplier Method in Elastic-Stability Analysis," NACA Technical Note No. 1558, May 1948.

35. Cox, H.L., "Buckling of Plates and Shells," International Series of Monographs on Aeronautics and Astronautics, Volume 4, Pergamon Press Ltd., 1963.

36. Al-Shareedah, E.M., and Seireg, A.A., "Use of Undetermined Multipliers in the Solution of Complex Plate Problems," *Computers in Mechanical Engineering,* Vol. 4, No. 3, November 1985, pp. 59-68.

37. Al-Shareedah, E.M., and Seireg, A.A., "The Design of Slabs With Constraining Columns Using the Undetermined Multipliers Method," *Computers in Mechanical Engineering,* Vol. 4, No. 4, January 1986, pp. 59-68.

38. Al-Shareedah, E.M., and Seireg, A.A., "Use of Undetermined Multipliers in the Design of Stiffened Plates," *Computers in Mechanical Engineering,* Vol. 4, No. 5, March 1986, pp. 57-64.

39. "Laminate Stacking Sequences for Special Orthotropy (Application to Fibre Reinforced Composites)," Engineering Sciences Data Unit, Item No. 82013, October 1982.

40. Budiansky, B., and Seide, P., "Compressive Buckling of Simply Supported Plates With Transverse Stiffeners," NACA Technical Note No. 1557, April 1948.

41. Seide, P., and Stein, M., "Compressive Buckling of Simply Supported Plates With Longitudinal Stiffeners," NACA Technical Note No. 1825, March 1949.

42. Hofmeister, D.L., and Felton, L.P., "Waffle Plates with Multiple Rib Sizes: I. Stability Analysis," *Journal of Spacecraft,* Vol. 7, No. 11, November 1970, pp. 1322-1327.

43. Hofmeister, D.L., and Felton, L.P., "Waffle Plates with Multiple Rib Sizes: II. Design Examples," *Journal of Spacecraft,* Vol. 7, No. 11, November 1970, pp. 1327-1331.

44. Slysh, P., Dyer, J.E., Furman, J.H., and Key, J.E., "Isogrid Structural Tests and Stability Analyses," *Journal of Aircraft,* Vol. 13, No. 10, October 1976, pp. 778-785.

45. Buskell, N., Davies, G.A.O., and Stevens, K.A., "Postbuckling Failure of Composite Panels," *Composite Structures 3,* Proceedings of the 3rd International Conference on Composite Structures, Paisley College of Technology, Scotland, September 1985, pp. 290-314.

46. Whitney, J.M., "Shear Correction Factors for Orthotropic Laminates Under Static Load," *Journal of Applied Mechanics,* Vol. 40, March 1973, pp. 302-304.

47. Durvasula, S., "Buckling of Simply Supported Skew Plates," *Journal of the Engineering Mechanics Division,* ASCE, Vol. 97, No. EM3, June 1979, pp. 967-979.

48. Kennedy, J.B., and Prabhakara, M.K., "Buckling of Simply Supported Orthotropic Skew Plates," *Aeronautical Quarterly,* Vol. 29, August 1978, pp. 161-174.

49. Kennedy, J.B., and Prabhakara, M.K., "Combined-Load Buckling of Orthotropic Skew Plates," *Journal of the Engineering Mechanics Division,* ASCE, Vol. 105, No. EM1, February 1979, pp. 71-79.

50. Whitney, J.M., and Leissa, A.W., "Analysis of a Simply Supported Laminated Anisotropic Rectangular Plate," *AIAA Journal,* Vol. 8, No. 1, January 1970, pp. 28-33.

51. Whitney, J.M., "Fourier Analysis of Clamped Anisotropic Plates," *Journal of Applied Mechanics,* Vol. 38, No. 2, June 1971, pp. 530-532.

52. Whitney, J.M., "Analysis of Anisotropic Rectangular Plates," *AIAA Journal,* Vol. 10, No. 10, October 1972, pp. 1344-1345.

53. Whitney, J.M., "Free Vibration of Anisotropic Rectangular Plates," *The Journal of the Acoustical Society of America,* Vol. 52, No. 1 (Part 2), 1972, pp. 448-449.

54. Whitney, J.M., "On The Analysis of Anisotropic Rectangular Plates," Air Force Materials Laboratory Technical Report AFML-TR-72-76, August 1972.

55. Ashton, J.E., "Anisotropic Plate Analysis - Boundary Conditions," *Journal of Composite Materials,* Vol. 4, April 1970, pp. 162-171.

56. Troitsky, M.S., "Stiffened Plates - Bending, Stability and Vibrations," Elsevier Scientific Publishing Co., 1976.

57. Green, A.E., "Double Fourier Series and Boundary Value Problems," *Proceedings of the Cambridge Philosophical Society,* Vol. 40, 1944, pp. 222-228.

58. Green, A.E., and Hearmon, R.F.S., "The Buckling of Flat Rectangular Plywood Plates," *Philosophical Magazine,* Ser. 7, Vol. 36, No. 261, October 1945, pp. 659-688.

59. Morley, L.S.D., "Skew Plates and Structures," International Series of Monographs on Aeronautics and Astronautics, Volume 5, Pergamon Press Ltd., 1963.

60. Sun, C.T., "Double Fourier Series Solution to General Anisotropic Plates," *Journal of Mathematical and Physical Sciences,* Vol. 6, 1972, pp. 205-223.

61. O'Neil, P.V., "Advanced Engineering Mathematics," Wadsworth Publishing Co., 1983.

62. Reddy, J.N., "Energy and Variational Methods in Applied Mechanics," John Wiley and Sons, Inc., 1984.

63. Stroud, W.J., Greene, W.H., and Anderson, M.S., "Buckling Loads of Stiffened Panels Subjected to Combined Longitudinal Compression and Shear: Results Obtained With PASCO, EAL, and STAGS Computer Programs," NASA Technical Paper No. 2215, January 1984.

64. Donnell, L.H., "Beams, Plates, and Shells," McGraw-Hill Book Co., 1976.

65. "Computational Structural Mechanics Testbed User's Manual," NASA Technical Memorandum No. 100644, October 1989.

66. Taylor, J.L., "Buckling and Vibration of Triangular Flat Plates," *Journal of the Royal Aeronautical Society,* Vol. 71, October 1967, pp. 727-728.

67. Stroud, W.J., "Optimization of Composite Structures," NASA Technical Note No. 84544, August 1982.

68. "IMSL MATH/LIBRARY FORTRAN Subroutines for Mathematical Applications," IMSL, Inc., 1987.

Appendix A. Sample Input File for PANSYS Design Code

The design package PANSYS allows efficient constrained optimization of flat and stiffened rectangular composite panels under compression and shear loads. Analysis routines estimate panel buckling, stiffener crippling, and material failure loads for flat plates, longitudinally stiffened panels, and two geodesically stiffened panels. The analysis capability is coupled with a versatile optimization package with many available options to permit automated design of minimum-weight panels. A post-processing option enables buckled mode shape contour plots to be created for the panels. PANSYS analysis routines are modular in form and written in FORTRAN 77. The code requires access to the numerical optimization program ADS[22] and several IMSL[68] library routines for matrix operations and solution of eigenvalue problems. To provide some insight into the capabilities of the PANSYS design code, this section briefly reviews a sample input file (Figure A1). The example presented is for a four cell cross-stiffened panel under combined loads of 1000 lbf/in compression and 100 lbf/in shear.

Data group (1) in Figure A1 controls the printed output from PANSYS and ADS. The parameter *IADS* is transferred to the ADS program to control output from various ADS functions during the optimization run. The remaining parameters are for various PANSYS analysis rou-

tines which calculate component geometric and elastic properties, panel load distribution, flat/stiffened plate buckling, stiffener crippling, and material failure. For the five lines with two values, the first parameter (*IPxxI*) controls output during the iteration process (generally used for debugging only), and the second parameter (*IPxxF*) controls output for the final design. For each print parameter, a value of 0 indicates no output, a value of 1 produces brief output, and a value of 2 produces detailed output. In addition, a value of 2 for the panel (*IP*45) or stiffener (*IP*60) buckling analysis output parameter causes an eigenvector for the buckled mode shape to be generated.

In the following two data groups, an *S* suffix on the variable name indicates that it is applicable to the skin of the panel, and an *R* suffix indicates that it is for the ribs or stiffeners.

Data group (2) primarily specifies material properties for the skin and stiffeners. The quantities required for the skin are moduli E_1, E_2, G_{12}, Poisson's ratio ν_{12}, and density ρ. The stiffeners require these same quantities, as well as transverse shear moduli G_{23} and G_{31}. The parameter *SCF* is the shear correction factor, commonly taken as 5/6 for fibrous composite materials.

Data group (3) specifies maximum strain allowables for the skin and stiffener material failure analyses. For the skin these are longitudinal normal strain allowables in tension and compression (ε_1^t, ε_1^c), transverse normal strain allowables in tension and compression (ε_2^t, ε_2^c), and shear strain allowable (γ_{12}). Since the stiffeners are assumed to be in a state of uniaxial stress, only longitudinal strain allowables (ε_1^t, ε_1^c) are required.

Data group (4) specifies panel planform geometry and loading. The variables include panel width and height, the geometry type, the number of stiffened cells, and the axial compressive and shear load intensities. For geometry, $IGEOM = 1$ indicates a flat plate, $IGEOM = 2$ a longitudinally stiffened panel, $IGEOM = 3$ a diagonally stiffened panel, and $IGEOM = 4$ a cross-stiffened panel.

Data group (5) specifies parameters for the buckling analyses. For the LMM panel buckling analysis, the number of skin deflection function terms in the X direction (MM) and Y direction (NN), and the number of constraint points per stiffener (KK) are specified. The number of terms in the stiffener buckling analysis shape functions are denoted by NWX, NWY, $NPXX$, $NPXY$, $NPYX$, $NPYY$, which stand for the factors N_w^x, N_w^y, $N_{\psi_x}^x$, $N_{\psi_x}^y$, $N_{\psi_y}^x$, $N_{\psi_y}^y$ from Section 3.3. The parameter $IEND$ specifies the assumed end restraint condition for the stiffener; $IEND = 1$ indicates simply supported ends and $IEND = 2$ clamped ends.

Data group (6) specifies starting or reference values for panel dimensions which are eligible to be design variables. Two possible design variables are the stiffener height (SH) and stiffener thickness (ST). In PANSYS, panel dimensions which are eligible to be design variables are retained in a vector called RDV, and the reference values remain unchanged through the design process. The number of plies in one-half of the skin laminate ($NHPLY$) is specified next, followed by eligible design variables of thickness and orientation for each lamina. As a symmetric laminate is assumed, only one-half of the laminate is specified. An error message will be issued if angle plies in the laminate are not balanced.

Data group (7) defines the design variables. As mentioned previously, the vector RDV contains a set of fixed reference dimensions. Each design variable acts as a scale factor which can be applied to any number of reference values in RDV. In the present example, $NDV = 3$ specifies that 3 design variables follow. For each design variable, it is first specified how many parameters in RDV it controls, or the number of parameters in the "design variable group" ($NDVG$). The locations in RDV of $NDVG$ geometric parameters for that design variable then follows. For example, the first design variable controls one geometric parameter, the stiffener height, which is located in $RDV(1)$. The second design variable also controls one geometric parameter, located in $RDV(2)$, which is the stiffener thickness. The third design variable controls 4 parameters, located in $RDV(11)$-$RDV(14)$, which are the ply thicknesses. Therefore, all plies will be scaled a like amount through the design process. Note that the ply orientations, located in $RDV(51)$-$RDV(54)$, will not change in this example because no design variable has been assigned

to them. The initial value (X), plus lower (VLB) and upper (VUB) bounds for each design variable, are then specified. Although any initial value can be used for the design variables, it is recommended that reasonable values for the geometric parameters be put in RDV so that the initial design variable values may be left at 1.0. This helps to ensure that all design variables are of approximately the same magnitude, which is beneficial to the optimization algorithm.

Data group (8) specifies the number of constraints ($NCON$) to be imposed, followed by the type of constraint(s) ($ICON$). Constraint $ICON = 1$ is panel buckling, $ICON = 2$ is stiffener crippling, $ICON = 3$ is skin material failure, and $ICON = 4$ is stiffener material failure. In the present example, two constraints, namely panel buckling and stiffener crippling, are imposed.

Data group (9) specifies optimization parameters for ADS. For more detailed information on ADS parameters, see the ADS user's manual[22]. The strategy ($ISTRAT$), optimizer ($IOPT$), and one-dimensional search ($IONED$) strategies are selected first. The next set of parameters is used if default values for constants (typically convergence criteria, tolerances, etc.) in ADS are to be over-ridden. Specifying $INFO = 0$ indicates that all default constants are to be used, whereas $INFO = -2$ indicates that one or more values are to be changed. If $INFO = -2$, the values of NIP and NRP specify the number of integer and real constants, respectively, to be changed. Following NIP and NRP are the locations of the constants in an ADS array and the new value that each is to take on. In the present example, 3 integer constants ($ISCAL, ITRMST, JTMAX$) and 5 real constants ($CT, CTMIN, FDCH, FDCHM, ZRO$) are to be altered. The ADS user's manual describes the purpose of the various constants, their locations in an integer or real array, and the default values.

Value	Parameter Name	Data Group
2310	IADS	(1) - print parameters
2	IP10	
0 2	IP20I, IP20F	
0 2	IP30I, IP30F	
0 2	IP45I, IP45F	
0 2	IP60I, IP60F	
0 2	IP90I, IP90F	
18.5E06	E1S	(2) - material data, skin
1.64E06	E2S	
0.87E06	G12S	
0.30	V12S	
0.057	RHOS	
18.5E06	E1R	- material data, stiffener
1.64E06	E2R	
0.87E06	G12R	
0.54E06	G23R	
0.87E06	G31R	
0.30	V12R	
0.057	RHOR	
0.83333	SCF	
0.0090	E1ALTS	(3) - strain allowables, skin
0.0080	E1ALCS	
0.0055	E2ALTS	
0.0100	E2ALCS	
0.0140	E12ALS	
0.0090	E1ALTR	- strain allowables, stiffener
0.0080	E1ALCR	
80.0	PW	(4) - panel geometry & loading
28.0	PH	
4	IGEOM	
4	NC	
1000.0	PNY	
100.0	PNXY	
17	MM	(5) - analysis parameters, panel buckling
11	NN	
11	KK	

Figure A1. Sample Input File for PANSYS Design Code

Value	Parameter Name	Data Group
5	NWX	(5) - analysis parameters, cont'd
5	NWY	- stiffener crippling
5	NPXX	
5	NPXY	
5	NPYX	
5	NPYY	
1	IEND	
2.00	SH [RDV(1)]	(6) - variable panel geometry
0.10	ST [RDV(2)]	
4	NHPLY	
0.015 -45.0	THICK(I),THETA(I) [RDV(11),RDV(51)]	
0.015 45.0	[RDV(12),RDV(52)]	
0.015 90.0	[RDV(13),RDV(53)]	
0.015 0.0	[RDV(14),RDV(54)]	
3	NDV	(7) - designate design variables
1 1	NDVG(I),NDVG locns in RDV	
1 2		
4 11 12 13 14		
1.0 0.2 5.0	X(I),VLB(I),VUB(I)	- bounds on design variables
1.0 0.2 5.0		
1.0 0.2 5.0		
2	NCON	(8) - define constraints
1 2	ICON(I)	
9	ISTRAT	- ADS optimization options
5	IOPT	
7	IONED	
-2	INFO	(9) - override ADS defaults
3	NIP	
2 0	ISCAL	
5 4	ITRMST	
7 20	JTMAX	
5	NRP	
3 -0.01	CT	
6 0.001	CTMIN	
21 0.001	FDCH	
22 0.0001	FDCHM	
37 1.0E-06	ZRO	

Sample Input File for PANSYS Design Code, cont'd

Appendix B. Design Data for Optimum Wing Rib Panels

Table B1. Flat Plate Design Data (Compression, Shear)

	PURE COMPRESSION			PURE SHEAR		
	$N_y = 100$ (lbf/in)	$N_y = 1000$ (lbf/in)	$N_y = 10000$ (lbf/in)	$N_{xy} = 100$ (lbf/in)	$N_{xy} = 1000$ (lbf/in)	$N_{xy} = 10000$ (lbf/in)
Flat Plate						
$DV(1)$ Skin Thickness (in)	0.210	0.453	0.975	0.121	0.261	0.562
OBJ Plate Mass (lbm)	26.82	57.78	124.5	15.46	33.32	71.78
$G(1)$ Skin Buckling	0.10E-3	-0.12E-5	0.21E-5	-0.15E-5	0.89E-5	-0.26E-6
$G(2)$ Skin Strength	-0.99E00	-0.97E00	-0.84E00	-0.97E00	-0.88E00	-0.43E00

$DV(i)$ = Design Variables, $G(i)$ = Constraints, OBJ = Objective Function
Constraints $G(i)$ are feasible when negative, violated when positive, range: $-1 \leq G(i) < \infty$
Skin laminate $[-45/45/90/0]_S$, all plies equal thickness, minimum skin thickness = 0.040 inch

Table B2. Longitudinally Stiffened Panel Design Data (Compression, Shear)

	PURE COMPRESSION			PURE SHEAR		
	$N_y = 100$ (lbf/in)	$N_y = 1000$ (lbf/in)	$N_y = 10000$ (lbf/in)	$N_{xy} = 100$ (lbf/in)	$N_{xy} = 1000$ (lbf/in)	$N_{xy} = 10000$ (lbf/in)
1 Cell						
$DV(1)$ Stiffener Height (in)						
$DV(2)$ Stiffener Thickness (in)						
$DV(3)$ Skin Thickness (in)						
OBJ Panel Mass (lbm)						
Stiffener Load Fraction (%)	N/A	N/A	N/A	N/A	N/A	N/A
Stiffener Mass Fraction (%)						
$G(1)$ Panel Buckling						
$G(2)$ Stiffener Buckling						
$G(3)$ Skin Strength						
$G(4)$ Stiffener Strength						
2 Cells						
$DV(1)$ Stiffener Height (in)	0.980	1.565	1.595	0.781	1.706	3.527
$DV(2)$ Stiffener Thickness (in)	0.040	0.128	0.294	0.040	0.040	0.040
$DV(3)$ Skin Thickness (in)	0.172	0.368	0.802	0.112	0.241	0.520
OBJ Panel Mass (lbm)	22.07	47.65	104.0	14.40	31.02	66.84
Stiffener Load Fraction (%)	0.013	0.030	0.032	0.000	0.000	0.000
Stiffener Mass Fraction (%)	0.006	0.013	0.014	0.007	0.007	0.007
$G(1)$ Panel Buckling	-0.13E-5	-0.43E-4	0.10E-2	0.20E-4	0.32E-5	-0.41E-6
$G(2)$ Stiffener Buckling	-0.12E00	-0.15E-1	-0.78E-1	-0.10E01	-0.10E01	-0.10E01
$G(3)$ Skin Strength	-0.99E00	-0.96E00	-0.82E00	-0.97E00	-0.87E00	-0.39E00
$G(4)$ Stiffener Strength	-0.99E00	-0.96E00	-0.82E00	-0.10E01	-0.10E01	-0.10E01
3 Cells						
$DV(1)$ Stiffener Height (in)	0.716	1.268	1.494	0.804	1.727	3.681
$DV(2)$ Stiffener Thickness (in)	0.040	0.114	0.300	0.040	0.040	0.040
$DV(3)$ Skin Thickness (in)	0.143	0.305	0.652	0.099	0.214	0.462
OBJ Panel Mass (lbm)	18.45	39.88	86.17	12.91	27.81	59.92
Stiffener Load Fraction (%)	0.022	0.051	0.072	0.000	0.000	0.000
Stiffener Mass Fraction (%)	0.010	0.023	0.033	0.016	0.016	0.016
$G(1)$ Panel Buckling	0.11E-2	-0.17E-4	0.32E-1	0.10E-5	0.18E-5	0.10E-4
$G(2)$ Stiffener Buckling	-0.43E00	-0.14E-1	-0.66E-1	-0.10E01	-0.10E01	-0.10E01
$G(3)$ Skin Strength	-0.99E00	-0.95E00	-0.78E00	-0.97E00	-0.85E00	-0.31E00
$G(4)$ Stiffener Strength	-0.99E00	-0.95E00	-0.78E00	-0.10E01	-0.10E01	-0.10E01
4 Cells						
$DV(1)$ Stiffener Height (in)	0.656	1.000	1.394	0.830	1.769	3.815
$DV(2)$ Stiffener Thickness (in)	0.040	0.097	0.302	0.040	0.040	0.040
$DV(3)$ Skin Thickness (in)	0.123	0.262	0.559	0.089	0.192	0.414
OBJ Panel Mass (lbm)	15.90	34.36	75.36	11.69	25.19	54.28
Stiffener Load Fraction (%)	0.035	0.059	0.113	0.000	0.000	0.000
Stiffener Mass Fraction (%)	0.016	0.027	0.053	0.027	0.027	0.027
$G(1)$ Panel Buckling	0.73E-3	0.72E-2	-0.12E-7	0.21E-4	0.27E-8	0.95E-4
$G(2)$ Stiffener Buckling	-0.45E00	-0.86E-2	-0.95E-1	-0.10E01	-0.10E01	-0.10E01
$G(3)$ Skin Strength	-0.99E00	-0.95E00	-0.76E00	-0.96E00	-0.83E00	-0.23E00
$G(4)$ Stiffener Strength	-0.99E00	-0.95E00	-0.76E00	-0.10E01	-0.10E01	-0.10E01

$DV(i)$ = Design Variables, $G(i)$ = Constraints, OBJ = Objective Function, N/A = Not Applicable
Constraints $G(i)$ are feasible when negative, violated when positive, range: $-1 \leq G(i) < \infty$
Skin laminate $[-45/45/90/0]_S$, all plies equal thickness, minimum skin thickness = 0.040 inch
Minimum stiffener thickness = 0.040 inch

Longitudinally Stiffened Panel Design Data (Compression, Shear), cont'd

	PURE COMPRESSION			PURE SHEAR		
	$N_y = 100$ (lbf/in)	$N_y = 1000$ (lbf/in)	$N_y = 10000$ (lbf/in)	$N_{xy} = 100$ (lbf/in)	$N_{xy} = 1000$ (lbf/in)	$N_{xy} = 10000$ (lbf/in)
5 Cells						
$DV(1)$ Stiffener Height (in)	0.619	0.956	1.293	0.947	1.994	4.323
$DV(2)$ Stiffener Thickness (in)	0.040	0.098	0.338	0.040	0.040	0.040
$DV(3)$ Skin Thickness (in)	0.108	0.229	0.477	0.080	0.173	0.372
OBJ Panel Mass (lbm)	14.06	30.43	66.49	10.72	23.08	49.73
Stiffener Load Fraction (%)	0.050	0.085	0.172	0.000	0.000	0.000
Stiffener Mass Fraction (%)	0.023	0.039	0.084	0.045	0.044	0.044
$G(1)$ Panel Buckling	0.21E-3	0.70E-3	0.58E-3	0.35E-4	0.37E-4	-0.87E-6
$G(2)$ Stiffener Buckling	-0.45E00	-0.10E-1	-0.31E00	-0.10E01	-0.10E01	-0.10E01
$G(3)$ Skin Strength	-0.99E00	-0.94E00	-0.73E00	-0.96E00	-0.82E00	-0.14E00
$G(4)$ Stiffener Strength	-0.99E00	-0.94E00	-0.73E00	-0.10E01	-0.10E01	-0.10E01
6 Cells						
$DV(1)$ Stiffener Height (in)	0.603	0.888	1.265	0.932	1.988	4.286
$DV(2)$ Stiffener Thickness (in)	0.040	0.099	0.326	0.040	0.040	0.040
$DV(3)$ Skin Thickness (in)	0.096	0.206	0.421	0.073	0.158	0.341
OBJ Panel Mass (lbm)	12.67	27.75	60.33	9.975	21.49	46.30
Stiffener Load Fraction (%)	0.066	0.108	0.217	0.000	0.000	0.000
Stiffener Mass Fraction (%)	0.030	0.051	0.109	0.060	0.059	0.059
$G(1)$ Panel Buckling	0.65E-4	-0.62E-8	0.40E-2	0.47E-4	0.41E-4	-0.12E-6
$G(2)$ Stiffener Buckling	-0.42E00	-0.92E-1	-0.24E00	-0.10E01	-0.10E01	-0.10E01
$G(3)$ Skin Strength	-0.99E00	-0.93E00	-0.72E00	-0.96E00	-0.80E00	-0.65E-1
$G(4)$ Stiffener Strength	-0.99E00	-0.93E00	-0.72E00	-0.10E01	-0.10E01	-0.10E01
7 Cells						
$DV(1)$ Stiffener Height (in)	0.596	0.880	1.255	0.966	2.081	3.764
$DV(2)$ Stiffener Thickness (in)	0.040	0.102	0.302	0.040	0.040	0.040
$DV(3)$ Skin Thickness (in)	0.087	0.185	0.381	0.067	0.145	0.319
OBJ Panel Mass (lbm)	11.58	25.32	55.92	9.313	20.06	43.63
Stiffener Load Fraction (%)	0.085	0.141	0.253	0.000	0.000	0.000
Stiffener Mass Fraction (%)	0.039	0.068	0.130	0.079	0.079	0.066
$G(1)$ Panel Buckling	0.76E-3	-0.12E-7	-0.32E-6	0.77E-4	0.69E-4	-0.44E-6
$G(2)$ Stiffener Buckling	-0.39E00	-0.79E-1	-0.80E-1	-0.10E01	-0.10E01	-0.10E01
$G(3)$ Skin Strength	-0.98E00	-0.93E00	-0.70E00	-0.95E00	-0.78E00	-0.98E00
$G(4)$ Stiffener Strength	-0.98E00	-0.93E00	-0.70E00	-0.10E01	-0.10E01	-0.10E01
8 Cells						
$DV(1)$ Stiffener Height (in)	0.599	0.895	1.217	0.893	1.922	3.109
$DV(2)$ Stiffener Thickness (in)	0.040	0.102	0.301	0.040	0.040	0.040
$DV(3)$ Skin Thickness (in)	0.080	0.167	0.350	0.063	0.136	0.319
OBJ Panel Mass (lbm)	10.71	23.38	52.80	8.851	19.07	43.52
Stiffener Load Fraction (%)	0.106	0.178	0.293	0.000	0.000	0.000
Stiffener Mass Fraction (%)	0.050	0.087	0.155	0.090	0.090	0.064
$G(1)$ Panel Buckling	0.90E-3	0.57E-3	-0.98E-7	0.44E-4	0.10E-4	0.65E-7
$G(2)$ Stiffener Buckling	-0.34E00	-0.16E-3	-0.95E-1	-0.10E01	-0.10E01	-0.10E01
$G(3)$ Skin Strength	-0.98E00	-0.93E00	-0.69E00	-0.95E00	-0.77E00	0.41E-4
$G(4)$ Stiffener Strength	-0.98E00	-0.93E00	-0.69E00	-0.10E01	-0.10E01	-0.10E01

$DV(i)$ = Design Variables, $G(i)$ = Constraints, OBJ = Objective Function
Constraints $G(i)$ are feasible when negative, violated when positive, range: $-1 \leq G(i) < \infty$
Skin laminate $[-45/45/90/0]_S$, all plies equal thickness, minimum skin thickness = 0.040 inch
Minimum stiffener thickness = 0.040 inch

Table B3. Diagonally Stiffened Panel Design Data (Compression, Shear)

	PURE COMPRESSION			PURE SHEAR		
	$N_y = 100$ (lbf/in)	$N_y = 1000$ (lbf/in)	$N_y = 10000$ (lbf/in)	$N_{xy} = 100$ (lbf/in)	$N_{xy} = 1000$ (lbf/in)	$N_{xy} = 10000$ (lbf/in)
1 Cell						
$DV(1)$ Stiffener Height (in)	1.707	2.170	2.845	0.852	1.031	1.223
$DV(2)$ Stiffener Thickness (in)	0.040	0.108	0.302	0.048	0.124	0.321
$DV(3)$ Skin Thickness (in)	0.151	0.329	0.717	0.108	0.232	0.501
OBJ Panel Mass (lbm)	20.10	44.67	101.1	14.19	31.02	68.30
Stiffener Load Fraction (%)	0.010	0.015	0.025	0.045	0.065	0.089
Stiffener Mass Fraction (%)	0.038	0.059	0.095	0.032	0.046	0.064
$G(1)$ Panel Buckling	0.23E-6	0.56E-4	0.89E-4	-0.71E-3	0.75E-6	-0.16E-2
$G(2)$ Stiffener Buckling	0.19E-4	-0.18E-3	-0.22E-3	0.64E-3	-0.20E-2	-0.34E-3
$G(3)$ Skin Strength	-0.99E00	-0.95E00	-0.79E00	-0.97E00	-0.87E00	-0.42E00
$G(4)$ Stiffener Strength	-1.00E00	-0.99E00	-0.93E00	-0.98E00	-0.92E00	-0.63E00
2 Cells						
$DV(1)$ Stiffener Height (in)	0.876	1.149	1.619	0.908	1.121	1.331
$DV(2)$ Stiffener Thickness (in)	0.040	0.088	0.269	0.052	0.138	0.352
$DV(3)$ Skin Thickness (in)	0.131	0.283	0.601	0.098	0.210	0.456
OBJ Panel Mass (lbm)	17.28	37.69	83.52	13.20	29.22	65.55
Stiffener Load Fraction (%)	0.032	0.042	0.081	0.080	0.116	0.155
Stiffener Mass Fraction (%)	0.032	0.042	0.082	0.056	0.083	0.112
$G(1)$ Panel Buckling	-0.12E-7	0.15E-1	0.15E-1	0.16E-7	0.49E-8	0.18E-4
$G(2)$ Stiffener Buckling	-0.39E00	-0.18E-3	-0.34E-1	0.44E-4	-0.45E-5	-0.45E-2
$G(3)$ Skin Strength	-0.99E00	-0.95E00	-0.77E00	-0.97E00	-0.87E00	-0.41E00
$G(4)$ Stiffener Strength	-0.99E00	-0.97E00	-0.85E00	-0.98E00	-0.91E00	-0.62E00
3 Cells						
$DV(1)$ Stiffener Height (in)	0.846	0.981	1.366	0.881	1.114	1.362
$DV(2)$ Stiffener Thickness (in)	0.040	0.089	0.264	0.050	0.134	0.347
$DV(3)$ Skin Thickness (in)	0.109	0.236	0.492	0.082	0.179	0.393
OBJ Panel Mass (lbm)	14.62	32.01	70.45	11.47	25.97	60.16
Stiffener Load Fraction (%)	0.072	0.085	0.155	0.080	0.120	0.164
Stiffener Mass Fraction (%)	0.049	0.058	0.109	0.081	0.122	0.167
$G(1)$ Panel Buckling	0.69E-8	0.12E-6	0.22E-1	0.13E-4	-0.28E-3	-0.18E-3
$G(2)$ Stiffener Buckling	-0.20E00	0.24E-6	-0.28E-3	-0.51E-3	0.20E-4	-0.66E-3
$G(3)$ Skin Strength	-0.99E00	-0.94E00	-0.74E00	-0.96E00	-0.84E00	-0.32E00
$G(4)$ Stiffener Strength	-0.99E00	-0.95E00	-0.79E00	-0.98E00	-0.92E00	-0.64E00
4 Cells						
$DV(1)$ Stiffener Height (in)	0.813	0.914	1.274	0.844	1.109	1.393
$DV(2)$ Stiffener Thickness (in)	0.040	0.092	0.269	0.047	0.130	0.342
$DV(3)$ Skin Thickness (in)	0.091	0.197	0.406	0.070	0.152	0.342
OBJ Panel Mass (lbm)	12.46	27.40	61.13	10.03	23.37	56.56
Stiffener Load Fraction (%)	0.119	0.139	0.242	0.073	0.116	0.162
Stiffener Mass Fraction (%)	0.071	0.083	0.152	0.108	0.168	0.229
$G(1)$ Panel Buckling	0.36E-8	0.56E-7	0.31E-2	0.66E-4	0.19E-5	0.79E-8
$G(2)$ Stiffener Buckling	-0.80E-1	0.13E-6	-0.24E-3	-0.18E-3	-0.65E-5	-0.61E-4
$G(3)$ Skin Strength	-0.99E00	-0.93E00	-0.71E00	-0.96E00	-0.82E00	-0.22E00
$G(4)$ Stiffener Strength	-0.99E00	-0.94E00	-0.75E00	-0.98E00	-0.92E00	-0.66E00

$DV(i)$ = Design Variables, $G(i)$ = Constraints, OBJ = Objective Function
Constraints $G(i)$ are feasible when negative, violated when positive, range: $-1 \leq G(i) < \infty$
Skin laminate $[-45/45/90/0]_S$, all plies equal thickness, minimum skin thickness = 0.040 inch
Minimum stiffener thickness = 0.040 inch

Diagonally Stiffened Panel Design Data (Compression, Shear), cont'd

	PURE COMPRESSION			PURE SHEAR		
	$N_y = 100$ (lbf/in)	$N_y = 1000$ (lbf/in)	$N_y = 10000$ (lbf/in)	$N_{xy} = 100$ (lbf/in)	$N_{xy} = 1000$ (lbf/in)	$N_{xy} = 10000$ (lbf/in)
5 Cells						
$DV(1)$ Stiffener Height (in)	0.685	1.007	1.414	0.824	1.092	1.270
$DV(2)$ Stiffener Thickness (in)	0.040	0.107	0.304	0.045	0.126	0.301
$DV(3)$ Skin Thickness (in)	0.078	0.160	0.320	0.060	0.133	0.322
OBJ Panel Mass (lbm)	10.81	23.98	55.10	8.956	21.52	53.86
Stiffener Load Fraction (%)	0.151	0.254	0.403	0.068	0.109	0.122
Stiffener Mass Fraction (%)	0.084	0.149	0.259	0.139	0.212	0.236
$G(1)$ Panel Buckling	-0.33E-5	0.43E-4	0.18E-4	0.22E-3	-0.26E-4	0.44E-6
$G(2)$ Stiffener Buckling	-0.23E00	-0.24E-2	-0.21E-5	-0.18E-3	0.93E-6	0.60E-6
$G(3)$ Skin Strength	-0.98E00	-0.93E00	-0.72E00	-0.95E00	-0.79E00	-0.13E00
$G(4)$ Stiffener Strength	-0.99E00	-0.93E00	-0.74E00	-0.98E00	-0.92E00	-0.69E00
6 Cells						
$DV(1)$ Stiffener Height (in)	0.765	1.084	1.422	0.800	1.053	1.072
$DV(2)$ Stiffener Thickness (in)	0.041	0.117	0.306	0.043	0.118	0.239
$DV(3)$ Skin Thickness (in)	0.066	0.133	0.272	0.055	0.123	0.329
OBJ Panel Mass (lbm)	9.662	21.92	51.91	8.378	20.57	52.04
Stiffener Load Fraction (%)	0.229	0.374	0.500	0.059	0.093	0.073
Stiffener Mass Fraction (%)	0.128	0.228	0.331	0.161	0.237	0.194
$G(1)$ Panel Buckling	0.51E-2	0.65E-2	-0.15E-5	0.22E-5	-0.77E-6	-0.66E-4
$G(2)$ Stiffener Buckling	-0.30E-3	-0.34E-3	-0.36E-3	-0.33E-5	0.27E-6	-0.74E-4
$G(3)$ Skin Strength	-0.98E00	-0.93E00	-0.72E00	-0.95E00	-0.77E00	-0.10E00
$G(4)$ Stiffener Strength	-0.98E00	-0.93E00	-0.73E00	-0.98E00	-0.93E00	-0.72E00
7 Cells						
$DV(1)$ Stiffener Height (in)	0.778	1.047	1.370	0.773	1.011	0.945
$DV(2)$ Stiffener Thickness (in)	0.043	0.115	0.298	0.040	0.109	0.201
$DV(3)$ Skin Thickness (in)	0.058	0.117	0.242	0.052	0.117	0.323
OBJ Panel Mass (lbm)	8.886	20.43	49.44	7.997	19.95	49.95
Stiffener Load Fraction (%)	0.300	0.435	0.557	0.051	0.077	0.050
Stiffener Mass Fraction (%)	0.171	0.270	0.376	0.176	0.252	0.173
$G(1)$ Panel Buckling	0.73E-4	-0.44E-5	-0.15E-3	-0.91E-6	0.49E-8	1.00E-8
$G(2)$ Stiffener Buckling	0.59E-4	-0.18E-4	-0.14E-3	-0.75E-6	-0.34E-5	-0.81E-5
$G(3)$ Skin Strength	-0.98E00	-0.93E00	-0.72E00	-0.94E00	-0.75E00	-0.63E-1
$G(4)$ Stiffener Strength	-0.98E00	-0.93E00	-0.73E00	-0.98E00	-0.93E00	-0.75E00
8 Cells						
$DV(1)$ Stiffener Height (in)	0.761	1.063	1.322	0.786	0.972	0.907
$DV(2)$ Stiffener Thickness (in)	0.043	0.117	0.288	0.040	0.101	0.187
$DV(3)$ Skin Thickness (in)	0.052	0.101	0.219	0.048	0.111	0.306
OBJ Panel Mass (lbm)	8.284	19.37	47.69	7.708	19.35	47.85
Stiffener Load Fraction (%)	0.352	0.516	0.601	0.050	0.065	0.042
Stiffener Mass Fraction (%)	0.204	0.334	0.414	0.212	0.265	0.184
$G(1)$ Panel Buckling	0.54E-3	0.76E-3	-0.21E-7	0.15E-4	-0.38E-7	0.28E-4
$G(2)$ Stiffener Buckling	0.86E-5	-0.34E-3	-0.23E-4	-0.78E-2	-0.92E-4	-0.64E-4
$G(3)$ Skin Strength	-0.98E00	-0.93E00	-0.72E00	-0.94E00	-0.73E00	-0.56E-3
$G(4)$ Stiffener Strength	-0.98E00	-0.93E00	-0.73E00	-0.99E00	-0.94E00	-0.76E00

$DV(i)$ = Design Variables, $G(i)$ = Constraints, OBJ = Objective Function
Constraints $G(i)$ are feasible when negative, violated when positive, range: $-1 \leq G(i) < \infty$
Skin laminate $[-45/45/90/0]_S$, all plies equal thickness, minimum skin thickness = 0.040 inch
Minimum stiffener thickness = 0.040 inch

Table B4. Cross-Stiffened Panel Design Data (Compression, Shear)

	PURE COMPRESSION			PURE SHEAR		
	$N_y = 100$ (lbf/in)	$N_y = 1000$ (lbf/in)	$N_y = 10000$ (lbf/in)	$N_{xy} = 100$ (lbf/in)	$N_{xy} = 1000$ (lbf/in)	$N_{xy} = 10000$ (lbf/in)
1 Cell						
$DV(1)$ Stiffener Height (in)	2.613	3.614	5.084	0.911	1.205	1.538
$DV(2)$ Stiffener Thickness (in)	0.040	0.113	0.321	0.047	0.133	0.362
$DV(3)$ Skin Thickness (in)	0.116	0.256	0.570	0.082	0.177	0.390
OBJ Panel Mass (lbm)	16.85	40.56	104.2	11.29	25.74	60.53
Stiffener Load Fraction (%)	0.004	0.006	0.012	0.048	0.080	0.120
Stiffener Mass Fraction (%)	0.120	0.195	0.302	0.074	0.121	0.178
$G(1)$ Panel Buckling	0.78E-3	0.58E-3	0.12E-2	0.21E-4	0.46E-4	-0.52E-8
$G(2)$ Stiffener Buckling	-0.25E-1	-0.18E-3	0.71E-4	-0.18E-3	-0.22E-3	-0.27E-4
$G(3)$ Skin Strength	-0.99E00	-0.94E00	-0.74E00	-0.96E00	-0.83E00	-0.28E00
$G(4)$ Stiffener Strength	-1.00E00	-0.99E00	-0.97E00	-0.98E00	-0.93E00	-0.69E00
2 Cells						
$DV(1)$ Stiffener Height (in)	1.333	1.796	2.515	0.670	0.855	1.142
$DV(2)$ Stiffener Thickness (in)	0.040	0.098	0.283	0.041	0.113	0.327
$DV(3)$ Skin Thickness (in)	0.118	0.257	0.555	0.085	0.182	0.381
OBJ Panel Mass (lbm)	16.21	36.69	86.78	11.46	25.34	56.92
Stiffener Load Fraction (%)	0.019	0.029	0.052	0.075	0.117	0.197
Stiffener Mass Fraction (%)	0.073	0.107	0.183	0.054	0.085	0.146
$G(1)$ Panel Buckling	0.52E-3	0.23E-3	0.62E-3	0.44E-4	0.23E-4	0.16E-2
$G(2)$ Stiffener Buckling	-0.25E00	-0.17E-3	-0.31E-3	0.21E-4	0.14E-4	-0.43E-1
$G(3)$ Skin Strength	-0.99E00	-0.94E00	-0.74E00	-0.97E00	-0.85E00	-0.33E00
$G(4)$ Stiffener Strength	-1.00E00	-0.98E00	-0.91E00	-0.98E00	-0.90E00	-0.57E00
3 Cells						
$DV(1)$ Stiffener Height (in)	0.952	1.324	1.815	0.559	0.706	0.995
$DV(2)$ Stiffener Thickness (in)	0.040	0.095	0.270	0.040	0.099	0.311
$DV(3)$ Skin Thickness (in)	0.107	0.231	0.495	0.078	0.168	0.345
OBJ Panel Mass (lbm)	14.64	32.81	76.12	10.58	28.25	52.18
Stiffener Load Fraction (%)	0.044	0.066	0.113	0.087	0.123	0.231
Stiffener Mass Fraction (%)	0.069	0.102	0.170	0.056	0.080	0.157
$G(1)$ Panel Buckling	0.38E-3	0.21E-3	0.59E-3	0.27E-4	0.23E-4	-0.12E-3
$G(2)$ Stiffener Buckling	-0.33E00	-0.13E-3	-0.97E-3	-0.15E00	0.48E-4	-0.96E-1
$G(3)$ Skin Strength	-0.99E00	-0.94E00	-0.73E00	-0.96E00	-0.83E00	-0.29E00
$G(4)$ Stiffener Strength	-0.99E00	-0.97E00	-0.86E00	-0.97E00	-0.89E00	-0.51E00
4 Cells						
$DV(1)$ Stiffener Height (in)	0.787	1.104	1.536	0.477	0.638	0.918
$DV(2)$ Stiffener Thickness (in)	0.040	0.094	0.267	0.040	0.092	0.278
$DV(3)$ Skin Thickness (in)	0.094	0.203	0.427	0.071	0.152	0.313
OBJ Panel Mass (lbm)	13.05	29.14	67.34	9.652	21.26	48.04
Stiffener Load Fraction (%)	0.075	0.111	0.190	0.088	0.121	0.226
Stiffener Mass Fraction (%)	0.076	0.111	0.191	0.062	0.087	0.167
$G(1)$ Panel Buckling	0.85E-4	0.47E-3	0.11E-2	-0.21E-6	0.66E-3	0.35 -4
$G(2)$ Stiffener Buckling	-0.36E00	-0.99E-3	0.32E-3	-0.35E00	-0.11E-2	-0.32E-3
$G(3)$ Skin Strength	-0.99E00	-0.93E00	-0.71E00	-0.96E00	-0.82E00	-0.21E00
$G(4)$ Stiffener Strength	-0.99E00	-0.96E00	-0.81E00	-0.97E00	-0.88E00	-0.49E00

$DV(i)$ = Design Variables, $G(i)$ = Constraints, OBJ = Objective Function
Constraints $G(i)$ are feasible when negative, violated when positive, range: $-1 \leq G(i) < \infty$
Skin laminate $[-45/45/90/0]_S$, all plies equal thickness, minimum skin thickness = 0.040 inch
Minimum stiffener thickness = 0.040 inch

Cross-Stiffened Panel Design Data (Compression, Shear), cont'd

	PURE COMPRESSION			PURE SHEAR		
	$N_y = 100$ (lbf/in)	$N_y = 1000$ (lbf/in)	$N_y = 10000$ (lbf/in)	$N_{xy} = 100$ (lbf/in)	$N_{xy} = 1000$ (lbf/in)	$N_{xy} = 10000$ (lbf/in)
5 Cells						
$DV(1)$ Stiffener Height (in)	0.689	0.987	1.374	0.442	0.623	0.899
$DV(2)$ Stiffener Thickness (in)	0.040	0.094	0.265	0.040	0.090	0.273
$DV(3)$ Skin Thickness (in)	0.082	0.175	0.362	0.064	0.137	0.282
OBJ Panel Mass (lbm)	11.52	25.74	59.62	8.810	19.53	44.98
Stiffener Load Fraction (%)	0.110	0.164	0.271	0.088	0.125	0.232
Stiffener Mass Fraction (%)	0.088	0.132	0.224	0.074	0.106	0.201
$G(1)$ Panel Buckling	0.88E-4	0.18E-3	0.14E-2	0.17E-4	0.37E-3	0.23E-2
$G(2)$ Stiffener Buckling	-0.38E00	-0.17E-3	0.38E-3	-0.44E00	-0.22E-3	-0.36E-2
$G(3)$ Skin Strength	-0.98E00	-0.93E00	-0.69E00	-0.95E00	-0.80E00	-0.13E00
$G(4)$ Stiffener Strength	-0.99E00	-0.95E00	-0.77E00	-0.97E00	-0.88E00	-0.49E00
6 Cells						
$DV(1)$ Stiffener Height (in)	0.624	0.918	1.244	0.408	0.627	0.890
$DV(2)$ Stiffener Thickness (in)	0.040	0.095	0.258	0.040	0.091	0.270
$DV(3)$ Skin Thickness (in)	0.072	0.151	0.311	0.058	0.122	0.250
OBJ Panel Mass (lbm)	10.22	22.90	53.38	8.079	17.97	42.11
Stiffener Load Fraction (%)	0.148	0.224	0.340	0.084	0.132	0.238
Stiffener Mass Fraction (%)	0.104	0.161	0.255	0.086	0.135	0.242
$G(1)$ Panel Buckling	-0.31E-6	0.21E-3	0.54E-3	0.15E-3	0.96E-3	0.15E-2
$G(2)$ Stiffener Buckling	-0.40E00	-0.34E-2	-0.14E-3	-0.52E00	-0.41E-3	-0.23E-3
$G(3)$ Skin Strength	-0.98E00	-0.92E00	-0.68E00	-0.95E00	-0.77E00	-0.27E00
$G(4)$ Stiffener Strength	-0.99E00	-0.94E00	-0.74E00	-0.97E00	-0.88E00	-0.48E00
7 Cells						
$DV(1)$ Stiffener Height (in)	0.572	0.828	1.178	0.391	0.605	0.831
$DV(2)$ Stiffener Thickness (in)	0.040	0.091	0.257	0.040	0.088	0.243
$DV(3)$ Skin Thickness (in)	0.063	0.132	0.264	0.053	0.112	0.258
OBJ Panel Mass (lbm)	9.138	20.53	48.36	7.497	16.91	42.75
Stiffener Load Fraction (%)	0.186	0.264	0.419	0.082	0.124	0.190
Stiffener Mass Fraction (%)	0.121	0.178	0.302	0.101	0.151	0.228
$G(1)$ Panel Buckling	-0.20E-6	0.45E-3	0.16E-2	0.73E-4	0.17E-1	0.19E-8
$G(2)$ Stiffener Buckling	-0.42E00	-0.71E-4	-0.10E-2	-0.56E00	-0.17E-1	-0.50E-5
$G(3)$ Skin Strength	-0.98E00	-0.92E00	-0.66E00	-0.95E00	-0.75E00	-0.56E-6
$G(4)$ Stiffener Strength	-0.98E00	-0.93E00	-0.71E00	-0.97E00	-0.88E00	-0.52E00
8 Cells						
$DV(1)$ Stiffener Height (in)	0.546	0.844	1.216	0.400	0.618	0.763
$DV(2)$ Stiffener Thickness (in)	0.040	0.097	0.265	0.040	0.088	0.213
$DV(3)$ Skin Thickness (in)	0.056	0.113	0.220	0.048	0.102	0.274
OBJ Panel Mass (lbm)	8.324	18.91	45.63	7.000	15.98	43.81
Stiffener Load Fraction (%)	0.228	0.352	0.525	0.084	0.129	0.141
Stiffener Mass Fraction (%)	0.143	0.234	0.383	0.124	0.186	0.201
$G(1)$ Panel Buckling	0.35E-2	0.22E-2	0.13E-2	0.95E-3	0.96E-2	0.23E-6
$G(2)$ Stiffener Buckling	-0.41E00	-0.23E-1	-0.10E-3	-0.54E00	-0.22E-3	-0.67E-6
$G(3)$ Skin Strength	-0.98E00	-0.91E00	-0.67E00	-0.94E00	-0.73E00	-0.40E-6
$G(4)$ Stiffener Strength	-0.98E00	-0.92E00	-0.71E00	-0.97E00	-0.88E00	-0.56E00

$DV(i)$ = Design Variables, $G(i)$ = Constraints, OBJ = Objective Function
Constraints $G(i)$ are feasible when negative, violated when positive, range: $-1 \leq G(i) < \infty$
Skin laminate $[-45/45/90/0]_S$, all plies equal thickness, minimum skin thickness = 0.040 inch
Minimum stiffener thickness = 0.040 inch

Table B5. Longitudinally, Diagonally, and Cross-Stiffened Panels Design Data (10000 lbf/in Shear with Material Failure Constraint Violation)

	PURE SHEAR N_{xy} = 10000 lbf/in	
	7 Cells	8 Cells
Longitudinally Stiffened Panel		
$DV(1)$ Stiffener Height (in)	4.473	4.160
$DV(2)$ Stiffener Thickness (in)	0.040	0.040
$DV(3)$ Skin Thickness (in)	0.312	0.293
OBJ Panel Mass (lbm)	43.23	41.08
Stiffener Load Fraction (%)	0.000	0.000
Stiffener Mass Fraction (%)	0.079	0.091
$G(1)$ Panel Buckling	-0.20E-6	0.49E-3
$G(2)$ Stiffener Buckling	-0.10E01	-0.10E01
$G(3)$ Skin Strength	0.24E-1	0.91E-1
$G(4)$ Stiffener Strength	-0.10E01	-0.10E01
Diagonally Stiffened Panel		
$DV(1)$ Stiffener Height (in)		0.912
$DV(2)$ Stiffener Thickness (in)		0.188
$DV(3)$ Skin Thickness (in)		0.305
OBJ Panel Mass (lbm)		47.83
Stiffener Load Fraction (%)	N/A	0.043
Stiffener Mass Fraction (%)		0.186
$G(1)$ Panel Buckling		0.10E-2
$G(2)$ Stiffener Buckling		-0.15E-3
$G(3)$ Skin Strength		0.20E-2
$G(4)$ Stiffener Strength		-0.76E00
Cross-Stiffened Panel		
$DV(1)$ Stiffener Height (in)	0.886	0.884
$DV(2)$ Stiffener Thickness (in)	0.267	0.265
$DV(3)$ Skin Thickness (in)	0.229	0.211
OBJ Panel Mass (lbm)	40.67	39.63
Stiffener Load Fraction (%)	0.237	0.235
Stiffener Mass Fraction (%)	0.281	0.320
$G(1)$ Panel Buckling	0.13E-1	0.65E-2
$G(2)$ Stiffener Buckling	-0.34E-3	-0.36E-2
$G(3)$ Skin Strength	0.63E-1	0.16E00
$G(4)$ Stiffener Strength	-0.49E00	-0.50E00

$DV(i)$ = Design Variable, $G(i)$ = Constraint, OBJ = Objective Function, N/A = Not Applicable
Constraints $G(i)$ are feasible when negative, violated when positive, range: $-1 \leq G(i) < \infty$
Skin laminate $[-45/45/90/0]_S$, all plies equal thickness, minimum skin thickness = 0.040 inch
Minimum stiffener thickness = 0.040 inch

Table B6. Flat Plate and Longitudinally, Diagonally, and Cross-Stiffened Panels Design Data (Combined Compression-Shear)

	COMBINED COMPRESSION-SHEAR $N_y = N_{xy} = N$					
	$N = 100$ (lbf/in)	$N = 300$ (lbf/in)	$N = 1000$ (lbf/in)	$N = 3000$ (lbf/in)	$N = 10000$ (lbf/in)	$N = 30000$ (lbf/in)
Flat Plate						
$DV(1)$ Skin Thickness (in)	0.212	0.305	0.456	0.657	0.982	1.416
OBJ Plate Mass (lbm)	27.01	38.96	58.19	83.93	125.4	180.8
$G(1)$ Skin Buckling	-0.23E-6	-0.14E-5	-0.13E-5	0.12E-5	0.93E-4	-0.46E-6
$G(2)$ Skin Strength	-0.99E00	-0.97E00	-0.94E00	-0.87E00	-0.70E00	-0.37E00
Longitudinally Stiffened Panel						
$DV(1)$ Stiffener Height (in)	0.965	1.132	1.324	1.535	1.717	1.257
$DV(2)$ Stiffener Thickness (in)	0.049	0.080	0.136	0.219	0.352	0.357
$DV(3)$ Skin Thickness (in)	0.081	0.117	0.173	0.248	0.378	0.849
OBJ Panel Mass (lbm)	11.44	16.92	26.13	39.22	61.81	118.4
Stiff. Load Frac. - Comp. (%)	0.187	0.236	0.292	0.349	0.388	0.173
Stiff. Load Frac. - Shear (%)	0.000	0.000	0.000	0.000	0.000	0.000
Stiffener Mass Fraction (%)	0.092	0.120	0.154	0.191	0.219	0.085
$G(1)$ Panel Buckling	0.91E-2	0.22E-3	0.11E-2	0.80E-3	0.87E-3	-0.15E-5
$G(2)$ Stiffener Buckling	-0.46E-2	-0.13E-3	-0.19E-2	-0.50E-3	0.21E-3	0.21E-4
$G(3)$ Skin Strength	-0.97E00	-0.93E00	-0.84E00	-0.68E00	-0.30E00	-0.76E-3
$G(4)$ Stiffener Strength	-0.99E00	-0.97E00	-0.94E00	-0.88E00	-0.75E00	-0.55E00
Diagonally Stiffened Panel						
$DV(1)$ Stiffener Height (in)	0.844	0.973	1.126	1.229	0.981	0.962
$DV(2)$ Stiffener Thickness (in)	0.058	0.093	0.154	0.233	0.276	0.344
$DV(3)$ Skin Thickness (in)	0.057	0.083	0.125	0.193	0.377	0.808
OBJ Panel Mass (lbm)	9.830	15.22	24.91	39.49	62.24	120.3
Stiff. Load Frac. - Comp. (%)	0.423	0.485	0.547	0.562	0.383	0.262
Stiff. Load Frac. - Shear (%)	0.063	0.079	0.099	0.105	0.054	0.031
Stiffener Mass Fraction (%)	0.256	0.307	0.362	0.377	0.226	0.143
$G(1)$ Panel Buckling	0.58E-3	0.75E-3	-0.19E-5	0.81E-3	0.34E-2	0.95E-5
$G(2)$ Stiffener Buckling	-0.13E-3	0.65E-3	0.56E-6	0.73E-3	-0.26E-3	0.43E-4
$G(3)$ Skin Strength	-0.96E00	-0.91E00	-0.81E00	-0.63E00	-0.33E00	-0.78E00
$G(4)$ Stiffener Strength	-0.97E00	-0.95E00	-0.89E00	-0.79E00	-0.57E00	-0.32E00
Cross-Stiffened Panel						
$DV(1)$ Stiffener Height (in)	0.508	0.591	0.707	0.836	1.003	0.910
$DV(2)$ Stiffener Thickness (in)	0.041	0.068	0.119	0.199	0.344	0.499
$DV(3)$ Skin Thickness (in)	0.061	0.086	0.126	0.175	0.251	0.715
OBJ Panel Mass (lbm)	8.887	13.20	20.62	31.38	50.85	115.9
Stiff. Load Frac. - Comp. (%)	0.206	0.261	0.336	0.418	0.510	0.325
Stiff. Load Frac. - Shear (%)	0.087	0.114	0.156	0.208	0.275	0.150
Stiffener Mass Fraction (%)	0.127	0.165	0.221	0.287	0.368	0.213
$G(1)$ Panel Buckling	0.32E-3	0.84E-3	0.13E-2	0.24E-2	0.17E-2	-0.16E-3
$G(2)$ Stiffener Buckling	-0.22E-3	-0.94E-3	-0.13E-4	-0.11E-2	-0.25E-3	-0.43E00
$G(3)$ Skin Strength	-0.96E00	-0.91E00	-0.81E00	-0.63E00	-0.22E00	-0.63E-4
$G(4)$ Stiffener Strength	-0.96E00	-0.92E00	-0.84E00	-0.68E00	-0.34E00	-0.12E00

$DV(i)$ = Design Variable, $G(i)$ = Constraint, OBJ = Objective Function
Constraints $G(i)$ are feasible when negative, violated when positive, range: $-1 \leq G(i) < \infty$
Skin laminate $[-45/45/90/0]_S$, all plies equal thickness, minimum skin thickness = 0.040 inch
Minimum stiffener thickness = 0.040 inch

Appendix C. Buckled Mode Shapes for Optimum Wing Rib Panels

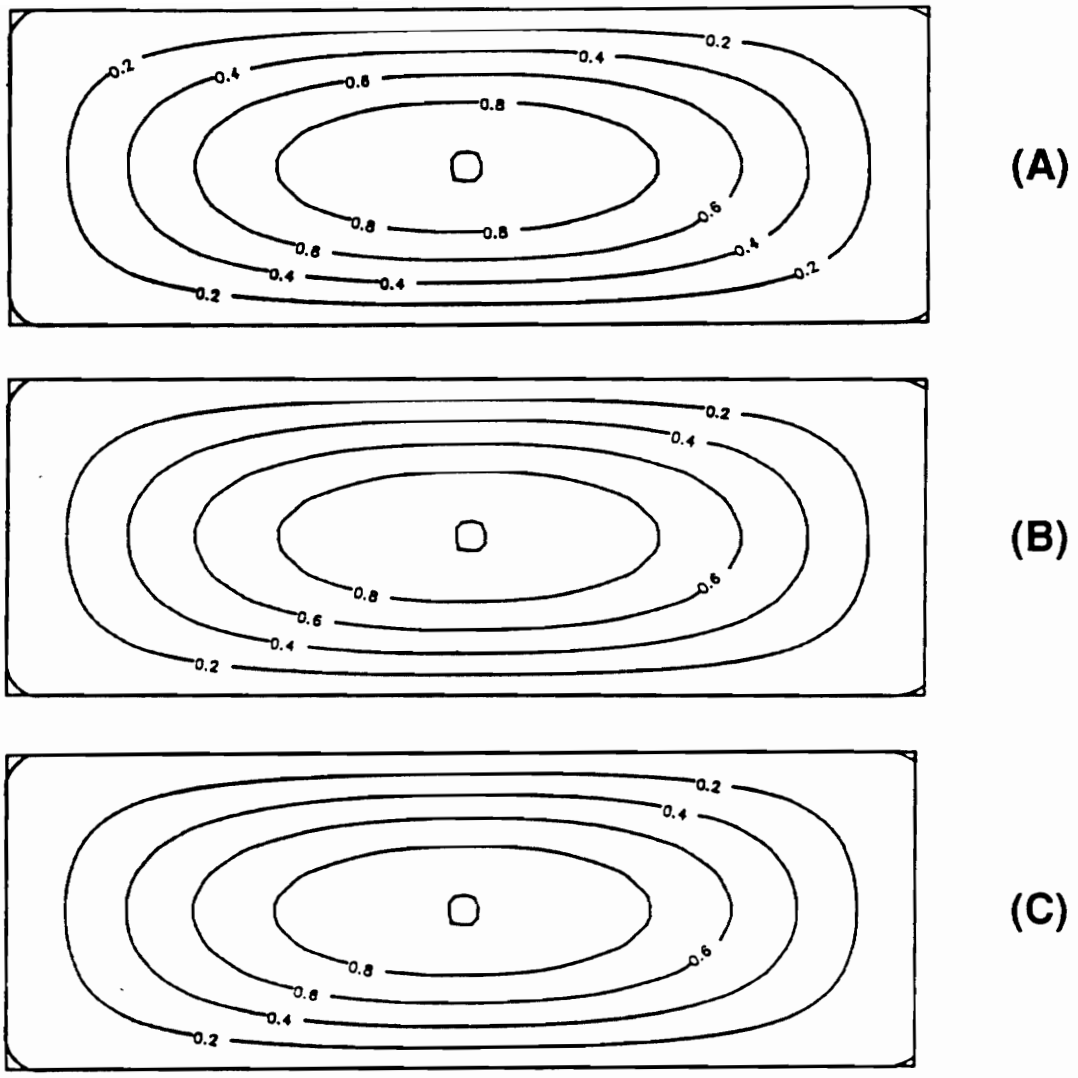

Figure C1. Flat Plate Buckled Mode Shapes, Compression: A) 100 lbf/in B) 1000 lbf/in C) 10000 lbf/in

Not Applicable (A)

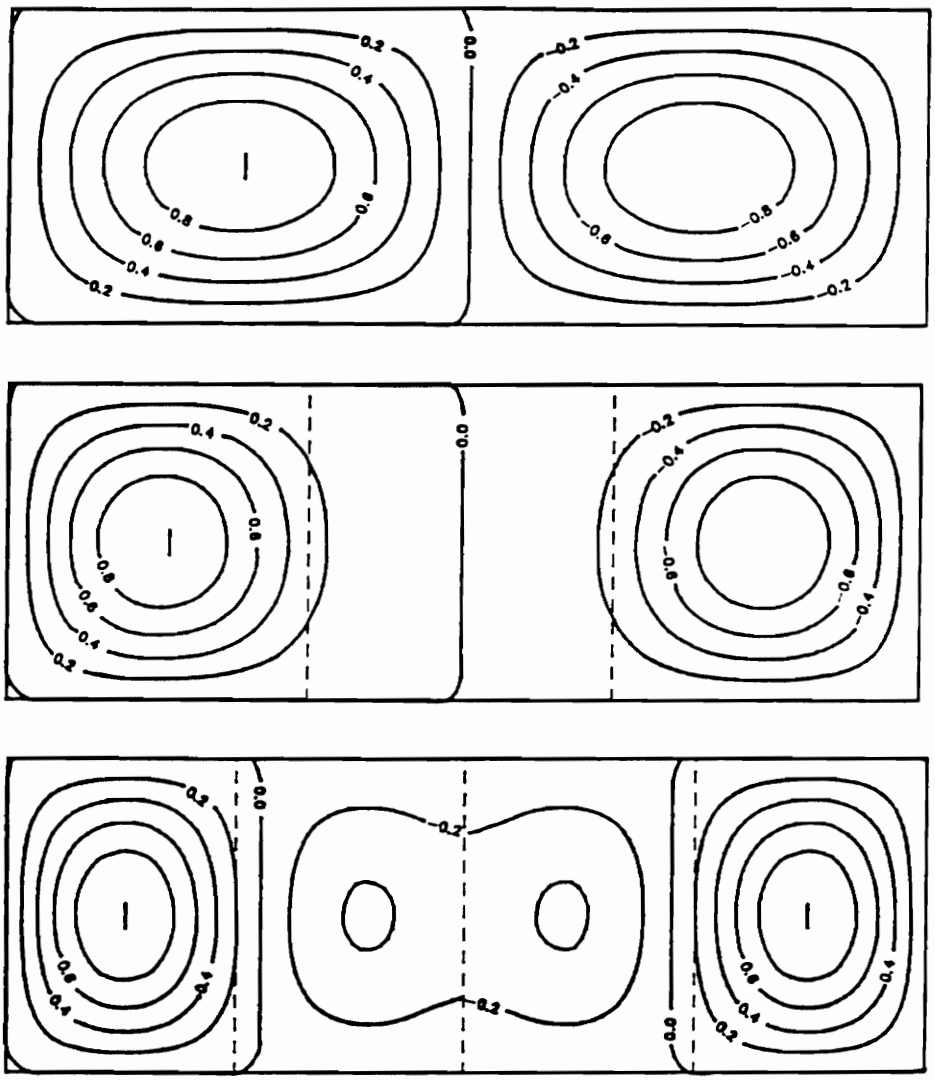

Figure C2. Longitudinally Stiffened Panel Buckled Mode Shapes, 100 lbf/in Compression: A) 1 Cell B) 2 Cells C) 3 Cells D) 4 Cells E) 5 Cells F) 6 Cells G) 7 Cells H) 8 Cells

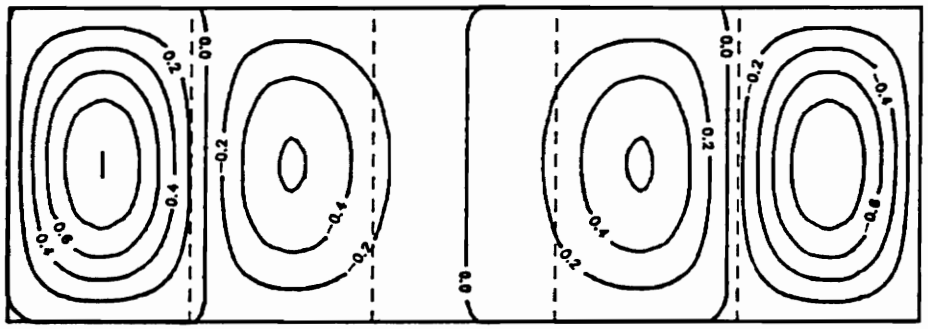

(E)

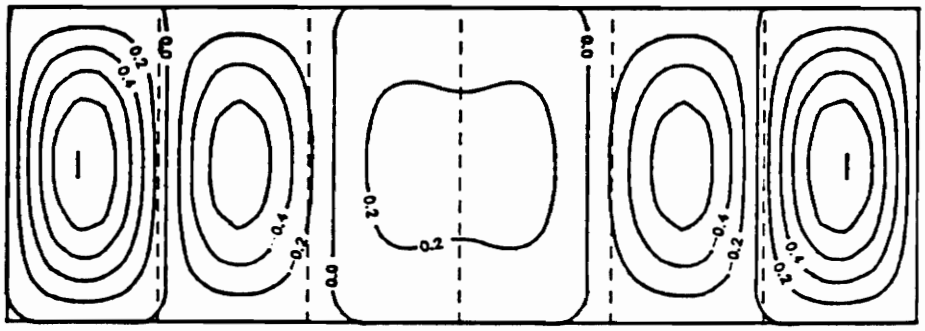

(F)

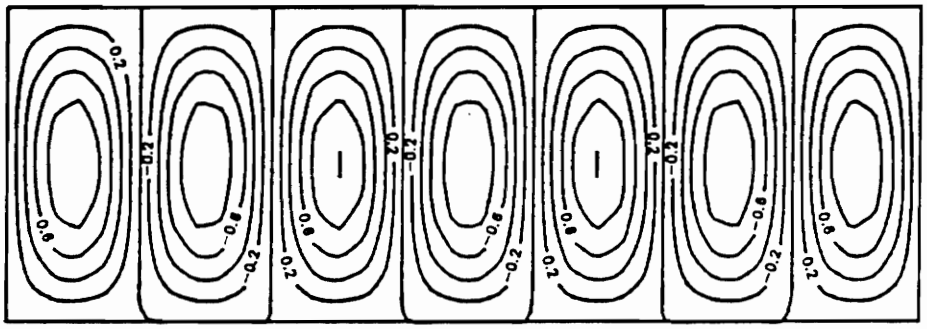

(G)

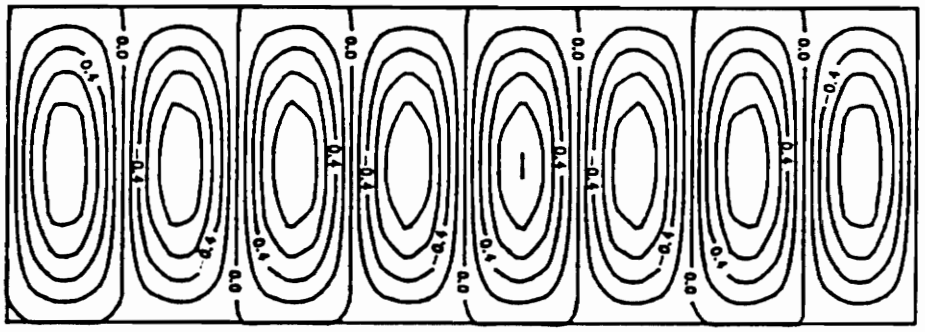

(H)

Longitudinally Stiffened Panel Buckled Mode Shapes, 100 lbf/in Compression, cont'd

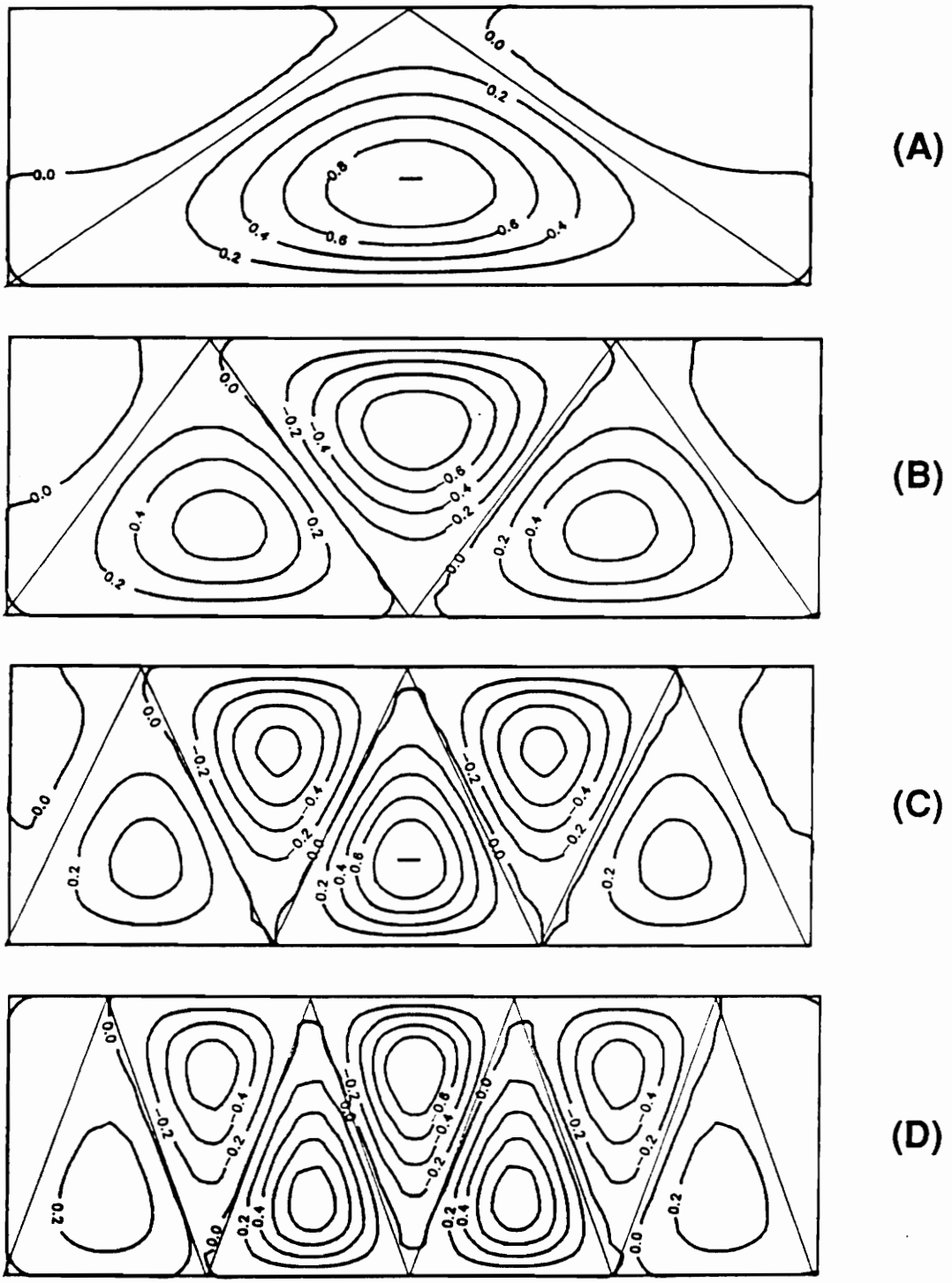

Figure C3. Diagonally Stiffened Panel Buckled Mode Shapes, 100 lbf/in Compression: A) 1 Cell B) 2 Cells C) 3 Cells D) 4 Cells E) 5 Cells F) 6 Cells G) 7 Cells H) 8 Cells

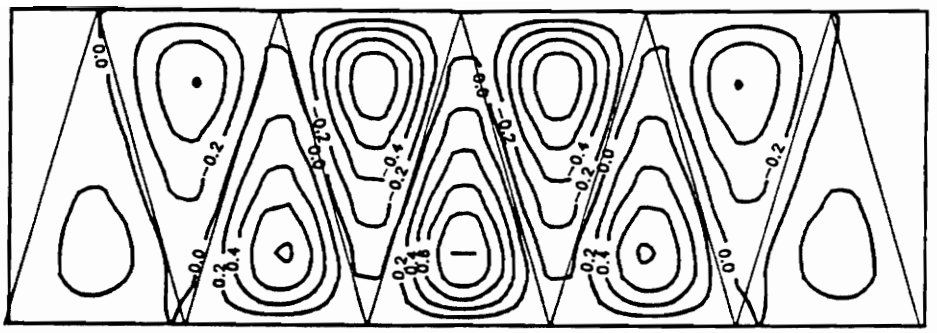

(E)

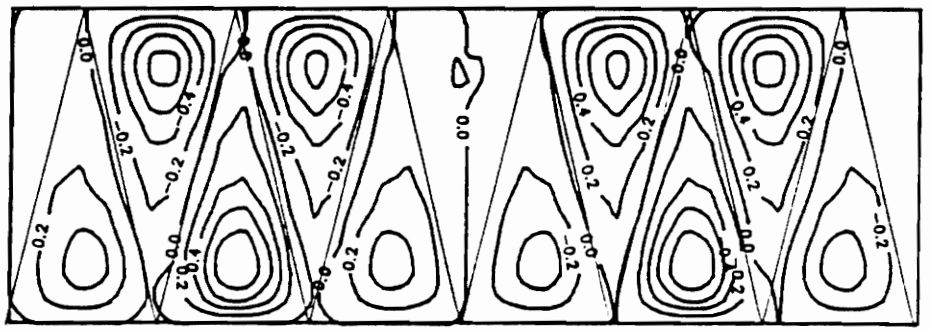

(F)

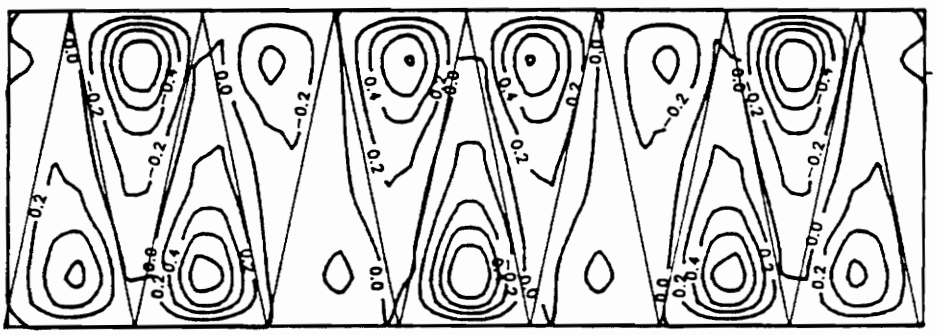

(G)

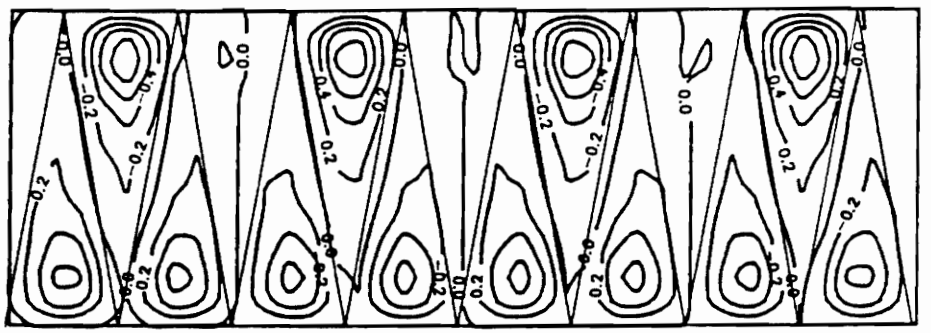

(H)

Diagonally Stiffened Panel Buckled Mode Shapes, 100 lbf/in Compression, cont'd

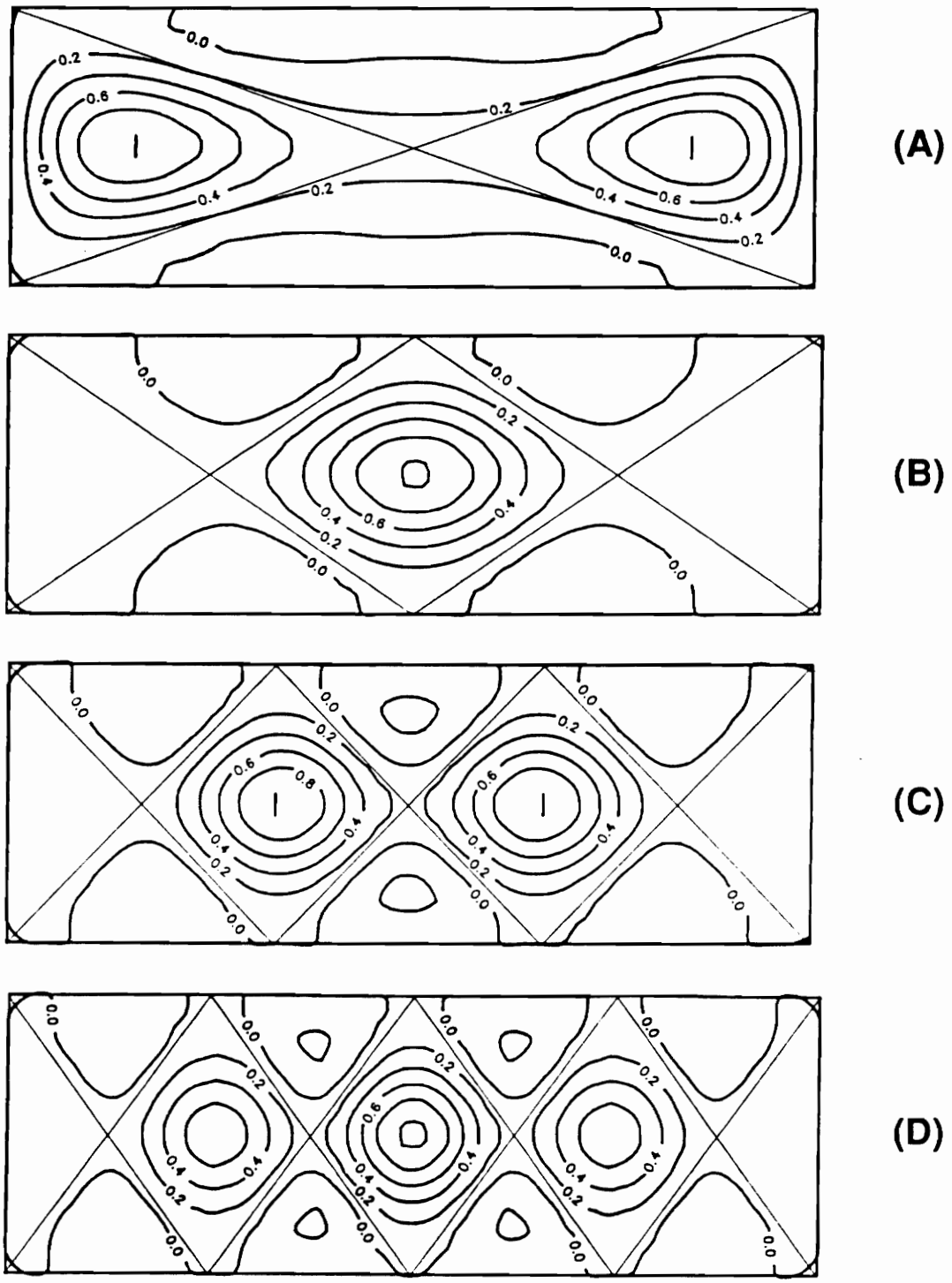

Figure C4. **Cross-Stiffened Panel Buckled Mode Shapes, 100 lbf/in Compression:** A) 1 Cell B) 2 Cells C) 3 Cells D) 4 Cells E) 5 Cells F) 6 Cells G) 7 Cells H) 8 Cells

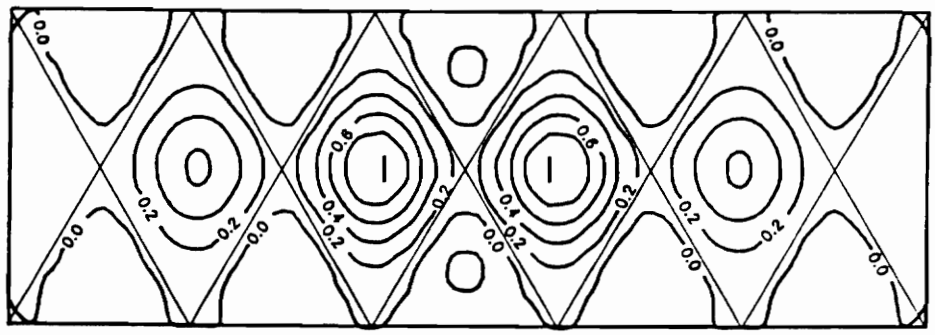

(E)

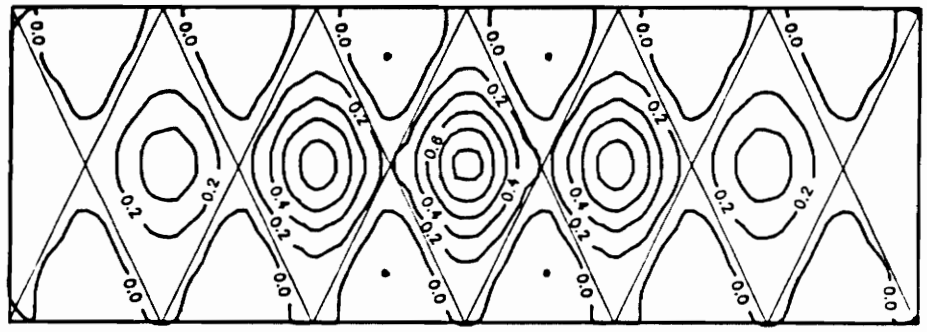

(F)

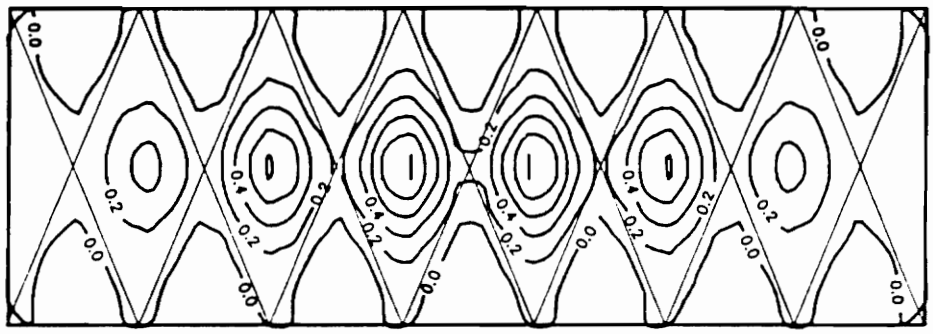

(G)

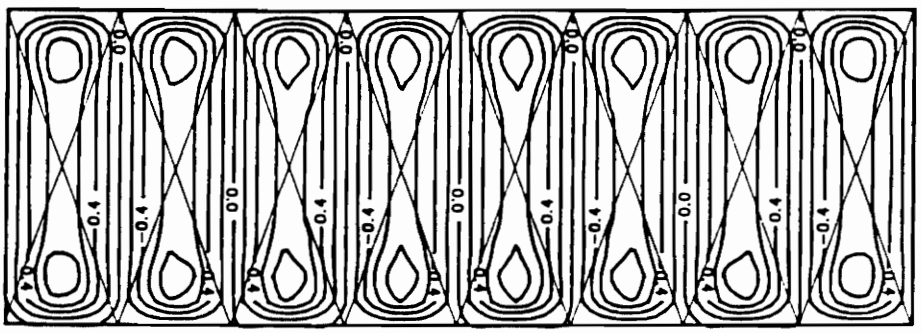

(H)

Cross-Stiffened Panel Buckled Mode Shapes, 100 lbf/in Compression, cont'd

Not Applicable (A)

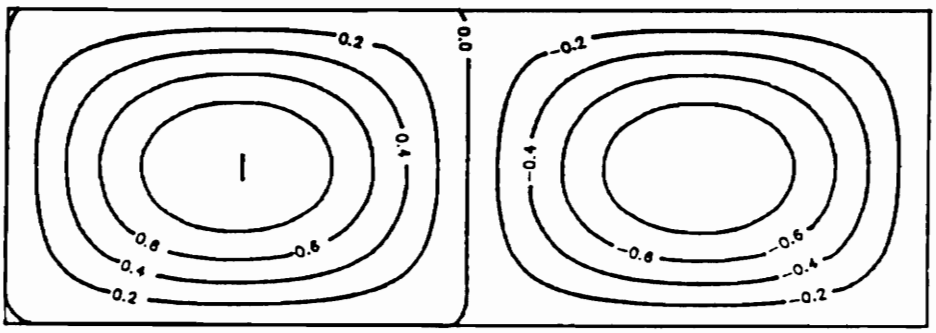

(B)

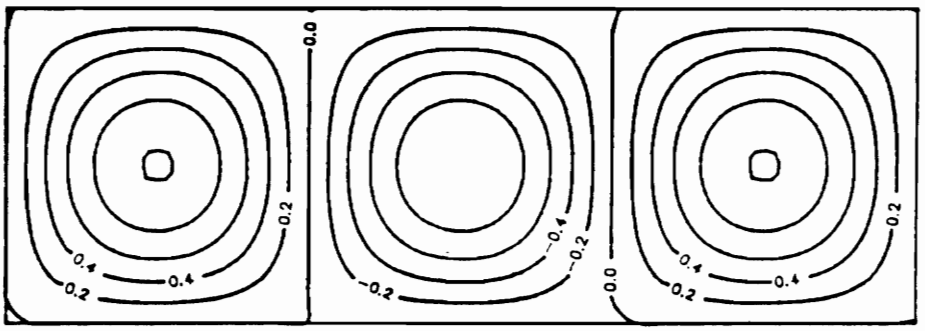

(C)

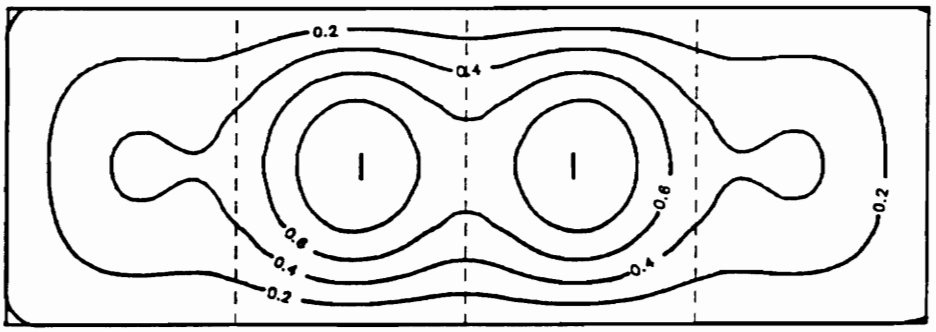

(D)

Figure C5. **Longitudinally Stiffened Panel Buckled Mode Shapes, 1000 lbf/in Compression:** A) 1 Cell B) 2 Cells C) 3 Cells D) 4 Cells E) 5 Cells F) 6 Cells G) 7 Cells H) 8 Cells

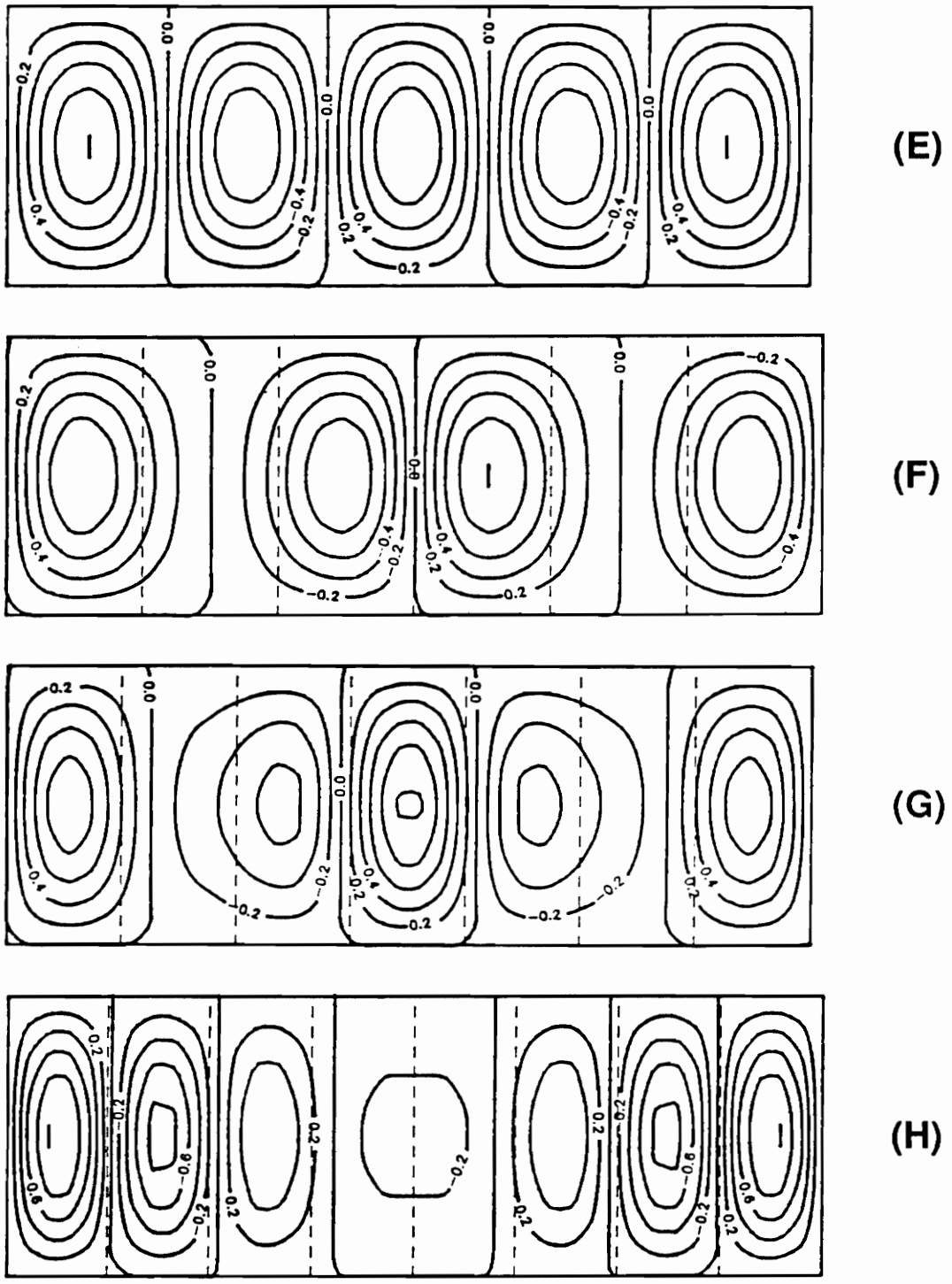

Longitudinally Stiffened Panel Buckled Mode Shapes, 1000 lbf/in Compression, cont'd

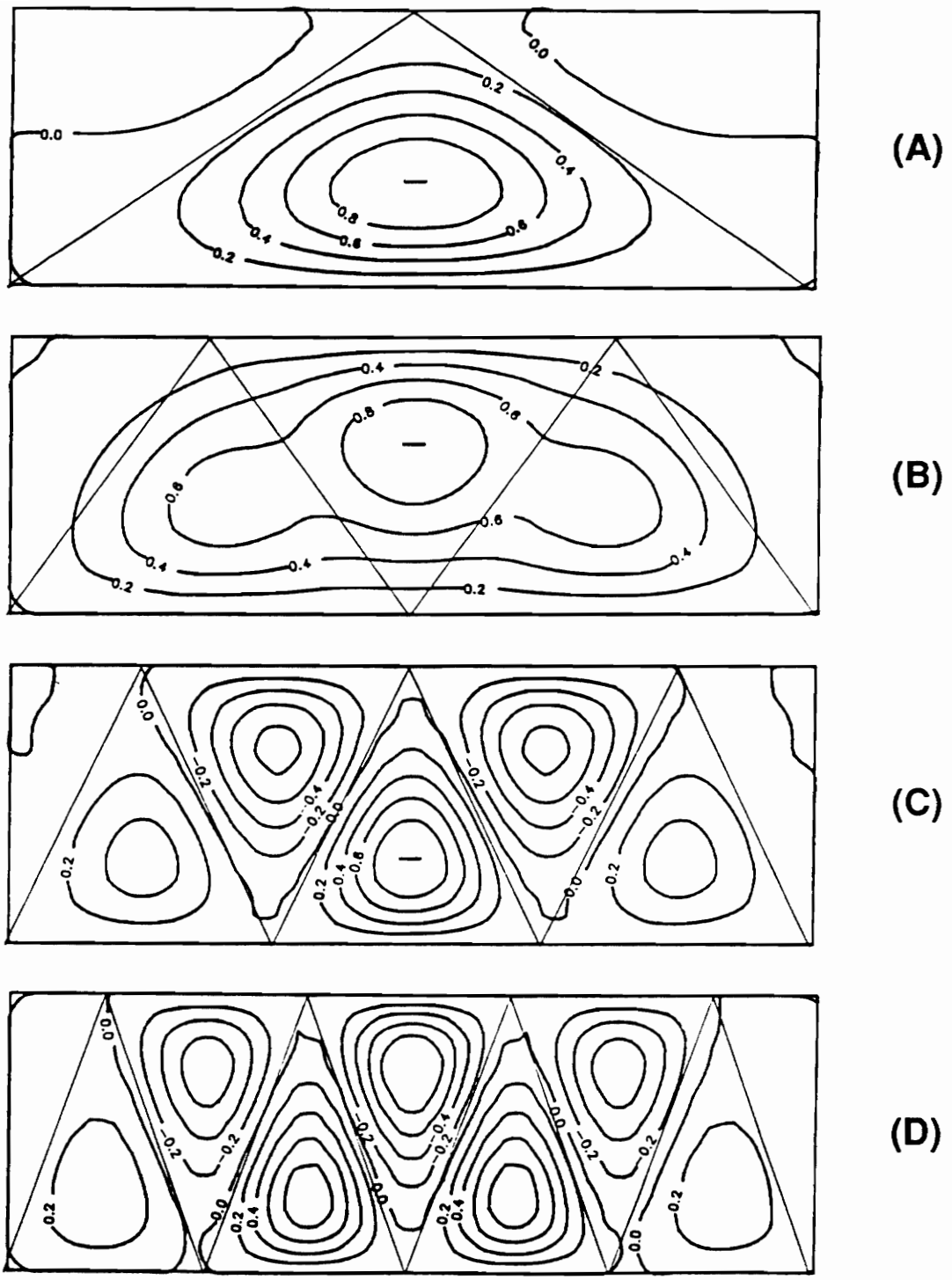

Figure C6. **Diagonally Stiffened Panel Buckled Mode Shapes, 1000 lbf/in Compression:** A) 1 Cell B) 2 Cells C) 3 Cells D) 4 Cells E) 5 Cells F) 6 Cells G) 7 Cells H) 8 Cells

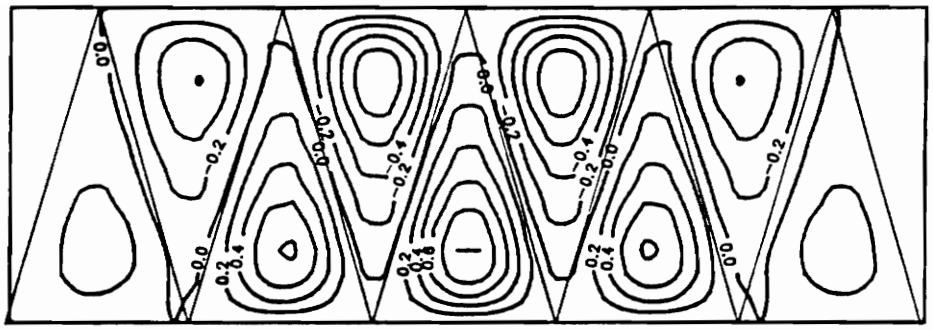

(E)

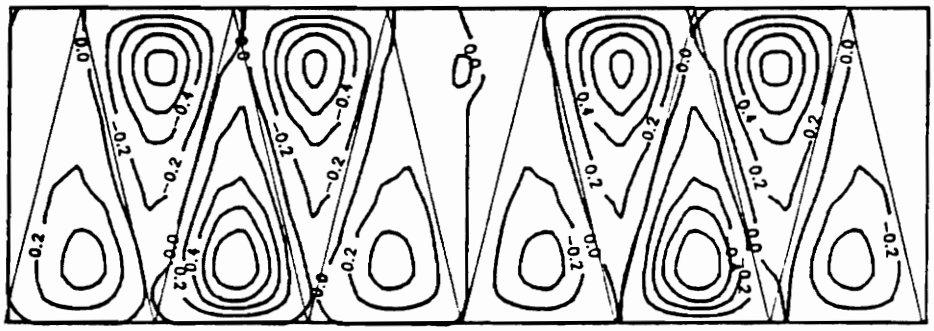

(F)

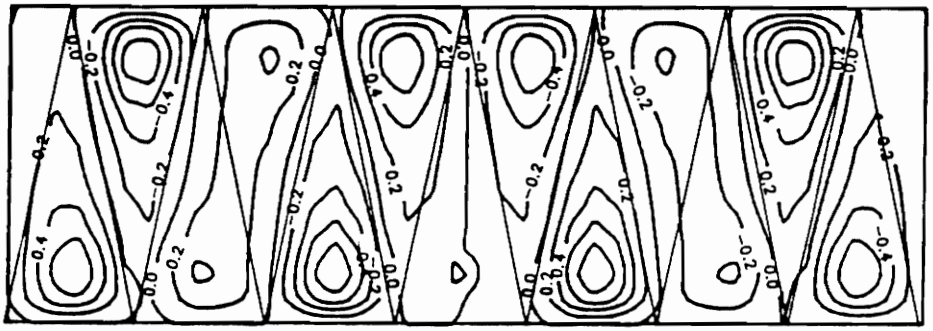

(G)

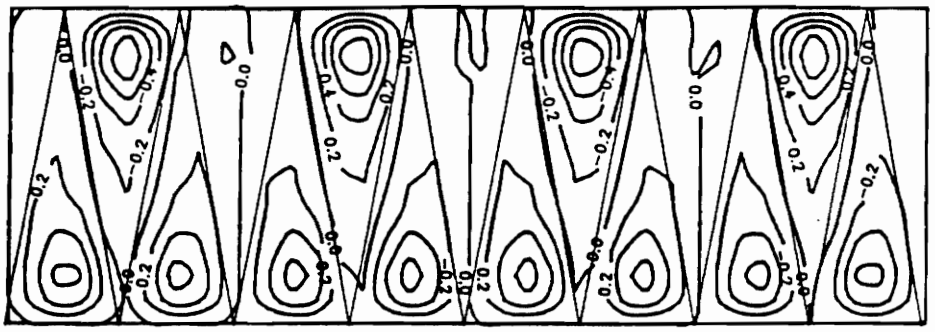

(H)

Diagonally Stiffened Panel Buckled Mode Shapes, 1000 lbf/in Compression, cont'd

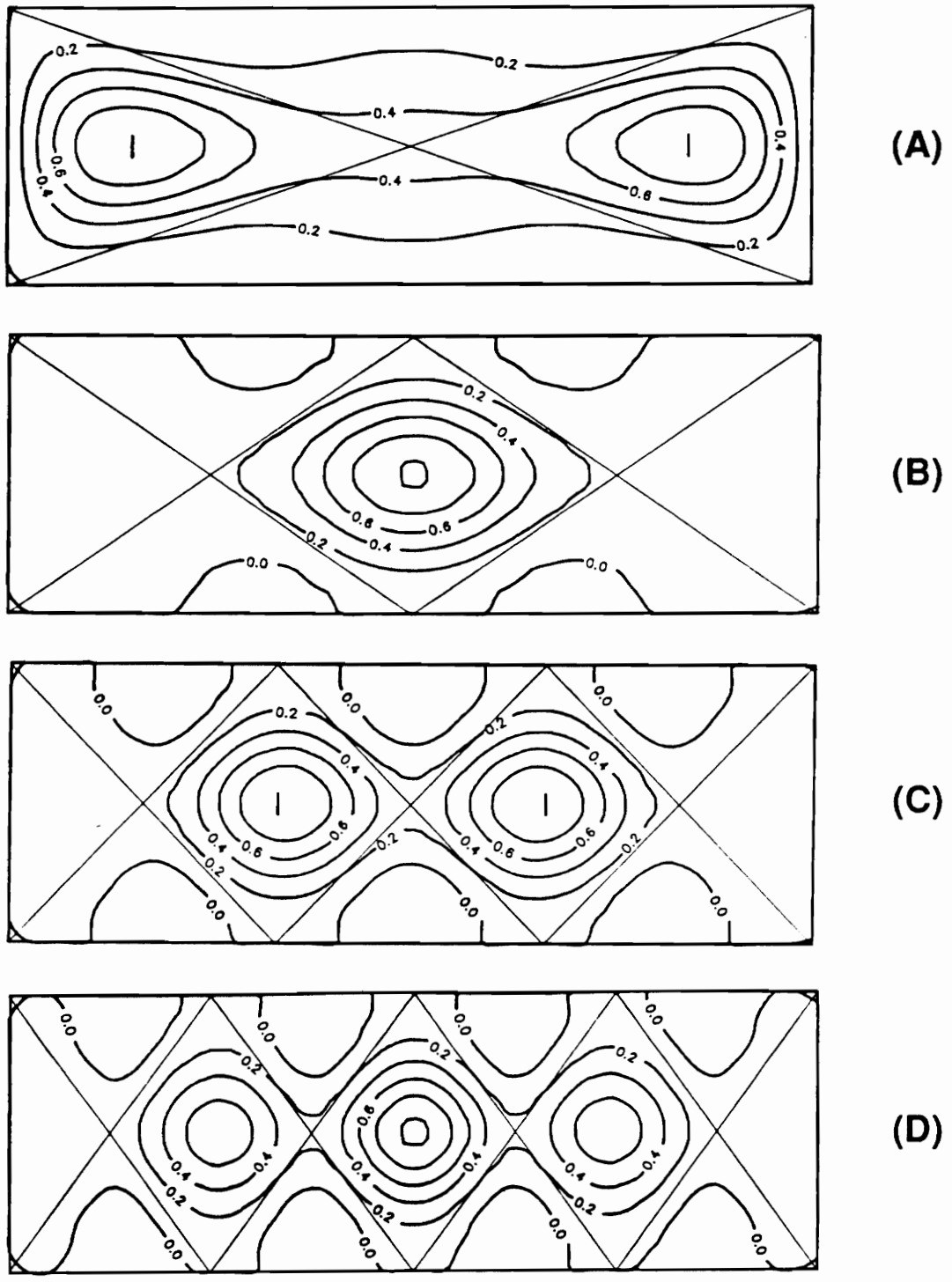

Figure C7. Cross-Stiffened Panel Buckled Mode Shapes, 1000 lbf/in Compression: A) 1 Cell B) 2 Cells C) 3 Cells D) 4 Cells E) 5 Cells F) 6 Cells G) 7 Cells H) 8 Cells

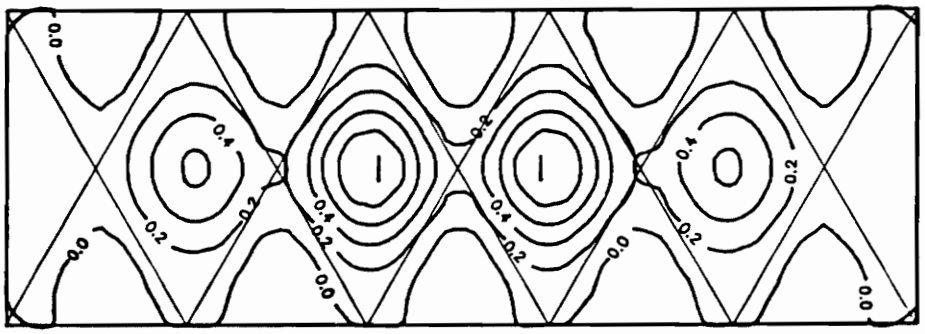

(E)

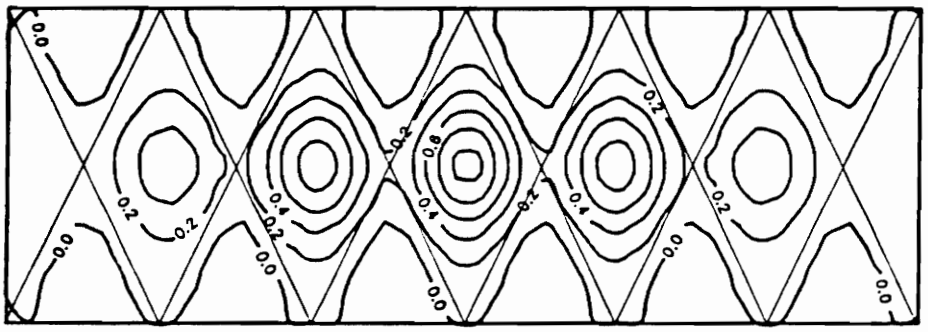

(F)

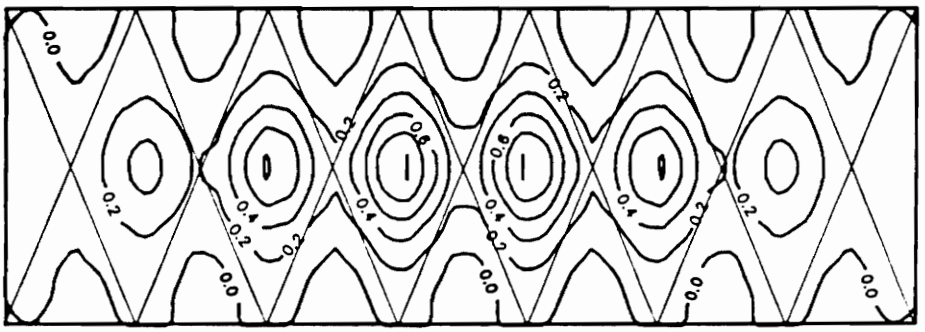

(G)

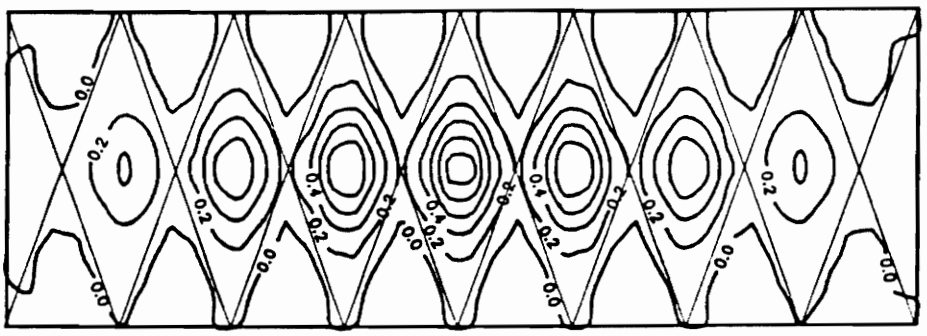

(H)

Cross-Stiffened Panel Buckled Mode Shapes, 1000 lbf/in Compression, cont'd

Not Applicable (A)

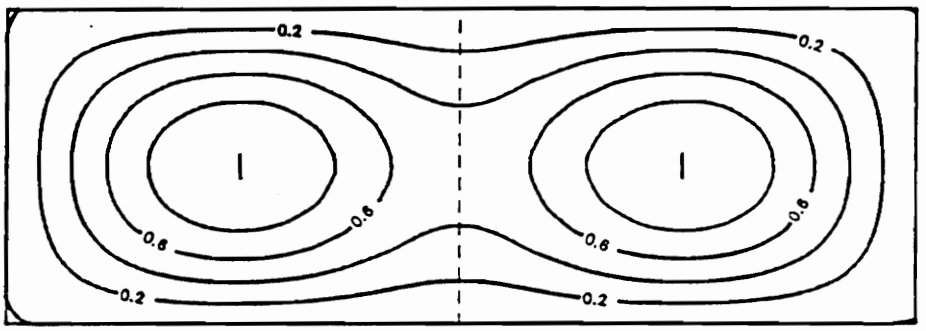

(B)

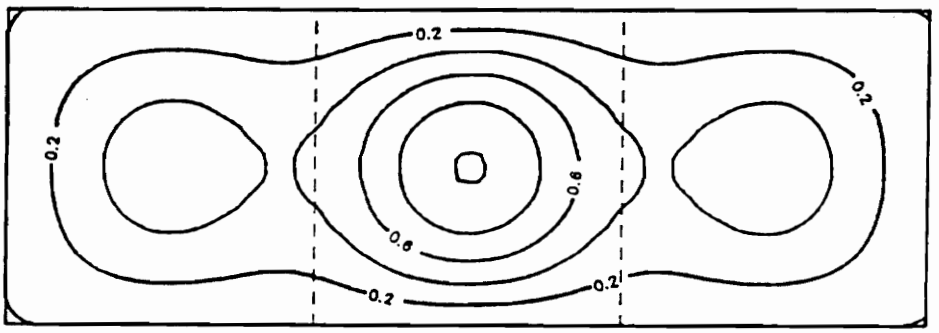

(C)

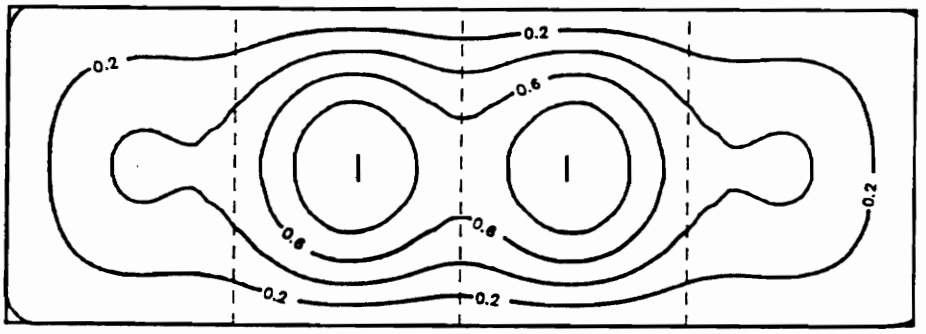

(D)

Figure C8. Longitudinally Stiffened Panel Buckled Mode Shapes, 10000 lbf/in Compression: A) 1 Cell B) 2 Cells C) 3 Cells D) 4 Cells E) 5 Cells F) 6 Cells G) 7 Cells H) 8 Cells

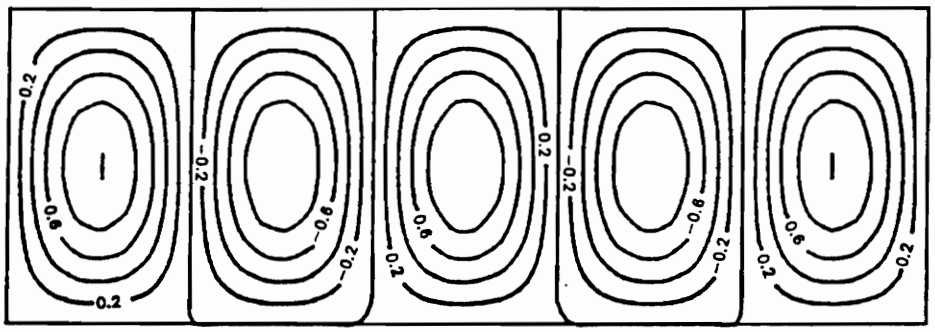

(E)

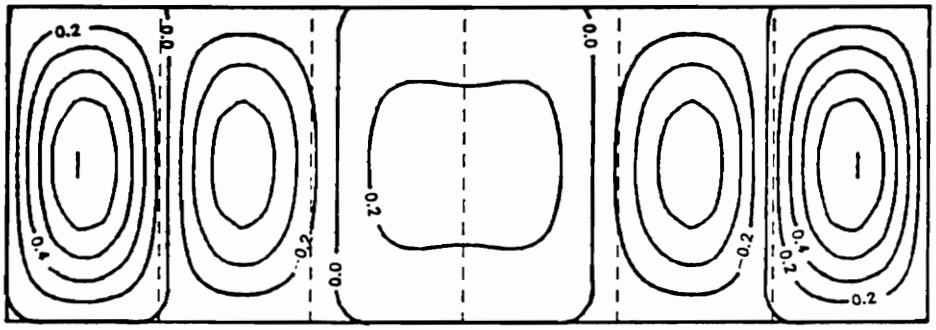

(F)

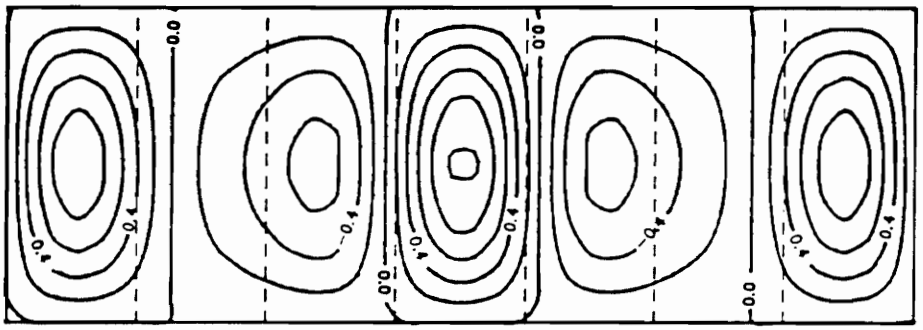

(G)

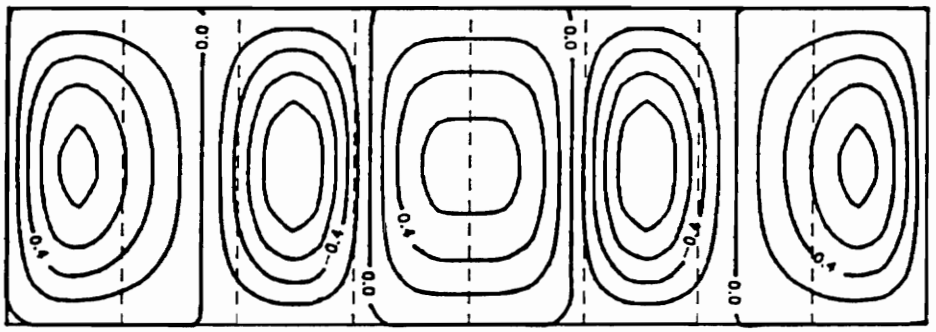

(H)

Longitudinally Stiffened Panel Buckled Mode Shapes, 10000 lbf/in Compression, cont'd

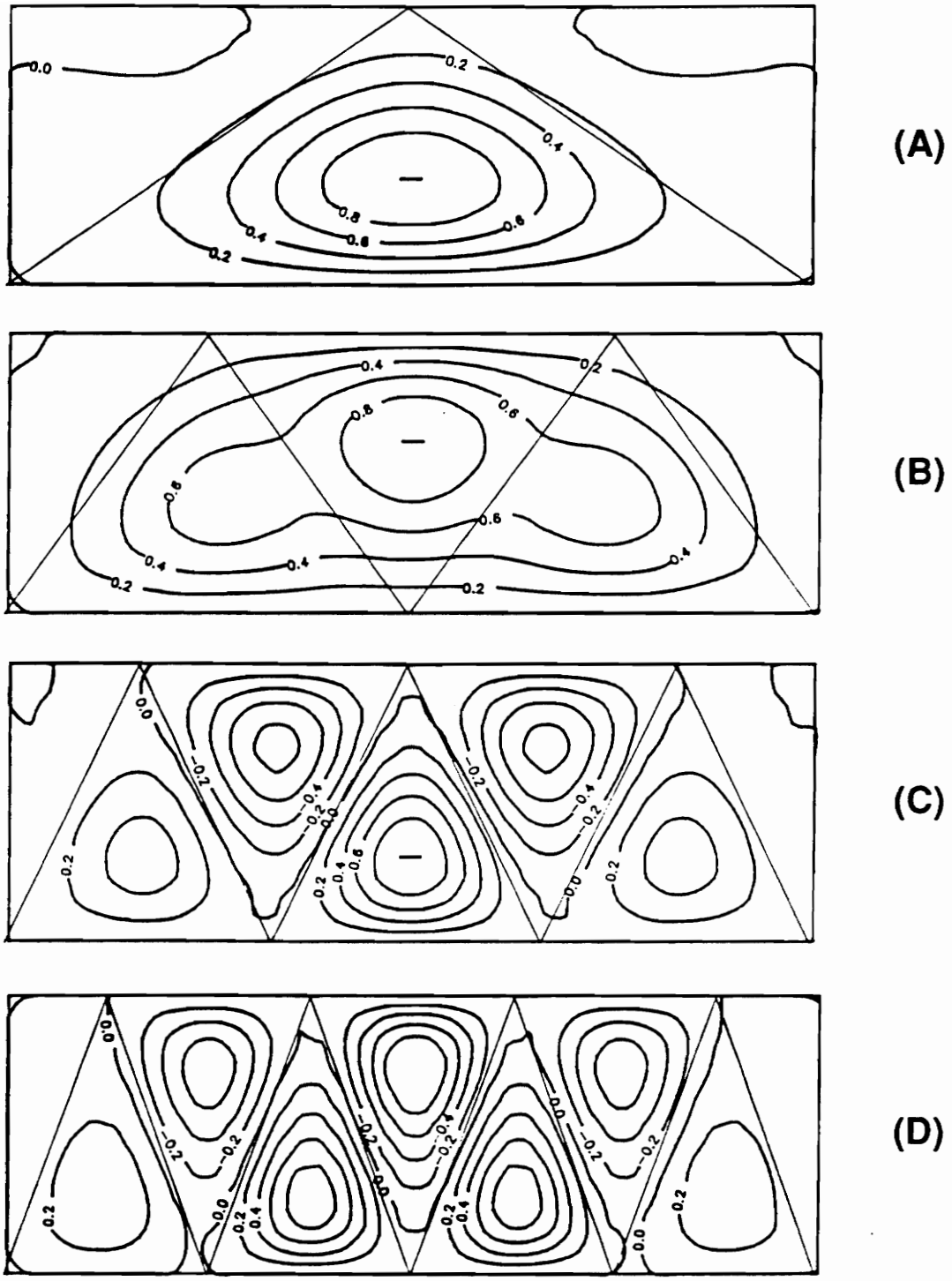

Figure C9. **Diagonally Stiffened Panel Buckled Mode Shapes, 10000 lbf/in Compression:** A) 1 Cell B) 2 Cells C) 3 Cells D) 4 Cells E) 5 Cells F) 6 Cells G) 7 Cells H) 8 Cells

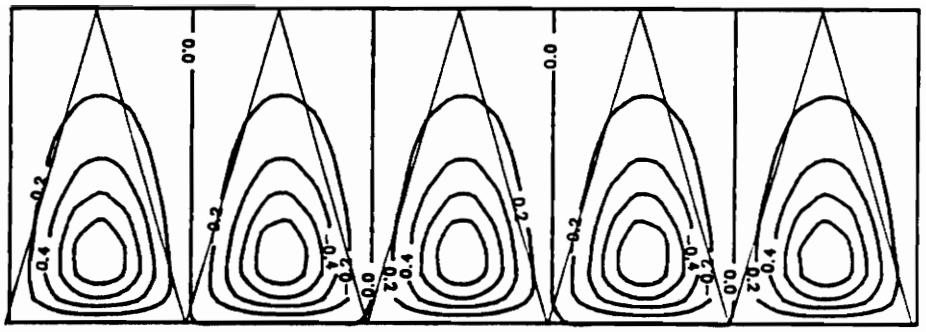

(E)

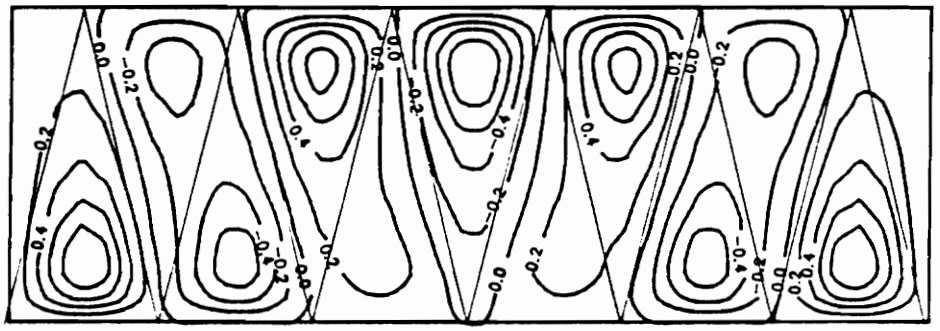

(F)

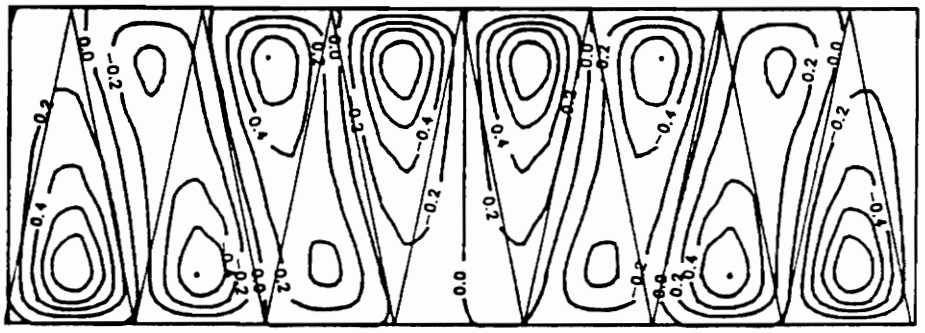

(G)

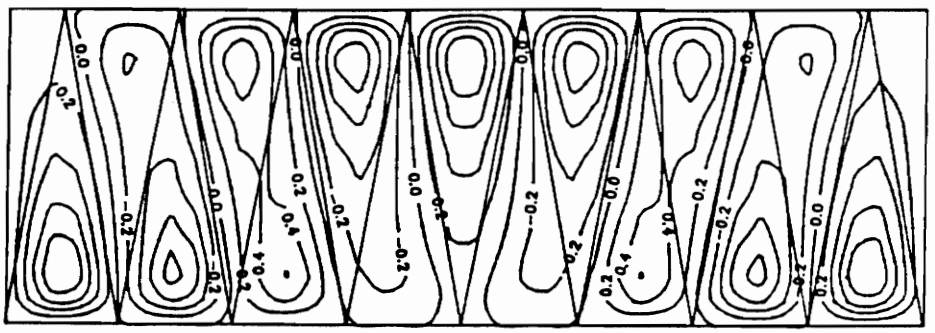

(H)

Diagonally Stiffened Panel Buckled Mode Shapes, 10000 lbf/in Compression, cont'd

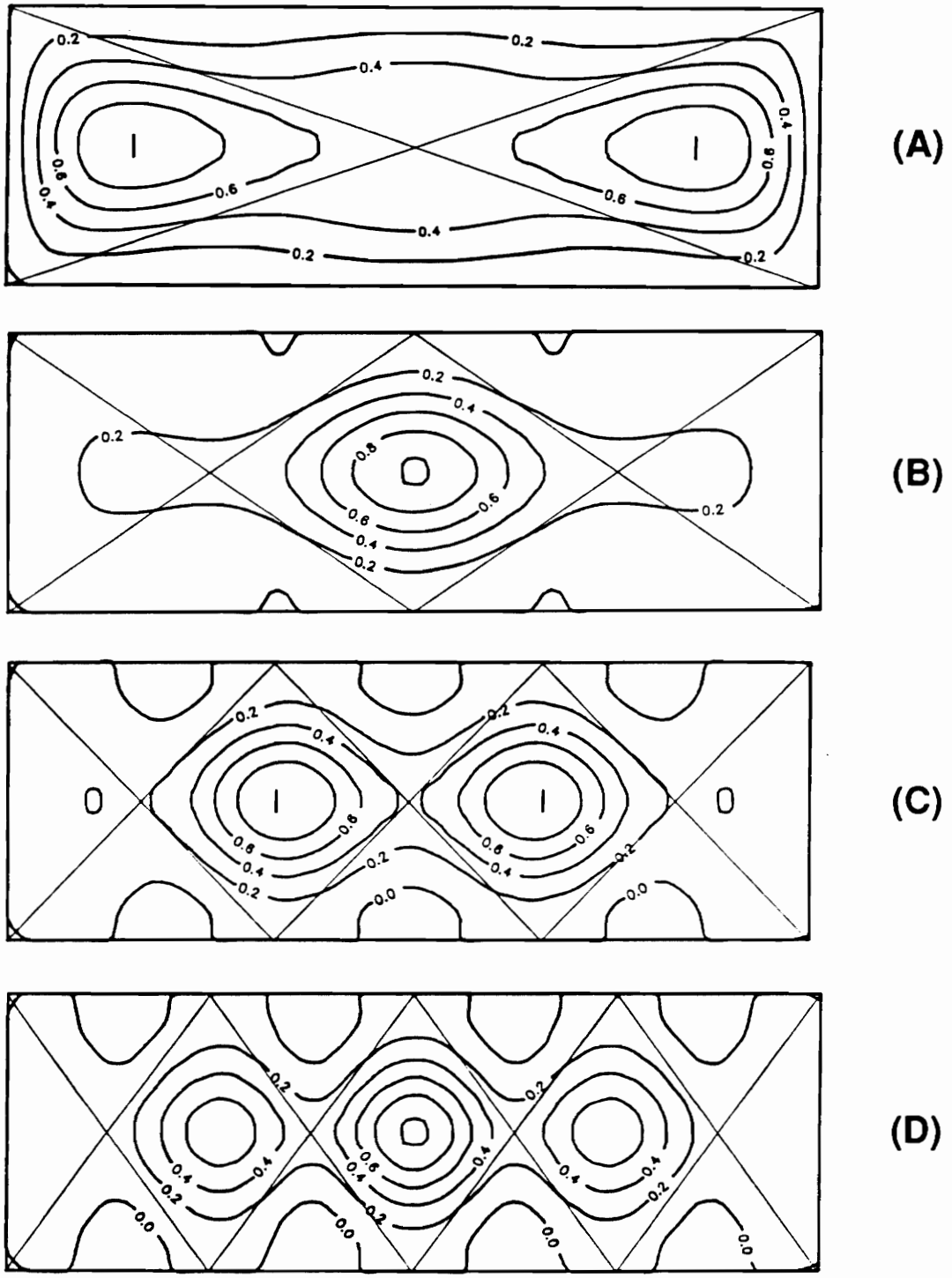

Figure C10. **Cross-Stiffened Panel Buckled Mode Shapes, 10000 lbf/in Compression:** A) 1 Cell B) 2 Cells C) 3 Cells D) 4 Cells E) 5 Cells F) 6 Cells G) 7 Cells H) 8 Cells

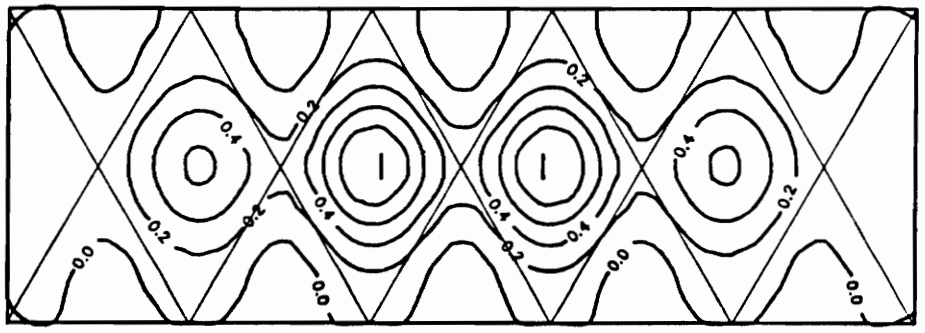

(E)

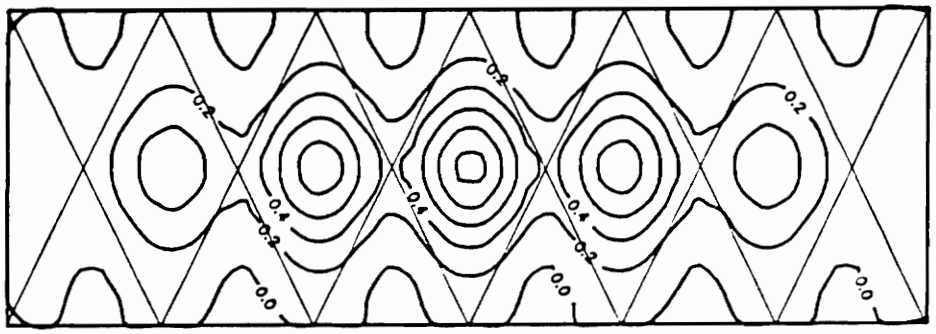

(F)

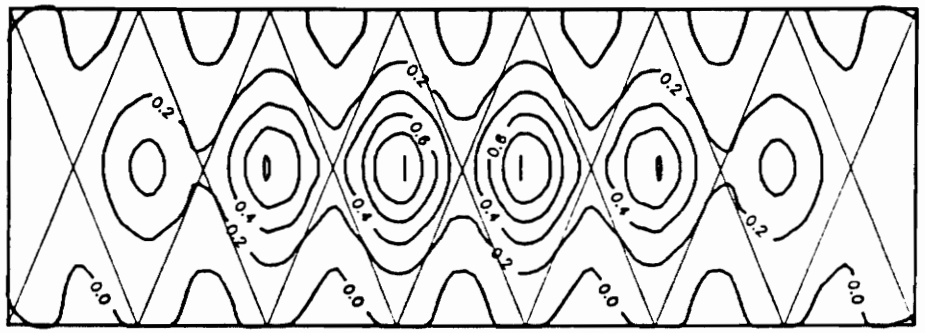

(G)

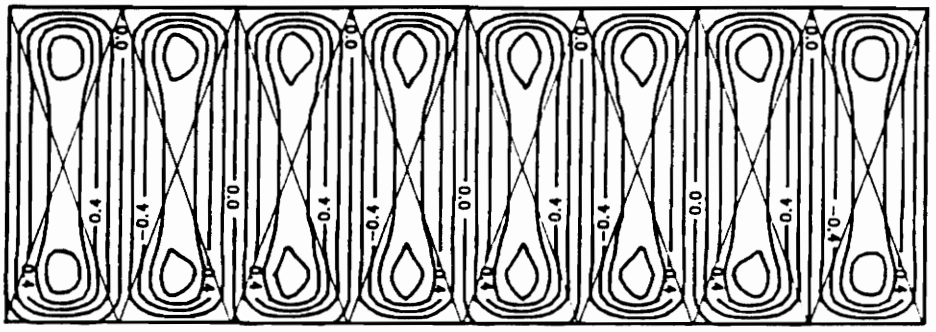

(H)

Cross-Stiffened Panel Buckled Mode Shapes, 10000 lbf/in Compression, cont'd

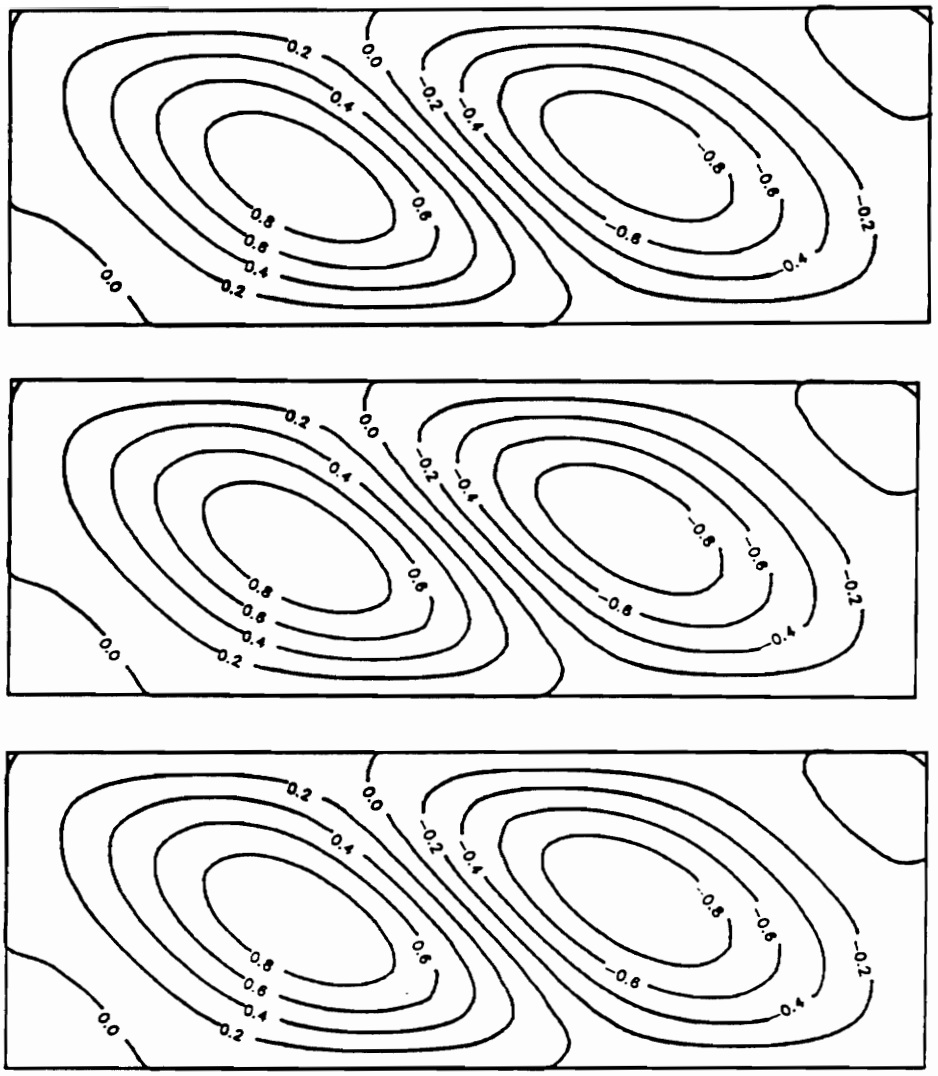

Figure C11. Flat Plate Buckled Mode Shapes, Shear: A) 100 lbf/in B) 1000 lbf/in C) 10000 lbf/in

Not Applicable (A)

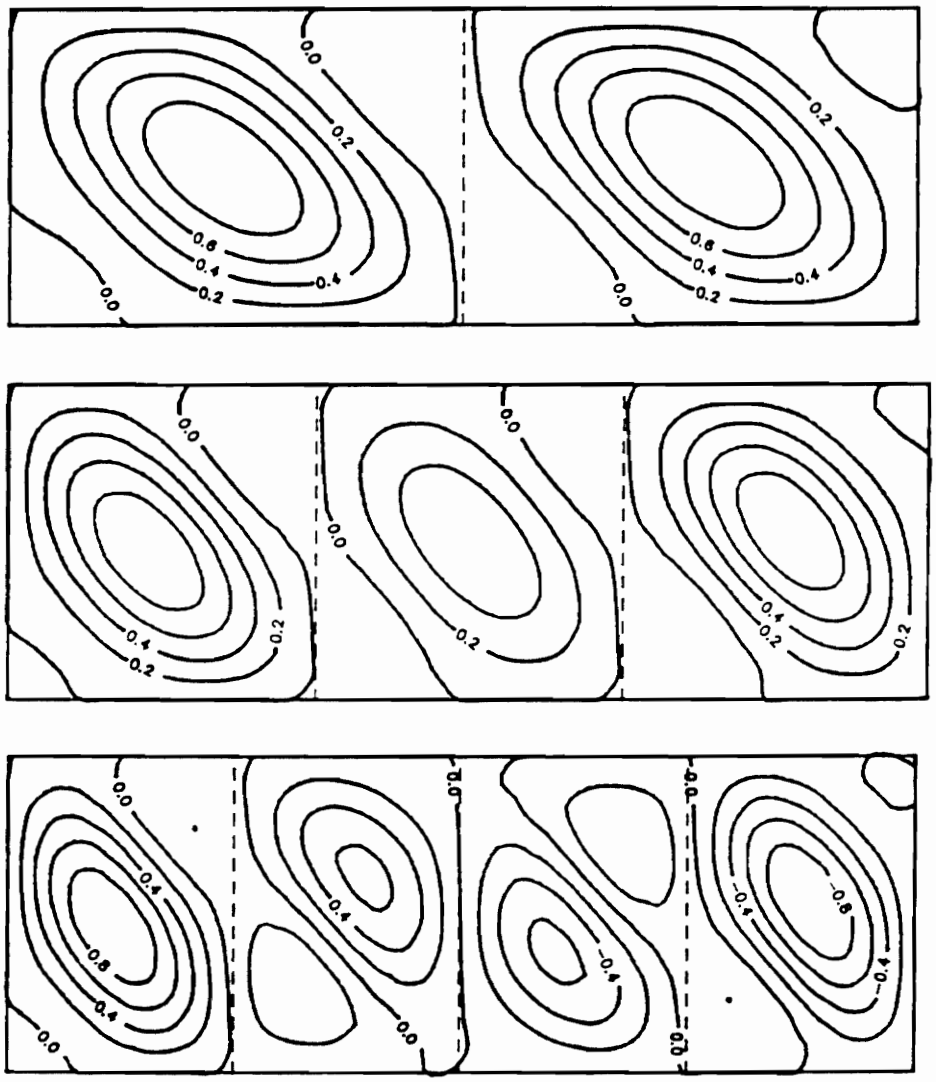

Figure C12. Longitudinally Stiffened Panel Buckled Mode Shapes, 100 lbf/in Shear: A) 1 Cell B) 2 Cells C) 3 Cells D) 4 Cells E) 5 Cells F) 6 Cells G) 7 Cells H) 8 Cells

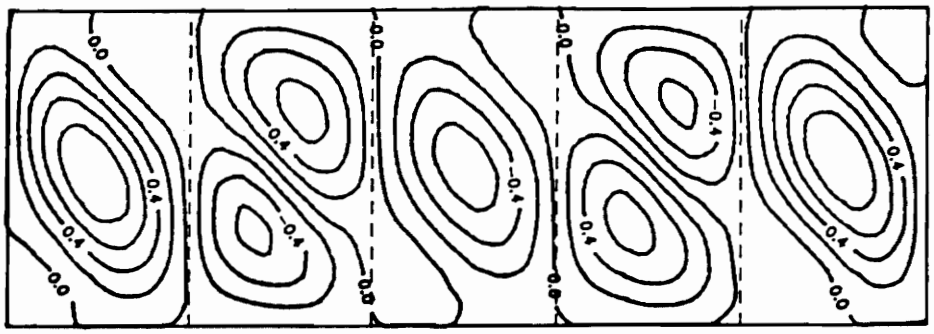

(E)

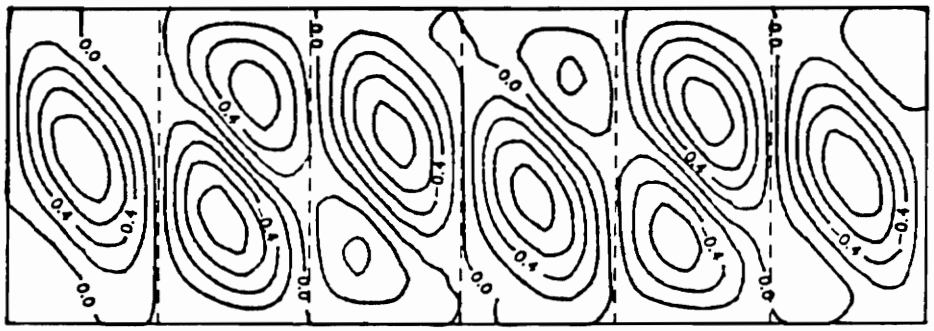

(F)

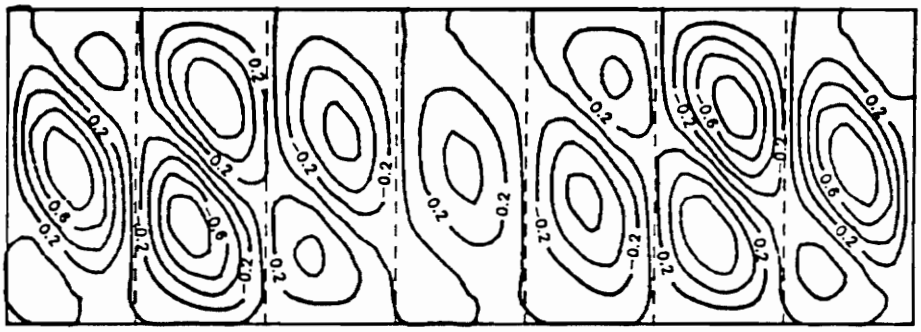

(G)

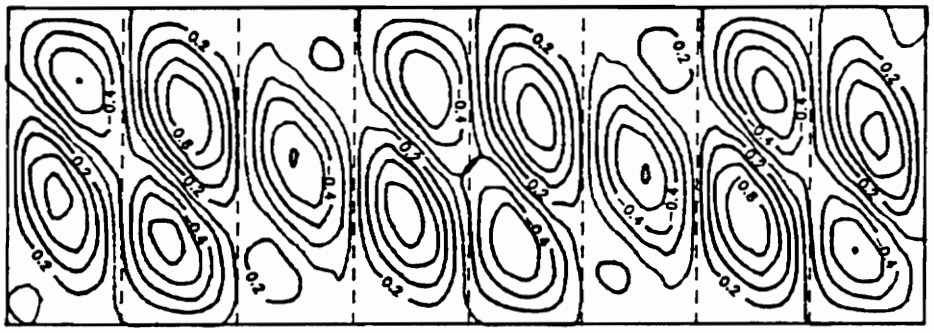

(H)

Longitudinally Stiffened Panel Buckled Mode Shapes, 100 lbf/in Shear, cont'd

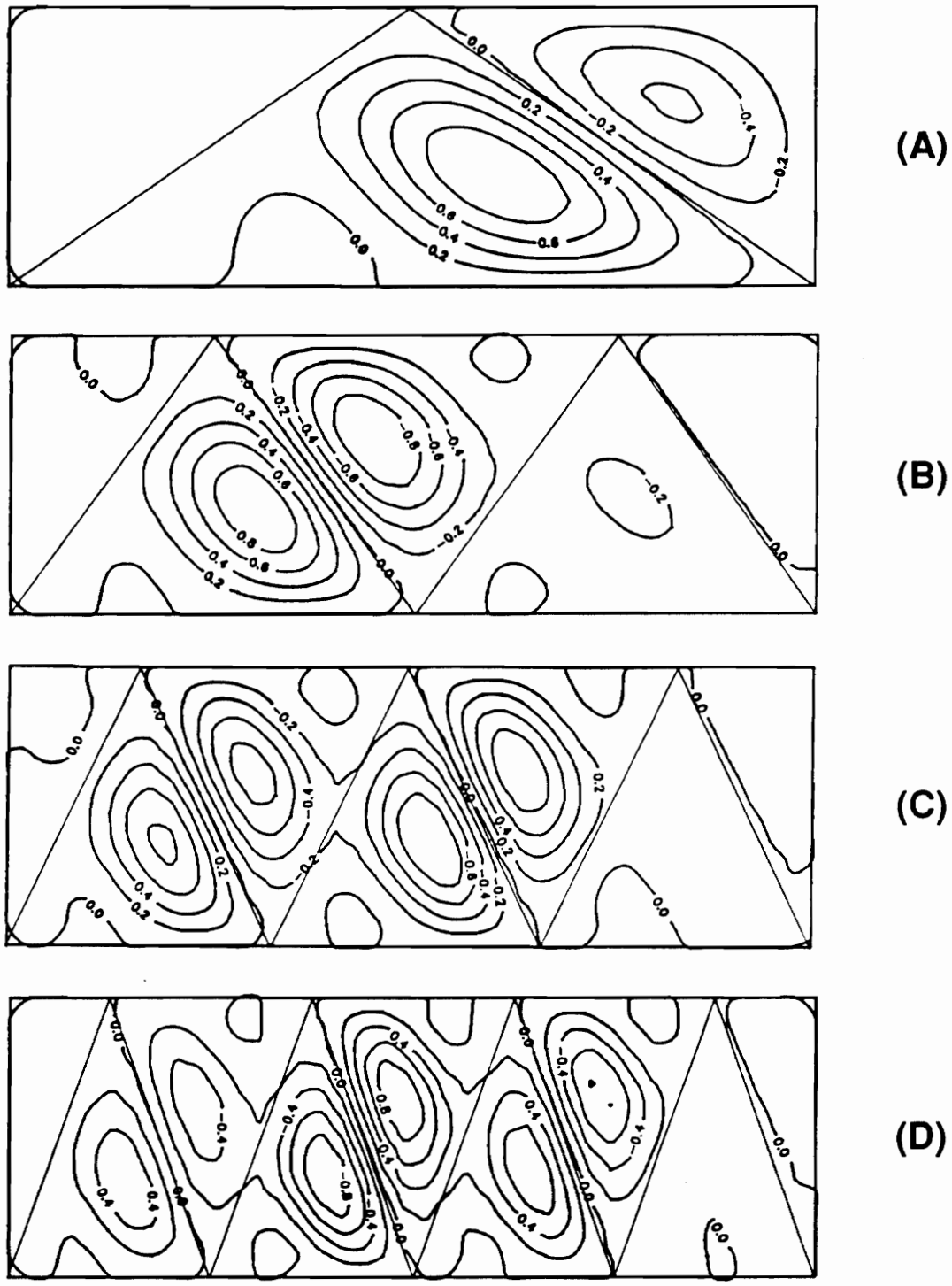

Figure C13. Diagonally Stiffened Panel Buckled Mode Shapes, 100 lbf/in Shear: A) 1 Cell B) 2 Cells C) 3 Cells D) 4 Cells E) 5 Cells F) 6 Cells G) 7 Cells H) 8 Cells

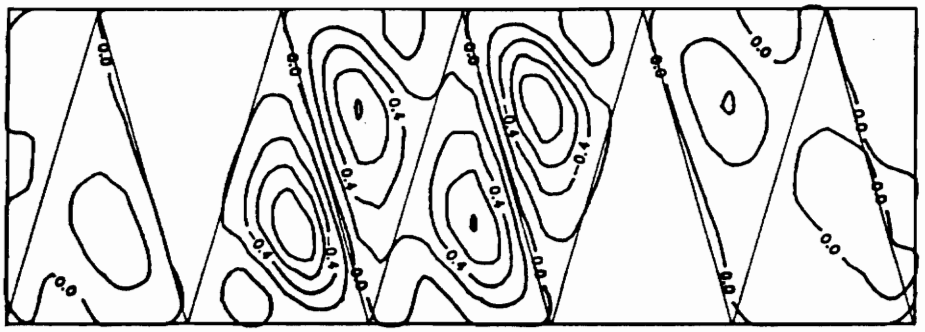

(E)

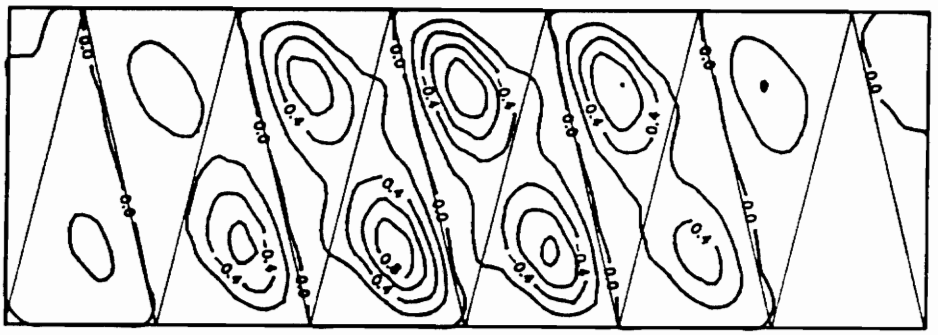

(F)

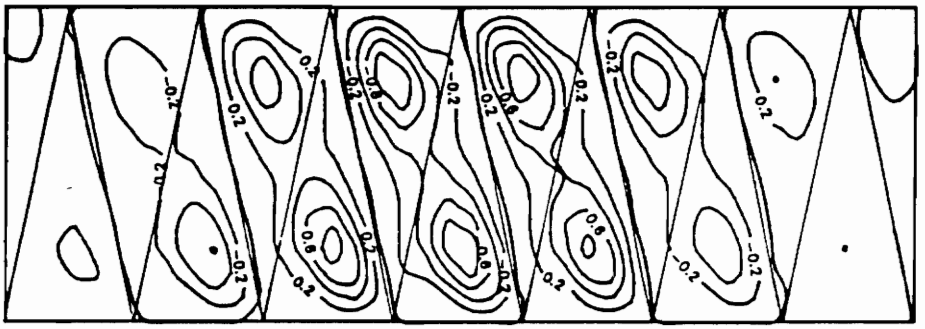

(G)

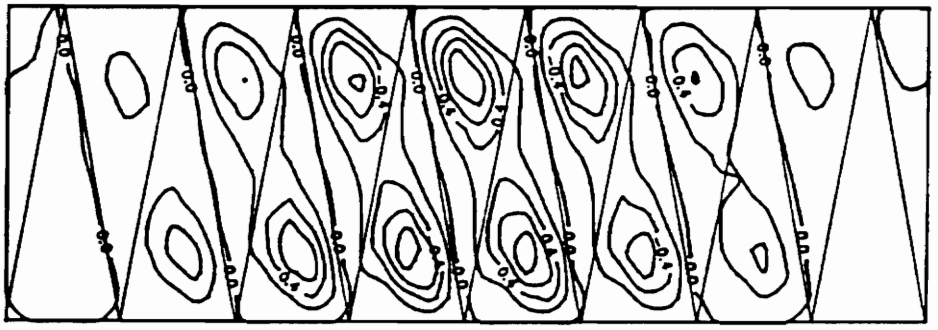

(H)

Diagonally Stiffened Panel Buckled Mode Shapes, 100 lbf/in Shear, cont'd

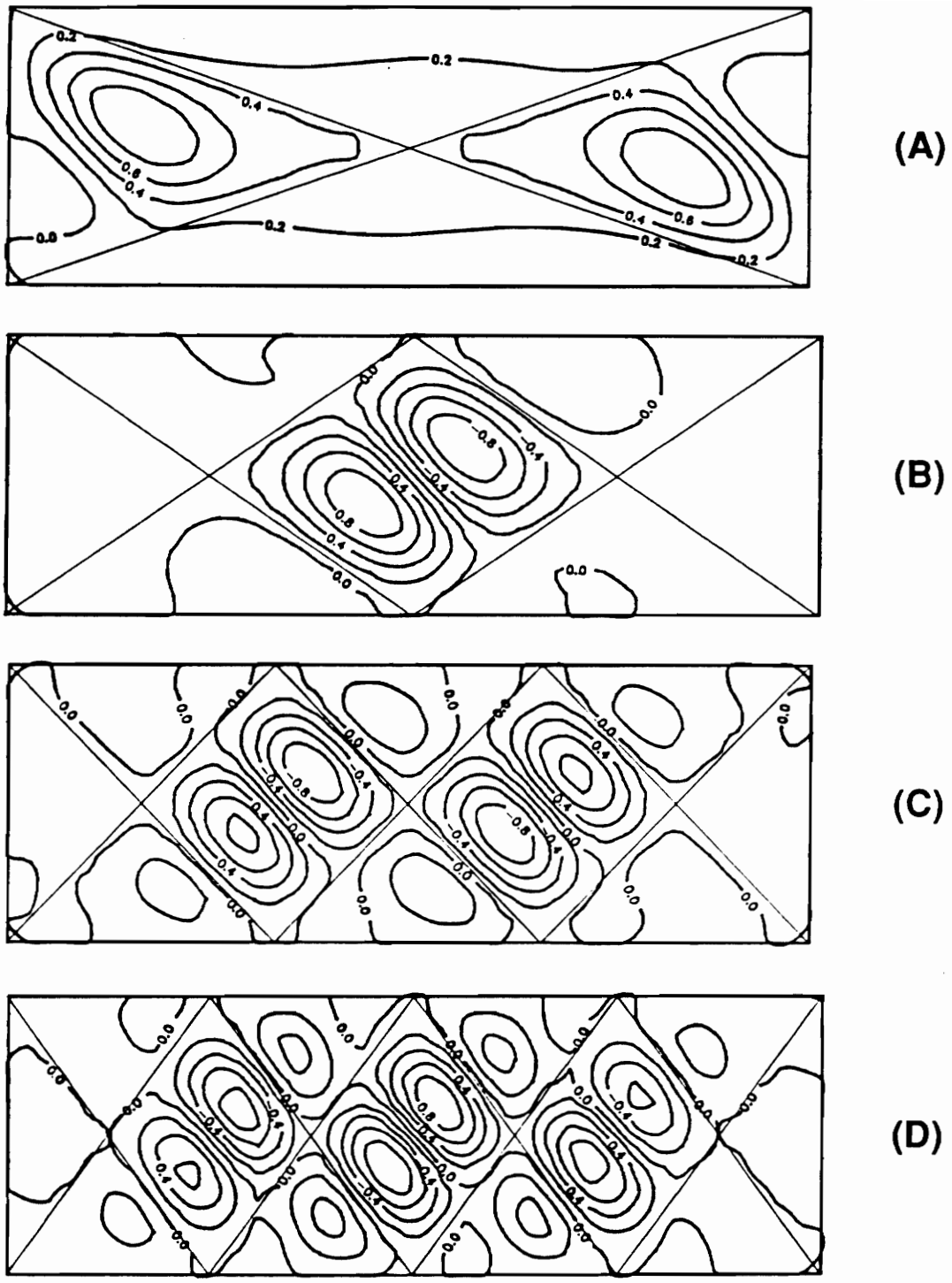

Figure C14. **Cross-Stiffened Panel Buckled Mode Shapes, 100 lbf/in Shear:** A) 1 Cell B) 2 Cells C) 3 Cells D) 4 Cells E) 5 Cells F) 6 Cells G) 7 Cells H) 8 Cells

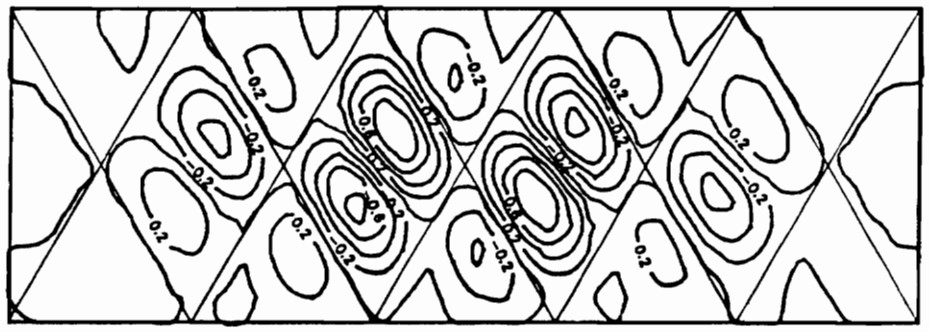

(E)

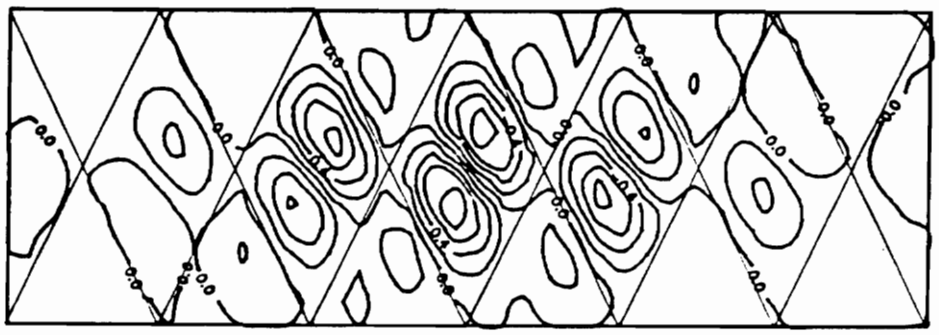

(F)

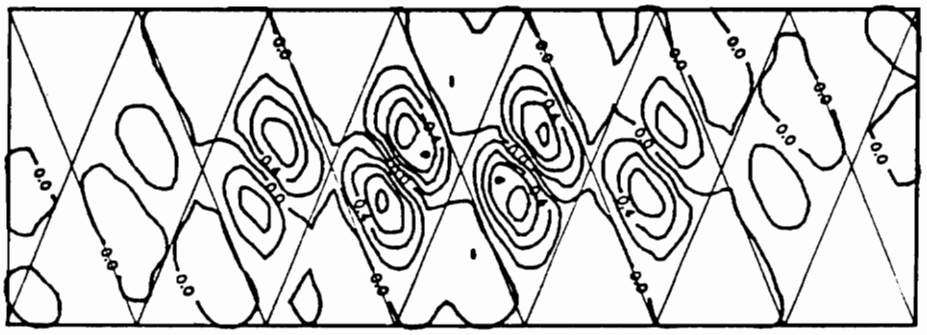

(G)

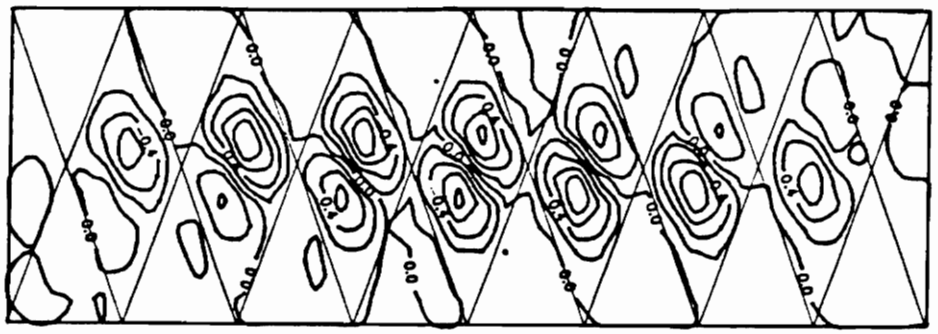

(H)

Cross-Stiffened Panel Buckled Mode Shapes, 100 lbf/in Shear, cont'd

Not Applicable (A)

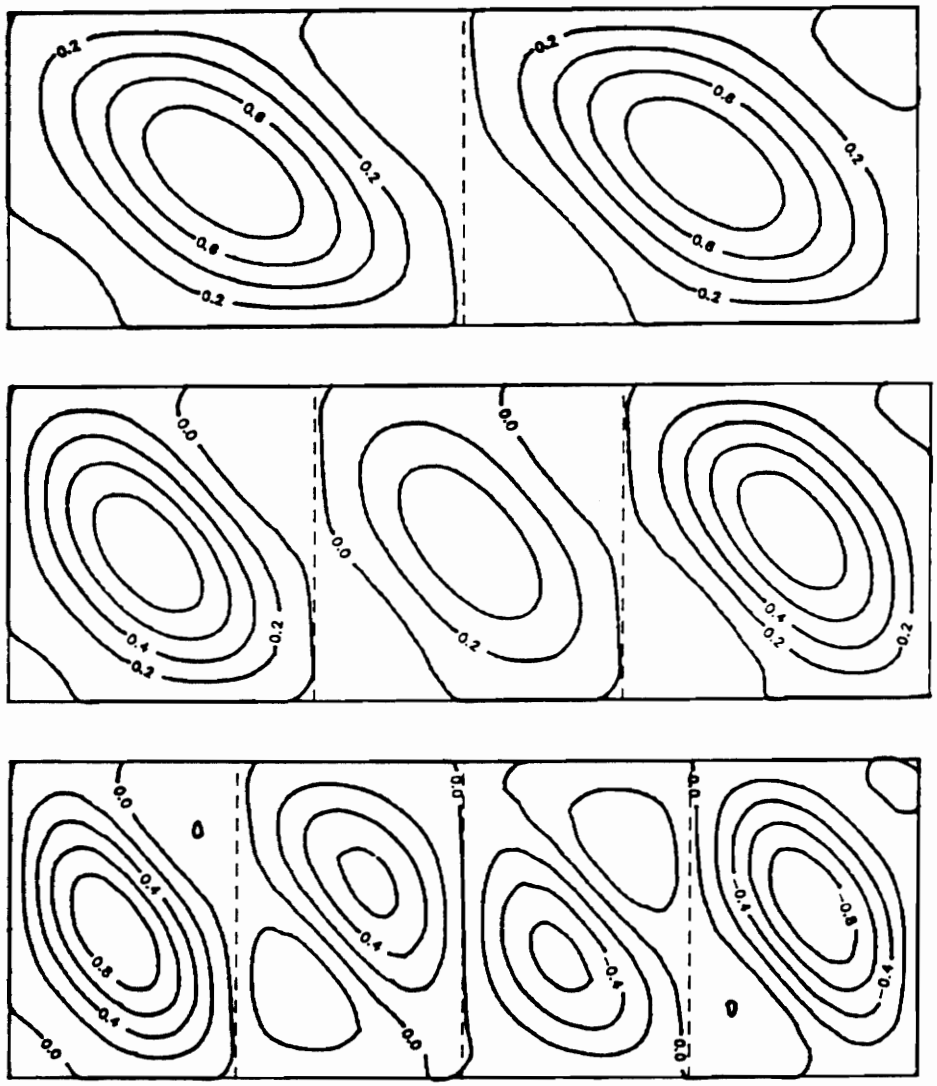

Figure C15. Longitudinally Stiffened Panel Buckled Mode Shapes, 1000 lbf/in Shear: A) 1 Cell B) 2 Cells C) 3 Cells D) 4 Cells E) 5 Cells F) 6 Cells G) 7 Cells H) 8 Cells

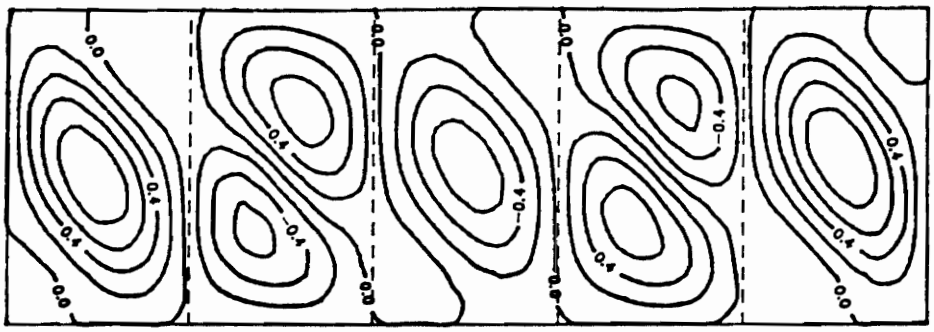

(E)

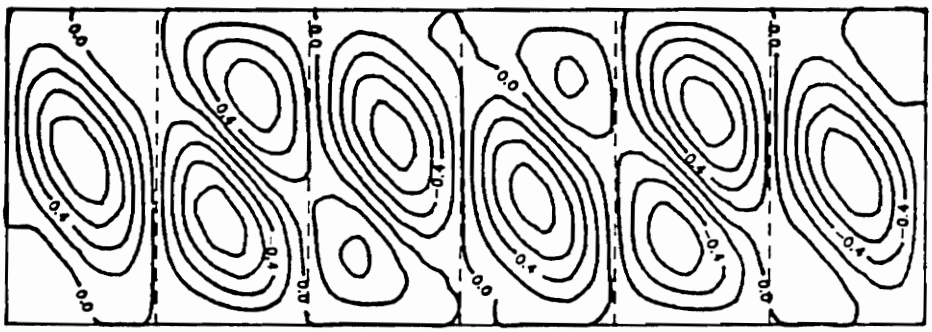

(F)

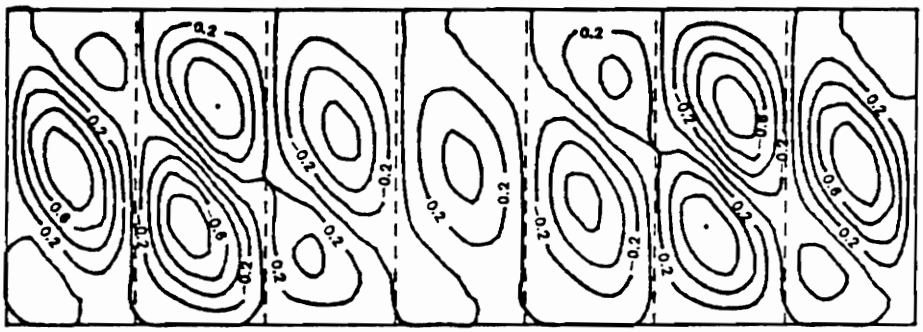

(G)

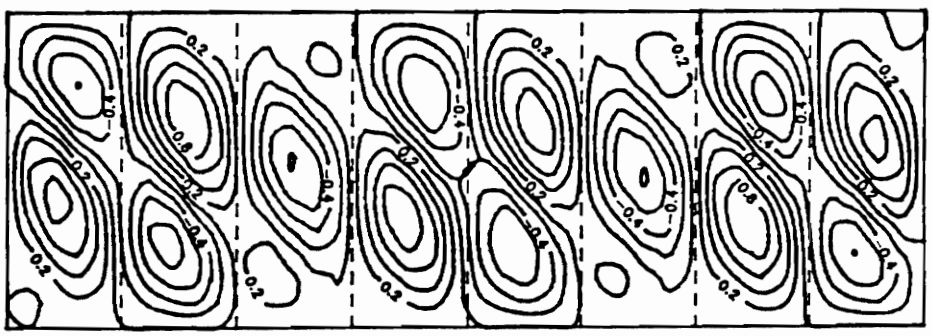

(H)

Longitudinally Stiffened Panel Buckled Mode Shapes, 1000 lbf/in Shear, cont'd

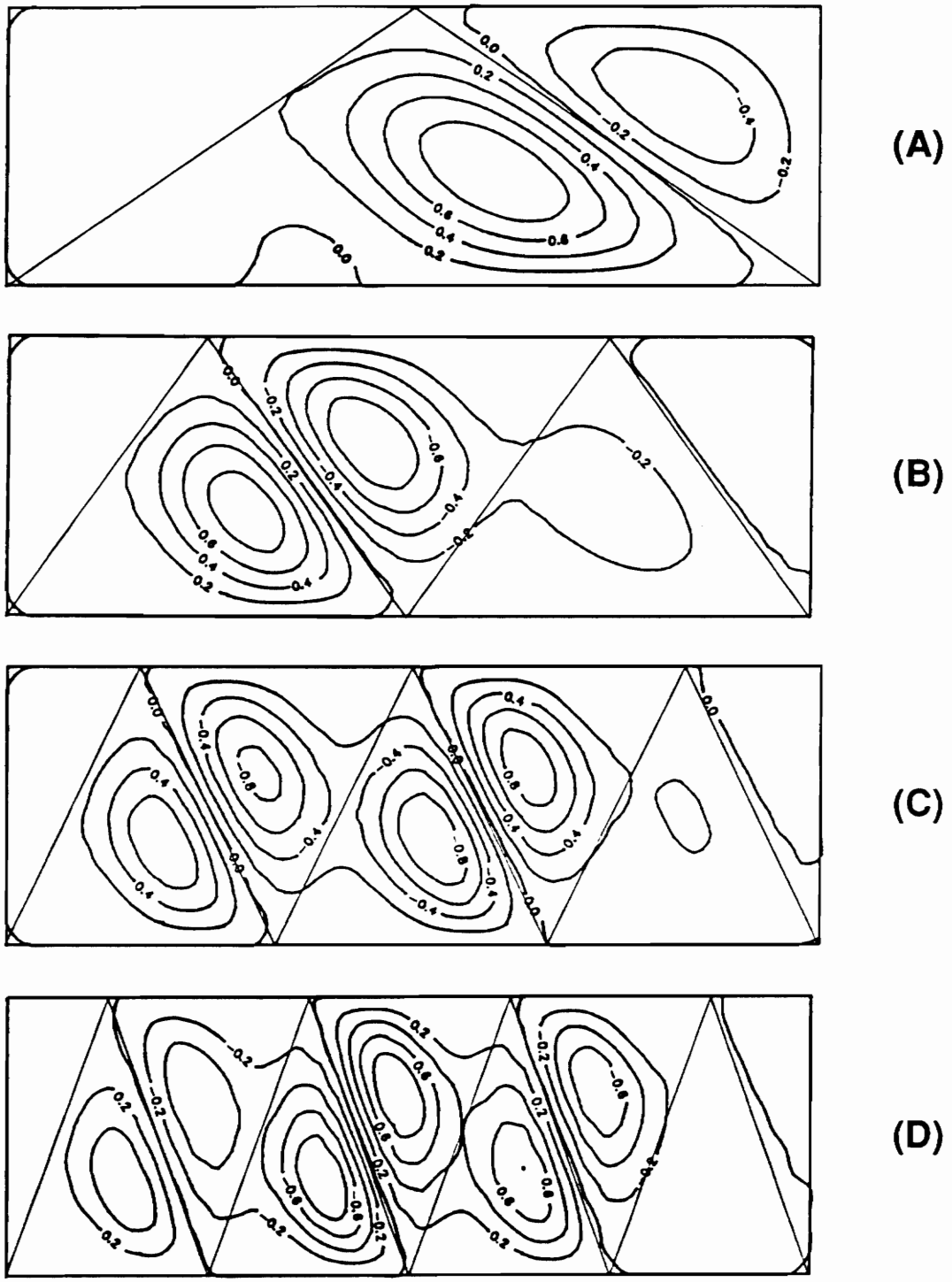

Figure C16. **Diagonally Stiffened Panel Buckled Mode Shapes, 1000 lbf/in Shear:** A) 1 Cell B) 2 Cells C) 3 Cells D) 4 Cells E) 5 Cells F) 6 Cells G) 7 Cells H) 8 Cells

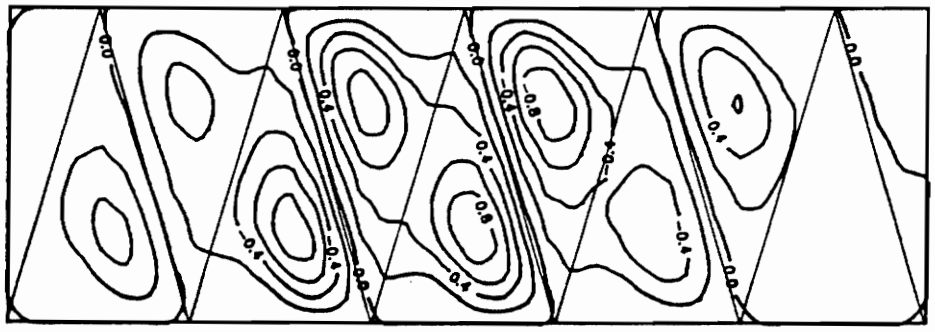

(E)

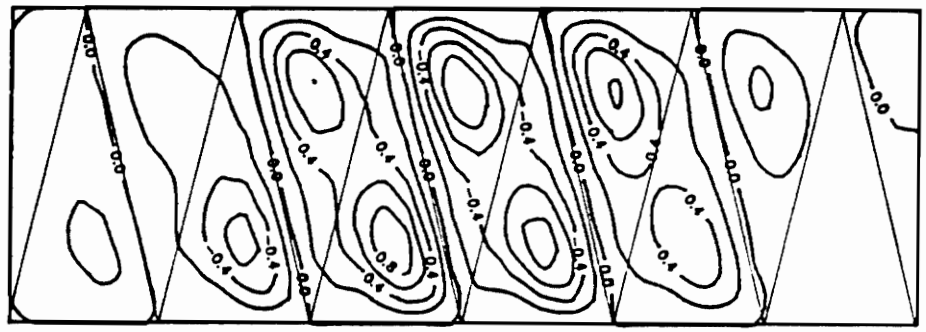

(F)

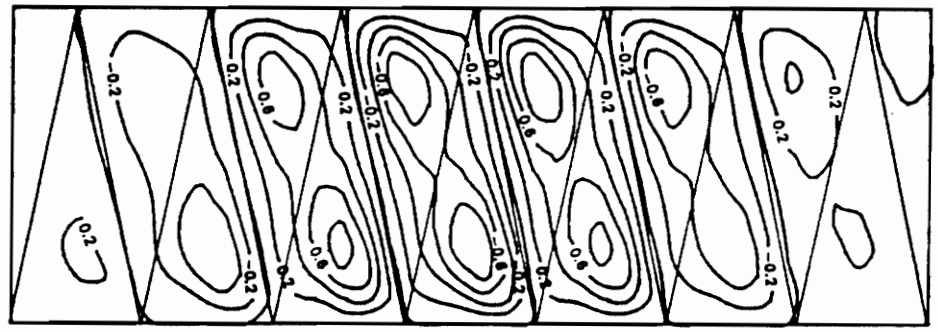

(G)

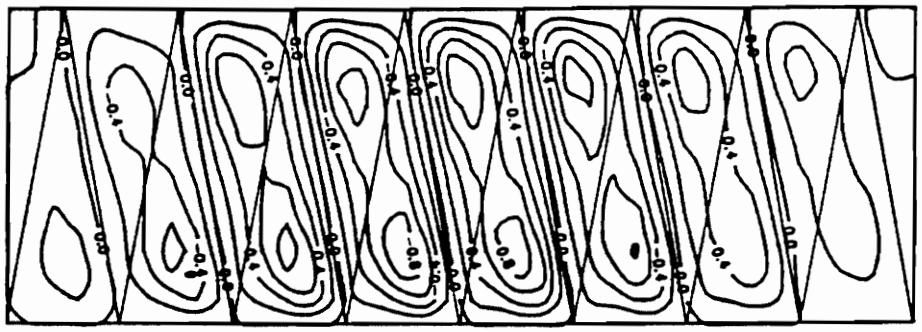

(H)

Diagonally Stiffened Panel Buckled Mode Shapes, 1000 lbf/in Shear, cont'd

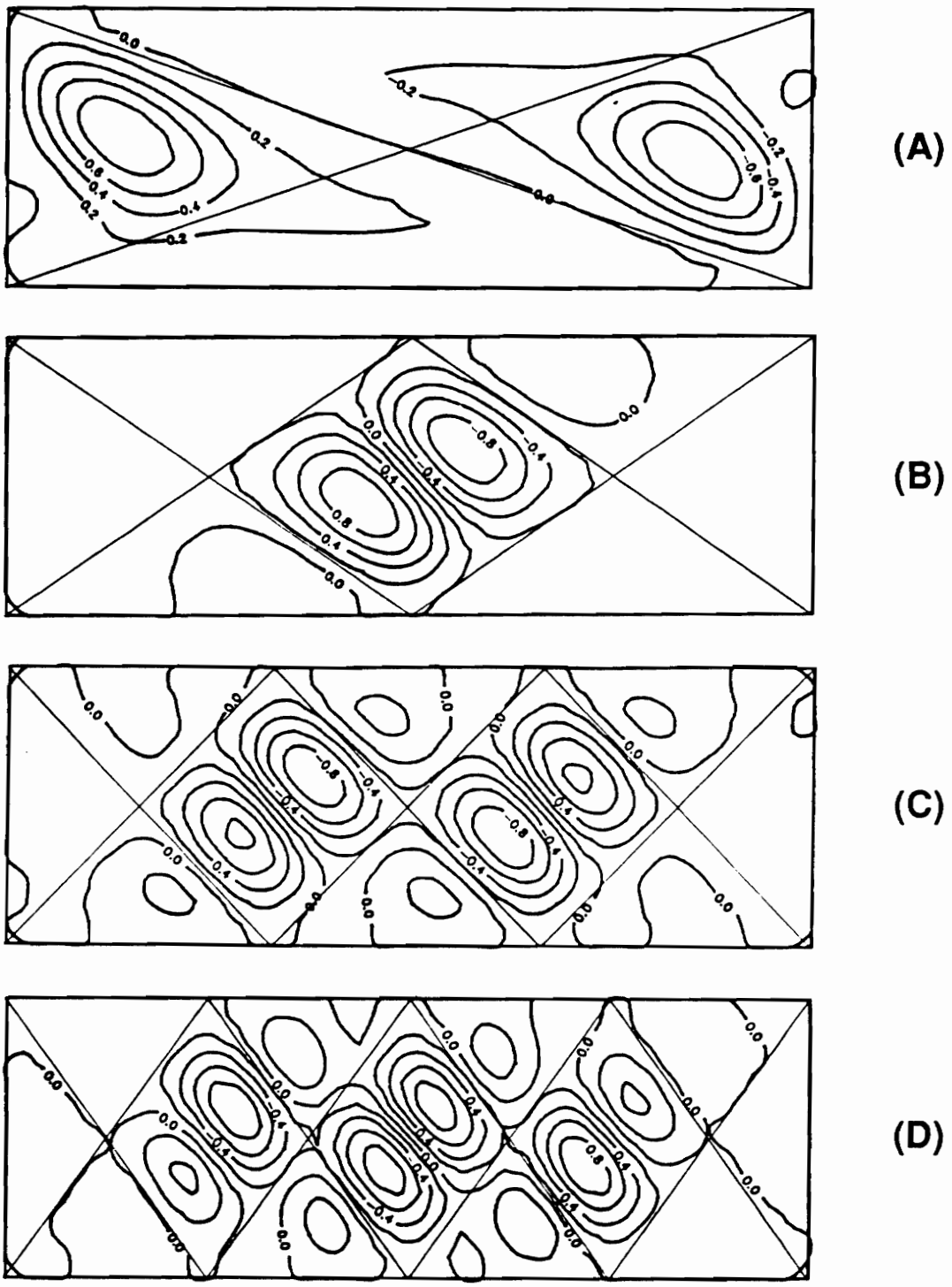

Figure C17. Cross-Stiffened Panel Buckled Mode Shapes, 1000 lbf/in Shear: A) 1 Cell B) 2 Cells C) 3 Cells D) 4 Cells E) 5 Cells F) 6 Cells G) 7 Cells H) 8 Cells

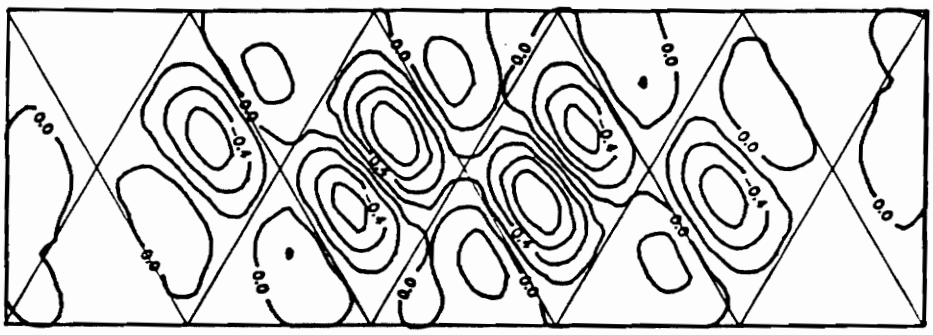

(E)

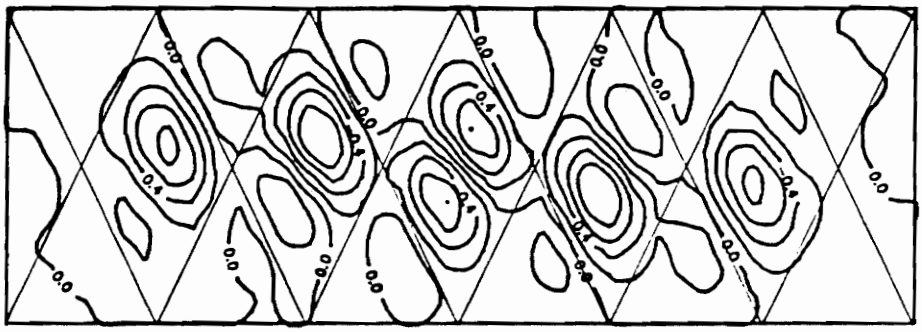

(F)

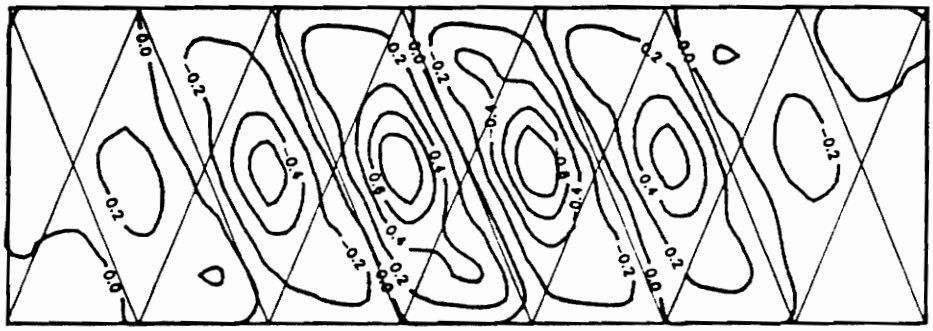

(G)

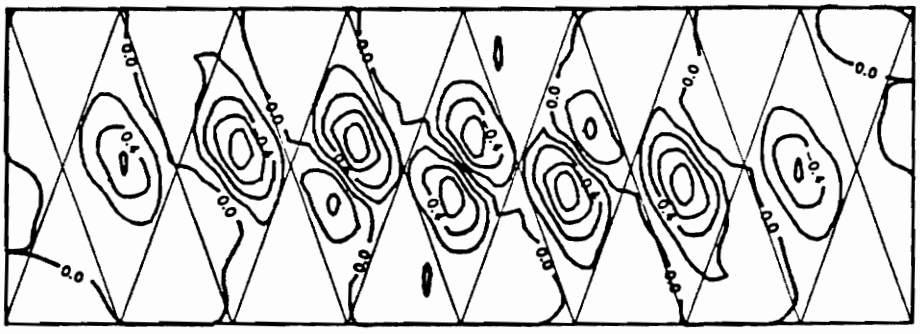

(H)

Cross-Stiffened Panel Buckled Mode Shapes, 1000 lbf/in Shear, cont'd

Not Applicable (A)

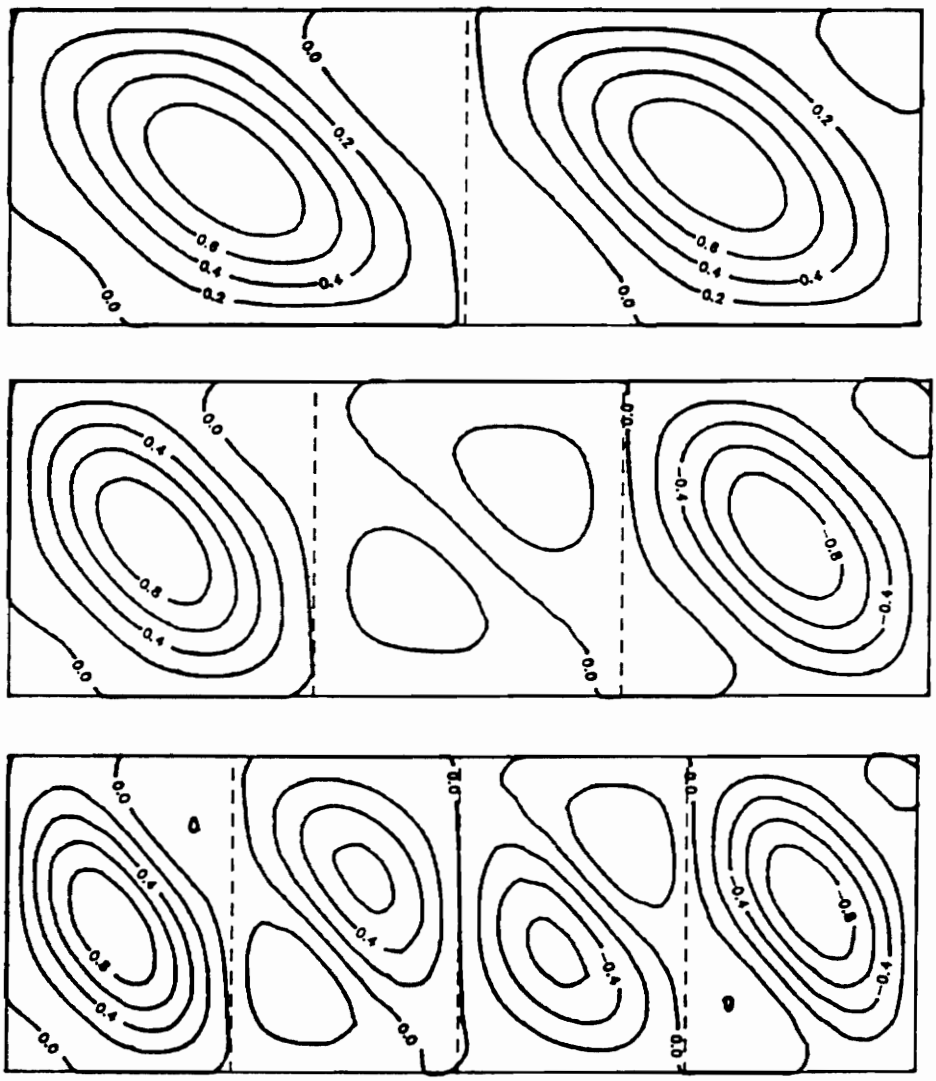

Figure C18. **Longitudinally Stiffened Panel Buckled Mode Shapes, 10000 lbf/in Shear:** A) 1 Cell B) 2 Cells C) 3 Cells D) 4 Cells E) 5 Cells F) 6 Cells G) 7 Cells H) 8 Cells

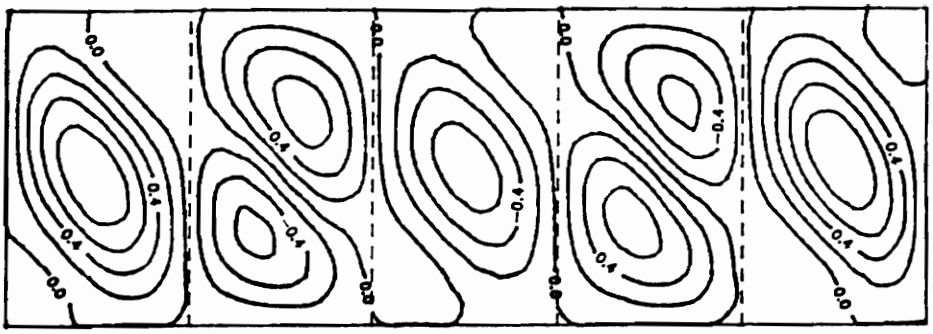

(E)

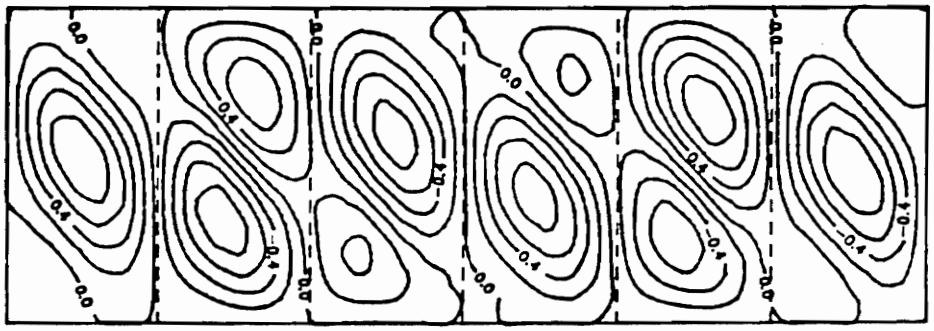

(F)

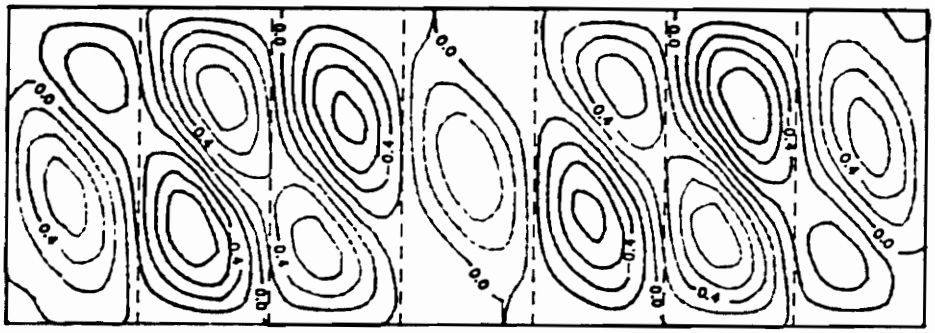

(G)

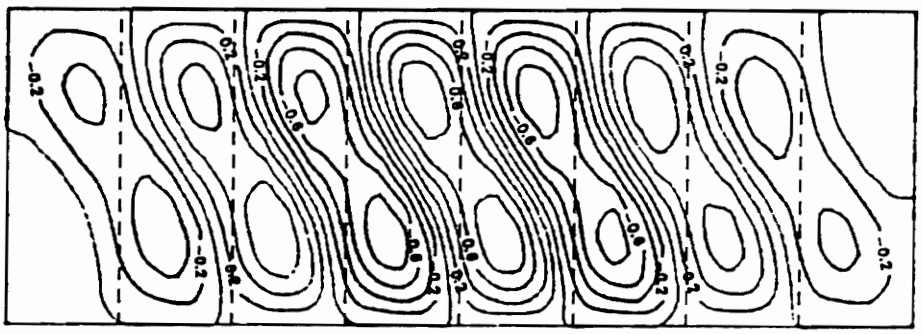

(H)

Longitudinally Stiffened Panel Buckled Mode Shapes, 10000 lbf/in Shear, cont'd

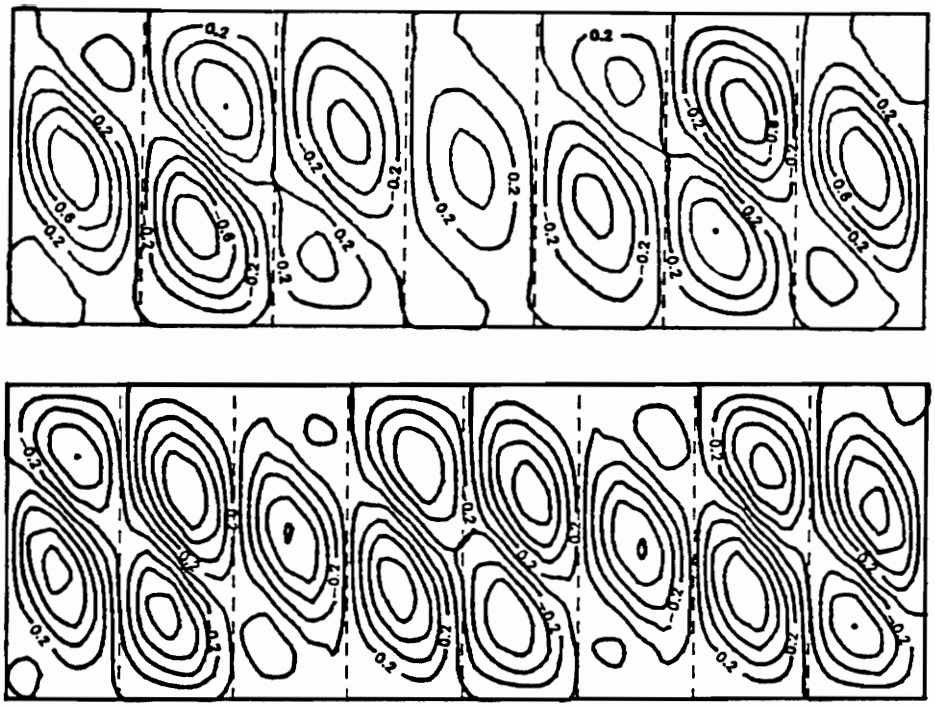

Figure C19. Longitudinally Stiffened Panel Buckled Mode Shapes, 10000 lbf/in Shear, Material Constraint Violation: A) 7 Cells B) 8 Cells

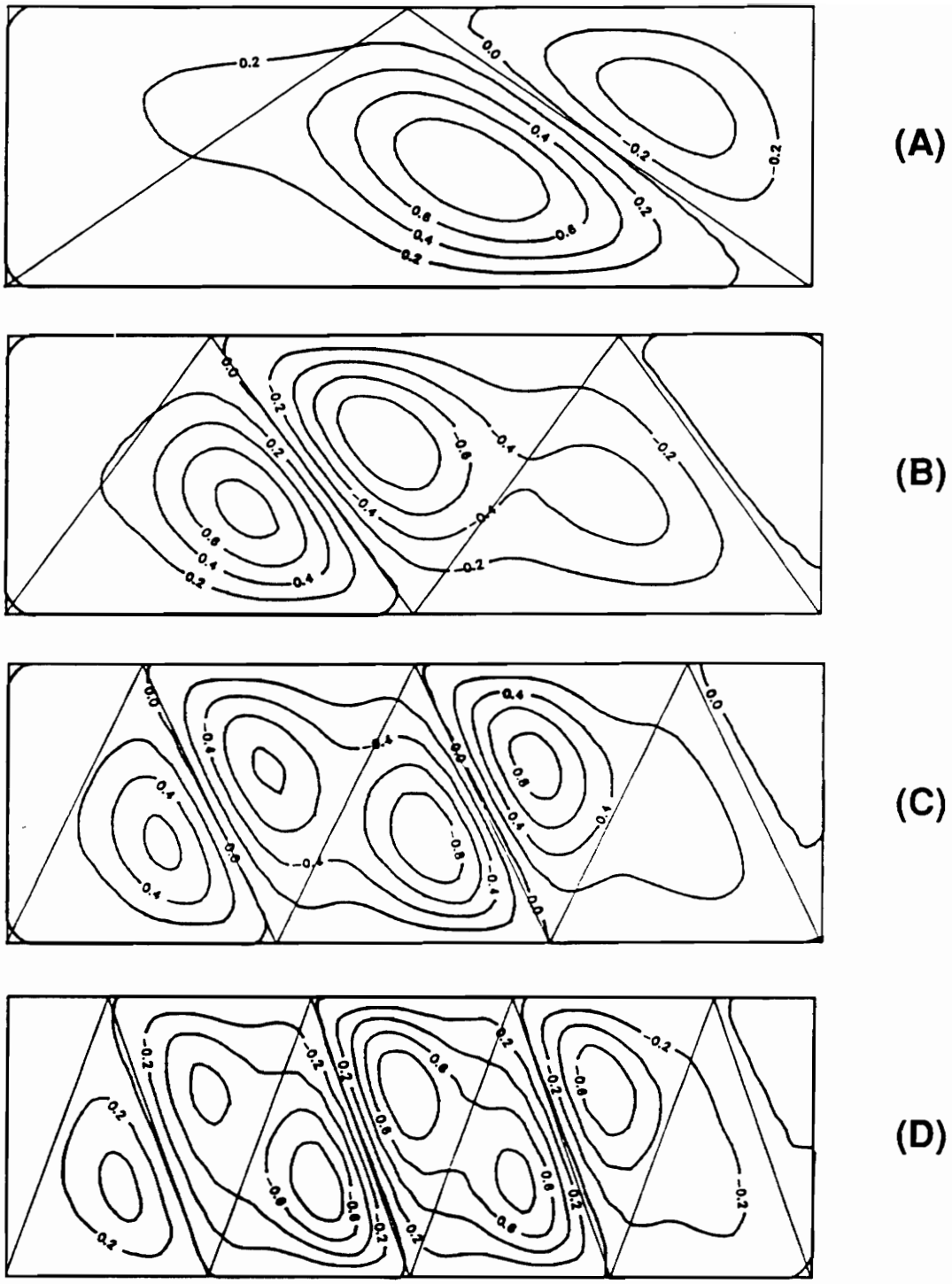

Figure C20. Diagonally Stiffened Panel Buckled Mode Shapes, 10000 lbf/in Shear: A) 1 Cell B) 2 Cells C) 3 Cells D) 4 Cells E) 5 Cells F) 6 Cells G) 7 Cells H) 8 Cells

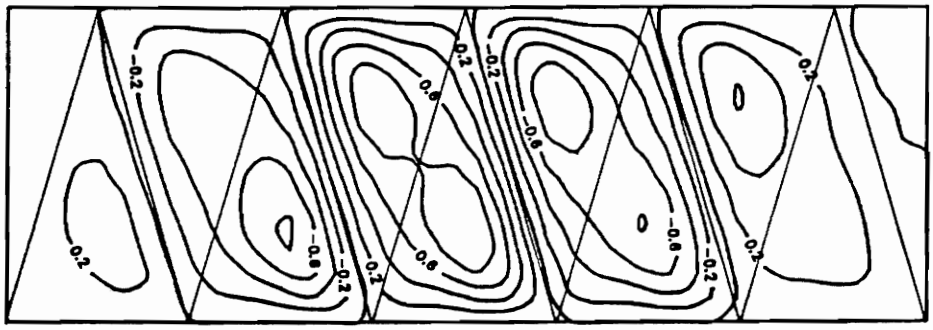

(E)

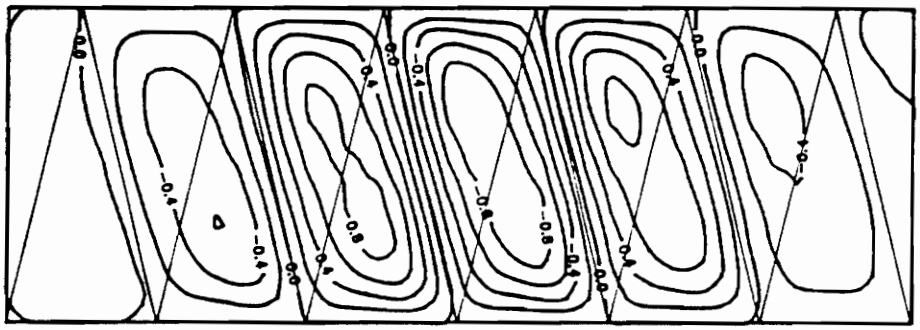

(F)

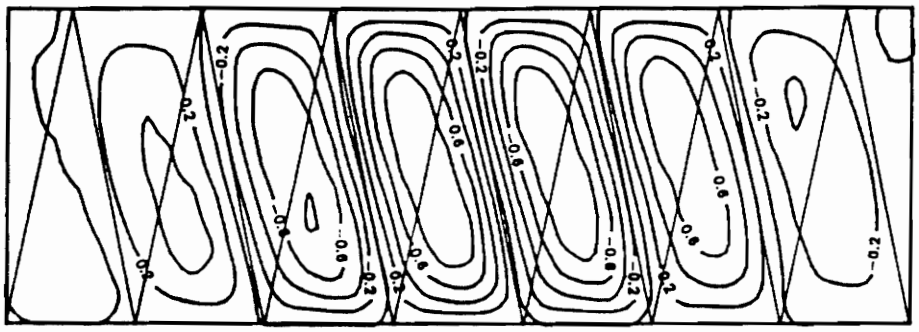

(G)

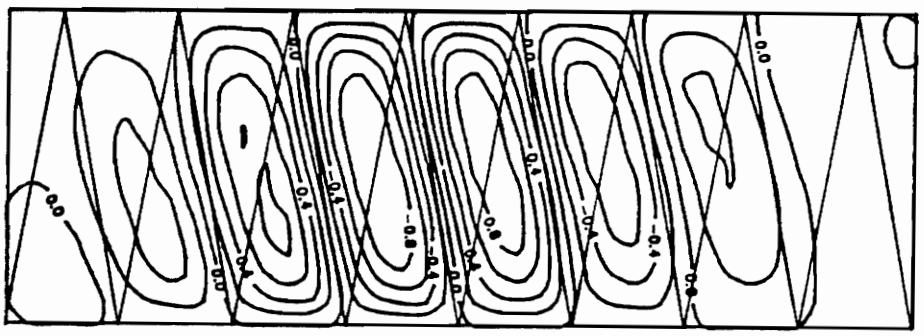

(H)

Diagonally Stiffened Panel Buckled Mode Shapes, 10000 lbf/in Shear, cont'd

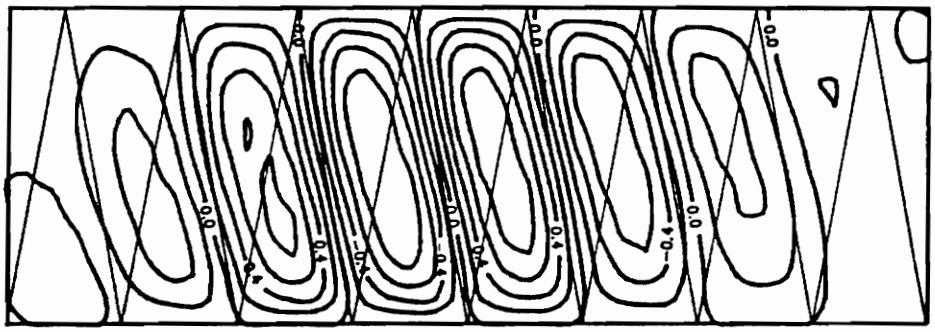

(A)

Figure C21. Diagonally Stiffened Panel Buckled Mode Shapes, 10000 lbf/in Shear, Material Constraint Violation: A) 8 Cells

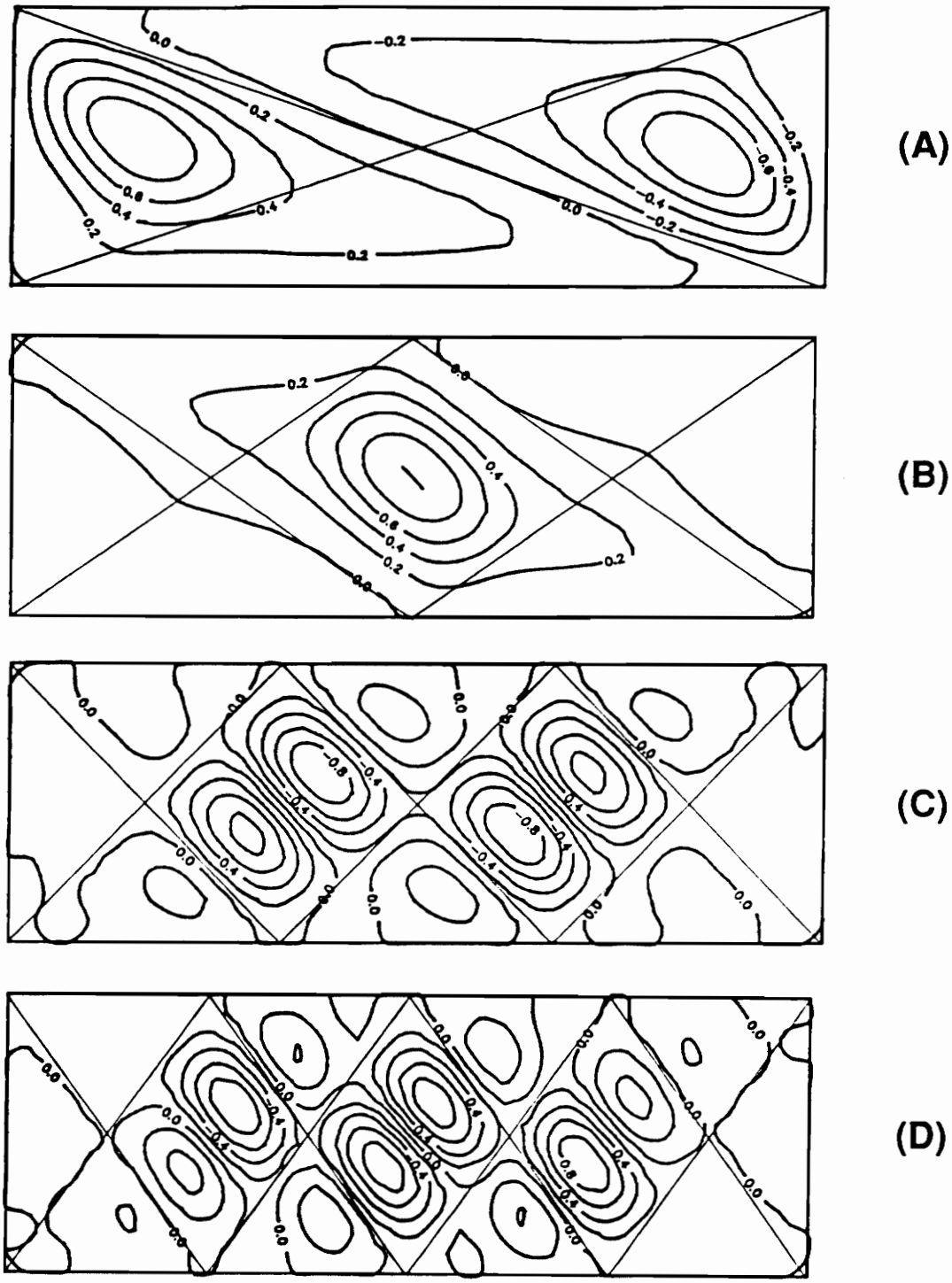

Figure C22. **Cross-Stiffened Panel Buckled Mode Shapes, 10000 lbf/in Shear:** A) 1 Cell B) 2 Cells C) 3 Cells D) 4 Cells E) 5 Cells F) 6 Cells G) 7 Cells H) 8 Cells

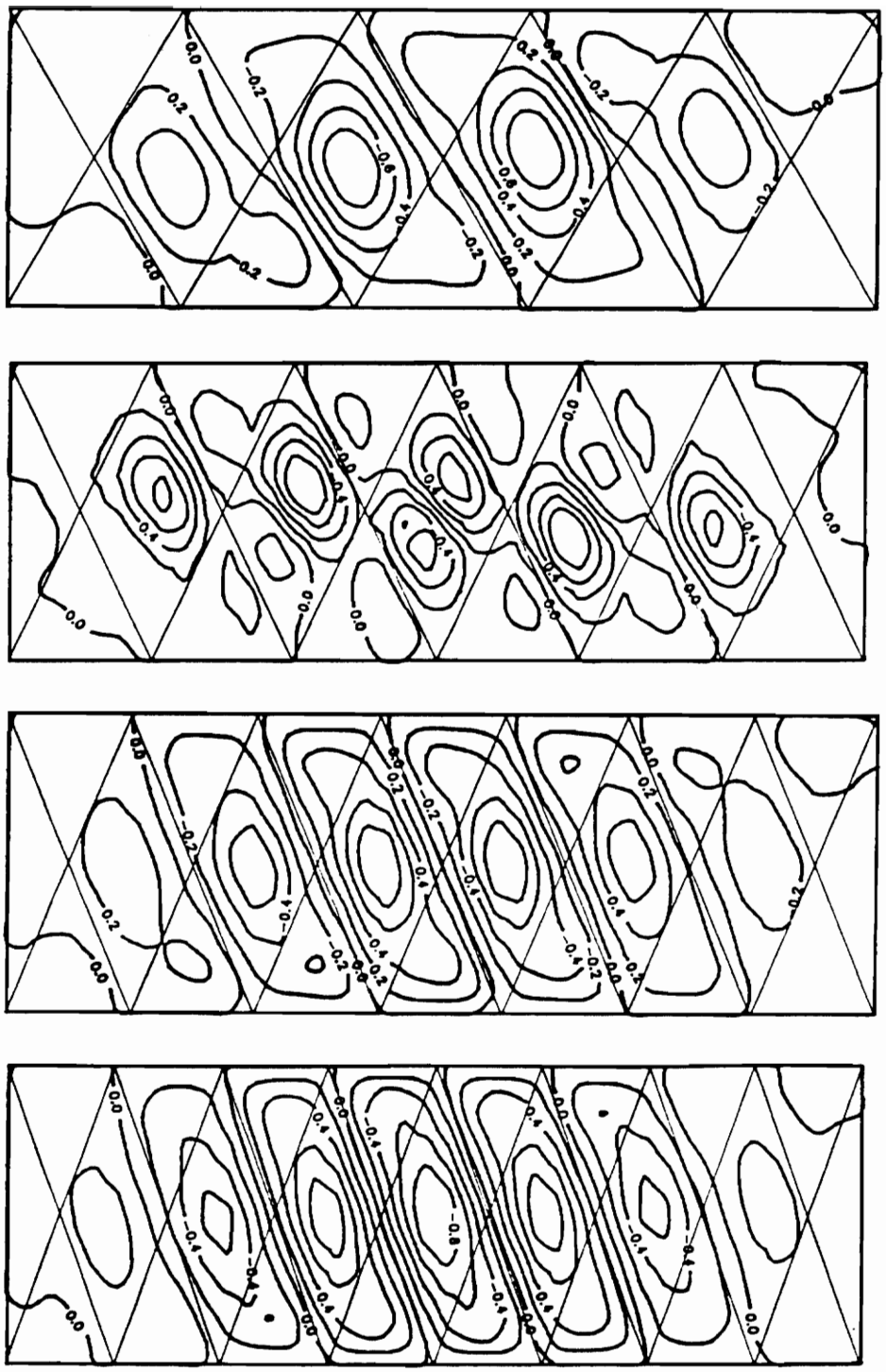

Cross-Stiffened Panel Buckled Mode Shapes, 10000 lbf/in Shear, cont'd

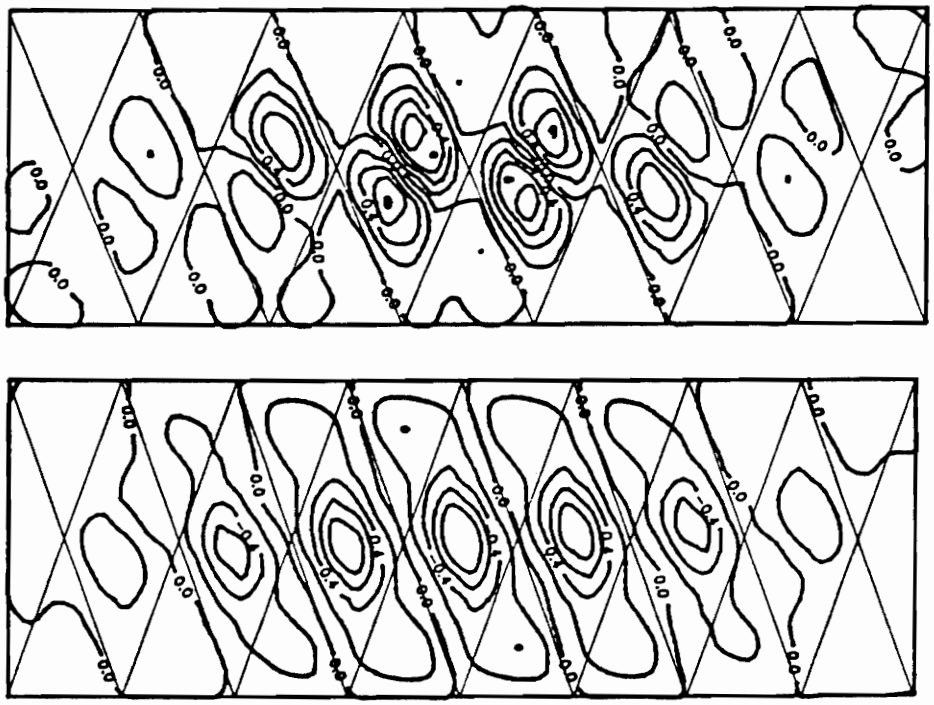

Figure C23. Cross-Stiffened Panel Buckled Mode Shapes, 10000 lbf/in Shear, Material Constraint Violation: A) 7 Cells B) 8 Cells

Vita

The author was born on July 16, 1962 in Trail, British Columbia, Canada. Upon graduation from J. Lloyd Crowe Senior Secondary School in June 1980, he completed a pre-Engineering program at Selkirk College in Castlegar, British Columbia. Beginning in September 1982, he participated in the Co-operative Engineering program at the University of Waterloo in Waterloo, Ontario. In May 1987, he graduated with First Class Honors and on the Dean's Honors List with a Bachelor of Applied Science degree in Mechanical Engineering. He then enrolled in the Engineering Mechanics program at Virginia Polytechnic Institute and State University in September 1987 to pursue a Master's degree specializing in composite materials.